School of Mathematical, Physical and Computational Sciences

Modelling PDEs in Population Dynamics using Fixed and Moving Meshes

by

Katerina Christou

Thesis submitted for the degree of Doctor of Philosophy

in Mathematics
School of Mathematical, Physical and Computational Sciences

University of Reading

December 2022

Declaration

I confirm that this is my own work and that the use of all material from other sources has been properly and fully acknowledged.

Katerina Christou

Publications

The work in Chapters 6 and 7 of this thesis is strongly based on the following publications:

- Baines, M. J., & Christou, K. (2021). A moving-mesh finite-difference method for segregated two-phase competition-diffusion. *Mathematics*, 9(4), 386.

- Baines, M. J., & Christou, K. (2022). A numerical method for multispecies populations in a moving domain using combined masses. *Mathematics*, 10(7), 1124.

All work undertaken in these publications was carried out by Katerina Christou with coauthors providing guidance and review.

Abstract

This thesis concerns the modelling of partial differential equations in population dynamics and examines two approaches to the choice of meshes for the numerical approximation of the equations. The first part describes a fixed-mesh approach to the predator-prey Lotka-Volterra equations and applies it to a two-dimensional temperature-dependent parasitism system. A climate function is used to incorporate the effect of climate change with the aim to explore the impact of ongoing warming on the spatial distribution and community formation of the interacting species. The second part concerns an adaptive approach to meshes for populations with moving boundaries, internal and external. In particular, a velocity-based moving mesh method based on conservation is applied to systems of competitive species with moving boundaries by which species interact, arise or disappear. The application of the method to epidemic models is also examined where the spreading of the disease through the domain is modelled by a moving front. This is achieved using a moving mesh technique governed by conservation in which the masses of coexisting species are combined. We conclude that fixed mesh methods are adequate for many problems in population dynamics, but where there are significant moving boundaries, as in evolving population domains, the moving mesh method based on conservation is an advantageous choice, as it allows the accurate handling of the moving boundaries and the efficient treatment of topological changes.

Acknowledgements

First and foremost, I would like to express my heartfelt thanks to my supervisors, Prof Mike Baines and Dr Peter Sweby, for their excellent guidance in both my scientific research as well as my professional development. I am truly grateful for our countless discussions, your patience and your encouragement through the years. None of this would have been possible without your wealth of knowledge and exciting ideas. I am honoured to have you as my mentors and I really value all the knowledge that you have shared along our four-year-long journey.

My collaborators for the work in Chapter 3, Dr Hélène Audusseau (Department of Zoology, Stockholm University) and Dr Reto Schmucki (UK Centre for Ecology and Hydrology), have also been beyond helpful with mentorship. Thank you for sharing your biological knowledge and allowing me to see my project from a biological perspective, alongside the mathematical one.

I extend my gratitude to Reading University Mathematics Department who organised everything from the funding to the constructive monitoring meetings.

Outside academia, I would like to thank my parents for always giving me the best education they could and I hope this thesis gives you pride and gratification. Thank you for teaching me to dream big and that in life there are no locked doors, every door is open, I just need to knock first. A huge thanks to my sister who has always been my biggest supporter and my first-to-go person for any advice I need.

I am grateful to my friends here in the UK and the ones back in Cyprus who have never failed to provide limitless emotional support. Especially to my partner who has created for me a home away from home. Thank you for all the unconditional support, your useful suggestions and your willpower to understand moving meshes.

This work has been accomplished with the financial support of the Natural Environment Research Council for Doctoral Training in the Quantitative and Modelling skills in Ecology and Evolution.

Contents

List of Figures

List of Tables

Chapter 1

Introduction

Partial differential equations (PDEs) are fundamental to the modelling of natural phenomena and are used in almost every field of science and engineering. PDEs provide the means for tackling a vast and ever-growing range of real-world problems from the simple heat equation to systems describing financial models, to weather forecasting or equations describing population dynamics. Consequently, the desire to understand the solutions to these equations has always had a prominent place in the efforts of mathematicians. Numerical approximation for such models may sometimes be challenging, though greater understanding and insights can be gained on the different characteristics of the phenomena as well as providing valuable predictions.

Techniques for numerically approximating such equations are well established and are subject to continual refinement and improvement. Throughout the years, several sophisticated numerical techniques, such as finite difference or finite element method, have been developed and used to solve PDEs. The basic idea of such methods is that the space variables are discretized on a selected space mesh, using finite-difference or finite-element approximations. In effect, in the particular case of time-dependent PDEs, the only independent variable remaining is time and hence the resulting system of ordinary differential equations (ODEs) is time-stepped to approximate the original PDE. These methods have been extensively used to approximate a broad class of problems and have been proven to be highly robust, and reliable. Considerations of such methods arise in regard to their accuracy. To improve the accuracy one must decrease the spacing of discretised nodes in the domain. Due to stability considerations, the time step must be decreased in accordance with the increase in spatial nodes which results in a highly computationally expensive scheme.

These methods, referred to as fixed mesh methods, work very adequately, especially for problems where the solution does not exhibit a high degree of spatial activity, but also for problems where regions of rapid variation of the solution do not move in space when time evolves in which case a finer grid must be used around these regions.

However, for certain phenomena in which the solution exhibits sharp moving features like inner or outer travelling wave-fronts or emerging boundary and interior layers, a fixed mesh method where the grid remains unchanged for the entire calculation (for all time steps) can be very computationally inefficient as it would require the use of a very fine grid throughout the space domain.

In such cases, having a mesh that moves with time is desirable to track these features accurately without the computational expense of increasing the resolution everywhere. Methods of such an approach belong to the realm of adaptive or moving-grid methods.

In the broad field of mesh adaptation there are three basic approaches: *h-refinement* which includes the addition of extra mesh points around an area of interest; *p-refinement* which involves the use of a higher-order polynomial in each spatial node intervals to better approximate the values between the mesh points and hence the solution; *r-refinement* which describes the dynamic movement of existing mesh points to track a feature of interest.

The former two belong to the static category while the latter to the dynamic. For the static methods, an initial mesh must be created on which the solution and the equation are defined. During the calculation, the number of nodes in the domain might differ as a new mesh is constructed, based on properties of a certain function that measures the quality of the approximation. Interpolation of the solution on a new mesh is then required and a new approximation to the solution is constructed on the new mesh. The adjustment of the already existing nodes, the insertion of new nodes and the interpolation of the dependent variables on the new mesh are done at a fixed time. The continual redistribution and interpolation lead to a slow computational scheme and, while static methods have proven to be robust for problems with sharp or moving spatial transitions, they can be very inefficient.

Dynamic methods, also known as moving mesh methods, require a mesh equation which gives the nodal velocities. The number of nodes remains constant for all calculations and existing nodes are relocated in the domain to better approximate critical regions. A mesh equation and the original differential equation are often solved simultaneously for the physical solution and the mesh. Hence, readjustment of the node number is not required nor continual interpolation. These

features make moving mesh methods most appropriate for problems exhibiting sharp spatial variations in the solution or at moving boundaries.

Velocity-based moving mesh methods have been developed through the years which differ in the way the nodal positions equation is derived. In this thesis, special attention is given to a specific type of moving mesh method where the moving mesh equation is constructed using the concept of mass conservation. In the context of population dynamics, mass refers to the total number of individuals in a population. This approach involves assigning a local proportion of mass within each patch of elements. Then the local "mass" of the species remains constant in time as the solution evolves, implying that regions with increasing density will have a denser mesh. The method is not only applicable to systems which conserve global mass, a version of the method has also been developed for non-mass conserving problems. This approach is similar to one of mass conserving but instead of local proportions of mass, uses relative proportions of mass or density.

The moving mesh method based on conservation has a very wide range of applications as the desired quantity does not have to be mass or density. Other quantities, such as volume, concentration or temperature, may be appropriate alternative choices.

In particular, the approach taken in this thesis is a one-dimensional finite difference version of the moving mesh finite element approach proposed by Baines, Hubbard and Jimack [14]. This technique has very few studied applications, particularly for population systems. In this thesis, we apply the velocity-based moving mesh method of [14] to a range of moving boundary problems emerging in population dynamics by which species arise, overlap or disappear. We mainly concentrate on its application to one-dimensional spatial systems since they offer greater scope for understanding the mechanism involved, and for analysis which may be expanded to more general situations.

Although the application of the moving mesh method to a two-dimensional Cartesian coordinate space domain is not considered in the thesis, we do illustrate its application to a two-dimensional radial case. We also solve a two-dimensional Cartesian coordinate system with a fixed mesh method.

Population Models

The scope of this thesis is to examine the application of different numerical schemes to equations regarding population dynamics. The time-dependent interactions between modelling species are of great interest to ecologists. Starting from the best-known set of equations, the predator-prey Lotka-Volterra equations, which were first derived in the 1920s [111] [165], mathematical modellers

have extended this pair of equations to much more complicated systems which describe many more biological scenarios, other than the predator-prey relationship, such as competitive species, symbiosis, disease models (SIR susceptible-infected-recovered models) and many more. However, these sets of ordinary differential equations do not consider spatial effects. The inclusion of a diffusion term was first introduced by Conway and Smoller in [44] along with spatial dependence giving rise to partial differential equations. This allowed the study of a vastly increased range of phenomena, such as ecological invasions, the effect of habitat geometry and size, coexistence, and the effect of non-homogeneous resource distribution. Alongside the standard Laplacian diffusion of [44] describing the random walk of species, advection terms have also been included in many population models which describe the directed movement of species towards favourable spatial regions with better environmental conditions, giving rise to reaction-diffusion-advection models.

In this thesis, we examine the numerical approximation of a variety of reaction-diffusion(-advection) population models including a temperature-dependent predator-prey model with directed movement based on species' fecundity gradient (Chapter 3) and a model of two highly competitive species which are spatially segregated and separated by a moving interface (Chapter 6). Moreover, we focus on a system of two cohabiting species with moving boundaries where species compete for the same resources (Chapter 7) and a SI(R) and a SIRV (susceptible-infected-recovered-vaccinated) model with cross- and self-diffusion where the spread of the epidemic is modelled through a moving front (Chapter 8).

The nature of the problem being solved indicates the correct choice of a numerical technique, e.g., if the system being solved exhibits spatial variations.

The simulations in the thesis are novel and the illustrations of the results derived from a range of different parameter choices indicate that the population models and the numerical methods used are suitable to realistically model many ecological relationships and real-world situations.

The first part of the thesis concerns a model suitable to describe many real-life complications such as climate change and aims to answer a crucial ongoing question in ecology; how global warming and increasing temperatures through the years affect the patterns of coexistence of interacting species. The climate function which is used to incorporate climatic influence in the model is general and can be easily adjusted and adapted to many situations. The model and results appear to be a good overarching starting point to understand the implications of global warming to species.

The novelty of the second part of the thesis (Chapter 4 - Chapter 8) lies in the

theoretical and numerical treatment of moving boundaries in population dynamics as well as a combined mass approach for cohabiting species, which are not standard in the numerical modelling literature. The emphasis of this part of the thesis is on the role of the moving mesh method based on conservation in tracking free and moving boundaries in population dynamics.

1.1 Outline

The thesis is structured as follows.

In Chapter 2 we provide a general background on the predator-prey models of the literature and discuss the inclusion of different spatial effects in the model. We particularly focus on a system describing a parasitoid-host relation. Parasitoids are insects whose larvae develop by feeding on the bodies of their hosts, which are usually other arthropods, often insects. Parasitoids are considered intermediate between predators and parasites since like predators, they kill the host they attack. The system is modelled by one-dimensional coupled reaction-diffusion-advection equations with directed movement based on a fecundity gradient. This extra velocity term (the advection term) can alter the direction of species dispersal by accounting for both spatial heterogeneous environments, i.e., food resources, and the species interactions. After carrying out a stability analysis of the model, we provide a detailed procedure for the approximation of the system by two fixed mesh numerical methods, the finite element and the finite difference methods. We briefly discuss the stability considerations associated with the explicit integration scheme and we proceed with the application of a semi-implicit finite difference scheme to approximate the system which avoids such concerns.

In Chapter 3 we extend our model of Chapter 2 to two dimensions where we also include the climatic influence by the use of a climate function affecting both species' movement and the logistic growth of the prey. Following the stability analysis of the two-dimensional temperature-dependent model and the numerical approximation, we provide illustrations of the results derived by gathering the maximum temperatures observed in Spain and Portugal in 1950 and 2020 and the temperature projections for the year 2050. The scope of this work is to investigate how the parasitoid and host spatial distribution is affected by the increase in temperature through the years. This work is a collaboration with Dr Hélène Audusseau (Department of Zoology, Stockholm University) and Dr Reto Schmucki (UK Centre for Ecology and Hydrology).

In Chapter 4 we provide the background to moving mesh methods with a particular focus on the moving mesh method based on mass conservation which will be the main focus for the rest of the thesis.

Following the discussion in Chapter 2 regarding the inability of the classical Fickian diffusion to realistically reflect the species dispersal, in Chapter 5 we focus on the Porous medium equation which provides the most widely used density-dependent diffusion and we show some of its properties using simulations. We then use the method described in Chapter 4 to numerically solve a two-cluster population system with non-linear density-dependent diffusion. We consider both the non-mass-conserving and mass-conserving versions of the two-cluster system.

Later in Chapter 6, the velocity-based moving finite difference method based on conservation is applied to a one-dimensional two-species competition system in which the competition is sufficiently strong to segregate the two populations separated by a moving interface spatially. The model is implemented numerically with a variety of parameter combinations, illustrating how the populations may evolve over time. We conclude that the model and the method are likely to be able to satisfy the requirements for modelling a wide variety of competition systems. This chapter is based on the paper of Baines and Christou [11].

In Chapter 7 we introduce a new feature of the moving mesh method based on conservation which considers the combined mass of the species. The combined mass of the species in the system is the quantity which is preserved within each patch of elements (or the relative combined mass in case of non-mass conserving problems). This approach is beneficial when dealing with coupled equations where species have overlapping domains as it avoids the interpolation of the species meshes at each time step and only one velocity equation is required as the whole system is solved on a single mesh. Motivated by the highly competitive system of Chapter 6, here we consider a two-competitive species system in which species coexist in space but still compete for common resources. This system consists of both moving external boundaries and moving interior interfaces by which species spread out in the domain or disappear. The method is illustrated in this one-dimensional competition system in which a range of parameters is explored. We also extend our study to the two-dimensional radial case of the system. The results of this chapter indicate that the methodology can be generalised for more complex equations that more realistically describe species' behaviour and evolution through time. This chapter is based on the paper of Baines and Christou. [15].

Besides the classical Laplacian diffusion of Chapters 6 and 7 and the density-dependent diffusion of Chapter 5, many modellers have advanced these systems by the inclusion of advection terms to model species' bias or directed movement to more favourable parts of the domain. This motivates the study of a SI(R) (susceptible-infected-recovered) model with a free boundary in Chapter 8 where we incorporate self-isolation and social distancing of individuals by self-

and cross-diffusion. We again consider the concept of combined masses for applying the moving mesh finite difference method to the SI(R) model with Fickian diffusion. We then demonstrate that the combined mass approach can also be applied to systems consisting of more than two species by considering a SIRV (susceptible-infected-recovered-vaccinated) system with density-dependent nonlinear diffusion.

Finally, in Chapter 9 we present our main conclusions. We briefly summarise the different numerical methods used to approximate the population models of this thesis and describe the strategy taken for the study of the systems. This thesis provides readers with guidance on numerical implementations for the accurate approximation of partial differential equations in population dynamics and provides insights into additional terms which can be easily implemented in the model to realistically describe different ecological phenomena. The results of the thesis are general and can be refined in many different directions. We consider the implications of our findings for the wider modelling of population dynamics. Combining the knowledge into the different numerical techniques presented and described in this thesis together with the theoretical understanding of the modelling of species interactions ensures the use of an appropriate method for a given problem. Finally, we suggest future work that could be undertaken to extend the conclusions of this thesis.

1.2 Novel Material

The thesis contains the following novel contributions:

- A two-dimensional fixed mesh finite difference implementation of a reaction-diffusion-advection parasitism system with climate change.
- A moving mesh finite difference method based on conservation (MMFD) for the two-phase competition system derived by Hilhorst et al. [75].
- A numerical model for a two-cluster population system using the moving mesh finite difference method.
- A novel approach to moving mesh based on mass conservation for cohabiting species with coupled equations; the combined mass approach.
- An application of the combined mass approach using a finite difference framework to a system of two competitive cohabiting species satisfying coupled reaction-diffusion equations with overlapping domains.
  Extension of the study to the two-dimensional radial case.

- Approximate solution of an epidemic SI(R) numerical model with self-isolation and social-distancing effects using the MMFD method based on combined masses.
- Approximate solution of a reaction-diffusion-advection SIRV model with density-dependent diffusion by the combined mass approach of the MMFD method.

Chapter 2

Population Dynamics/ Predator-Prey

Population dynamics provide both the basis for studying complex communities and providing insights into many applied questions in ecology. Understanding population dynamics is the key to understanding the relative importance of competition for resources and predation in structuring ecological communities, which is a central question in ecology [72]. This chapter gives a background on systems describing population dynamics with a focus on the predator-prey relationship. A simple predator-prey system described by ordinary differential equations in Section 2.1 is followed by a discussion on spatial inclusivity (Section 2.3) resulting in a diffusion-advection-reaction system in Section 2.5. Of special attention in this study is a particular predator-prey system with directed movement based on a fecundity gradient (ability to reproduce), which was first used by Grindrod [63] in the context of competitive species. Stability analysis of the model is carried out in Section 2.5.2 to obtain constraints on the parameter values in order to produce stable steady states. Then in Section 2.6, the model is numerically approximated by the explicit finite difference and finite element methods in a one-dimensional domain and convergence analysis is carried out in Section 2.7 to obtain the rate of convergence of each method. As is well-known, the numerical solution of explicit schemes becomes unstable unless the time step is severely restricted. We therefore in Section 2.9 consider a semi-implicit scheme for the approximation of the system which avoids such a constraint.

2.1 Time-Dependent Predator-Prey

A classical predator-prey system can be written in the form

$$\frac{du}{dt} = ur(u) - \alpha v g(u,v) \qquad \frac{dv}{dt} = v(\alpha\varepsilon g(u,v) - d), \tag{2.1}$$

where u and v are the population densities at time t of the prey and the predator, respectively. The terms $\frac{du}{dt}$ and $\frac{dv}{dt}$ describe the rates of change of the population densities in time, where from an ecological point of view the conditions $u > 0$ and $v > 0$ must hold. The function $r(u)$ is the prey growth rate, and $g(u,v)$ is the functional response which describes how the temporal variation in prey density affects the rate at which prey are killed by predators. The constant α indicates the rate that the predator attacks prey. The functional response in the prey equation describes how many prey are being killed instead of eaten, the important factor from the point of view of prey being how many individuals are being removed from the community. The consumption part (how many prey are being eaten) is an important factor from the predator's point of view, hence the functional response $g(u,v)$ being multiplied by the constant ε which describes the rate of conversion of the hosts. The constant d is the *per capita* predator death rate.

2.2 Functional Response

There are many different kinds of functional responses $g(u,v)$ that have been used over the years to describe predator-prey dynamics. In the book [158], some of the well-known functional responses are listed and discussed. Functional responses can be classified into three categories, (i) prey-dependent, where the prey alone determines the response, i.e., the functional response depends only on the rate of change of prey density, (ii) predator-dependent where both the predator and the prey affect the response, leaving aside the issue of predator cooperation in hunting and subduing prey it is likely that predator encounters will lead to antagonistic interactions: intraspecific interactions can affect the birth and death rate of the predator as well as the efficiency of the predator in finding and killing the prey, (iii) multi species-dependent where species other than the predator and its prey influence the functional response.
Examples of functional responses used extensively over the years are the Beddington functional response [88, 56] which is classified as predator-dependent and the Holling Type I-III [78, 77, 145, 100, 149, 107] and Ivlev-type [169, 89] which are classified as prey-dependent. The Holling Type I gives a linear relationship

between the rate of change of prey density and the consumption rate, Type II (hyperbolic response) describes the effect when the gradient decreases as the prey population increases (similar to Ivlev), and Type III (sigmoid response) is used when the gradient first increases and then decreases with increasing prey population. Note that the functional response also describes the predator satiation effect as at high prey population density the rate of prey consumption levels off and the gradient of the graph approaches zero.
In this thesis, we are mainly interested in the well-known Holling type II which is similar to Ivlev-type and takes the form

$$g(u, v) = \frac{u}{A + u}, \tag{2.2}$$

where A is the prey population size at which the growth rate of the predator is half its maximum. Equation (2.2) describes the rate of prey consumption by a predator which rises as prey density increases, but eventually levels off at an asymptote at which the rate of consumption remains constant regardless of increases in prey density. Holling type II functional response is widely used and has stood up as the "null model" upon which much predator-prey theory has been constructed [30].
The ordinary differential sets of equations, such as (2.1), do not consider spatial effects. An important development was first made by Conway and Smoller in 1977 [45], where a diffusion term was included along with spatial dependence giving rise to partial differential equations.

2.3 Spatial Variation

Most of the elemental components of ecology, extending from individual behaviour to species interactions, and population dynamics, exhibit spatial variation. Partial differential equations provide a means of combining both temporal and spatial processes and have been widely used to illuminate the effects of spatial variation on populations.

2.3.1 Fickian diffusion

The most simple form of modelling species movement through PDEs is the reaction-diffusion heat equation, which assumes a homogeneous environment.
Such equations have the following form

$$\frac{\partial u}{\partial t} = \delta \frac{\partial^2 u}{\partial x^2} + f(u, x, t), \tag{2.3}$$

where $u(x,t)$ is the population density at time t and space x, the diffusion coefficient is δ, and f describes the reaction (source/sink) terms. The second derivative term represents random walk. In effect, the motility coefficient δ is constant and determines the rate at which each species disperses through a spatial domain. This diffusion term describes the movement of species from a region of high concentration to a region of low concentration in a homogeneous environment. However, in real life, species do not disperse randomly through space as does the behaviour described by the diffusive term. Moreover considering a homogeneous environment results in a very unrealistic model as species have the ability to sense the changes in the environment and adjust their movement accordingly.

2.3.2 Movement based on individuals' interactions

Although most applications of PDEs to spatial processes assume random diffusion of individuals there are many studies, mostly theoretical, for addressing more complex movement behaviour [122, 79, 36, 124]. For example, we can alter equation (2.3) so that it also includes interactions between conspecifics. Conspecifics are individuals that belong to the same species. If animals are only either attracted to one another or repelled from one another, then the sole diffusion model (2.3) can be replaced by a biased random motion model through an aggregation component ([68]), as in

$$\frac{\partial u}{\partial t} = \delta \frac{\partial^2 u}{\partial x^2} + \frac{\partial}{\partial x}\left(ku\frac{\partial u}{\partial x}\right) + f(u,x,t). \tag{2.4}$$

The first term on the right-hand-side of (2.4) describes the random diffusion of species where δ is the diffusion coefficient and the second term describes the dispersal of species according to the sign of the constant k, which is a measure of the tendency to move away from conspecifics when $k > 0$ and move towards conspecifics when $k < 0$.

The same concept can be applied to species of different populations. For example, an animal of another species with a population density, v say, that is attracted or repelled by individuals of population u can be modelled by a term

$$\pm \frac{\partial}{\partial x}\left(kv\frac{\partial u}{\partial x}\right).$$

These cross and self-diffusion terms have been used extensively in the context of predator-prey modelling to describe the tendency of the prey to move away from the predator and the attraction of the predator to move towards or chase the prey [99, 54, 113, 136, 64]. Apart from the species interactions, that can alter species dispersal, many organisms also modify their movement in response to environmental heterogeneity.

2.3.3 Movement based on fecundity gradient

The movement based on environmental heterogeneity is driven by features of the physical environment. For example, individuals move to higher-quality neighbouring areas depending on the state of the environment they momentarily occupy to increase their net rate of reproduction.
Animals who assess their physical environment can be modelled by [62, 148], as in

$$\frac{\partial u}{\partial t} = \delta \frac{\partial^2 u}{\partial x^2} - \frac{\partial}{\partial x}(u\nu) + f(u, x, t), \tag{2.5}$$

where ν is the velocity in which the populations advect towards an optimal direction.
Grindrod in [63] proposed a directed movement by which each species is moving along a fecundity gradient. This extra velocity term accounts for both spatial heterogeneous environments, i.e., food resources, and the species interactions and is solved by using additional equations as illustrated below. These additional equations express ν in terms of the species fecundity gradient as the directed velocity of species (ν) describes the movement of species towards an optimal direction in an effort to increase their fecundity gradient.
For example, let E be the net rate of reproduction per individual at x, at time t, within a local population density, i.e.,

$$E(u, x, t) = \text{average birth rate - average death rate,}$$

which increases as the quality of the habitat increases.
The relationship between ν and $E(u)$ is constructed with ν as a local average of $\frac{\partial E}{\partial x}$, i.e.,

$$-\epsilon \frac{\partial^2 \nu}{\partial x^2} + \nu = \frac{\partial E}{\partial x},$$

where ϵ ($\epsilon \geq 0$) is a small parameter which smooths any sharp variations between ν and $\frac{\partial E}{\partial x}$. Note that $-\epsilon \frac{\partial^2 \nu}{\partial x^2}$ is the effective local average for smoothing which gives some notion of imprecise knowledge of fitness gradients and helps regularize the advective dynamics.
Hence by [63], an equation such as (2.5) assumes that an individual's random walk is biased by some ideal or optimal velocity ν. Then an individual with velocity ν disperses deterministically so as to increase its expected rate of reproduction, taking into account both overcrowding and the quality of the habitat. Therefore, by taking random walks biased by ν, the population is, on average, dispersing in an ideal direction. Using the law of population balance we can derive an expression for the total velocity, say w, by which individuals are dispersing which accounts for both the random walks and the directed movement.

The law of population balance states that given a and b are the two outer boundaries,

$$\frac{d}{dt}\int_a^b u \, \mathrm{d}x + [uw]_a^b = \int_a^b f \, \mathrm{d}x. \tag{2.6}$$

where w is the velocity by which individuals are dispersing and f consists of source/sink terms. Equation (2.6) expresses that the rate of change of the population u in the domain (a, b) plus the rate at which individuals leave or enter the domain through the boundaries a and b must be equal to the rate at which individuals are supplied directly into the domain.

Since the mass in (a, b) is not time-dependent,

$$\int_a^b \frac{\partial u}{\partial t} \, \mathrm{d}x = -[uw]_a^b + \int_a^b f \, \mathrm{d}x. \tag{2.7}$$

Using (2.5) we obtain,

$$\int_a^b \frac{\partial}{\partial x}\left(\delta\frac{\partial u}{\partial x} - u\nu\right) \, \mathrm{d}x = -[uw]_a^b \,. \tag{2.8}$$

Performing the integration on the left-hand-side of (2.8) gives

$$\left[\delta\frac{\partial u}{\partial x} - u\nu\right]_a^b = -[uw]_a^b \,.$$

Choosing an anchor point such that the value of $\delta\partial u/\partial x - u\nu + uw$ vanishes leads to the equation for the velocity

$$w = -\delta\frac{1}{u}\Big(\frac{\partial u}{\partial x}\Big) + \nu. \tag{2.9}$$

given $u \neq 0$, where the minus sign indicates the direction.
Hence the velocity w per individual can be expressed as the sum of a random dispersion velocity and a biased velocity.

Since f in (2.5) denotes the rate at which individuals are supplied to the population at space x and time t due to births and deaths,

$$f(u, x, t) = uE(u, x, t).$$

Moreover, to simplify the solution procedure a potential function ϕ is introduced such that $\nu = \frac{\partial\phi}{\partial x}$, where ϕ is a velocity potential of ν. Hence, equation (2.5) becomes,

$$\frac{\partial u}{\partial t} = \delta\frac{\partial^2 u}{\partial x^2} - \frac{\partial}{\partial x}\Big(u\frac{\partial\phi}{\partial x}\Big) + uE(u, x, t) \tag{2.10}$$

and the additional equation for the advection direction in terms of fecundity is given by

$$-\epsilon\frac{\partial^2\phi}{\partial x^2}+\phi=E(u,x,t). \tag{2.11}$$

In the next section, we show how the classical Fickian diffusion described in Section 2.3.1 may be unsuitable to reflect a realistic dispersal of species in cases where the population density is extremely high or extremely low and discuss how a non-linear diffusion may be preferable to model species movement.

2.4 Density-Dependent Diffusion

As explained in Section 2.3.1, the classical theory of Fickian diffusion is based on the assumption that individual movement is driven solely by a certain type of random walk, in which the direction of flow is from regions of high concentration to regions of low concentration. Consider the following diffusion equation in a one-dimensional domain $\mathcal{R}$,

$$\frac{\partial u}{\partial t}=\frac{\partial}{\partial x}\left(\delta\frac{\partial u}{\partial x}\right)+f \quad x\in\mathcal{R}, \quad t\geq 0 \tag{2.12}$$

which describes how the population density $u(x,t)$ changes in time, where δ is the constant diffusion coefficient and f denotes the reaction terms.

At the initial time

$$u=u_0(x)\geq 0 \quad x\in\mathcal{R}, \quad t=0.$$

As in Section 2.3.3, by the law of population balance the velocity w is given by

$$w=-\frac{\delta}{u}\frac{\partial u}{\partial x}, \tag{2.13}$$

(*cf.* (2.9)), given $u\neq 0$, where the minus sign indicates the direction.
By (2.13), for a finite $\partial u/\partial x$ the diffusion velocity tends to infinity as u tends to 0, which is unphysical. If the diffusive velocity implies that individuals disperse to avoid crowding we would expect the diffusion velocity to decrease as u decreases.

This effect can be seen by supposing that $u_0(x)$ has compact support, i.e., u_0 is non-zero only inside a closed and bounded subset of $\mathcal{R}$ and zero throughout the rest of the domain.
The solution of (2.12) is given, using the heat kernel, by

$$u(x,t)=\frac{1}{\sqrt{4\pi\delta t}}\int_{\mathcal{R}}u_0 e^{\frac{-(x-y)^2}{4\pi\delta t}}\,\mathrm{d}y, \quad t>0.$$

Thus, if u_0 is non-zero, then $u(x,t) > 0$ for all $t > 0$ throughout the domain $\mathcal{R}$. Therefore the support of u is equal to the whole of $\mathcal{R}$ (not only in the bounded subset) for $t > 0$. Consequently, this means that a small number of individuals must move over arbitrarily large distances in any time interval $[0, \Delta t]$.

Therefore, while the Fickian diffusion is an appropriate model for many diverse transport processes and has been used by many population dynamics modellers, it is sometimes unsuitable, especially at extremely low or extremely high densities, [63].

Many studies over the years [59, 120, 174, 24] have used non-linear density-dependent diffusion as an alternative to the Fickian diffusion. For example, the partial differential equation for the rate of change of the density u with a density-dependent diffusion takes the form,

$$\frac{\partial u}{\partial t} = \frac{\partial}{\partial x}\left(D(u)\frac{\partial u}{\partial x}\right), \tag{2.14}$$

with appropriate boundary conditions where D is a function satisfying

$$D(0) = 0, \quad D_u(u) > 0 \quad \text{for} \quad u > 0.$$

By the law population balance equation (2.7) and (2.14),

$$\frac{\partial}{\partial x}\left(D(u)\frac{\partial u}{\partial x}\right) = -\frac{\partial}{\partial x}\left(uw\right). \tag{2.15}$$

Integrating (2.15) with respect to x implies that the velocity by which individuals are moving in the domain with the density-dependent diffusion takes the form,

$$w = -\frac{D(u)}{u}\frac{\partial u}{\partial x}.$$

Depending on the choice of the density-dependent function D, the velocity will not tend to infinity when $u \to 0$, for example, when $D = u$ (*cf.*(2.13)).

The use of a non-linear diffusion in population biology is becoming popular over the years but still, the majority of modellers use a linear diffusion to describe species dispersion mainly due to the easier application and the similar effect to the non-linear diffusion. Thus the following population system considers the standard Fickian diffusion to describe species diffusion.

Having described how spatial variation can be incorporated in the equations for modelling species evolution we apply equations (2.10) and (2.11) in the content of a one-dimensional predator-prey model with Holling type II functional response.

2.5 1-D Reaction-Diffusion-Advection Predator-Prey System

The predator-prey system with directed species movement takes the form

$$\frac{\partial u}{\partial t} = \delta_u \frac{\partial^2 u}{\partial x^2} - \frac{\partial}{\partial x}\Big(u \frac{\partial \phi_u}{\partial x}\Big) + uE_u \tag{2.16}$$

for the prey, and

$$\frac{\partial v}{\partial t} = \delta_v \frac{\partial^2 v}{\partial x^2} - \frac{\partial}{\partial x}\Big(v \frac{\partial \phi_v}{\partial x}\Big) + \ vE_v \tag{2.17}$$

for the predator. Then, the expressions for the net rate of reproduction of the two populations are

$$E_u(u, v, x, t) = r\left(1 - \frac{u}{K}\right) - \frac{\alpha v}{A + u} \tag{2.18}$$

and

$$E_v(u, v, x, t) = \frac{\alpha \varepsilon u}{A + u} - d. \tag{2.19}$$

Finally, the equations which give the value of the directed velocity potentials ϕ_u and ϕ_v are

$$E_u(u, v, x, t) = -\epsilon_u \frac{\partial^2 \phi_u}{\partial x^2} + \phi_u \tag{2.20}$$

and

$$E_v(u, v, x, t) = -\epsilon_v \frac{\partial^2 \phi_v}{\partial x^2} + \phi_v, \tag{2.21}$$

respectively. The constants ϵ_u and ϵ_v are very small parameters for smoothing any sharp variations in $E_u(u, v, x, t)$ and ϕ_u and $E_v(u, v, x, t)$ and ϕ_v.

The one-dimensional system (2.16)-(2.21) is applied on a domain defined by $[a, b]$ where the zero Neumann boundary conditions

$$\frac{\partial u}{\partial x} = \frac{\partial v}{\partial x} = 0, \quad t > 0 \quad x = a, b$$

are imposed, implying no migration across the boundaries.

This general predator-prey model is used in the thesis to model parasitoid-host interactions. The definitions of the parameters in the model in the context of a parasitoid-host system are described below which are strongly based on the paper of Pearce et al. [127] with different notations. Pearce et al. [127] used an Ivlev functional response to model parasitism whereas here we have chosen the Holling type II functional response as described in Section 2.2. The host (in the absence

of the parasitoid) is modelled as having logistic, density-dependent growth, with the intrinsic growth rate denoted by r and the carrying capacity denoted by K. Parasitism rate is denoted by α and ε is the predator conversion efficiencies of hosts to parasites. The parasitoid is subject to intrinsic mortality rate d where A denotes the half-saturation constant of the parasitoid. The motility coefficients δ_u and δ_v of the two species are constants and determine the rate at which each species disperses randomly through the domain. Definitions of the variables and parameters are available below in Table 2.1.

Parameter/Variable	Description
u, v	Population density
δ_u, δ_v	Diffusive parameter
r	Intrinsic growth rate for prey
K	Carrying capacity for prey
ε	Parasitoid conversion efficiencies of hosts to parasitoids
α	Parasitism rate
d	Intrinsic mortality rate of parasitoids
$\phi_{1,2}$	velocity potential of ν (see (2.9))
A	Predator half-saturation constant

Table 2.1: Model variables and parameters for the parasitoid-prey model defined by (2.16)-(2.21).

In the next section, we carry out a stability analysis for the system (2.16) and (2.17). We first non-dimensionalise the equations to simplify the system and interpret complex interactions of variables. Then, we find the biologically relevant equilibrium points of the movement-free version of the system (2.16) and (2.17) and we present some results on the stability of equilibria and the existence of Hopf bifurcation through numerical simulations.

2.5.1 The dimensionless model

It is much more transparent to work with equations that have been scaled to non-dimensional form. Thus we define the following non-dimensional variables: $\hat{x} = x/\chi$, $\hat{t} = t/\tau$, $\hat{u} = u/U$, $\hat{v} = v/U$, $\hat{\phi}_{i=u,v} = \phi_{i=u,v}/\Phi$ (where U is a normalising density and Φ is a normalising velocity potential $\phi_{u,v}$) in the system (2.16) and (2.17) which gives the following dimensionless equations.

Substituting the above non-dimensional variables and setting $\Phi\tau/\chi^2 = 1$ and

$r\tau = 1$, the non-dimensional form of the equation (2.16) is given by

$$\frac{\partial \hat{u}}{\partial \hat{t}} = D_u \frac{\partial^2 \hat{u}}{\partial \hat{x}^2} + \Big(\frac{\partial}{\partial \hat{x}}\Big(\hat{u}\frac{\partial \hat{\phi}_u}{\partial \hat{x}}\Big)\Big) + \hat{u}\Big(1-\hat{u}\Big) - \frac{s_1 \hat{u}\hat{v}}{z+\hat{u}}, \tag{2.22}$$

where $s_1 = \alpha/r$, $D_u = \delta_u/r\chi^2$, $z = A/K$.
Rewriting equation (2.17) in terms of the dimensionless variables gives the non-dimensional form

$$\frac{\partial \hat{v}}{\partial \hat{t}} = D_v \frac{\partial^2 \hat{v}}{\partial \hat{x}^2} + \Big(\frac{\partial}{\partial \hat{x}}\Big(\hat{v}\frac{\partial \hat{\phi}_v}{\partial \hat{x}}\Big)\Big) + \frac{s_2 \hat{u}\hat{v}}{z+\hat{u}} - \beta \hat{v}, \tag{2.23}$$

where $D_v = \delta_v/r\chi^2$, $s_2 = \alpha\varepsilon/r$, $\beta = d/r$.
Hence, the dimensionless expressions for $\hat{\phi}_u$ and $\hat{\phi}_v$ are as follows.
For $\hat{\phi}_u$ (2.20), by substituting the expression for $\hat{E}_u(\hat{u},\hat{v},\hat{x},\hat{t})$ from the dimensionless equation (2.22) and since $\Phi\tau/\chi^2 = 1$ and $r\tau = 1$ gives

$$\frac{1}{\kappa}\Big(1-\hat{u}\Big) - \frac{m_1 \hat{v}}{z+\hat{u}} = -\frac{\epsilon_u}{\chi^2}\frac{\partial^2 \hat{\phi}_u}{\partial \hat{x}^2} + \hat{\phi}_u,$$

where $\kappa = r\chi^2$ and $m_1 = \alpha/r^2\chi^2$.
Similarly for $\hat{\phi}_v$ (2.21) we have

$$\frac{m_2 \hat{u}}{z+\hat{u}} - \gamma = -\frac{\epsilon_v}{\chi^2}\frac{\partial^2 \hat{\phi}_v}{\partial \hat{x}^2} + \hat{\phi}_v,$$

where $m_2 = \alpha\varepsilon/r^2\chi^2$ and $\gamma = d/r^2\chi^2$.
Hence, the dimensionless parameters are

$$\begin{aligned} s_1 = \alpha/r, D_u = \delta_u/rL^2, D_v = \delta_v/rL^2, s_2 = \alpha\varepsilon/r, z = A/K, \beta = d/r, \\ m_1 = \alpha/r^2\chi^2, \kappa = r\chi^2, m_2 = \alpha\varepsilon/r^2\chi^2, \gamma = d/r^2\chi^2. \end{aligned} \tag{2.24}$$

2.5.2 Stability analysis

In order to provide guidelines on the appropriate choice of parameters for the numerical simulation of the full reaction-diffusion-advection system, it is important to consider the *local* dynamics of the system, i.e., the properties of (2.22) and (2.23) without diffusion and advection terms. Hence, we determine the behaviour of the movement-free version of equations (2.22) and (2.23) by setting space derivatives equal to zero, giving

$$\frac{du}{dt} = u\Big(1-u\Big) - \frac{s_1 uv}{z+u} = F(u,v) \tag{2.25}$$

$$\frac{dv}{dt} = \frac{s_2 uv}{z+u} - \beta v = G(u,v). \tag{2.26}$$

To simplify notations, hats ($\hat{}$) are omitted from now on.
It is, naturally, the dynamics in the biologically meaningful region $u \geq 0$, $v \geq 0$ that are of interest. We obtain the equilibrium states of the spatial homogeneous equations (2.25) and (2.26) by setting F and G equal to zero. Then, the local asymptotic stability of each equilibrium point is studied by computing the Jacobian matrix and finding the eigenvalues evaluated at each equilibrium point. For the stability of the equilibrium points, the real parts of the eigenvalues of the Jacobian matrix must be negative. By the equations (2.25) and (2.26), the Jacobian matrix of the system is given by

$$J_i = \begin{bmatrix} \frac{\partial F}{\partial u} & \frac{\partial F}{\partial v} \\ \\ \frac{\partial G}{\partial u} & \frac{\partial G}{\partial v} \end{bmatrix}, \qquad (i = 1, 2, 3),$$

where $i = 1, 2, 3$ represent the equilibrium points $(0,0)$, $(1,0)$ and (u^*, v^*), respectively.
There are three biologically relevant, non-negative equilibrium states including:

- the unstable trivial state, $(0,0)$, which represents the total extinction of both species. The eigenvalues of J_1 are 1 and $-\beta$ implying that $(0,0)$ is an unstable saddle point.

- the locally asymptotically stable host-only state, $(1,0)$, where the parasitoids become extinct and the hosts are spreading throughout the domain at their maximum carrying capacity. The eigenvalues of J_2 are negative if

$$\beta > \frac{s_2}{z+1}.$$

  Otherwise $(1,0)$ is an unstable saddle point.

- the two-species coexistent state, (u^*, v^*), which represents the coexistence of both hosts and parasites in the domain, where

$$u^* = \frac{\beta z}{s_2 - \beta}$$

and

$$v^* = \frac{(1-u^*)(z+u^*)}{s_1}.$$

Since the population density cannot be negative the third steady state is feasible only if

$$0 < \frac{\beta z}{s_2 - \beta} < 1. \tag{2.27}$$

The unique positive equilibrium point (u^*, v^*) is locally asymptotically stable provided

$$z > (s_2 - \beta)/(s_2 + \beta). \tag{2.28}$$

See [137] for a brief overview of continuous dynamical systems.

We have observed that the equilibrium point $(0, 0)$ is always unstable for positive parameters. Some kind of bifurcation may occur at $(1, 0)$ but we focus on the coexistence steady state (u^*, v^*). In the next section, we examine the Hopf bifurcation near the coexisting equilibrium (u^*, v^*) by presenting some numerical results to illustrate the outcomes which are beyond the theoretical finding.

2.5.3 Numerical simulations of the ODE system

We numerically approximate equations (2.25) and (2.26) with initial conditions $u(0) = 0.7$ and $v(0) = 0.5$. We fix the following parameters:

$$\beta = 0.175, \quad s_1 = 0.875 \quad \text{and} \quad s_2 = 0.35$$

while we take z as the control parameter. The values of β, s_1 and s_2 are chosen based on the ones used by Pearce et al. in [127] for one parasitoid species where $r = 0.4$, $\alpha = 0.35$, $\varepsilon = 0.4$ and $d = 0.07$. For this set of parametric values, the coexistence equilibrium point exists whenever $0 < z < 1$ (see equation (2.27)) and is locally asymptotically stable for $z > 0.33$ (see equation (2.28)). Let us define the critical value $z_0 = 0.33$. We intend to show that equilibrium point (u^*, v^*) undergoes a Hopf bifurcation when the parameter z crosses its critical value $z_0 = 0.33$.

We present Figures 2.1 and 2.2 as evidence of Hopf bifurcation at $z = z_0$. It is observed by Figure 2.1 that the system of equations (2.25) and (2.26) has a stable positive equilibrium point $(u^*, v^*) = (0.3751, 0.5359)$ for $z = 0.375$. Figure 2.1a represents the positive equilibrium that is locally asymptotically stable and 2.1b represents the phase-portrait of $(u^*, v^*) = (0.3751, 0.5359)$ that is locally asymptotically stable.

In Figure 2.2 we show that the coexisting equilibrium becomes unstable for some $z = 0.3 < z_0$. We observe that solutions of $u(t)$ and $v(t)$ oscillate around (u^*, v^*). This represents the occurrence of a limit cycle and the destabilisation of coexisting equilibria. Thus, Hopf bifurcation is verified for $z < z_0$. Figure 2.2a represents

the stable and periodic oscillations around the positive equilibrium $(u^*, v^*) = (0.3751, 0.5359)$ and the phase plane diagram Figure 2.2b represents the stable limit cycle around (u^*, v^*) when $z = 0.3 < z_0 = 0.33$. The stability of the limit cycle is determined by the direction of the neighbouring trajectories. If the neighbouring trajectories are approaching the limit cycle, as time increases, then the limit cycle is stable. Otherwise the limit cycle is unstable if the trajectories tend away from the limit cycle.

Hence from Figures 2.1 and 2.2 we observe that as we decrease the value of the control parameter z, the coexistence of prey-predator changes from stable equilibrium to stable oscillatory coexistence.

The existence of a limit cycle can also be confirmed using the Poincaré-Bendixson theorem [115]. Based on the theorem one can prove that a closed orbit exists by establishing a close region, say R, to be a closed bounded subset of the plane and assuming that the vector field is continuously differentiable on this region. Then R must not contain any fixed points. Finally, one must establish that there exists a trajectory, say C, which is confined to R; that is, starts in R and stays in R for all future time. A typical approach is to construct the plane of the system (2.25) and (2.26) by looking at the nullclines ($\frac{du}{dt} = \frac{dv}{dt} = 0$) and construct a trapping region R where the vector field along the boundaries is pointing inwards towards R. Note that the theorem can not be applied to dynamical systems whose phase space has three or more dimensions.

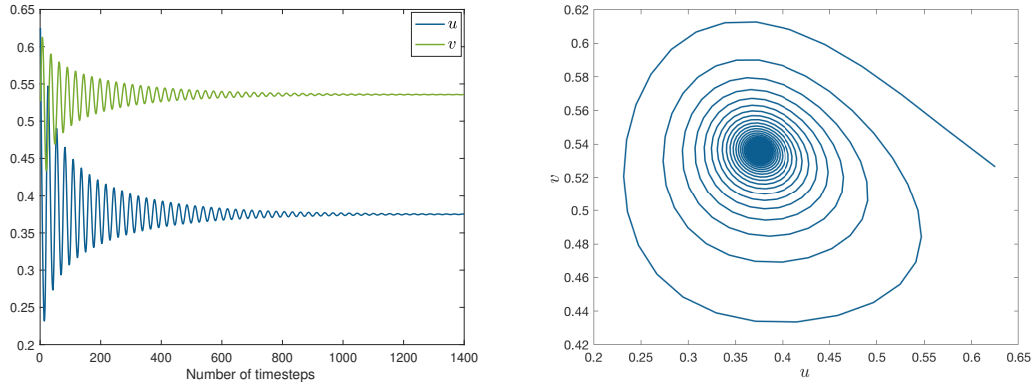

(a) Time evolution.

(b) Phase-portait.

Figure 2.1: Stable coexisting equilibrium $(u^*, v^*) = (0.3751, 0.5359)$ for $z = 0.375 > z_0$ for the system (2.25) and (2.26).

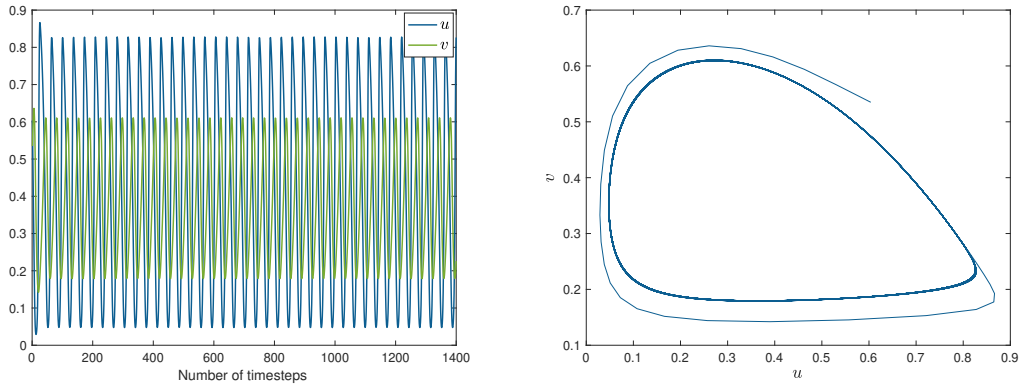

(a) Time evolution

(b) Phase-portait.

Figure 2.2: Stable limit cycle surrounding the coexisting equilibrium $(u^*, v^*) = (0.3751, 0.5359)$ for $z = 0.3 < z_0$ for the system (2.25) and (2.26).

In this section, we have carried out the model analysis of the movement-free ODE system for a predator-prey model with Holling-type II functional response. We have gained insights into the parameter values required to produce biologically realistic behaviour by looking at the three non-negative equilibrium steady states. Special attention was given to the coexistence state (u^*, v^*) where by choosing parameter z as a bifurcation parameter, sufficient conditions for the existence of Hopf bifurcation have been presented using numerical simulations. The conditions derived in this section regarding the range of parameter values which must be used to achieve a stable coexistence steady state will be used in the following section where we numerically approximate the whole reaction-diffusion-advection system of (2.16)-(2.21). We now look at numerical methods for the approximation of (2.16)-(2.21).

2.6 Numerical Techniques for the 1-D Diffusion-Advection-Reaction Predator-Prey Model

For the numerical approximation of the one-dimensional predator-prey model with directed movement (2.16)-(2.21), we use the finite difference and finite element approximations. The two methods differ in both the domain discretization and computation. The finite representation of a function in finite difference calculations is considered by taking isolated values of the function at given points: such an approximation is only defined at these points. In the finite element

method, the function is represented as a combination of both points and simple functions (such as low-order polynomials): this kind of function is both finite-dimensional and defined at all points (nodes). The computations of the former one are based on finite difference approximations to the governing differential equations using a grid of spatial nodes while the finite element method is based on the approximation of an equivalent governing integral relation, known as the weak form, using finite segments. In the finite element method integration by parts allows the possibility of lower order approximations like piecewise-linear to be substituted. The implementation and computation of the finite element method are more complicated compared to the finite difference as integration is required followed by the formation of symmetrical and sparse matrices resulting in more calculations per time step. In both methods, the use of a finer grid is needed to increase the accuracy. The key advantage of the finite element method, in higher dimensions, is that it has the ability to compute solutions on complex geometries while finite difference basic form is restricted to handling rectangular shapes. In the following sections, we give a brief description of the application of these two methods to the predator-prey system followed by some results.

2.6.1 Explicit finite element

For the numerical approximation of (2.16)-(2.21) using the finite element numerical technique, we first require the weak form of the system which is constructed by introducing the test functions $w(x)$, which are once differentiable and twice integrable in (a, b). Since the approximation of (2.16) and (2.17) require ϕ_u and ϕ_v respectively, we begin with equations (2.20) and (2.21).

Following the multiplication of the equations by the test functions, the application of integration and the boundary conditions, the weak forms are as follows.

For ϕ_u, by (2.20),

$$\int_a^b w(x) r \left(1 - \frac{u}{K}\right) \, \mathrm{d}x - \int_a^b w(x) \frac{\alpha v}{A + u} \, \mathrm{d}x = - \int_a^b \epsilon_u \frac{\partial w}{\partial x} \frac{\partial \phi_u}{\partial x} \, \mathrm{d}x + \int_a^b w(x) \phi_u \, \mathrm{d}x$$

and for ϕ_v from (2.21),

$$\int_a^b w(x) \frac{\alpha \varepsilon u}{A + u} \, \mathrm{d}x - \int_a^b w(x) d \, \mathrm{d}x = - \int_a^b \epsilon_v \frac{\partial w}{\partial x} \frac{\partial \phi_v}{\partial x} \, \mathrm{d}x + \int_a^b w(x) \phi_v \, \mathrm{d}x.$$

The weak form of (2.16) is given by

$$\int_a^b w(x)\frac{\partial u}{\partial t}\,\mathrm{d}x = -\delta_u \int_a^b \frac{\partial w}{\partial x}\frac{\partial u}{\partial x}\,\mathrm{d}x + \int_a^b u\frac{\partial w}{\partial x}\frac{\partial \phi_u}{\partial x}\,\mathrm{d}x + \int_a^b w(x)\left(ru\left(1-\frac{u}{K}\right) - \frac{\alpha u v}{A+u}\right)\,\mathrm{d}x$$

and for $\frac{\partial v}{\partial t}$ by (2.17),

$$\int_a^b w(x)\frac{\partial v}{\partial t}\,\mathrm{d}x = -\delta_v \int_a^b \frac{\partial w}{\partial x}\frac{\partial v}{\partial x}\,\mathrm{d}x + \int_a^b v\frac{\partial w}{\partial x}\frac{\partial \phi_v}{\partial x}\,\mathrm{d}x + \int_a^b w(x)\left(\frac{\alpha\varepsilon u v}{A+u} - dv\right)\,\mathrm{d}x.$$

The integral of the reaction terms in the above equations is approximated using the trapezoidal rule.
The weak formulations of (2.16) and (2.17) have reduced the derivative terms to first order and are ready for lower-order finite element substitutions to be made. After the domain discretization, the piecewise linear trial function approximation substitutions are made giving a system of equations which can be written in matrix forms and solved by linear algebra. After computing the stiffness, mass and the weighted stiffness matrix (see [178] Section 3.2.1) the system is solved to give $\phi_{u,v}$ and u_t, v_t. Then to update the population densities a time integration scheme is required, e.g., the explicit Euler scheme

$$\begin{aligned} u_i^{n+1} &= u_i^n + \Delta t\ u_{t_i}^n, \\ v_i^{n+1} &= v_i^n + \Delta t\ v_{t_i}^n, \end{aligned} \tag{2.29}$$

where the subscript i denotes the x from the space discretization (i.e., $x_i = i\Delta x$ where Δx is the space interval) and the superscript n (and $n+1$) denotes the time (i.e., $t^n = n\Delta t$ where Δt is the time step).
For the complete analysis and application of the finite element method see [152, 87].

2.6.2 Explicit finite difference

As described earlier at the beginning of Section 2.6, the finite difference method uses approximations for the space derivative terms which are substituted directly in the governing equations in order to reduce the system into equations of ordinary differential equations.
We partition the domain in space using a mesh $x_0, ..., x_I$ and in time using a

mesh $t_0, ..., t_N$. We assume a uniform partition both in space and in time, so the difference between two consecutive space points will be Δx and between two consecutive time points will be Δt. Then $u_i^n, v_i^n, \phi_{u_{(i)}}^n$ and $\phi_{v_{(i)}}^n$ will represent the numerical approximation of $u(x_i, t_n), v(x_i, t_n), \phi_u(x_i, t_n)$ and $\phi_v(x_i, t_n)$, respectively .
We begin by applying central approximation to the second order term in (2.20) giving

$$-\epsilon_u \left(\frac{\phi_{u_{(i+1)}}^n - 2\phi_{u_{(i)}}^n + \phi_{u_{(i-1)}}^n}{\Delta x^2} \right) + \phi_{u_{(i)}}^n = r\left(1 - \frac{u_i^n}{K}\right) - \frac{\alpha v_i^n}{A + u_i^n} \tag{2.30}$$

and for ϕ_v, the equation (2.21) becomes

$$-\epsilon_v \left(\frac{\phi_{v_{(i+1)}}^n - 2\phi_{v_{(i)}}^n + \phi_{v_{(i-1)}}^n}{\Delta x^2} \right) + \phi_{v_{(i)}}^n = \frac{\alpha \varepsilon u_i^n}{A + u_i^n} - d. \tag{2.31}$$

Using a forward difference in time and a second-order central difference for the space derivative of equations (2.16) and (2.17) gives

$$\begin{aligned} \frac{u_i^{n+1} - u_i^n}{\Delta t} =& \delta_u \left(\frac{u_{i-1}^n - 2u_i^n + u_{i+1}^n}{\Delta x^2} \right) \\ & - \frac{1}{2\Delta x^2} \Big(\big(u_{i+1}^n + u_i^n\big)\big(\phi_{u_{(i+1)}}^n - \phi_{u_{(i)}}^n\big) - \big(u_i^n + u_{i-1}^n\big)\big(\phi_{u_{(i)}}^n - \phi_{u_{(i-1)}}^n\big) \Big) \\ & + r u_i^n \left(1 - \frac{u_i^n}{K}\right) - \frac{\alpha u_i^n v_i^n}{A + u_i^n} \end{aligned} \tag{2.32}$$

and

$$\begin{aligned} \frac{v_i^{n+1} - v_i^n}{\Delta t} =& \delta_v \left(\frac{v_{i-1}^n - 2v_i^n + v_{i+1}^n}{\Delta x^2} \right) \\ & - \frac{1}{2\Delta x^2} \Big(\big(v_{i+1}^n + v_i^n\big)\big(\phi_{v_{(i+1)}}^n - \phi_{v_{(i)}}^n\big) - \big(v_i^n + v_{i-1}^n\big)\big(\phi_{v_{(i)}}^n - \phi_{v_{(i-1)}}^n\big) \Big) \\ & + \frac{\alpha \varepsilon u_i^n v_i^n}{A + u_i^n} + d v_i^n, \end{aligned} \tag{2.33}$$

respectively.

Following the domain discretization, the solution for ϕ_u and ϕ_v is obtained from (2.30) and (2.31), respectively, using tridiagonal matrices. Having $\phi_{u,v}$, u and v we solve (2.32) and (2.33) for u and v at the forward time level.
The book [121] provides an excellent analysis of the finite difference method.

2.6.3 Parameter values

We now proceed with deriving some simulations for the system (2.16)-(2.21) using both finite difference and finite element methods. The choice of parameter values used for the following simulations are strongly based on the paper of Pearce et al. [127] where authors studied a system of four reaction-diffusion equations describing the dynamics of two hosts and two parasites. In our system, prey dispersal is considered to be greater than the predator dispersal and therefore the parameters used for the simulations are

$$\begin{aligned} \delta_u &= 0.001, \\ \delta_v &= 0.003, \\ r &= 0.4, \\ K &= 250, \\ \varepsilon &= 0.4, \\ \alpha &= 0.35, \\ d &= 0.09, \\ A &= 80, \\ \text{and} \quad \epsilon_{u,v} &= 0.25. \end{aligned} \tag{2.34}$$

The value of A is chosen in such a way that the condition for a stable coexisting steady state (2.28) is satisfied, e.g., the condition for a stable coexisting steady state is

$$z > (s_2 - \beta)/(s_2 + \beta), \tag{2.35}$$

as given by (2.28), implying that

$$\frac{A}{K} > \left(\frac{\alpha\varepsilon}{r} - \frac{d}{r}\right) / \left(\frac{\alpha\varepsilon}{r} + \frac{d}{r}\right) \tag{2.36}$$

from (2.24).
From the parameter values in (2.34)

$$0.32 > 0.22 \tag{2.37}$$

and hence the condition is satisfied.

2.6.4 Results

For both methods, we discretized the spatial domain ($a = 0, b = 1$) into 81 equally spaced nodes ($\Delta x = 0.0125$) and use a time step value of $\Delta t = 0.01$. The same initial conditions are used as shown in Figure 2.3a and the results for both

methods at $t = 2$ can be seen in Figure 2.3b. The results are shown in red and blue colour for the finite difference and finite element method, respectively, while solid lines show the results of the prey population and dotted and/or dashed lines the results of the predator population. The results of the two methods at $t = 2$ are very nearly equal, giving confidence that the two methods have been implemented correctly.

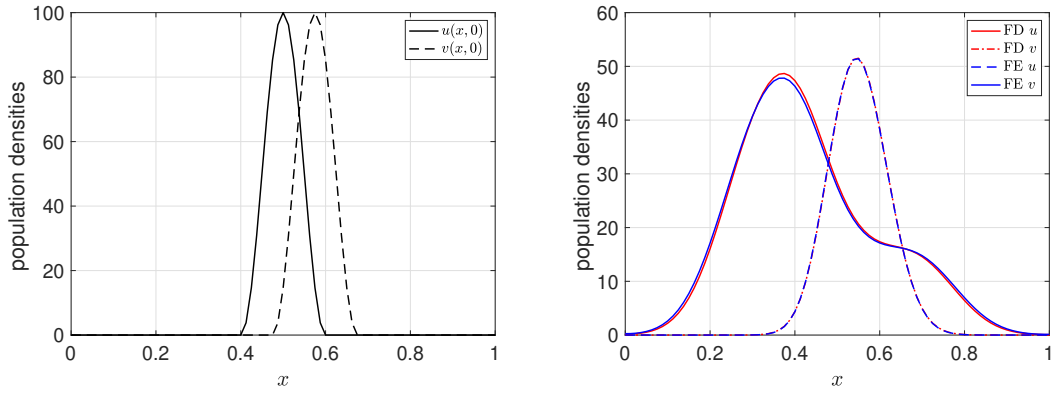

(a) $t = 0$. (b) $t = 2$.

Figure 2.3: Initial conditions used for both methods (a) and comparison of the results of finite difference and finite element at $t = 2$ (b).

2.7 Convergence

We examine the orders of convergence q with respect to time and space for finite difference and finite element method. We carry out a sequence of calculations using the same initial data (Figure 2.3a) and the same value of $\Delta t/\Delta x$, but with successive refinement of the two meshes, so that $\Delta t \to 0$ and $\Delta x \to 0$. Since these are explicit schemes we make sure that $\delta_{u,v}\Delta t/(\Delta x)^2 \leq 1/2$ [121] (see the end of this section).

Let N denote the number of nodes in the spatial domain, i.e., $\Delta x = 1/N$. We run the results for $N = 40, 80, 160, 320, 640$ while varying Δt, i.e., $\Delta t = 3.2 \times 10^{-4},\ 1.6 \times 10^{-4},\ 0.8 \times 10^{-4},\ 0.4 \times 10^{-4},\ 0.2 \times 10^{-4}$ respectively. We assume

$$E_N = \mathsf{A}(\Delta x)^q + \mathsf{B}(\Delta t)^p,$$

where E_N is the error in the solution between the analytical and numerical solution, A and B are constants and q and p are the orders of convergence. Since we are only accounting for the spatial errors we consider

$$E_N = \mathsf{A}(\Delta x)^q \tag{2.38}$$

and

$$E_2N = \mathsf{A}(\Delta 2x)^q. \tag{2.39}$$

Dividing (2.39) by (2.38) we get

$$q = -\log_2\left(\frac{E_{2N}}{E_N}\right).$$

The analytical solution of the system is not available so we consider the exact solution to be the approximation of the system by using $N = 1280$ and $\Delta t = 0.1 \times 10^{-4}$, assuming to be close to the actual exact solution of the problem.

The error is calculated for both the prey and predator solution ($E_N(u)$ and $E_N(v)$). Table 2.2 shows the results for the finite difference method. We observe an order of convergence of approximately 2 for both u and v solutions. In the finite element results, in Table 2.3, we observe that the convergence rate increases as Δx decreases and approaches a convergence rate of 2. Interestingly we observe a significant difference in the magnitudes of the errors in u between the two methods. We can not make a certain conclusion for the reason of this difference in magnitudes as the error calculations were constructed by assuming the exact solution in each case to be the approximated solution with a denser mesh of the corresponding numerical method. One possible reason could be the build-up of round-off errors in the finite element case.

N	Δx	Δt	$E_N(u)$	q_u	$E_N(v)$	q_v
40	2.5×10^{-2}	3.2×10^{-4}	8.7×10^{-3}		9.9×10^{-3}	
80	1.25×10^{-2}	1.6×10^{-4}	2.2×10^{-3}	1.9	2.5×10^{-3}	1.9
160	6.25×10^{-3}	0.8×10^{-4}	5.4×10^{-4}	2.0	6.1×10^{-4}	2.0
320	3.125×10^{-3}	0.4×10^{-4}	1.3×10^{-4}	2.1	1.5×10^{-4}	2.0
640	1.5625×10^{-3}	0.2×10^{-4}	2.7×10^{-5}	2.2	3.8×10^{-5}	2.1
1280	7.8125×10^{-4}	0.1×10^{-4}				

Table 2.2: Relative errors for u and v with rates of convergence using the explicit finite difference method.

N	Δx	Δt	$E_N(u)$	q_u	$E_N(v)$	q_v
40	2.5×10^{-2}	3.2×10^{-4}	0.5×10^{-1}		0.1×10^{-1}	
80	1.25×10^{-2}	1.6×10^{-4}	0.2×10^{-1}	1.2	4.5×10^{-3}	1.6
160	6.25×10^{-3}	0.8×10^{-4}	8.9×10^{-3}	1.3	1.3×10^{-3}	1.7
320	3.125×10^{-3}	0.4×10^{-4}	2.9×10^{-3}	1.6	3.6×10^{-4}	1.9
640	1.5625×10^{-3}	0.2×10^{-4}	1.0×10^{-3}	1.7	1.0×10^{-4}	1.8
1280	7.8125×10^{-4}	0.1×10^{-4}				

Table 2.3: Relative errors for u and v with rates of convergence using the explicit finite element method.

As stated at the beginning of this section, these explicit numerical schemes are restricted by conditions regarding the time and space meshes. A well-known condition which describes the restriction on the time step value associated with the space mesh size is given by

$$\delta_{u,v}\Delta t/(\Delta x)^2 \leq 1/2. \tag{2.40}$$

This condition is derived from the von Neumann stability analysis which examines the stability of the finite difference method for the heat equation [121, 133]. In cases where the model includes an advection term, the stability analysis is much more complicated and is beyond our scope (related work can be found in [42, 76, 182]). Even though the stability condition from the von Neumann analysis concerns the heat equation (diffusion term) we have used it throughout the numerical calculations of the reaction-diffusion-advection system as a guide for the time-step value to avoid instability in the solutions.

In the following sections, we numerically show that the explicit finite difference scheme for a reaction-diffusion model is restricted by the stability condition (2.40) and we concentrate on a semi-implicit scheme for the numerical approximation of the reaction-diffusion-advection system (2.16)-(2.21) which avoids such restriction on the time step value.

2.8 Time Integration Schemes

As shown above, the application of the numerical methods using the explicit Euler time-stepping scheme is straightforward. As we shall show, however, the numerical solution becomes unstable unless the time step is severely restricted, hence, we proceed by considering other numerical methods which can avoid such a restriction.

For the following analysis, we neglect the advection term of the system (2.16)-(2.21) ($\phi_u = \phi_v = 0$) giving the following set of reaction-diffusion equations

$$\frac{\partial u}{\partial t} = \delta_u \frac{\partial^2 u}{\partial x^2} + f(u, v, x, t) \tag{2.41}$$

$$\frac{\partial v}{\partial t} = \delta_v \frac{\partial^2 v}{\partial x^2} + g(u, v, x, t), \tag{2.42}$$

where f and g refer to the reaction terms of (2.16) and (2.17) respectively.
We discretize the domain by letting $[a, b]$ be a closed interval and

$$[a = x_1, ...x_{i-1}, x_i, x_{i+1}, ...x_{N+1} = b]$$

be (not necessarily uniform) points (nodes) in the interval. We generate an approximation for equation (2.41) using the forward difference for the time derivative and the centred difference for the second-order space derivative, giving

$$u_i^{n+1} = u_i^n + \Lambda \left(u_{i+1}^n - 2u_i^n + u_{i-1}^n \right) + f(u_i^n, v_i^n), \tag{2.43}$$

where

$$\Lambda = \delta_u \frac{\Delta t}{\Delta x^2}.$$

Clearly, each value at time level t^{n+1} can be independently calculated from values at time level t^n, hence the name explicit.
If we carry out a calculation using (2.43), assuming no predator (i.e., $v = 0$) we soon discover that the numerical results depend critically on the value of Λ, which is related to the size of the time-step and the space-step.
In Figure 2.4 we show results corresponding to the parameter values (2.34) and to the initial data

$$u^0(x) = \begin{cases} 100 \cos\left(\frac{\pi}{0.20}(x - 0.5)\right), & \text{if} \quad 0.4 \leq x \leq 0.6, \\ 0, & \text{otherwise.} \end{cases} \tag{2.44}$$

Two sets of results are displayed. Both examples use the same number of nodes $N = 80$, space step value $\Delta x = 0.0125$. The first set uses $\Delta t = 0.026$ which satisfies the condition given in (2.40) while the second one uses $\Delta t = 0.027$ for which the condition in (2.40) is not satisfied. We observe that the latter exhibits oscillation which grows gradually with increasing values of time t while the results of the first case are smooth for all time simulations. This is a typical example of instability or stability depending on the value of the mesh ratio Λ. The solutions use time steps which are very nearly equal, but different enough to show the qualitative difference in the numerical solutions.

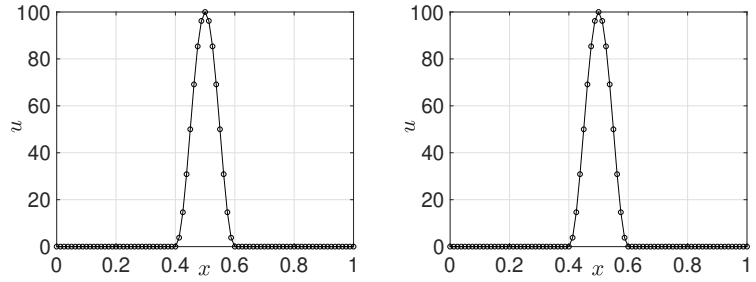

(a) $t = 0$

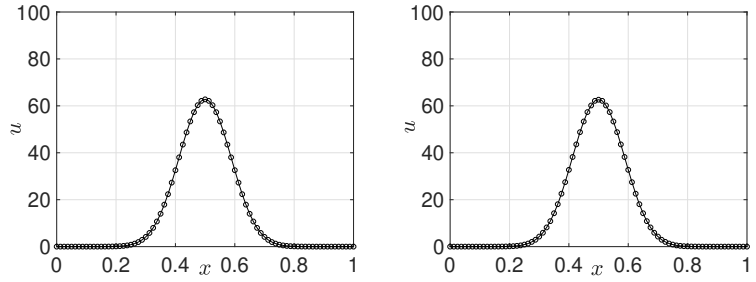

(b) $t = 1$

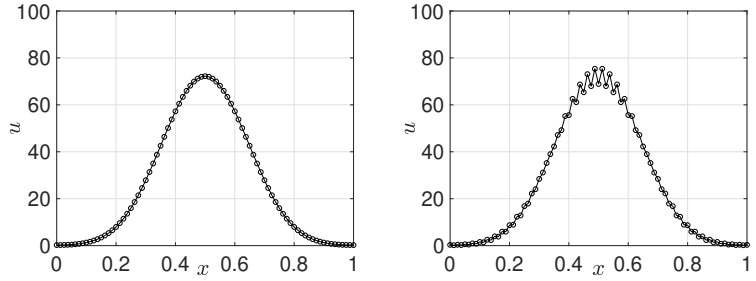

(c) $t = 3$

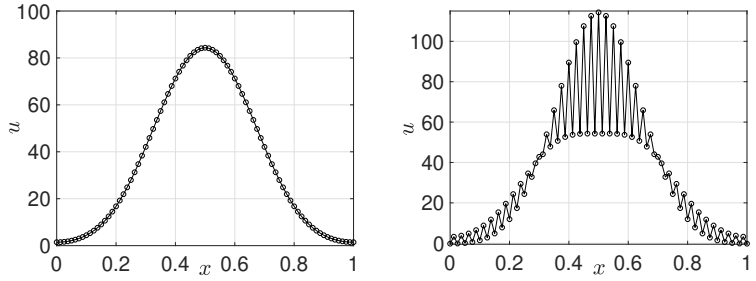

(d) $t = 4$

Figure 2.4: Results obtained for the data of (2.44) with the explicit method; $N = 80$, $\Delta x = 0.0125$.

2.9 Semi-Implicit Scheme

The stability consideration associated with the explicit scheme $\Delta t \leq \frac{1}{2\delta}(\Delta x)^2$, as shown in [121], is a severe restriction and implies that many time steps will be necessary to follow the solution over a reasonably large time interval. Also, if we need to reduce Δx to improve the accuracy of the solution the amount of work involved increases rapidly since we shall also have to reduce Δt^2. Moreover, decreasing the value of Δt implies more time steps which will lead to an increase in the round-off errors.

Such a restriction can be avoided by the use of a backward time difference which results in an implicit scheme. Even though an implicit scheme is unburdened of stability considerations regarding the time step, the solution requires a slightly more sophisticated calculation.

If we apply the backward time difference to the system (2.41) and (2.42),(instead of the forward time difference as in (2.43)), the space difference remains the same, we obtain the scheme

$$u_i^{n+1} = u_i^n + \Lambda_u \left(u_{i+1}^{n+1} - 2u_i^{n+1} + u_{i-1}^{n+1}\right) + \Delta t \; f(u_i^{n+1}, v_i^{n+1}) \tag{2.45}$$

$$v_i^{n+1} = v_i^n + \Lambda_v \left(v_{i+1}^{n+1} - 2v_i^{n+1} + v_{i-1}^{n+1}\right) + \Delta t \; g(u_i^{n+1}, v_i^{n+1}), \tag{2.46}$$

where

$$\Lambda_u = \delta_u \frac{\Delta t}{\Delta x^2} \quad \text{and} \quad \Lambda_v = \delta_v \frac{\Delta t}{\Delta x^2}.$$

Usually, an implicit scheme's solution involves forming tri-diagonal matrices. For example, the equation number i in the system only involves unknowns with numbers $i-1$, i and $i+1$, so the matrix of the system has non-zero elements only on the diagonal and in the positions immediately to the left and to the right of the diagonal. However, due to the nonlinearity of the reaction terms in (2.45) and (2.46), as given by (2.16) and (2.17), a fully implicit scheme is clearly inefficient for the approximation of the system (2.45) and (2.46). Hence we apply a semi-implicit scheme to approximate the coupled equations. A semi-implicit application in the context of the reaction-diffusion system of (2.41) and (2.42) is given by

$$u_i^{n+1} = u_i^n + \Lambda_u \left(u_{i+1}^{n+1} - 2u_i^{n+1} + u_{i-1}^{n+1}\right) + \Delta t \left(r u_i^{n+1} \left(1 - \frac{u_i^n}{K}\right) + \frac{\alpha u_i^n v_i^{n+1}}{A + u_i^n}\right) \tag{2.47}$$

and

$$v_i^{n+1} = v_i^n + \Lambda_v \left(v_{i+1}^{n+1} - 2v_i^{n+1} + v_{i-1}^{n+1}\right) + \Delta t \left(\frac{\alpha \varepsilon u_i^n v_i^{n+1}}{A + u_i^n} - d v_i^{n+1}\right). \tag{2.48}$$

This is an example of a semi-implicit scheme, which is not as easy to implement as the explicit scheme described earlier. The equations (2.47) and (2.48) involve three unknown values of u and v on the new time level $n+1$, respectively. We cannot immediately calculate the values of u_i^{n+1} and v_i^{n+1} since the equations involve the two neighbouring values u_{i-1}^{n+1} and u_{i+1}^{n+1} and v_{i-1}^{n+1} and v_{i+1}^{n+1}, which are also unknown. Note also that equation (2.48) requires also the value of v_i^{n+1}.
A solution of the system (2.47)and (2.48) can be derived by combining the two equations and constructing a sparse matrix equation which is solved to update the values of u and v at forward time levels. Note that operations of sparse matrices using standard dense-matrix structures and algorithms are slow and inefficient when applied to large sparse matrices as processing and memory are wasted on the zeros. Hence, it is beneficial and sometimes necessary to use specialized algorithms and data structures that take advantage of the sparsity of the matrices.

In the context of the diffusion-advection-reaction system (2.16)-(2.21) the semi-implicit approximations to the system take the form

$$\begin{aligned} u_i^n = & \left(\Upsilon\left(\phi_{u(i+1)}^n - \phi_{u(i)}^n\right) - \Lambda_u\right) u_{i+1}^{n+1} \\ & + \left(1 + 2\Lambda_u + \Upsilon\left(\phi_{u(i+1)}^n - 2\phi_{u(i)}^n + \phi_{u(i-1)}^n\right) - \Delta t\ r\left(1 - \frac{u_i^n}{K}\right)\right) u_i^{n+1} \\ & + \left(\Upsilon\left(\phi_{u(i-1)}^n - \phi_{u(i)}^n\right) - \Lambda_u\right) u_{i-1}^{n+1} \\ & + \left(\Delta t \frac{\alpha u_i^n}{A + u_i^n}\right) v_i^{n+1} \end{aligned} \tag{2.49}$$

and

$$\begin{aligned} v_i^n = & \left(\Upsilon\left(\phi_{v(i+1)}^n - \phi_{v(i)}^n\right) - \Lambda_v\right) v_{i+1}^{n+1} \\ & + \left(1 + 2\Lambda_v + \Upsilon\left(\phi_{v(i+1)}^n - 2\phi_{v(i)}^n + \phi_{v(i-1)}^n\right) - \Delta t\ \frac{\alpha\varepsilon u_i^n}{A + u_i^n} + \Delta t\ d\right) v_i^{n+1} \\ & + \left(\Upsilon\left(\phi_{v(i-1)}^n - \phi_{v(i)}^n\right) - \Lambda_v\right) v_{i-1}^{n+1}, \end{aligned} \tag{2.50}$$

where

$$\Upsilon = \frac{\Delta t}{2\Delta x^2}.$$

Equations (2.49) and (2.50) are constructed by grouping the coefficients and ϕ_u and ϕ_v are evaluated from (2.30) and (2.31), respectively.

Hence the solution of the predator-prey system with directed movement using a semi-implicit scheme can be derived from a sparse matrix equation which solves both (2.49) and (2.50).

2.9.1 Results

The time step is still limited by the requirement that the truncation error must stay small, as shown in the book of Morton and Mayers [121]. In practice, though it is found that in most problems the semi-implicit method can use a much larger Δt than the explicit method. Figure 2.5 shows a comparison of the results of each method, the explicit and the semi-implicit finite difference, for the diffusion-advection-reaction system (2.16)-(2.21) using the initial conditions shown on Figure 2.3a and the parameter values of (2.34). The results are shown in red and blue colour for the semi-implicit and explicit finite difference methods, respectively, while solid lines and dashed lines distinguish the solutions of u and v for each method. The two approaches produce almost the same results for $\Delta t = 0.02$ but the use of a slightly bigger Δt ($\Delta t = 0.027$) resulted in oscillations in the solution of the explicit method. The oscillations are first visible in the u solution as the prey population is assigned a greater diffusion coefficient compared to the predator. Figure 2.6 shows the results of the semi-implicit method for various values of Δt. Even though no oscillations occur in the solution for large values of Δt the method fails to capture similar results to the ones obtained with smaller Δt. Although each step of the semi-implicit method requires more work compared to the explicit approach, the overall amount of work needed to reach the final time is much less.

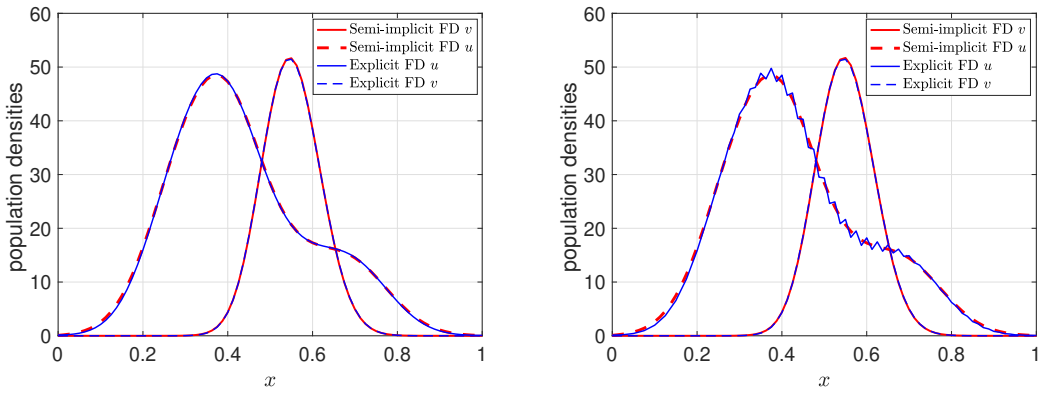

(a) $t = 2$; $\Delta t = 0.02$. (b) $t = 2$; $\Delta t = 0.027$.

Figure 2.5: Comparison of explicit and semi-implicit finite difference method for different Δt.

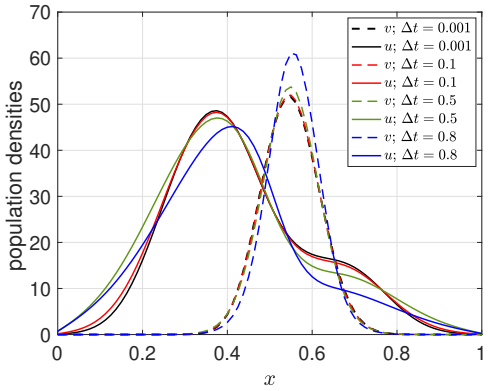

Figure 2.6: Semi-implicit results at $t = 2$ for different values of Δt.

2.10 Summary

In this chapter, we considered a diffusion-reaction-advection predator-prey system with bias velocity based on a fecundity gradient. Model analysis was carried out by looking at the possible equilibrium points and derived conditions for the parameter values in order to produce stable steady states. Focus was given to the coexistence steady state where the existence of Hopf bifurcation was presented by numerical simulations.

Two numerical methods were considered to approximate the system; the explicit finite difference and explicit finite element method, and the results of the two numerical approaches were compared. Convergence analysis of each method was then carried out by keeping the value of $\Delta t/\Delta x$ the same but with successive refinement of the two meshes so that $\Delta t \to 0$ and $\Delta x \to 0$. We found an order of convergence 2 for the finite difference method while we observed that the order of convergence of the finite element method is approaching 2 as Δx decreases. Since the explicit scheme is associated with stability considerations we applied a semi-implicit finite difference method to approximate the system which avoids such constraints on the time-step value. Using numerical simulations we showed that the semi-implicit method remains numerically stable for large values of Δt, though as $\Delta t \to 1$, the method fails to produce accurate results.

The model analysis (non-dimensionalisation and stability analysis) and the analysis of the numerical techniques (convergence analysis and numerical stability) carried out in this chapter provide the foundations for the study of the 2-D reaction-diffusion-advection predator-prey system in the following chapter where environmental variations are included in the model, such as climate change, which

impact species massively. More precisely, together with my collaborators for the next chapter, Dr Hélène Audusseau (Department of Zoology, Stockholm University) and Dr Reto Schmucki (UK Centre for Ecology and Hydrology), we model a reaction-diffusion-advection parasite-host system with temperature dependence and observe how global warming is affecting species patterns of coexistence.

Chapter 3

Modeling Predator-Prey Dynamics and Climate Influence in a Two-Dimensional Domain on a Static Mesh

In this chapter, we extend our study of the fixed-mesh finite difference for the diffusion-advection-reaction predator-prey system of Chapter 2 to two dimensions. Specifically, we model a parasite-host relationship and illustrate how climatic influence can be incorporated into the model by the use of a climate function, and numerically solve the temperature-dependent model by the fixed mesh finite difference method. Results are derived using the maximum temperatures observed in Spain and Portugal in 1950 and 2020 and the temperature projections for the year 2050.
This chapter is a collaboration with Dr Hélène Audusseau (Department of Zoology, Stockholm University) and Dr Reto Schmucki (UK Centre for Ecology and Hydrology).

3.1 Chapter Overview

Temperature increase impacts species, but we know little about their cascading effect, that is their effect on trophic interactions, e.g., on predation or parasitism. In particular, the impact of temperature on species interactions is likely to strongly rely on species phenotypic plasticity and dispersal ability (capacity and behaviour) to warming [21]. Ectotherms are a good study model as they are very sensitive to temperature and temperature affects both the probability of a

species to move and its dispersal distance. We numerically solve a 2-D diffusion-advection-reaction parasitoid-host system where climate influence is modelled in this partial differential equations framework as an exogenous driver which affects the dispersal of species as well as the prey growth rate. Mathematically, this exogenous driver is a function of time and space, the climate function, that describes how favourable is the climate, on a scale from 0 to 1. In [168] authors have shown that the summer season will last nearly half a year in the next 100 years. Here we investigate how the parasitoid and host spatial distribution is affected by the increase in temperature through the years based on the maximum temperatures reported in years 1950 and 2020 in Spain and Portugal, and the projected maximum temperatures for the year 2050.

3.2 Introduction

The impact of global warming on species is well known but less is known about its impact on species interactions and how it affects patterns of co-occurrence. We know, however, that differences in the sensitivity of different species to rising temperature will disrupt biotic interactions because species' responses are not necessarily consistent between species groups, and vary among species according to their trophic position, role in the ecosystem, or else, according to their life-history characteristics. Understanding and predicting these changes in biotic interactions is fundamental because these interactions govern biological communities and are involved in a wide range of regulatory processes of ecosystems.

To improve forecasting of the impact of climate change, a large body of literature has stressed the need to focus on species attributes that are temperature dependent and that affect species interaction [21]. Species' abilities to adapt or disperse are two functional traits likely to reflect species' adaptive potential to climate change. The first, species adaptive potential, is also referred to as plasticity. Species plasticity reflects the large diversity of phenotype that related individuals can develop if placed under different environmental conditions, such as different temperatures. The plasticity of species to temperature variations, such as in the relative growth rate or developmental rate, varies greatly among species (Fig. 1 from Berg et al. 2010 [21]). These developmentally related traits are, additionally, often good indicators of species adaptive potential [91, 135, 23]. Further studies at the scale of communities also indicated that the robustness of species interactions under climate change is determined by these variations in the sensitivity of each species of a community to temperature [3]. The second, the dispersal ability, determines species' ability to escape adverse direct and indirect consequences of temperature changes [179] by colonizing new habitats as they become available. Here also, species differ greatly in their dispersal ability (Fig.

2 from Berg et al. 2010 [21]). Differences among species in the timing and rates of dispersal can result in spatial or temporal mismatches of important species associations [163, 126]. For example, Van Grunsven et al in [159] showed that plant species that have colonized northwestern Europe from southern climate regions because of the warming may become temporarily released from soil pathogenic activity, as they disperse faster than their natural enemies. Although species plasticity and dispersal abilities are commonly accepted as important drivers of species' adaptive potential to climate change, at present hardly any comparative data are presented on the temperature sensitivity of life-history traits between species that are in trophic interactions (or for species within communities). We also lack reliable data on the dispersal rate of many species [21], even though dispersal is often assumed to be proportional to species size [80].

Ectotherms are a good model to study the impact of rising temperatures. First, they reflect a large part of the biodiversity on Earth (99.6%) which makes of particular importance the understanding of their response to warming. Second, because ectotherms organisms are unable to regulate their body temperature, they strongly depend on the external temperature condition for their development and movement [144, 7, 125]. Many aspects of the individual performance of ectotherms, such as behaviour, metabolic rate and associated growth rate, or reproduction rate, are influenced by the temperature of their environment, due to an increase in physiological rates at higher temperatures. Typically, the relationship between traits and temperature in ectotherms shows a characteristic shape, in which performance increases with increasing temperature, reaches a maximum, and then declines rapidly with further increases in temperature [96]. Understanding how climate conditions affect species distribution and dynamics is therefore essential to predict species co-occurrence in a changing environment. This is even more important for species involved in strong trophic interactions, such as the dependence of a predator on its prey species. Voigt et al. in [164] showed that the vulnerability of predators to global warming is twice as high as the vulnerability of plants (they studied: xerothermic grasslands, primary producers, arthropod herbivores, and their predators). In aquatic systems, Petchey et al. in [128] also showed that in response to warming, communities lose more top predators.

As very few experimental works have explored the range of sensitivity of interacting species to warming and how the warming impacts species interactions, the goal here is to use a modelling approach to explore the impact of climate change on a pair of model species, in interaction. We focus on two traits, thermal sensitivity and dispersal ability, and explore the impact of differences in the thermal sensitivity of each species for these traits on species pattern of coexistence. Basically, we model species distribution in a wide range of thermal conditions and

explore the range of physiological thermal tolerance of each species that allow species coexistence. The idea is to explore the impact of ongoing warming on the spatial distribution and community formation of a pair of interacting species.

3.3 Mathematical Model of Climate Effect on Population Systems

We consider a mathematical model which focuses on the dynamics of a parasitoid-host system. The temporal dynamics of the system are modelled by a coupled system of two ordinary differential equations. The species interactions considered in our model exhibit oscillatory temporal dynamics. We extend the ODE system spatially where spatial interactions are considered via the random motility of each species, giving rise to a system of two partial differential equations (diffusion-reaction equations) that model the spatio-temporal dynamics of the host-parasitoid community described here.

Species' spatial movement plays an important factor in shaping ecological communities, as many ecological processes are driven by spatial structures. In certain ecological contexts, reaction-diffusion models may not adequately describe how organisms move and disperse through space [139]. Particularly, in [139] Rowell explains how models which incorporate the dispersal of species only by random diffusion fail to explain certain ecological phenomena and do not accurately reflect the non-Brownian motion of individuals. Species are not completely ignorant of the surrounding environment as the behaviour described by the random diffusion. Hence, spatial heterogeneity has been the subject of much study where authors are extending the standard diffusion-reaction systems to systems where species dispersal is a combination of random and biased movement. Mathematical modellers are accounting for bias velocities by the use of advection terms (diffusion-advection-reaction models) (for example, see [4, 146, 51, 132, 106] and references therein).

In our model, we account for the bias velocity of species by the advection term first proposed by Grindrod [63] where each species is moving along a fecundity gradient (see Section 2.3.3). This extra velocity term accounts for both spatial heterogeneous environments, e.g. food resources, and the species interactions. Grindrod [63] considered the dynamics of a competitive species model in one spatial domain and Kurowski et al. [102] in two spatial dimensions. In [154] authors extend the model studied in [62], [63] and [102] by considering more than two species or populations.

Apart from spatial variation, environmental variations, including climate change

[20, 29], can also impact species massively. In the paper of Y. Sekerci and S. Petrovskii [143], authors have shown that when the oxygen production rate in the ocean becomes too low or too high, which depends on the water temperature and hence affected by global warming, the plankton-oxygen system dynamics change abruptly, resulting in the oxygen depletion and plankton extinction. In [134] authors showed that warming can strongly stabilize or destabilize populations and food webs by changing the interaction strengths between predators and their prey.

Understanding the impact of global warming on the stability of populations is currently one of the most critical scientific challenges. However, the literature still lacks mechanistic understanding of how warming affects population dynamics, species' extinction risks and ecosystem functions.

In [142], the authors looked at the effects of climate change on a predator-prey model of ordinary differential equations by setting the predation rate to depend on temperature while in [61] authors set the temperature to only affect the predators indirectly by varying the rate of growth and carrying capacity of the prey according to fluctuations describing good and bad temperature years.

The above studies, although informative, neglect the influence of climate change on species dispersal. Species dispersal is likely to strongly influence patterns of co-occurrence [186, 99]. Moreover, very few studies are considering numerical schemes for the approximation of such systems and most numerical simulations found in the literature are accounting for a one-dimensional spatial domain. This acts as motivation for our work where we aim to numerically solve a two-dimensional predator-prey model with temperature dependence on both species dispersal as well as the rate of growth and carrying capacity of the prey.

Predator-prey systems have been studied extensively, and there are many different classical models. As a starting point, we present the (temperature-free) two-dimensional version of the diffusion-advection-reaction system studied in the previous chapter where Holling type II functional response is used to model the parasitism.

3.4 Two-Dimensional Diffusion-Advection-Reaction Parasite-Host Model

The mathematical model is based on a system of partial differential equations which incorporates the modification of species' movement in response to their interactions and the condition of their physical habitat. The host species of which the population density is denoted by u are modelled as having logistic,

density-dependent growth, with intrinsic growth rate r and carrying capacity K. Parasitoids' population density is defined by v and the parasitism is modelled by the Holling Type II functional response which describes the effect when the rate of prey consumption by a predator rises as prey density increases, but eventually levels off at an asymptote at which the rate of consumption remains almost constant regardless of increases in prey density [77]. Type II functional responses are the most frequently studied functional responses and are well-documented in empirical studies [60, 145, 90, 50]. The rate of parasitism is denoted by α while A is the prey population size at which the growth rate of the predator is half its maximum. The constant ε represents the number of viable eggs that a parasitoid lays on a single host, i.e., a parasitised host gives rise to ε next-generation parasitoids. In effect, ε is a dimensionless parameter (number of parasitoids per number of hosts) describing the parasitoid conversion efficiencies of hosts to parasitoids, often given as a fraction or decimal. Finally, parasitoids are subject to intrinsic mortality rates d and the motility coefficients δ_u and δ_v of the two species are constants and determine the rate at which each species disperses randomly through the domain. The full diffusion-advection-reaction system is thus as follows:

$$\begin{aligned}\frac{\partial u}{\partial t} = \underbrace{\delta_u \nabla^2 u}_{\text{random motility}} - \overbrace{\nabla \cdot (u \nabla \phi_u)}^{\text{movement driven by environment quality}} + \\ \underbrace{u r \left(1 - \frac{u}{K}\right)}_{\text{logistic growth}} - \overbrace{\frac{\alpha u v}{A + u}}^{\text{mortality due to parasitism}}\end{aligned} \tag{3.1}$$

$$\begin{aligned}\frac{\partial v}{\partial t} = \underbrace{\delta_v \nabla^2 v}_{\text{random motility}} - \overbrace{\nabla \cdot (v \nabla \phi_v)}^{\text{movement driven by environment quality}} + \\ \overbrace{\frac{\alpha \varepsilon u v}{A + u}}^{\text{growth due to parasitism}} - \underbrace{d v}_{\text{mortality}}\end{aligned} \tag{3.2}$$

where the expressions for $E_u(u, v, x, y)$ and $E_v(u, x, y)$ are

$$E_u(u, v, x, y) = r \left(1 - \frac{u}{K}\right) - \frac{\alpha v}{A + u}$$

and

$$E_v(u, x, y) = \frac{\alpha \varepsilon u}{A + u} - d,$$

respectively.
Then, the expressions for the velocity potentials ϕ_u and ϕ_v are (*cf.* (2.11))

$$E_u = -\epsilon_u \nabla^2 \phi_u + \phi_u \quad \text{and} \quad E_v = -\epsilon_v \nabla^2 \phi_v + \phi_v \tag{3.3}$$

where ϵ_u and ϵ_v are very small parameters for smoothing any sharp variations in $E_v(u, v, x, y)$ and ϕ_u and $E_v(u, x, y)$ and ϕ_v, respectively. The system is posed on a given domain say Ω of length L, i.e., $\Omega = (0, L) \times (0, L)$, with zero-flux Neumann boundary conditions on the boundaries $\partial\Omega$ to close the system.
The list containing all the variables and parameters used in the model can be seen in Table 2.1.

Even though the above model is set to include many real-life complexities it still has some limitations.

3.4.1 Limitations

The system equations (3.1) and (3.2) assume that species live in an ecosystem where external factors such as droughts, fires, and epidemics are stable or have a similar effect on the interacting species. Moreover, the predator is completely dependent on the prey as the only favourite food source. The logistic growth of the prey in the absence of the predator or human poaching of the prey implies that the population of the prey would increase in a sigmoid curve shape until it reaches the maximum density of the living area, which is its carrying capacity. Moreover, the system assumes that there is no threat to the prey besides the predator species being studied.
Lastly, the system above assumes that climate changes varying in space and through time do not affect species' individual performance or their biotic interactions. Hence, we wish to add the climatic influence to our model through a climate function as described in the next section.

3.5 Climate Function

It is proven by historic data that climate change is happening, yet very little is known about how climate change can affect predator-prey dynamics. Following the paper of Gretchko, Marley and Tyson [61], we have incorporated temperature variation in the model through the use of a climate function. The response of the climate function to temperature, in our model, is based on the thermal performance curve of ectotherms.

Figure 3.1a shows the general thermal performance curve of ectotherms where the critical minimum and critical maximum temperatures indicate the lower and upper thermal limits of performance respectively. The optimal temperature is at which the performance is maximised and the performance breadth is the temperature range where the performance is half its maximum. Using the thermal performance curve for ectotherms, shown in Figure 3.1a, as an indicator of the relationship between the species' relative fitness and temperature, we introduce the climate function $g(T)$ which has a range of values between 0 and 1 where the value 0 corresponds to the optimal/favourable temperature and 1 corresponds to the lower or upper critical temperatures. Any values between these two extremes are allowed as shown in Figure 3.1b.

We have set the climate function g to affect the velocity of both species while only affecting the prey logistic growth directly. This means that, apart from the movement, predators respond indirectly to climate change through changes in prey density. This is achieved by making the movement of species and the growth rate and carrying capacity of the prey dependent on the climate function. By equation (2.9) the velocity by which the two populations are dispersing can be expressed by

$$w_u = -\delta_u \frac{1}{u} (\nabla u) + \nu_u$$

for the prey, and

$$w_v = -\delta_v \frac{1}{v} (\nabla v) + \nu_v$$

for the predator, where the bias velocities are defined by $\nu_u = \nabla \phi_u$ and $\nu_v = \nabla \phi_v$ (see equation (2.10)). Hence, the new temperature-dependent velocities of the prey and the predator are

$$\tilde{w}_u = w_u \left(1 - e_{w_u} g(T)\right)$$

and

$$\tilde{w}_v = w_v \left(1 - e_{w_v} g(T)\right)$$

respectively, where $0 < e_{w_u, w_v} < 1$ are scaling factors of the climate function. Usually, parasites have a smaller size than their prey, therefore climate change has a greater effect on the predator movement than on the prey movement and hence $e_{w_v} > e_{w_u}$.

In a similar way, the intrinsic growth rate and the carrying capacity of the prey are dependent on the temperature by the equations

$$\tilde{r} = r \left(1 - e\, g(T)\right)^2$$

and

$$\tilde{K} = K \left(1 - e\, g(T)\right)^2,$$

respectively. Again, $0 < e < 1$ are scaling factors of the climate function.

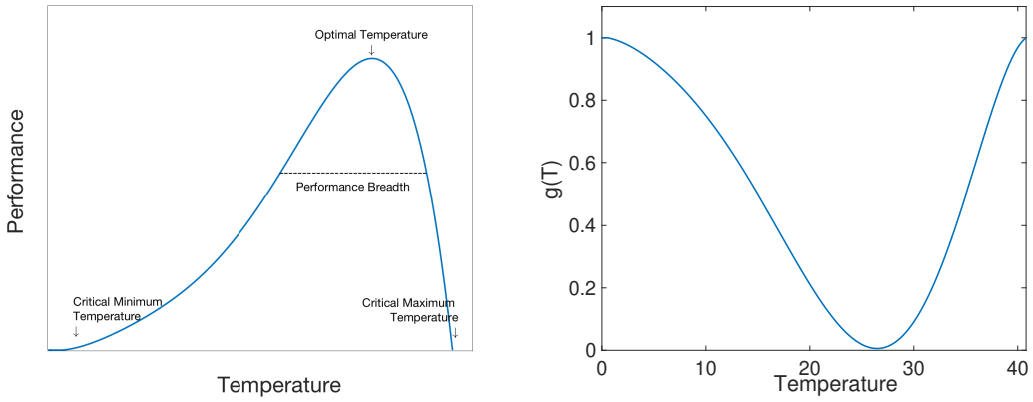

(a) Thermal performance curve of ectotherms.

(b) Climatic function $g(T)$.

Figure 3.1: The formation of the climate function $g(T)$ based on the general shape of the thermal performance curve for ectotherms.

Having defined the climate function and how it affects the chosen variables and parameters, we now include it in the full system of equations (3.1) and (3.2).

3.6 Temperature Dependent Two-Dimensional Parasite-Prey Model

The full reaction-diffusion-advection system of (3.1) and (3.2) for the two-dimensional predator-prey model with temperature dependence, as described above, is

$$\begin{aligned}\frac{\partial u}{\partial t} &= \left(\delta_u \nabla^2 u - \nabla \cdot (u \nabla \phi_u)\right)(1 - e_u g(T)) + \\ &\qquad u\tilde{r}\left(1 - \frac{u}{\tilde{K}}\right) - \frac{\alpha u v}{A + u} \\ &= \left(\delta_u \nabla^2 u - \nabla \cdot (u \nabla \phi_u)\right)(1 - e_u g(T)) + \\ &\qquad u r (1 - e g(T))\left(1 - e g(T) - \frac{u}{K(1 - e g(T))}\right) - \frac{\alpha u v}{A + u}\end{aligned} \tag{3.4}$$

and

$$\frac{\partial v}{\partial t} = \left(\delta_v \nabla^2 v - \nabla \cdot (v \nabla \phi_v)\right)(1 - e_v g(T)) + \frac{\alpha \varepsilon u v}{A + u} - d v. \tag{3.5}$$

The equations for $E(u,x,t)$ and $E(v,x,t)$ are given by the temperature-dependent system (3.4) and (3.5) in the following form

$$\begin{aligned} E_u(u,v,x,y) &= \tilde{r}\left(1-\frac{u}{\tilde{K}}\right)-\frac{\alpha v}{A+u} \\ &= r(1-e\,g(T))\left(1-e\,g(T)-\frac{u}{K(1-e\,g(T))}\right)-\frac{\alpha v}{A+u} \end{aligned} \tag{3.6}$$

and

$$E_v(u,x,y)=\frac{\alpha\varepsilon u}{A+u}-d. \tag{3.7}$$

As already stated in (3.3) the equations for the velocity potential ϕ_u and ϕ_v are

$$E_u=-\epsilon_u\nabla^2\phi_u+\phi_u \quad \text{and} \quad E_v=-\epsilon_v\nabla^2\phi_v+\phi_v. \tag{3.8}$$

Again, $0\leq\epsilon_u,\ \epsilon_v<1$.
We next carry out a stability analysis of the movement-free temperature-dependent system and compare the findings with the results obtained in Section 2.5.2 for the temperature-independent model.

3.6.1 Model stability analysis of the temperature-dependent model

Using the scaling in Section 2.5.1 and dropping the hats, the resulting non-dimensionalized system is given by,

$$\frac{\partial u}{\partial t}=\Big(\tilde{D}_u\nabla^2u+\nabla\cdot(u\nabla\phi_u)\Big)\left(1-e_u\,g(T)\right)+u\Big(1-e\,g(T)-u\Big)-\frac{\tilde{s}_1\,u\,v}{\tilde{z}+u} \tag{3.9}$$

and

$$\frac{\partial v}{\partial t}=\Big(\tilde{D}_v\nabla^2v+\nabla\cdot(v\nabla\phi_v)\Big)\left(1-e_v\,g(T)\right)+\frac{\tilde{s}_2\,u\,v}{\tilde{z}+u}-\tilde{\beta}\,v. \tag{3.10}$$

Therefore, by the non dimensional system (3.9) and (3.10), the dimensionless equations for $E(u,x,t)$ and $E(v,x,t)$ are given by

$$E_u(u,v,x,y)=(1-e\,g(T)-u)-\frac{\tilde{s}_1\,v}{\tilde{z}+u}$$

and

$$E_v(u,x,y)=\frac{\tilde{s}_2\,u}{\tilde{z}+u}-\tilde{\beta},$$

followed by the non-dimensional equations for ϕ_u and ϕ_v,

$$\phi_u - \frac{\epsilon_u}{L^2}\nabla^2\phi_u = \frac{1}{\kappa}\left(1 - e\,g(T) - u\right) - \frac{m_1\,v}{\tilde{z}+u} \tag{3.11}$$

$$\phi_v - \frac{\epsilon_v}{L^2}\nabla^2\phi_v = \frac{m_2\,u}{\tilde{z}+u} - \gamma \tag{3.12}$$

where

$$\begin{aligned}
\tilde{D}_u &= D_u/(1-eg(T)),\\
\tilde{D}_v &= D_v/(1-eg(T)),\\
\tilde{s}_1 &= s_1/(1-eg(T)),\\
\tilde{s}_2 &= s_2/(1-eg(T)),\\
\tilde{z} &= z/(1-eg(T)),\\
\tilde{\beta} &= d/(1-eg(T)),\\
m_1 &= \tilde{s}_1/(rL^2),\\
m_2 &= \tilde{s}_2/(rL^2),\\
\gamma &= \tilde{\beta}/(rL^2),\\
\text{and}\quad \kappa &= 1/(rL^2),
\end{aligned} \tag{3.13}$$

(*cf.* (2.24)).
We carry out the same linear stability analysis as the one in Section 2.5.2 which reveals the following three non-negative equilibrium states for the temperature-dependent model are:

- the unstable trivial state, $(0,0)$, with eigenvalues $1-eg(T)$ and $-\beta$. Since $0 \le eg(T) < 1$, $(0,0)$ is an unstable saddle point.
- the locally asymptotically stable host-only state, $(1-eg(T),0)$, where both eigenvalues are negative if

  $$\tilde{\beta} > \frac{\tilde{s}_2(1-e\,g(T))}{\tilde{z}+1-e\,g(T)}$$

  holds, or else $(1,0)$ is an unstable saddle point.
- the coexistent state, (u^*, v^*), where

  $$u^* = \frac{\tilde{\beta}\,\tilde{z}}{\tilde{s}_2 - \tilde{\beta}}$$

and

$$v^* = \frac{(1 - eg(T) - u^*)(\tilde{z} + u^*)}{\tilde{s}_1}.$$

This steady state is feasible only if

$$0 < \frac{\tilde{\beta}\tilde{z}}{\tilde{s}_2 - \tilde{\beta}} < 1 - eg(T) \tag{3.14}$$

and the positive equilibrium point (u^*, v^*) is locally asymptotically stable if

$$\tilde{z} > \frac{(\tilde{s}_2 - \tilde{\beta})(1 - eg(T))}{\tilde{s}_2 + \tilde{\beta}}. \tag{3.15}$$

If we express (3.15) in terms of the parameters given in (2.24) we would be able to compare the conditions (2.28) and (3.15) of the temperature-independent and temperature-dependent model, respectively.
The condition given in (3.15) for which the coexistence steady state of the temperature-dependent model undergoes a Hopf bifurcation in terms of the parameters in (2.24) is given by

$$z > (1 - eg(T))^2 \frac{(s_2 - \beta)}{(s_2 + \beta)}.$$

In fact, since $0 \leq eg(T) < 1$ the condition in (2.28) is sufficient for an asymptotically stable coexistence steady state for the temperature-dependent model.

Turning our attention now to the condition in (3.14) which gives the criterion expression for the feasibility of the coexistence steady state $E(u^*, v^*)$. If we express (3.14) in terms of the parameters given in (2.24) we have

$$0 < \frac{\beta z}{(s_2 - \beta)} < (1 - eg(T))^2. \tag{3.16}$$

Equation (3.16) implies that the coexistence steady state is only feasible for a range of favourable temperatures and the size of this range depends on the values of β, z, s_2 and e. Outside this range the coexistence steady state is not feasible any more, giving rise to the host-only state $(1-eg(T), 0)$ which is stable for those (very low or very high) temperatures. Therefore the climate function is set to change the dynamics of the predator-prey system.

In the section above we have shown that the inclusion of the climate function in our model does change the outcome of the predator-prey relationship. As in the temperature-independent model, the three usual predator-prey species outcomes

(both populations die out; prey wins; stable coexistence) are possible for the temperature-dependent model but with different equilibrium points. The conditions for the feasibility or the stability of those equilibrium points are different for each case.

In this thesis, we are mainly interested to see how temperature variation can influence the formation of communities and the patterns of species co-occurrence. Hence, we numerically solve the temperature-dependent predator-prey model by accounting for the maximum temperatures of three different years in Spain and Portugal. The results are reported and compared below.

3.7 Numerical Simulations

3.7.1 Environment and Climatic Data

In a recent study, [168], that examined how climate change is affecting the patterns and duration of the seasons in the Northern Hemisphere, scientists Wang et al. revealed that the average length of summer in Northern latitudes has already increased from 78 to 95 days between 1952 and 2011, while the length of winter, spring and autumn contracted with winter to shrunk from 76 to 73 days. In addition, authors have predicted that summer will last nearly half a year, but winter less than 2 months by 2100. Such a discovery is a good overarching starting point for understanding the implications of seasonal change and trigger reactions.

In this study, we aim to gain an overview of the effect of longer and hotter summer seasons on predator and prey space distributions. For the simulations in this chapter, we are considering the climatic map of the maximum temperatures observed in Spain and Portugal from March to November for the years 1950 to 2020. Spain and Portugal offer a wide range of temperatures, including warm temperatures which are likely to be beyond the tolerance range of our species (parasites and their prey). Such content will allow hypotheses on the impact of heat islands (urban zone) and heat stress and this would not have been possible with a limited range of temperatures.

Maps of the maximum temperatures for 1950 and 2020 can be seen in Figure 3.2. We have also used the data over the 70 years period (1950-2020) to project, using linear extrapolation, the estimated temperatures for the year 2050.

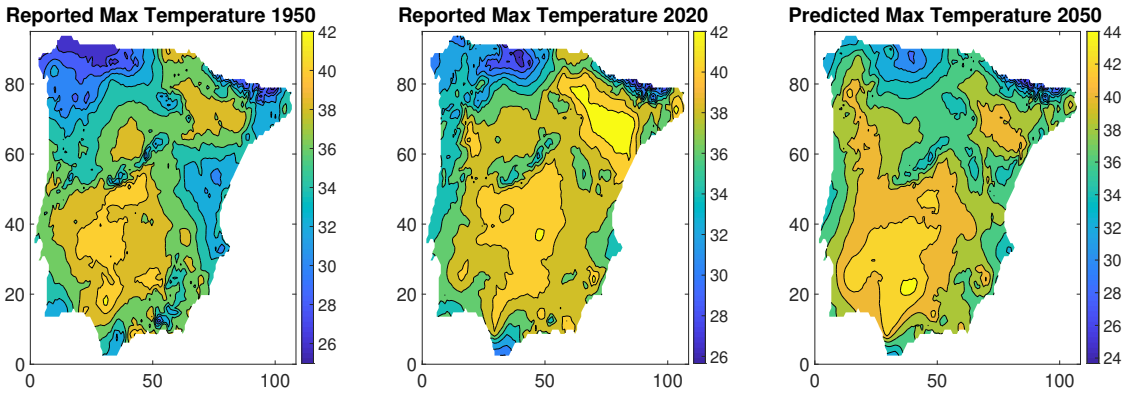

Figure 3.2: Map of the reported maximum temperatures for March to November for the years 1950 and 2020 and the predicted maximum temperatures for the year 2050 in Spain and Portugal.

3.7.2 Parameter values

The choice of the parameter values used for the following simulations is strongly based on the paper of Pearce et al. [127] where authors studied a system of four reaction-diffusion equations describing the dynamics of two hosts and two parasites. In this work, the host dispersal is considered to be greater than the one of the parasitoids.
The values of the parameters are as listed:

Parameter	Value	Description
δ_u	0.01	Prey diffusive parameter
δ_v	0.0003	Predator diffusive parameter
r	0.4	Intrinsic growth rate for prey
K	250	Carrying capacity for prey
ε	0.4	Parasitoid conversion efficiencies of hosts to parasitoids
α	0.35	Parasitism rate
d	0.09	Intrinsic mortality rate of parasitoids
A	80	Predator half-saturation constant
Constant	Value	Description
e_{w_u}	0.7	for the prey velocity
e_{w_v}	0.9	for the parasitoid velocity
e	0.4	for the prey growth rate and carrying capacity
ϵ	0.25	smoothing constant

Table 3.1: Parasite-prey model (3.4)-(3.8) parameter and constant values used for the simulations.

We consider a domain of lengths $L \times M = (1000^2\text{m} \times 1000^2\text{m})$, corresponding to the Spanish mainland extent, i.e., 1,085 km (674 mi) East-West and 950 km (590 mi) North-South. Given the above parameter values, the baseline non-dimensional parameter set (2.24) is: $D_u = 2.5 \times 10^{-6}, D_v = 1.0 \times 10^{-9}, s_1 = 0.875, s_2 = 0.35, z = 0.32, \beta = 0.225$. Thus the parameters in (3.13) for the dimensionless temperature-dependent model are given by

$$\begin{aligned}
\tilde{D}_u &= 2.5 \times 10^{-6}/(1 - e\,g(T)),\\
\tilde{D}_v &= 1.0 \times 10^{-9}/(1 - e\,g(T)),\\
\tilde{s}_1 &= 0.875/(1 - e\,g(T)),\\
\tilde{s}_2 &= 0.35/(1 - e\,g(T)),\\
\tilde{z} &= 0.32/(1 - e\,g(T)),\\
\tilde{\beta} &= 0.225/(1 - e\,g(T)),\\
m_1 &= 0.875/\left(4 \times 10^5(1 - e\,g(T))\right),\\
m_2 &= 0.35/\left(4 \times 10^5(1 - e\,g(T))\right),\\
\gamma &= 0.225/\left(4 \times 10^5(1 - e\,g(T))\right),\\
\kappa &= 1/(4 \times 10^5).
\end{aligned} \tag{3.17}$$

We now proceed with the numerical approximation of the non-dimensional system (3.9)-(3.12).

3.7.3 Finite difference scheme

The model is encoded on a two-dimensional rectangular domain defined by $0 \leq x \leq 108.5$ and $0 \leq y \leq 95$. We discretize the domain by 130×78 equally spaced nodes ($\Delta x = \frac{108.5}{130}$ and $\Delta y = \frac{95}{78}$), as shown in Figure 3.3.

Boundary conditions

For the outer boundaries of the rectangular domain, we apply zero Neumann boundary conditions which confine species, while to create the boundaries separating land and sea (see Figure 3.3) we set all the parameters to zero at the sea, including the diffusion parameters.

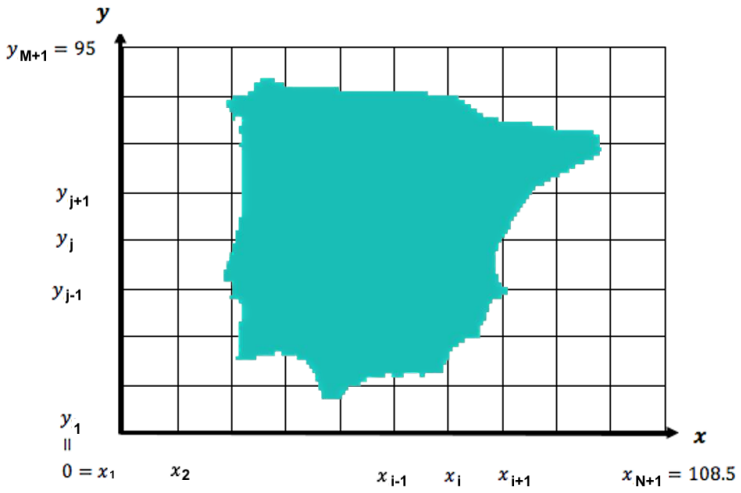

Figure 3.3: Two-dimensional finite difference grid; $N = 130$, $M = 78$. The blue colour depicts the land and the white colour the sea.

Numerical solution

The dimensionless system (3.9)-(3.12) is solved by the finite difference method and a forward Euler time-stepping method is used to integrate the equations. Second- and first-order terms are approximated using central difference and one-sided approximation, respectively. For the solutions of $\partial u/\partial t$ (3.9) and $\partial v/\partial t$ (3.10), the value of the velocity potentials $\phi_{u,v}$ are required. Hence, equations (3.11) and (3.12) are approximated first which need the formation of pentadiagonal matrices.
The equation approximating ϕ_u (3.11) after applying the finite difference approx-

imations is

$$
\begin{aligned}
&-\frac{\epsilon_u}{\Delta x^2}\phi^n_{u(i+1,j)}-\frac{\epsilon_u}{\Delta y^2}\phi^n_{u(i,j+1)}+\left(1+\frac{2\epsilon_u}{\Delta x^2}+\frac{2\epsilon_u}{\Delta y^2}\right)\phi^n_{u(i,j)}-\\
&\frac{\epsilon_u}{\Delta x^2}\phi^n_{u(i-1,j)}-\frac{\epsilon_u}{\Delta y^2}\phi^n_{u(i,j-1)}=\frac{1}{\kappa}\left(1-e\,g(T_{(i,j)})-u_{(i,j)}\right)-\frac{m_1\,v^n_{(i,j)}}{\tilde{z}+u^n_{(i,j)}} \qquad (3.18)\\
&\text{for}\quad i=2,...,N\quad\text{and}\quad j=2,...,M
\end{aligned}
$$

and for ϕ_v by (3.12),

$$
\begin{aligned}
&-\frac{\epsilon_v}{\Delta x^2}\phi^n_{v(i+1,j)}-\frac{\epsilon_v}{\Delta y^2}\phi^n_{v(i,j+1)}+\left(1+\frac{2\epsilon_v}{\Delta x^2}+\frac{2\epsilon_v}{\Delta y^2}\right)\phi^n_{v(i,j)}-\\
&\frac{\epsilon_v}{\Delta x^2}\phi^n_{v(i-1,j)}-\frac{\epsilon_v}{\Delta y^2}\phi^n_{v(i,j-1)}=\frac{m_2\,u^n_{(i,j)}}{\tilde{z}+u^n_{(i,j)}}-\gamma \qquad (3.19)\\
&\text{for}\quad i=2,...,N\quad\text{and}\quad j=2,...,M.
\end{aligned}
$$

The dimensionless equation for $\partial u/\partial t$ (3.9) after the finite difference approximations takes the form

$$
\begin{aligned}
&\frac{\partial u}{\partial t}=\\
&\left[-\frac{1}{\Delta x^2}\left(\frac{\left(u^n_{(i+1,j)}+u^n_{(i,j)}\right)\left(\phi^n_{u(i+1,j)}-\phi^n_{u(i,j)}\right)}{2}-\frac{\left(u^n_{(i,j)}+u^n_{(i-1,j)}\right)\left(\phi^n_{u(i,j)}-\phi^n_{u(i-1,j)}\right)}{2}\right)-\right.\\
&\frac{1}{\Delta y^2}\left(\frac{\left(u^n_{(i,j+1)}+u^n_{(i,j)}\right)\left(\phi^n_{u(i,j+1)}-\phi^n_{u(i,j)}\right)}{2}-\frac{\left(u^n_{(i,j)}+u^n_{(i,j-1)}\right)\left(\phi^n_{u(i,j)}-\phi^n_{u(i,j-1)}\right)}{2}\right)+\\
&\left.\delta_u\left(\frac{u^n_{(i-1,j)}-2u^n_{(i,j)}+u^n_{(i+1,j)}}{\Delta x^2}\right)+\delta_u\left(\frac{u^n_{(i,j-1)}-2u^n_{(i,j)}+u^n_{(i,j+1)}}{\Delta y^2}\right)\right]\left(1-eg(T_{(i,j)})\right)+\\
&u^n_{(i,j)}\left(1-eg(T_{(i,j)})-u^n_{(i,j)}\right)-\frac{\tilde{s}_1\,u^n_{(i,j)}\,v^n_{(i,j)}}{\tilde{z}+u^n_{(i,j)}}\qquad\text{for}\quad i=2,...,N\quad\text{and}\quad j=2,...,M.\\
&\qquad\qquad (3.20)
\end{aligned}
$$

and for $\partial v/\partial t$ by (3.10) we get

$$\frac{\partial v}{\partial t} =$$
$$\left[-\frac{1}{\Delta x^2}\left(\frac{\left(v^n_{(i+1,j)}+v^n_{(i,j)}\right)\left(\phi^n_{v(i+1,j)}-\phi^n_{v(i,j)}\right)}{2} - \frac{\left(v^n_{(i,j)}+v^n_{(i-1,j)}\right)\left(\phi^n_{v(i,j)}-\phi^n_{v(i-1,j)}\right)}{2} \right) -$$
$$\frac{1}{\Delta y^2}\left(\frac{\left(v^n_{(i,j+1)}+v^n_{(i,j)}\right)\left(\phi^n_{v(i,j+1)}-\phi^n_{v(i,j)}\right)}{2} - \frac{\left(v^n_{(i,j)}+v^n_{(i,j-1)}\right)\left(\phi^n_{v(i,j)}-\phi^n_{v(i,j-1)}\right)}{2} \right) +$$
$$\delta_v\left(\frac{v^n_{(i-1,j)}-2v^n_{(i,j)}+v^n_{(i+1,j)}}{\Delta x^2}\right)+\delta_v\left(\frac{v^n_{(i,j-1)}-2v^n_{(i,j)}+v^n_{(i,j+1)}}{\Delta y^2}\right)\Big]\left(1-eg(T_{(i,j)})\right)+$$
$$\frac{\tilde{s}_2\, u^n_{(i,j)}\, v^n_{(i,j)}}{\tilde{z}+u^n_{(i,j)}} - \tilde{\beta}\, v^n_{(i,j)} \qquad \text{for} \quad i=2,...,N \quad \text{and} \quad j=2,...,M. \tag{3.21}$$

The equations for ϕ_u, ϕ_v, $\partial u/\partial t$ and $\partial u/\partial t$ at the outer boundaries are evaluated by equations (3.18), (3.19), (3.20) and (3.21), respectively by accounting for zero Neumann boundary conditions.
For example, to evaluate $\phi_{u(1,1:M)}$ from (3.18) (at the left-hand-side boundary, x_1, of Figure 3.3) we consider the zero Neumann boundary condition

$$\frac{\partial \phi_u}{\partial x} = 0 \quad \text{at} \quad x = 0. \tag{3.22}$$

Applying a two-interval approximation gives

$$\frac{\phi_{u(2,1:M)} - \phi_{u(0,1:M)}}{2\Delta x} = 0 \tag{3.23}$$

and hence

$$\phi_{u(0,1:M+1)} = \phi_{u(2,1:M+1)}.$$

Having evaluated $\partial u/\partial t$ and $\partial v/\partial t$ we then use the Euler explicit scheme to update the population densities.
As already discussed in Chapter 2, the forward Euler time-stepping scheme for the heat equation is restricted by the stability condition $\Delta t/\Delta x^2 < 0.5$, where Δt and Δx define the time step value and the interval between the space nodes, respectively. Taking this restriction as a guide to avoid instability in the solution of our diffusion-reaction-advection system and according to the formation of our space, as mentioned above, we use the time step value $\Delta t < 0.1$ for the simulations.

Using the convergence analysis of the 1-D temperature-free system in Section 2.7, we observed that the error of the solution decays as we use a finer mesh and the approximation generated by the explicit scheme converges to the exact solution of the differential equations with a convergence rate of 2. Since the system of equations used in the model cannot be solved analytically, we use the case of having many space nodes as the exact solution for comparison. Even though the error of the approximation decays with increasing the mesh density, and is a critical issue which closely relates to the accuracy of the model, it can be impractical as it can result in a more computationally expensive scheme because of the more steps of calculation required by the stability criterion stated above. Also, as the spatial resolution increases, the rounding error increases accordingly, and eventually overtakes the truncation error. The repeated experiments of the 2-D temperature-dependent model with adjusting the space step Δx and time step Δt ensure that further reductions in the space step had no significant effect on the numerical results.

Initial conditions

We have used the same initial conditions for both species where they are set to initially occupy a region of the domain as shown in Figure 3.4. The function used which corresponds to the initial conditions shown in Figure 3.4 is

$$u^0_{m,n} = v^0_{m,n} = \cos^2\left(\frac{\pi}{20}\left(x_m - x_{40}\right)\right) \times \cos^2\left(\frac{\pi}{20}\left(y_n - y_{30}\right)\right), \tag{3.24}$$

where m and n denote the intervals (x_{30}, x_{50}) and (x_{20}, x_{40}), respectively, while the initial conditions of u and v are zero outside these intervals.

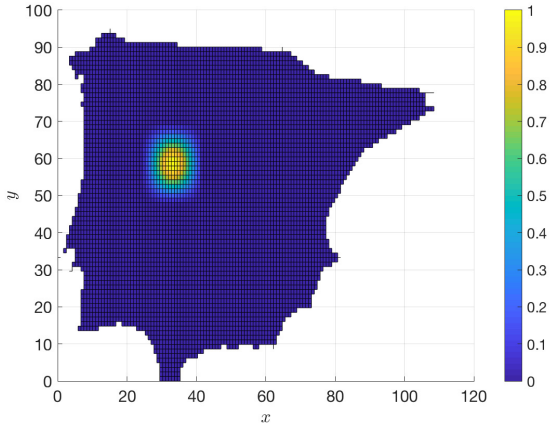

Figure 3.4: Initial conditions for the dimensionless parasitoid-host temperature-dependent system. The same initial conditions were used for both u and v ($u(x,0) = v(x,0)$).

3.8 Results

The following figures show the results from the simulations using three different temperature sets for the three years 1950, 2020 and 2050. For all cases, we have used the same initial conditions as illustrated in Figure 3.4 and the same parameter values as shown in (3.17) for the dimensionless temperature-dependent system. Figure 3.5 shows the results for $t = 20000$, Figure 3.6 for $t = 36000$ and Figure 3.7 for $t = 50000$. The left-hand side column in all the following plots illustrates the results of the host population density, the middle column shows the results for the parasitoid population density and the column on the right-hand side depicts the climatic map for the maximum temperature in each year. The different time plots allow us to see the time evolution of the community formation of each species in the domain. In general, we observe that high population density communities were formed in regions with relatively low temperatures. The host population (left-hand side graph) has spread throughout the domain where high populations are observed in regions with low temperatures except in parts of the domain where parasitoids exist. Due to species interactions, regions of coexistence are observed to have lower host densities.

Comparing the results of each year we clearly see that the increase in temperature through the years has led to a continual decrease in the expansion of the species in the domain. For the host population, fewer communities with high population density are found in the results of years 2020 and 2050 while the parasitoids are mostly found in the northern part of the domain in the corresponding year results. Moreover, we observe a decrease in the total mass of the species (the number of individuals). This phenomenon is more clear in the parasitoid results.

The model stability analysis carried out in Section 3.6.1 showed that the coexistence steady state is stable for a range of favourable temperatures. Outside this range, the only stable steady state is the host-only. This observation is also visible in the results below where the host population is shown to have spread throughout the domain while the parasitoid population only exist in regions of relatively low temperatures.

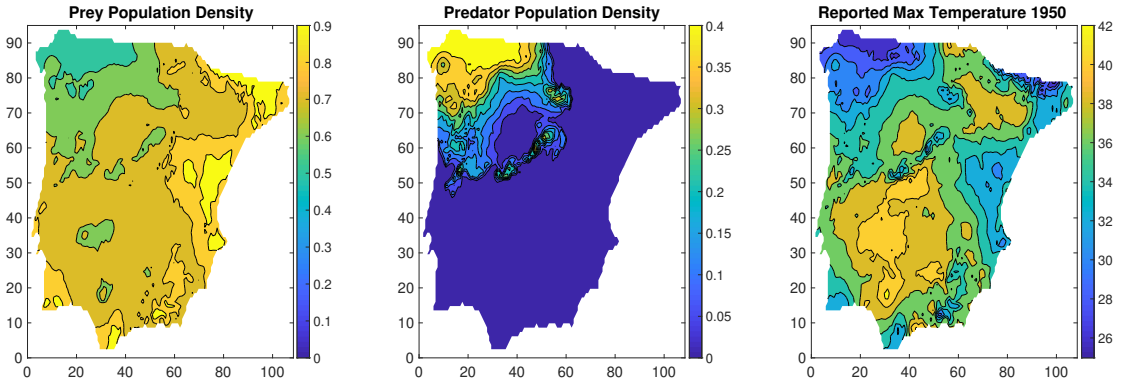

(a)

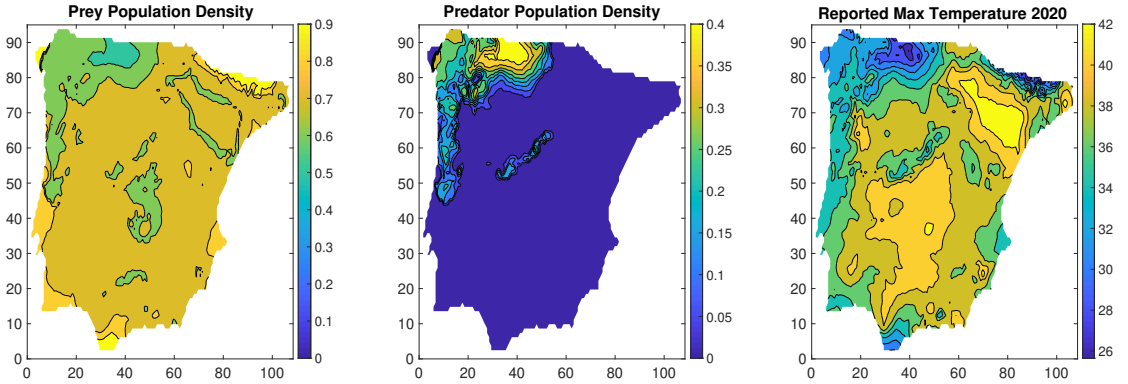

(b)

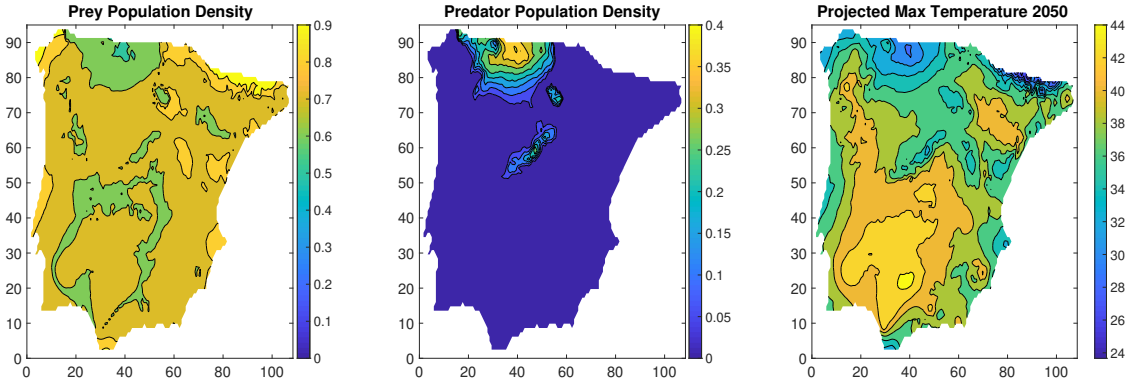

(c)

Figure 3.5: Representation of the distribution of prey and predator population densities in space for each year 1950 (a), 2020 (b), 2050 (c), at $t = 20000$. For each case, the maximum temperature of each year is considered (right-hand side plots).

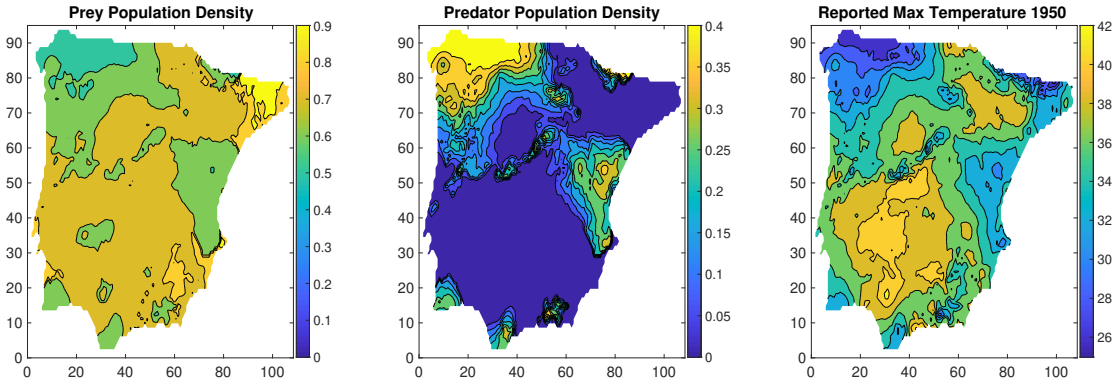

(a)

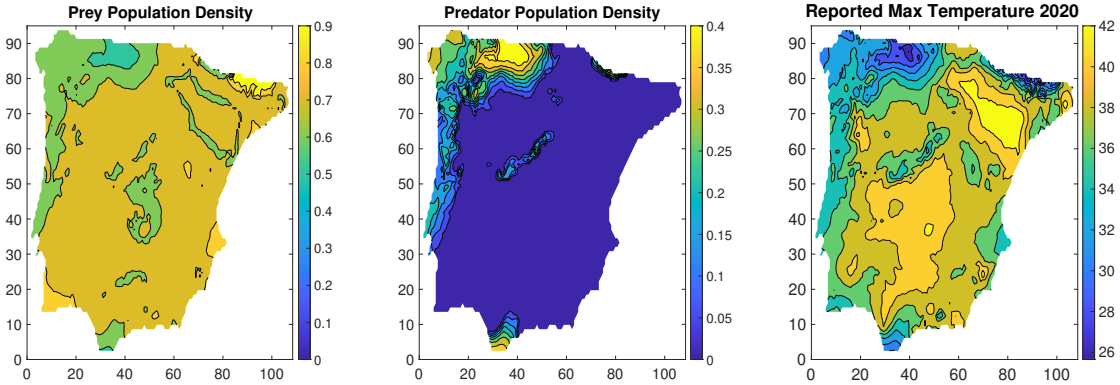

(b)

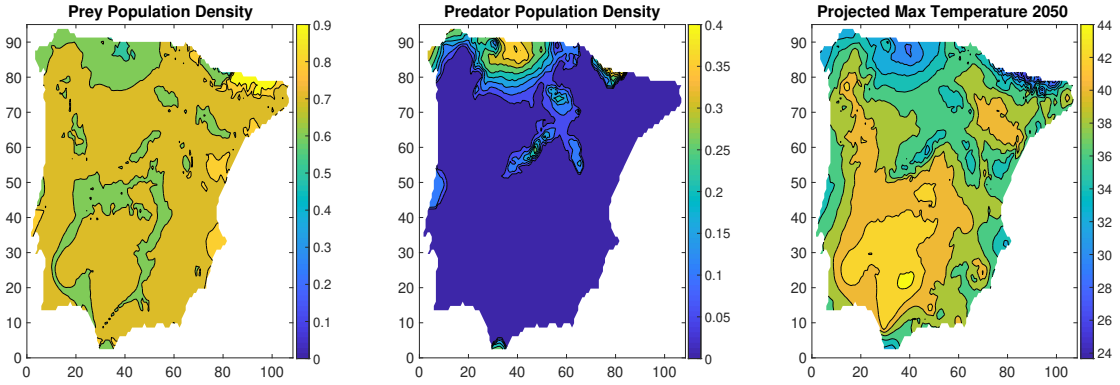

(c)

Figure 3.6: Representation of the distribution of prey and predator population densities in space for each year 1950 (a), 2020 (b), 2050 (c), at $t = 36000$. For each case, the maximum temperature of each year is considered (right-hand side plots).

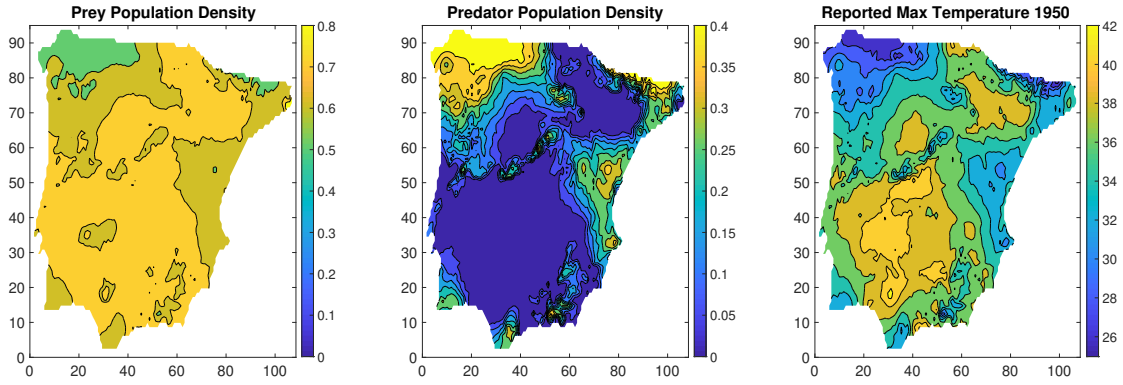

(a)

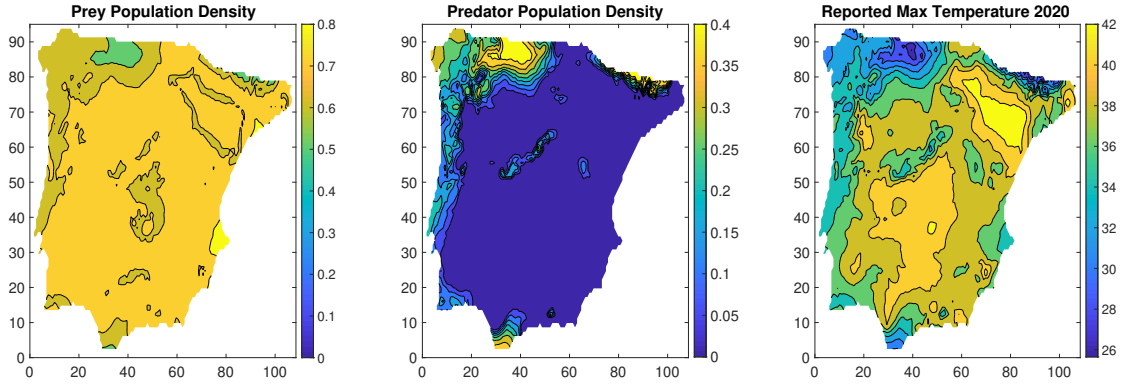

(b)

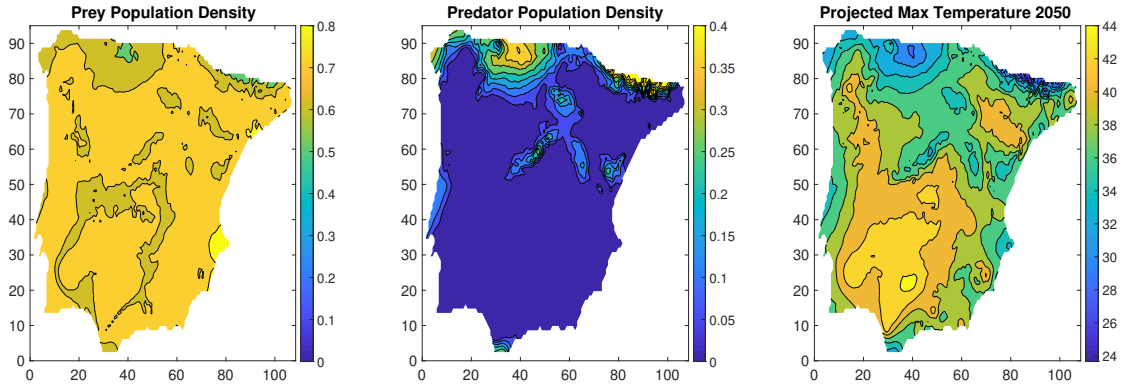

(c)

Figure 3.7: Representation of the distribution of prey and predator population densities in space for each year 1950 (a), 2020 (b), 2050 (c), at $t = 50000$. For each case, the maximum temperature of each year is considered (right-hand side plots).

3.9 Summary

In this chapter, we considered the numerical approximation of a reaction-diffusion-advection parasitoid-host system with climatic influence in a two-dimensional spatial domain using a fixed mesh method. The parasitoid-host relationship was described by a Holling type two functional response while the directed movement of species towards more favourable regions of the domain was modelled using an advection term depending on a fecundity gradient. This advection term describes a biased velocity of species taking into account the environmental conditions of their habitat as well as the conspecific interactions. The climate influence was modelled using a climate function that modified both the intrinsic growth rate and carrying capacity for prey and the dispersal velocity of both species (random diffusion and biased-directed velocity). The climate function was constructed based on the thermal performance curve of ectotherms and was set to take values from 0 to 1 corresponding to more and less favourable temperatures, respectively. Climate function scaling factors were used to describe the magnitude of the effect of temperature on each of the variables and parameters set to be influenced by climate change.

A model stability analysis of the temperature-dependent system was carried out to obtain conditions for the parameter values required to produce biological meaningful behaviour by looking at the non-negative equilibrium points. Then, these conditions were compared with the ones observed in Chapter 2 for the temperature-independent version of the system. The model stability analysis of the temperature-dependent model showed that the coexistence steady state is only feasible for a range of favourable temperatures while for very low or very high temperatures the coexistence steady state becomes unstable and only the host-only steady state is stable for those temperature ranges.

The central aim of this investigation was to observe the effect of the increasing temperature through the years on the distribution of species and community formation. Hence, results were obtained from a numerical approximation of the solution by considering the maximum temperatures observed in Spain and Portugal in the years 1950 and 2020 as well as the maximum temperature projections for the year 2050. The results reported in this chapter showed that the community formation and distribution of species in space correspond with the climatic map of the maximum temperature of each year (i.e., high population densities were observed in regions with low temperatures). Moreover, we observed that there is no predator existence in regions of very high temperatures while hosts were spread throughout the domain. This observation correlates with the insights gained from the model stability analysis.

In this investigation, we only considered the direct influence of climate change on species dispersal and intrinsic growth rate and carrying capacity of the prey. Other model parameters, however, may also be affected by climate change. Possible candidates are the predator kill rate and predator mortality rate if changing climatic conditions make it harder for the predators to hunt and kill prey or if climatic conditions could be fatal to the predator. By considering more specific parasitoid-host systems (i.e., specific species of parasitoid and their hosts) for which enough data has been collected we may be able to get a better description of the complex influence that global warming can exert upon those systems. The climate function used here is general and can be adapted to many situations. The climate function scaling factor makes the climate function suitable to be adjusted to influence many parameters of the model.

3.10 Fixed and Moving Meshes for Population Dynamics

The explicit finite difference numerical scheme used to approximate the parasitoid-host system of this chapter is a standard numerical technique used by a lot of modellers to approximate a range of different PDEs. Even though the method is widely used and is easy to implement there are some drawbacks. We now briefly describe the limitations associated with accuracy considerations of the explicit finite difference method followed by a short introduction to moving mesh methods which will form the substance of the rest of the thesis.

The leading term in the truncation error of a fixed-mesh explicit finite difference numerical scheme for a diffusion problem is proportional to $h\frac{d^4u}{dx^4}$, where $h = \frac{\delta\Delta x^2}{12}$, which is a numerical diffusion distinct from the diffusion intrinsic to the problem.

In convergence, as $\Delta x \to 0$ and hence h tends to zero this numerical diffusion term also tends to zero (as it should) and the truncation error decreases as the leading term is eliminated. But if $\frac{d^4u}{dx^4}$ is large the magnitude is always large even when h is small, and the results are adversely affected.

This situation occurs at a 'corner' of a near-discontinuity in u, for example at the base or top of a near-vertical part of a graph of u, particularly if it is moving.

In these circumstances, a superior description is to have a moving point at the discontinuity and replace the PDE by a jump condition, forming the so-called moving boundary. The moving mesh method based on conservation is well-suited to accommodate this description. The main feature of the moving mesh based on conservation is that moving nodes are concentrated in regions with increasing density u since the method is based on a conservation principle that "forces" the

mass (number of individuals of a population), i.e., the area under the graph of the density u, within each element of the discretised domain to remain constant for all time. Therefore, regions with increasing density u will have a denser mesh as the area under the graph of u within each element remains constant. Hence the derivative of the leading term in the truncation error balances out between the denominator and the numerator.

The systems of reaction-diffusion-advection equations coupled with moving inner or outer boundaries and interfaces (near discontinuities in the solution) have been widely used to describe the dynamics of spreading population in the context of competitive species, predator-prey or even in epidemic models where the disease is spreading in the domain through a moving front. To solve these systems numerically, new numerical challenges arise. On the one hand, extremely small time steps are usually needed due to the stiffness of the system. On the other hand, as described above for the truncation error considerations it is always difficult to accurately handle the moving boundaries and efficiently treat complicated topological changes. In the rest of the thesis, we demonstrate the feasibility of the moving mesh method based on conservation as a tool for ecological studies which overcomes these numerical difficulties and is suitable for handling and tracking the moving boundaries. We focus on moving the nodes through a geometric conservation approach, whereby the integral of a suitable quantity, e.g. mass, is constant within a given patch of elements, but the footprint and location of those elements are dynamic. We apply the method to a range of one-dimensional moving boundary population problems while we also examine the application of the method to a two-dimensional radially symmetric system. Several numerical examples are examined to illustrate the efficiency, accuracy and consistency of the moving mesh approach.

Chapter 4

Background on Moving Mesh Numerical Methods

Many systems of partial differential equations which are used to describe phenomena such as gas and fluid dynamics, conservation laws, nonlinear optics, free boundary problems, combustion, meteorology and mathematical biology often involve structures or features which evolve in time as the integration of the PDE proceeds. Such features may be interfaces, shocks, singularities, changes of phase, high vorticity or regions of complexity. As we saw earlier in the thesis, a traditional way to numerically approximate PDEs is to impose a spatial mesh and then discretize the solution on this mesh by using finite element or finite difference methods. Similar methods which are also used are the finite volume, the collocation method or the method of lines. We refer to these strategies as fixed mesh methods. However, these methods may not be effective in cases where the problem being solved involves structures like the ones mentioned above as it leads to large localized errors. It is beneficial to use some sort of nonuniform mesh, adapted to the solution, on which to perform all of the computations. Having a finer mesh around these features of interest will allow a better approximation of the solution and reduce the overall error. Even so, the approach fails when the structures move in space as time evolves. These extra levels of complexity to the system through adaptivity can also lead to additional computational costs and possible numerical instability.

As previously mentioned in the introduction, adaptive methods for solving partial differential equations broadly fit into three categories h-, p- and r-refinement (h- adding extra nodes, p- increasing the order of the approximating polynomials and r- changing the position of existing nodes). Here, we focus on the r-refinement which will form the substance of this chapter with the aim of concentrating on a

particular strategy of r-refinement later on in the thesis. While h- and p- or hp-methods are well-understood and are now well-established in many commercial codes, r-refinement methods are less well-developed but have some significant advantages. For example, sharp features or discontinuities (including moving boundaries) can be tracked, avoiding excessive high resolution and guesswork. The number of moving nodes can be kept constant which is advantageous from a programming point of view as it is much easier to work with a fixed number of nodes especially when the solution involves sparse matrices and hence has a constant sparsity throughout the calculations. Moreover, in r-refinement methods, the node movement can be linked to the PDE which allows the numerics to align with biological or physical modelling. For example, in a fluid flow problem, the mesh may move with the fluid flow itself. However, a major consideration in r-refinement methods is mesh tangling in which the mesh points can cross over during the evolution. This generally leads to additional spatial instability and a failure of the solution routine.

Typically r-refinement methods keep the mesh topology and the number of mesh points fixed as the solution evolves. Hence the synonymous term "Moving Mesh Methods". In such procedures, the criterion that motivates the movement of the already existing mesh points may be such that the nodes naturally concentrate around regions where the solution has 'interesting behaviour', such as moving boundaries or interfaces. Usually these features of interest exhibit sharp spatial variations of either the solution or one of its derivatives.

The feature which is used to determine the mesh movement typically manifests itself as a 'monitor function' and focuses on the equidistribution of mesh. For example, the re-location of the nodes is based on the idea that some quantity is equally distributed, other than just distance, area or volume. This quantity may be a physical one such as mass or a non-physical one such as arc length. Basically, the monitor function is a mathematical statement based on a quantity which can be numerically quantified and used to move the mesh nodes towards regions of high activity.

Following Budd, Huang and Russell [32], we will assume the monitor function is always non-negative and, as they claim, the monitor function is usually constructed in one of three ways:

- depending on *a priori* solution estimate; e.g., an estimate of a quantity related to the solution such as arc length or mass;
- depending upon a posteriori error estimates; e.g., as the approach used in moving finite element methods [13], or estimates of the derivative jump across element boundaries [153] where the key motivation for a monitor

function is the equidistribution principle which involves selecting mesh points such that some measure of the solution error is equalised over each subinterval;

- depending upon some underlying physics or biology related to the solution; e.g., the potential temperature or the vorticity in a meteorological problem

Constructions of moving mesh methods vary considerably, and in their final forms, the moving mesh equations are very different. By [37] we classify moving mesh methods into two groups depending on the mesh movement strategy: location-based and velocity-based methods. The former one depends upon time-dependent mappings which control directly the location of mesh points or in the continuous sense the mapping $x(\xi)$ from the auxiliary domain to the physical domain (ξ is the computational coordinate and x the physical one). In contrast, the latter targets directly the mesh velocity or the time derivative of the mapping $x_t(\xi)$. In velocity-based methods, a mesh velocity equation is constructed and the mesh point location is obtained by a time integration scheme, such as the forward Euler time-stepping scheme. We examine these two classes separately in Section 4.1 and in Section 4.2, discussing key examples in each class.

4.1 Location-based

Following [37], consider a one-dimensional spatial domain where the adaptive mapping $x(\xi, t)$ defines the mapping from a computational domain Ω_c to a physical domain Ω_p. If the mesh on Ω_c is uniform then $\frac{\partial \xi}{\partial x}$ measures the density of the mesh on Ω_p.

To control the mesh, we choose a monitor function $m(x) > 0$ such that is proportional to the mesh density at any given time t, i.e.,

$$\frac{\partial \xi}{\partial x} = cm(x), \tag{4.1}$$

where c is a constant.
This is equivalent to the equidistribution principle for the monitor function $m(x)$. Dividing (4.1) by $m(x)$ and differentiating we obtain

$$\frac{\partial}{\partial x}\left([m(x)]^{-1}\frac{\partial \xi}{\partial x}\right) = 0, \tag{4.2}$$

which, knowing $m(x)$, can be solved to give ξ. Equation (4.2) is the Euler–Lagrange equation of the quadratic functional

$$I[\xi] = \int_{\Omega_p} [m(x)]^{-1}\left(\frac{\partial \xi}{\partial x}\right)^2 \, \mathrm{d}x.$$

The two main types of location-based methods are Moving Mesh Partial differential equations (MMPDE) and optimal transport. In the former method, [83, 84, 85, 86, 38, 31], the equidistribution requirement, or a variational version of it, is used to define a second PDE, that relates the equidistributed co-ordinate ξ to the fixed coordinate x. The paper by Huang and Russell [82] provides a good review of MMPDE methods while the survey paper [37] gives a brief description of various location-based approaches including the work of Winslow [184], Thompson et al.[175], Brackbill and Saltzman [27], Dvinsky [55], Brackbill [28], Knupp [97] and Knupp and Robidoux [98] which propose various elliptic equations or variational methods for defining the adaptive mapping. The optimal transport methods [31], are a natural generalisation of MMPDE methods in one dimension [32]. The aim of this method is to be closest to a uniform mesh in a suitable norm, consistent with satisfying the equidistribution principle.

We now turn to a category of moving mesh methods known as velocity-based methods. The method used in the thesis is an example of a velocity-based method.

4.2 Velocity based

Velocity-based methods use a moving coordinate system to directly provide a mesh velocity. Such a moving coordinate system, usually referred to as Lagrangian, is where the spatial co-ordinates are themselves functions of time, these functions being mappings from a conventional fixed coordinate system to a moving one. For example, in fluid dynamics, the Lagrangian moving coordinate system is used to follow fluid particles. More precisely, if $w(x,t)$ denotes the velocity of the fluid, ξ the reference coordinate of a fluid particle, and $x(\xi,t)$ the position of the particle at time t, then the particle and therefore the Lagrangian coordinate lines evolve with

$$\frac{\partial x}{\partial t} = w.$$

We expand on this theory below using the Reynold Transport theorem and the Arbitrary Lagrangian Euler equation.

4.2.1 Fluid dynamics

In fluid dynamics, the motion of fluids may be described by taking either the Lagrangian or Eulerian point of view. In the Lagrangian description, each moving fluid particle (with its attributes) is followed individually and is identified by its initial position, whereas in the Eulerian description variables such as density and velocity are evaluated at fixed locations.

A link between these two approaches is given by the Reynolds Transport Theorem [181] in the form

$$\begin{aligned} \frac{d}{dt}\int_{\Omega(t)} u \, \mathrm{d}x &= \int_{\Omega(t)} u_t \, \mathrm{d}x + \oint_{\partial\Omega(t)} u w \cdot \hat{n} \, \mathrm{d}\sigma \\ \text{(by the divergence theorem)} \quad &= \int_{\Omega(t)} u_t + \nabla \cdot (u w) \, \mathrm{d}\Omega, \end{aligned} \tag{4.3}$$

where u is the fluid density and w is the velocity of the fluid. Here, $\Omega(t)$ denotes a general moving domain while $d\sigma$ is an element of the boundary $\partial\Omega(t)$ of $\Omega(t)$. The Lagrangian conservation of mass is demonstrated by

$$\int_{\Omega(t)} u \, \mathrm{d}x = \text{constant in time},$$

equivalent to

$$\frac{d}{dt}\int_{\Omega(t)} u \, \mathrm{d}x = 0$$

and the Eulerian conservation of mass is described by

$$u_t + \nabla \cdot (u w) = 0.$$

Both approaches have been used over the years to numerically describe the motion of fluids. The Eulerian description is more commonly used where the equations of motion are discretized on a fixed mesh whilst the discretization in the Lagrangian approach is to follow the velocities of the fluid particles using a moving mesh. There are some compromises associated with the Lagrangian approach which are mainly due to the tendency of the mesh to tangle [2, 71]. This and other considerations regarding the Lagrangian approach have prompted the use of the so-called ALE (Arbitrary Lagrangian Eulerian) methods, where local modifications of the Lagrangian velocities are made as the computation develops [17, 40].

4.2.2 ALE (Arbitrary Lagrangian Eulerian) methods

Consider the generic PDE

$$\frac{\partial u}{\partial t} = \mathcal{L}u, \tag{4.4}$$

where $u = u(x,t)$ is defined in a fixed frame of reference with coordinate x at time t and $\mathcal{L}$ is a differential operator involving only space derivatives. We rewrite this in a moving Lagrangian frame, by allowing x to be a moving coordinate $x(t)$,

the result of a time-dependent mapping from a fixed set of reference coordinates, $a = x(0)$ say. By the invertible mapping,

$$x = \hat{x}(a, t).$$

The hat denotes a mapping from the Eulerian frame to the moving frame. In the same manner, we define the solution $u(x, t)$ in the moving frame

$$u(x, t) = u(\hat{x}(a, t), t) = \hat{u}(a, t)$$

and by chain rule we obtain

$$\frac{\partial \hat{u}}{\partial t} = \frac{\partial \hat{x}}{\partial t} \cdot \nabla u + \frac{\partial u}{\partial t}.$$

Hence, the differential form of ALE is

$$\dot{u} = \dot{x} \cdot \nabla u + \mathcal{L}u$$

where $\dot{u} = \frac{\partial \hat{u}}{\partial t}$ and $\dot{x} = \frac{\partial \hat{x}}{\partial t}$.

The integral form of the ALE equation is the Reynolds transport theorem (4.3) applied to a moving domain $\Omega(t)$ with boundaries $\partial\Omega(t)$ which moves with the velocity w

$$\frac{d}{dt} \int_{\Omega(t)} u \, \mathrm{d}x = \int_{\Omega(t)} \mathcal{L}u + \oint_{\partial\Omega(t)} w \cdot \nabla u. \tag{4.5}$$

Equation (4.5) allows the solution u of (4.4) to be obtained in a frame moving with any given velocity, e.g. by the mesh velocity.

ALE methods are extensively used in the computation of fluid-structure interaction problems, for example in [73, 101, 116, 140] and is widely used for free-surface problems, based upon maintaining mesh quality [129, 131], Laplacian smoothing [147] or pseudo-solid deformation [35, 166]. Successful ALE algorithms have also been used for phase-change problems [141] and for the interaction of free surfaces with solid boundaries [8, 151, 167].

The ALE methods are not restricted to fluid flow problems as we will observe later on in this chapter.

4.2.3 Moving finite element

The moving finite element method was originally developed by Miller and Miller [117] and Miller [118], and stimulated the study of many upcoming papers and applications [1, 14, 18, 39, 176].

Their method involves taking a PDE of the form (4.4) and determining the solution and the mesh simultaneously. The continuous version of the MFE determines the solution and the mesh together by minimizing a discrete residual of the ALE form of the PDE in a moving domain. The MFE method determines a mesh velocity through a variational principle coupled to the solution of a PDE by using a finite element approximation.

In their first work [117] the authors introduced this new numerical method with the aim to deal with problems whose solutions develop sharp transition layers. These attempts made use of the simplest hyperbolic PDE with near-shocks, the Burgers' equation [34], as a test equation. This early work had some success in moving many nodes automatically into the critical regions of the solution.

This pioneering work inevitably led to the discovery of several common difficulties such as node tangling and hence instabilities and proved to be highly sensitive to particular user-defined parameters and unknowns.

To overcome the issue of node crossing and colliding, authors introduced viscous forces to encourage nodes to stay separated. Additional improvements were attempted in [117] which included the use of a variety of short and long-range internodal repellent forces to avoid node tangling.

Although questions such as numerical instability and computational efficiency remained unanswered these early works provide a method which allows the mesh nodes to follow a moving shock and hence improved the resolution compared with a static grid.

4.2.4 The Geometric Conservation Law (GCL)

In the 2002 paper [38], Cao, Huang and Russell introduce the concept of the Geometric Conservation Law (GCL) to MMPDEs where, as in MFE, a variational principle is used to construct a minimisation problem that determined the mesh speed instead of the mesh location as in MMPDE method. This new adaptive mesh movement strategy uses the GCL to drive a mesh movement algorithm obtaining the mesh velocities directly.

The idea behind the GCL is to preserve properties associated with the volume of each element, so that, for example, a moving fluid could not lose or generate mass by mesh movement alone. This is achieved by having the minimizer of the functional (of the mesh speed) driving the mesh points in such a way that the rate of change of the cell volumes is proportional to the rate of change of the monitor function, causing the desired mesh adaption.

The advantages of this approach are the ease of controlling the cell volumes

(and therefore mesh adaption) and a theoretical guarantee for existence and non-singularity of the coordinate transformation.

4.2.5 The Conservation Method

The Conservation Method was introduced in the 2005 paper by Baines, Hubbard and Jimack [14]. This method shares common roots with the GCL, but instead of using the variational principle to find the mesh velocities, they are directly calculated from the integral form of the PDE.

According to the finite element framework used in the paper, a weak form of the PDE is required that includes a set of weight functions that move with the mesh. Then the use of the Reynolds Transport Theorem allows the link between the Eulerian and Lagrangian descriptions. A system is constructed where the mesh velocity is given in terms of a potential at a particular location (Eulerian view), but the elements themselves track the movement of mass (Lagrangian view). Hence the static (Eulerian) and the moving (Lagrangian) reference frames are combined together in a single method.

The idea behind the conservation method is to use an integral to preserve a desired quantity, such as mass, within each patch of elements from which the velocities are constructed. The authors in [14] demonstrated the application of the method to mass-conserving problems, where the global mass is constant, e.g. the porous medium equation and a fourth-order nonlinear diffusion equation. In such problems, the quantity which is conserved is local mass. For non-conservative systems, the theory uses the concept of relative mass, the proportion of total mass associated with each element patch. This approach has been applied in the paper to a Stefan problem and a diffusion problem with a negative source term.

4.2.6 A distributed conservation principle

We saw earlier that equation (4.5) is directly derived from the governing PDE (4.4) using the moving coordinates. We proceed with a principle upon which the derivation of the moving coordinate system can be based.

We define the total mass by $\theta(t)$, i.e.,

$$\theta(t) = \int_{\Omega(t)} u \, \mathrm{d}\Omega, \tag{4.6}$$

where the domain $\Omega(t)$ denotes the entire spatial domain at time t the points of

which move with the velocity w. Differentiating (4.6) with respect to time yields

$$\frac{d}{dt}\int_{\Omega(t)} u \, \mathrm{d}\Omega = \frac{\partial \theta}{\partial t} = \dot{\theta}(t). \tag{4.7}$$

Substitute equation (4.7) in (4.5) to obtain

$$\dot{\theta}(t) = \int_{\Omega(t)} \mathcal{L}u \, \mathrm{d}\Omega + \oint_{\partial\Omega(t)} w \cdot \nabla u \, \mathrm{d}\sigma. \tag{4.8}$$

Equation (4.8) determines the velocity w uniquely if $\dot{\theta}$ and u are known.

In practice, for a mass conserving problem ($\dot{\theta} = 0$) the value of θ is calculated initially ($\theta(0)$) by the principle (4.6), using the initial conditions of u, and remains constant for all calculations. The velocity of the nodes is calculated using equation (4.8) over the subintervals of the discretized spatial domain, i.e., the mass within each element is conserved. Note that for mass conserving problems the right-hand side of (4.8) is zero, hence only u (or u initially ($u(x,0)$)) is required to uniquely obtain w. Having updated the mesh node positions using w and a time integration scheme for x, we update the solution of u from the principle (4.6) using a constant value of θ and the updated nodal positions.

For a non-mass conserving problem ($\dot{\theta} \neq 0$) the value of $\dot{\theta}$ is calculated by integrating (4.8) over the entire spatial domain where the terms with the velocity w are calculated using the boundary conditions of the problem. Knowing θ and u (initially from $u(x,0)$), equation (4.8) can be used over the subintervals of the discretized spatial domain which allow the calculation of the node velocities. Note here that the theory uses the concept of relative mass, i.e., the normalised function $u(x,t)/\theta(t)$. To update the total mass θ and the new node locations by $\dot{\theta}$ and w, a time integration scheme is required. Then the recovered solution of u is obtained by the principle (4.6) using the updated θ and the updated position of the nodes.

A necessary requirement for the moving mesh method based on conservation is that the solution $u(x,0)$ must have compact support. To successfully apply the moving mesh method, it is important that u maintains its compact support at all times. Equation (4.8) can be used to obtain the nodal velocities uniquely at all interior points provided the flux $[uw]$ is known at a point and that $u(x,t) > 0$ in the interior of the domain (compact support). To evaluate $\dot{\theta}$ by integrating (4.8) over the entire domain, we assume that $u(x,t)$ and $w(x,t)$ are continuous up to the boundary.

This thesis applies the conservation method used by Baines, Hubbard and Jimack, but whereas they use a finite element method, we investigate the application of

the finite volume method. The method is presented for the solution of non-linear time-dependent PDEs with moving boundaries, using a moving mesh. We apply this method only to one-dimensional problems and consequently refer to it as moving mesh finite difference method throughout this thesis.

A similar approach is used in [104, 103] where the method was applied to a one-dimensional moving boundary problems such as the mass-conserving porous medium equation, Richards' equation in hydrology, and the Crank-Gupta problem that does not conserve mass.

It is worth mentioning here the work of Watkins in [178] which provides the first application of the moving mesh finite element method based on mass conservation to a population system with a moving interface. This motivated our work in Chapter 6 using a finite difference framework where we were able to compare and validate the finite difference approach for a moving mesh based on conservation against the finite element used in [178].

Our work is mainly concentrated on the application of the moving mesh finite difference method based on mass conservation to one-dimensional population systems with the aim to gain a great understanding of the mechanism involved, and for analysis which may be expanded to more general situations. Note that in the context of population dynamics, the 'mass' refers to the total mass of the population, i.e., the number of individuals of a species.

We also demonstrate that the application of the method can be easily extended to the radially symmetric two-dimensional case. An advantage of using finite elements for the general two-dimensional case (instead of the radial case) is that the method can be applied to more general domains.

Later in the thesis (Chapter 7), we introduce a new feature of the conservation method for moving meshes, ideal for systems with coupled equations. We consider the combined mass of the species involved in the system to be the quantity which is preserved. Hence instead of allocating a separate mesh to solve each equation in the system, we use a single moving mesh for all the equations where the solution is then adjusted using the Arbitrary Lagrangian Euler equations. The mesh is generated by preserving the total sum of the local masses at a point in time. Hence a single moving mesh can be used in the overlapping regions and handles moving interfaces and free boundaries. The approach is advantageous in cases of coupled equations and overlapping domains, as the attractive aspect of the technique is that only one velocity equation is required to update the mesh nodes and hence avoids the need for interpolation of the meshes at each time step to approximate the coupled terms. The combined mass procedure is general and can be applied to many overlapping situations.

In the next chapter, following the study of a well-known non-linear diffusion, the Porous medium equation, we demonstrate the application of the moving mesh method based on mass conservation to a two-cluster population system with density-dependent diffusion.

Chapter 5

Density-Dependent Diffusion

Following Chapter 2, Section 2.4, this chapter discusses density-dependent diffusion and its effect in the well-established Porous Medium Equation. We illustrate some of the properties of the PME including mass conservation and stationary centre of mass in Section 5.2.2, which will be used later on for the application of the moving mesh finite difference numerical approximation in Section 5.3. A further property of the PME is similarity, in which invariance is used to obtain self-similar solutions. We use these self-similar solutions to compare the numerical solution to an exact solution through a convergence analysis in the Results Section 5.3.2. In Section 5.3.4 we illustrate using numerical simulations some of the properties of the PME such as the mass conservation and the convergence of the numerical approximation to the self-similar solution. Then we derive the Porous Medium Equation for a population model and in Section 5.4 we consider a system of two clusters of the same population initially occupying different spatial regions. We apply the moving mesh finite difference method based on mass conservation to the two-cluster system by excluding the reaction terms (mass-conserving problem) in Section 5.4.2 and including the reaction terms (non-mass conserving problem) in Section 5.4.4. Once the two clusters overlap, the two population groups are modelled as a united cluster by considering their combined mass. Time snapshots of the results of the mass and non-mass conserving cases are shown in Sections 5.4.2 and 5.4.4, respectively.

5.1 The Porous Medium Equation

Recall from Section 2.4 that the rate of change of the density u with a density-dependent diffusion takes the form,

$$\frac{\partial u}{\partial t} = \frac{\partial}{\partial x}\left(D(u)\frac{\partial u}{\partial x}\right), \tag{5.1}$$

(see equation (2.14)).
Usually, the theory of density-dependent diffusion equations is restricted to functions of the form $D(u) = u$ giving the PDE

$$\frac{\partial u}{\partial t} = \frac{\partial}{\partial x}\left(u\frac{\partial u}{\partial x}\right). \tag{5.2}$$

The function $D(u)$ in (5.1) is often chosen for physical or biological reasons, or wherever there exist group invariant (similarity) solutions for (5.2). Equation (5.2) is called the porous medium equation which can be derived from an empirical law called Darcy's Law [183]. The main applications of the porous medium equation found in the literature are gas flowing through a porous medium [123], nonlinear heat transfer [187], population dynamics [69] and groundwater flow [26]. Here we consider its relationship with evolving species.

5.2 The Derivation of the PME from a Population Model

Here, we show how the PME (5.2) arises out of a simple population model which will then be used to construct a system of two population clusters. Although the treatment of this chapter has been limited to a one-dimensional space, we derive the model in an n-dimensional setting. The substitution $n = 1$ leads back to the one-dimensional model.

Let us consider a hypothetical population in an n-dimensional space $\mathcal{R}^n$ ($n = 1, 2, \ldots$). We denote the density of the population by $u(\mathbf{x}, t)$ so that the population mass in an arbitrary region $\Omega \subset \mathcal{R}^n$ at time t is given by $\int_\Omega u(\mathbf{x}, t)\ \mathrm{d}\mathbf{x}$. The velocity by which individuals of the population are moving at space point $\mathbf{x}$ at time t is given by a vector function $\mathbf{v}(\mathbf{x}, t)$. Then the rate of increase of the population in the domain Ω equals the inflow of the population through the domain's boundaries plus the addition/reduction of individuals through the reaction terms f, that is,

$$\frac{\mathrm{d}}{\mathrm{d}t}\int_\Omega u\ \mathrm{d}\mathbf{x} = -\int_{\partial\Omega} u\mathbf{v}\cdot\mathbf{n}\ \mathrm{d}\sigma + \int_\Omega f(u, \mathbf{x}, t)\ \mathrm{d}\mathbf{x}, \tag{5.3}$$

where $\mathbf{n}$ is the outward unit normal to the boundary $\partial\Omega$ of Ω and $\mathrm{d}\sigma$ is an element of the boundary $\partial\Omega$. Since Ω is independent of time and by applying the divergence theorem to the first term on the right-hand side of (5.3) gives,

$$\int_\Omega \frac{\partial u}{\partial t}\ \mathrm{d}\mathbf{x} = -\int_\Omega \mathrm{div}(u\mathbf{v})\ \mathrm{d}\mathbf{x} + \int_\Omega f(u,\mathbf{x},t)\ \mathrm{d}\mathbf{x}.$$

Since the domain is arbitrary,

$$\frac{\partial u}{\partial t} + \mathrm{div}(u\mathbf{v}) - f(u,\mathbf{x},t) = 0. \tag{5.4}$$

The above equation is the equation of mass balance. It basically links a material's velocity and density functions and the material's creation or removal.

In the population dynamics concept, individuals have the tendency to move to neighbouring areas where the population density is lower than the region they are momentarily occupying. This feature we wish to add to equation (5.4) by supposing that members of the population move in the opposite direction of the density gradient ∇u and the speed of the movement is a function of the density u, implying that $\mathbf{v} = -\phi(u)\nabla u$.
Then equation (5.4) becomes,

$$\frac{\partial u}{\partial t} = \mathrm{div}(u\,\phi(u)\nabla u) + f(x,\mathbf{x},t). \tag{5.5}$$

The simple choice of function $\phi(u) = 1$ leads back to equation (5.2).

We describe a class of exact solutions to the radially symmetric PME that are invariant under a scaling group in the variables and take the so-called self-similar form [16].

5.2.1 Self-similar solutions

We seek solutions for the radially symmetric PME,

$$\frac{\partial u}{\partial t} = \frac{1}{r^{k-1}}\frac{\partial}{\partial r}\left(r^{k-1}\,u\frac{\partial u}{\partial r}\right), \quad (0 \le r \le b), \tag{5.6}$$

where r is the radial coordinate and $k = 1, 2, 3$ is the number of spatial dimensions. Setting $k = 1$ leads to the one-dimensional case, which is denoted in Cartesian coordinates.

A derivation of the self-similar solutions of (5.6) is presented in [104] and takes the form

$$u(r,t) = t^{-k/k+2}\left(A - \frac{r^2}{2\,(k+2)\,t^{\frac{2}{k+2}}}\right), \quad t \in [1,\infty), \tag{5.7}$$

where $A = E/(2k+2)$ and E is a constant of integration.

For the purpose of demonstrating some of the properties of the PME and for numerical comparisons, a specific set of parameters is chosen which will be used later in this chapter. As in [104], we consider the constant of integration $E = 2k+2$ leading to $A = 1$.

If $[0, b(t)]$ is the support of u, by setting $u(r,t) = 0$ we can find an expression for the moving boundary b (where $u = 0$), as

$$b(t) = \sqrt{2(k+2)t^{\frac{2}{k+2}}}, \quad t \in [1, \infty). \tag{5.8}$$

Substituting expression (5.8) back in equation (5.7), we have

$$u(r,t) = \frac{1}{t^{\frac{k}{k+2}}}\left(1 - \frac{r^2}{b(t)^2}\right) t \in [1, \infty). \tag{5.9}$$

Initial conditions for the self-similar solutions which are going to be used later on for the numerical comparison can be found by setting $t = 1$.
At time $t = 1$,

$$u(r,1) = \left(1 - \frac{r^2}{b(1)^2}\right)$$

and the initial position ($t = 1$) of the moving boundary is given by

$$b(1) = \sqrt{2(k+2)}.$$

Apart from the self-similarity property of the PME, it is useful to mention the two relevant properties of the PME on which our numerical approach relies. These properties are also discussed in [160].

5.2.2 Properties of the PME in one-dimension

Consider the following one-dimensional (Cartesian coordinates) PME

$$\frac{\partial u}{\partial t} = \frac{\partial}{\partial x}\left(u\frac{\partial u}{\partial x}\right) \tag{5.10}$$

with boundary conditions

$$u = 0 \quad at \quad x = a(t), b(t), \quad t \geq 0 \tag{5.11}$$

at the edge of the support.
We prove two well-established properties in which our numerical approach relies upon the conservation of mass, and stationary centre of mass.

Conservation of global mass

The first property is the conservation of the global mass in time.
Using the Leibniz Integral rule,

$$\frac{\mathrm{d}}{\mathrm{d}t}\int_{a(t)}^{b(t)} u(x,t)\ \mathrm{d}x = \int_{a(t)}^{b(t)} \frac{\partial u}{\partial t}\ \mathrm{d}x + u(b,t)\frac{\mathrm{d}b}{\mathrm{d}t} - u(a,t)\frac{\mathrm{d}a}{\mathrm{d}t}$$

and substituting equation (5.10) gives,

$$\begin{aligned}\frac{\mathrm{d}}{\mathrm{d}t}\int_{a(t)}^{b(t)} u(x,t)\ \mathrm{d}x &= \int_{a(t)}^{b(t)} \frac{\partial}{\partial x}\left(u(x,t)\frac{\partial u}{\partial x}\right)\ \mathrm{d}x + u(b,t)\frac{\mathrm{d}b}{\mathrm{d}t} - u(a,t)\frac{\mathrm{d}a}{\mathrm{d}t} \\ &= u(b,t)\frac{\partial b}{\partial x} - u(a,t)\frac{\partial a}{\partial x} + u(b,t)\frac{\mathrm{d}b}{\mathrm{d}t} - u(a,t)\frac{\mathrm{d}a}{\mathrm{d}t}.\end{aligned}$$

Using the boundary conditions given in (5.11) we obtain,

$$\frac{\mathrm{d}}{\mathrm{d}t}\int_{a(t)}^{b(t)} u(x,t)\ \mathrm{d}x = 0. \tag{5.12}$$

Hence, we have shown that the integral of the density, therefore the mass, is constant in time.

Stationary centre of mass

The second property is that the PME has a stationary centre of mass.
The average position of the centre of mass, say $\overline{\chi}(t)$, in one dimension is defined by

$$\overline{\chi}(t) = \frac{\int_{a(t)}^{b(t)} x\ u(x,t)\ \ \mathrm{d}x}{\int_{a(t)}^{b(t)} u(x,t)\ \mathrm{d}x}$$

In order to prove that the centre of mass is stationary, it is sufficient to show that

$$\frac{\mathrm{d}}{\mathrm{d}t}\int_{a(t)}^{b(t)} x\ u(x,t)\ \ \mathrm{d}x = 0,$$

since the integral is a measure of the average distance of x from the origin for any $a(t)$,$b(t)$, at which $u = 0$.

We again make use of the Leibniz integral rule,

$$\frac{\mathrm{d}}{\mathrm{d}t}\int_{a(t)}^{b(t)} x\ u(x,t)\ \ \mathrm{d}x = \int_{a(t)}^{b(t)} x\ \frac{\partial u}{\partial t}\ \mathrm{d}x + u(b,t)\ b(t)\frac{\mathrm{d}b}{\mathrm{d}t} - u(a,t)\ a(t)\frac{\mathrm{d}a}{\mathrm{d}t}.$$

Substituting the original PDE (PME) (5.10)

$$\frac{\mathrm{d}}{\mathrm{d}t}\int_{a(t)}^{b(t)} x\,u(x,t)\ \ \mathrm{d}x = \int_{a(t)}^{b(t)} x\ \frac{\partial}{\partial x}\left(u(x,t)\frac{\partial u}{\partial x}\right)\mathrm{d}x + u(b,t)\ b(t)\frac{\mathrm{d}b}{\mathrm{d}t} - u(a,t)\ a(t)\frac{\mathrm{d}a}{\mathrm{d}t},$$

where the last two terms vanish due to the boundary conditions in (5.11). Applying the integration on the first term on the right-hand-side gives,

$$\frac{\mathrm{d}}{\mathrm{d}t}\int_{a(t)}^{b(t)} x\ u(x,t)\ \ \mathrm{d}x = b(t)u(b,t)\frac{\partial b}{\partial x} - a(t)u(a,t)\frac{\partial a}{\partial x} - \int_{a(t)}^{b(t)} u(x,t)\frac{\partial u}{\partial x}\ \mathrm{d}x.$$

Again, we can eliminate the first two terms on the right-hand-side using the boundary conditions, giving,

$$\frac{\mathrm{d}}{\mathrm{d}t}\int_{a(t)}^{b(t)} x\ u(x,t)\ \ \mathrm{d}x = -\int_{a(t)}^{b(t)} u(x,t)\frac{\partial u}{\partial x}\ \mathrm{d}x.$$

Rearranging the final term on the right-hand-side gives

$$\begin{aligned}\frac{\mathrm{d}}{\mathrm{d}t}\int_{a(t)}^{b(t)} x\ u(x,t)\quad \mathrm{d}x &= -\frac{1}{2}\int_{a(t)}^{b(t)} \frac{\partial}{\partial x}\left(u(x,t)^2\right)\ \mathrm{d}x \\ &= -\frac{1}{2}\left(u(b,t)^2 - u(a,t)^2\right). \quad (5.13)\end{aligned}$$

Again, applying the boundary condition (5.11) to equation (5.13) the terms on the right-hand-side vanish, giving

$$\frac{\mathrm{d}}{\mathrm{d}t}\int_{a(t)}^{b(t)} x\ u(x,t)\ \ \mathrm{d}x = 0.$$

Hence, we have shown that the centre of mass is stationary.

5.3 A Moving Mesh Finite Difference Method for the PME

We now move on to the numerical solution of the PME (5.10) using the moving mesh finite difference method based on conservation. As shown above, one of the

properties of the PME with zero boundary conditions is that it conserves its mass (5.12). Hence in this section, it is consistent to apply the concept of partial mass to any interval in order to numerically approximate the mass-conserving PME equation.

We assume the initial data is symmetrical about its centre of mass, taken to be the origin, therefore we set the left-hand side boundary $a(t) = -b(t)$.
The boundary conditions of (5.10) are then

$$u(-b(t), t) = u(b(t), t) = 0 \tag{5.14}$$

As shown above, the total mass of (5.10) is conserved and the centre of mass is fixed in time, from which it follows that the solution retains the symmetry of the initial data for all time about the line $x = 0$. We can therefore model only half of the region, i.e.,

$$\frac{\partial u}{\partial t} = \frac{\partial}{\partial x}\left(u\frac{\partial u}{\partial x}\right), \quad t > 0, \quad x \in (0, b(t)) \tag{5.15}$$

with the conditions

$$u\left(b\left(t\right), t\right) = 0 \quad u(b(t), t)\frac{\mathrm{d}b}{\mathrm{d}t} = 0 \tag{5.16}$$

at the moving boundary $b(t)$.
Due to symmetry, two more conditions arise at $x = 0$, given by,

$$\frac{\partial u}{\partial x} = 0 \quad \text{and} \quad \frac{dx}{dt} = 0 \quad \text{at} \quad x = 0. \tag{5.17}$$

5.3.1 Conservation of partial masses

We recall from (5.12) that the integral of a solution of the PME (the mass) is conserved in time, i.e.,

$$\dot{\theta}(t) = \frac{\mathrm{d}}{\mathrm{d}t}\int_0^{b(t)} u(x, t)\ \mathrm{d}x = 0.$$

In such cases, where $\theta(t)$ remains constant for all $t \geq 0$, the theory is based on the conservation of partial masses, i.e., since the total mass is constant in time, it is consistent to suppose that the mass within each interval between the nodes is also constant. We introduce a time-dependent space coordinate $\tilde{x}(x, t)$ which coincides instantaneously with the fixed coordinate x. Consider two such coordinates, $\tilde{x}(x_1, t)$ and $\tilde{x}(x_2, t)$, in $(0, b(t))$, abbreviated to $\tilde{x}_1(t)$ and $\tilde{x}_2(t)$. The conservation of partial masses is

$$\int_{\tilde{x}_1(t)}^{\tilde{x}_2(t)} u(\varsigma, t)\ \mathrm{d}\varsigma = \gamma_\eta, \tag{5.18}$$

where γ_η is constant in time and η indicates the interval $(\tilde{x}_1(t), \tilde{x}_2(t))$.
Therefore, using the Leibniz integral rule, the rate of change of the mass in the subinterval is given in the form

$$\frac{\mathrm{d}}{\mathrm{d}t}\int_{\tilde{x}_1(t)}^{\tilde{x}_2(t)} u(\varsigma, t)\ \mathrm{d}\varsigma = \int_{\tilde{x}_1(t)}^{\tilde{x}_2(t)} \left(\frac{\partial u(\varsigma, t)}{\partial t} + \frac{\partial}{\partial \varsigma}\left(u(\varsigma, t)\, w(\varsigma, t)\right)\right)\ \mathrm{d}\varsigma,$$

where w is a local velocity given by $w(\tilde{x}, t) = \left.\frac{\mathrm{d}\tilde{x}}{\mathrm{d}t}\right|_{\tilde{x}=x}$.
Since the mass within each interval is constant,

$$0 = \int_{\tilde{x}_1(t)}^{\tilde{x}_2(t)} \left(\frac{\partial u(\varsigma, t)}{\partial t} + \frac{\partial}{\partial \varsigma}\left(u(\varsigma, t)\, w(\varsigma, t)\right)\right)\ \mathrm{d}\varsigma. \tag{5.19}$$

By substituting the original PDE (5.10) in (5.19) we can obtain a unique solution for the local velocity w by integrating and setting one node as an anchor point. Since we have shown above that the centre node of the domain, $x = 0$, is stationary, it provides an obvious choice of an anchor point. Another convenient choice of the anchor point is at the boundary $x = b(t)$.

Discretisation of the domain

We now define a finite difference method based on this theory, with the following notation. Given a time step $\Delta t > 0$ and a fixed number of spatial nodes $N + 1$, choose discrete times $t^n = n\Delta t$, $n = 0, 1, \ldots$, and discretise the interval at each discrete time t^n using the nodal points $x_i^n = \tilde{x}_i(t^n)$, $i = 1, 2, \ldots, N+1$, for which

$$0 = x_1 < x_2^n < \ldots < x_{N+1}^n = b^n.$$

The approximations $u_i^n \approx u(\tilde{x}_i(t^n), t^n)$ and $w_i^n \approx w(\tilde{x}_i(t^n), t^n)$ denote the solution and mesh velocity at these nodes.

Mesh velocities

Taking the anchor point at $x = 0$ and substituting the original PDE in (5.19), gives

$$\int_0^{x_i^n} \left(\frac{\partial}{\partial x}\left(u\frac{\partial u}{\partial x}\right) + \frac{\partial}{\partial \varsigma}\left(u(\varsigma, t)\, w(\varsigma, t)\right)\right)\ \mathrm{d}x = 0. \tag{5.20}$$

Note here that the interval of (5.19) between the two successive nodes $(\tilde{x}_1(t), \tilde{x}_2(t))$ is now taken to be the interval from the fixed node $x_1 = 0$ to a moving internal node x_i^n.
Finally, performing the integration to (5.20)

$$\left[u \frac{\partial u}{\partial x} + u w \right]_0^{x_i^n} = 0. \tag{5.21}$$

From the boundary conditions given in (5.17), equation (5.21) becomes,

$$w_i^n = -\frac{1}{u} \left(u \frac{\partial u}{\partial x} \right) \Big|_{x_i^n} = -\frac{\partial u}{\partial x} \Big|_{x_i^n}, \quad (i = 2, \ldots, N), \tag{5.22}$$

while the velocity at x_0 is zero and, at the moving boundary x_{N+1}^n, the velocity w_{N+1}^n is linearly extrapolated using w_{N-1}^n and w_N^n.

Updating the nodal positions

The new mesh x_i^{n+1} is obtained from w_i^n by a time-stepping scheme, for example, the Euler time-stepping scheme,

$$x_i^{n+1} = x_i^n + \Delta t \, w_i^n, \quad (i = 1, \ldots, N+1). \tag{5.23}$$

Hence, given a mesh x_i^n with corresponding solution u_i^n, we can calculate the updated mesh x_i^{n+1} by computing the mesh velocity w_i^n.
Although only first-order in time this time-stepping scheme serves to test the spatial theory of the method. More sophisticated schemes can easily be substituted.

Recovering the solution

Once the updated mesh has been determined, the updated solution u_i^{n+1} is given by (5.18) using a mid-point approximation of the integral, i.e.,

$$\int_{x_{i-1}^{n+1}}^{x_{i+1}^{n+1}} u_i^{n+1} \, \mathrm{d}x = \gamma(x_{i-1}, x_{i+1})$$

$$u_i^{n+1} = \frac{\gamma(x_{i-1}, x_{i+1})}{x_{i+1}^{n+1} - x_{i-1}^{n+1}}, \quad (i = 2, \ldots, N). \tag{5.24}$$

The population density u_1^{n+1} can be approximated from the boundary condition given in (5.17) by $u_1^{n+1} = u_2^{n+1}$ while the population density u_{N+1}^{n+1} is given by the boundary condition (5.16).
The finite-difference moving mesh algorithm for mass-conserving problems is then as follows.

Algorithm

Choose initial node positions x_i^0, with corresponding solution values $u_i^0 > 0$, and use them to determine the approximate masses $\gamma_(x_{i-1}^0, x_{i+1}^0)$, $i = 2, \ldots, N$, of (5.18)

$$\gamma(x_{i-1}, x_{i+1}) = u_i^0(x_{i+1}^0 - x_{i-1}^0), \quad (i = 2, \ldots, N).$$

Then at each time step, we proceed by

1. Calculating the velocity at each node w_i^n, $i = 2, \ldots, N$, by equation (5.22). The velocity w_1^n is zero at all times while the velocity w_{N+1}^n is evaluated by extrapolation.

2. The new mesh is obtained at the time by the explicit Euler time-stepping scheme (5.23).

3. Finally, having updated the new node positions, we can recover the solution u_i^{n+1}, $i = 2, \ldots, N$, using (5.24). The population density at x_1 is given in (5.17) by $u_1^{n+1} = u_2^{n+1}$ while u_{N+1}^{n+1} is given by the boundary condition (5.16).

5.3.2 Results of the MMFDM

In this section, we present results from applying the moving mesh method of Section 5.3 to the one-dimensional Cartesian equation (5.14). We run the results for 101 and 21 discretised nodes ($N = 100, N = 20$) using the self-similar solution as the initial data.

Figure 5.1a represents time snapshots of the evolution of the approximated solution using the self-similar initial conditions. We initially divided the domain into 100 ($N = 100$) equally spaced nodes and ran the simulations up to $t = 10$ using the time-step value of $\Delta t = 1/N^2 = 10^{-4}$. Figure 5.1b shows the evolution of the boundary $x_{N+1}(t)$, up to $t = 10$. The approximated position of the boundary using the numerical method is plotted by a dotted black line while the exact position evaluated by the self-similar solutions is plotted by a solid blue line. We have observed a minimal relative error between the approximated and the exact boundary position of 1.74×10^{-6}. The last figure (c) of Figure 5.1 shows the mesh trajectories. We observe a smooth even spread of the nodes, without mesh tangling.

The same sequence of results is shown in Figure 5.2 using the self-similar initial condition but with 21 spatial nodes instead of 101, with the corresponding time step size $\Delta t = 1/N^2 = 2.5 \times 10^{-3}$.

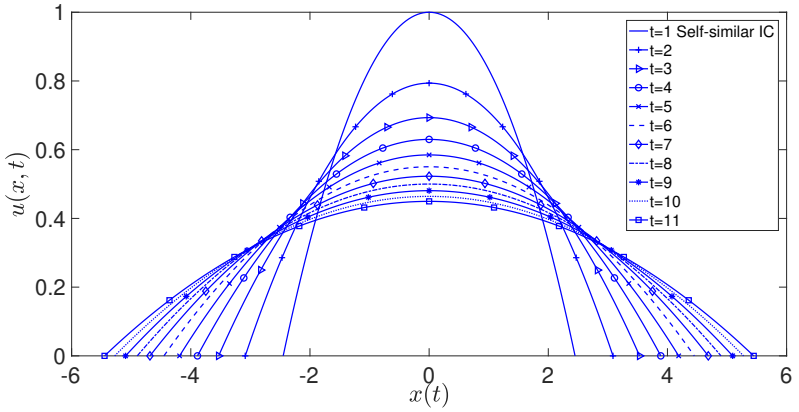

(a) The evolution of the approximated solution for $t = 11$.

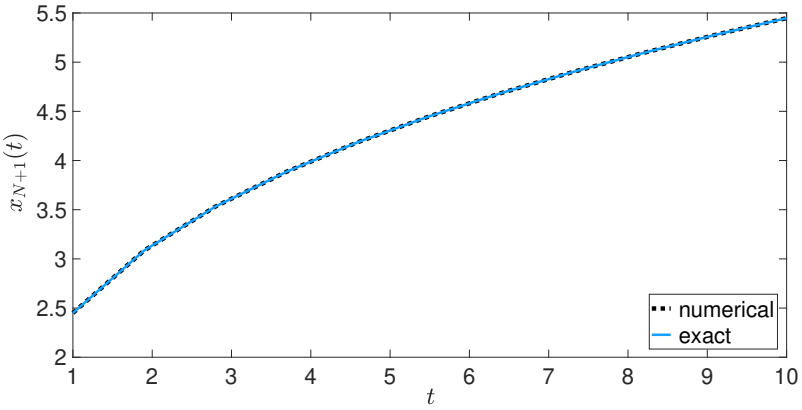

(b) The evolution of the boundary position for $t = 11$. The relative error at $x_{N+1}(10)$ is 2.42×10^{-6}.

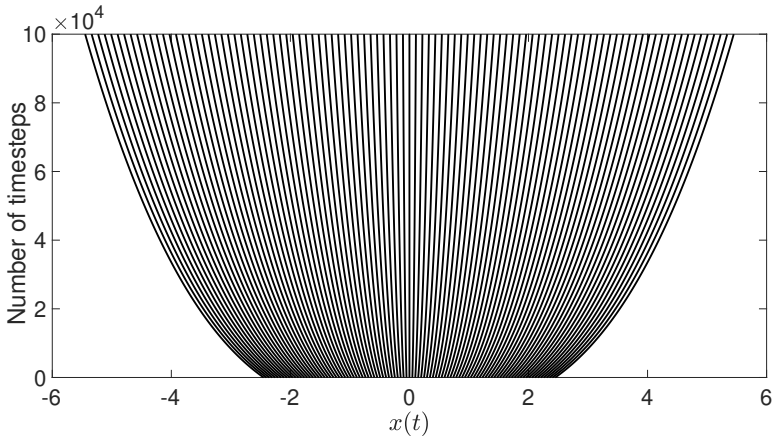

(c) The evolution of the mesh trajectory for $t = 11$.

Figure 5.1: The PME approximation with self-similar initial conditions with $N = 100$ and $\Delta t = 1/N^2 = 10^{-4}$.

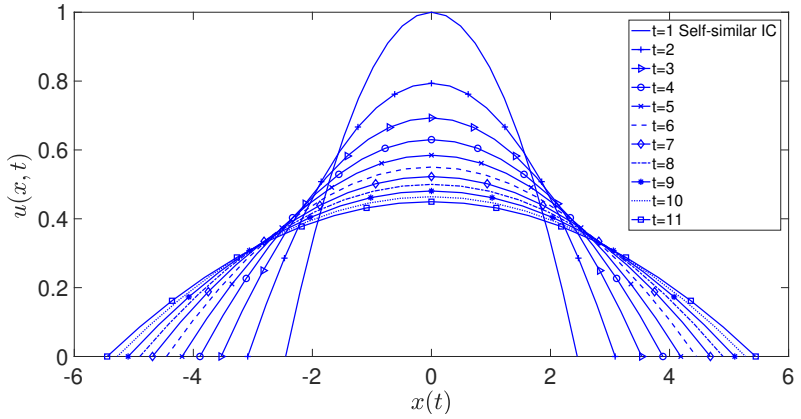

(a) The evolution of the approximated solution for $t = 11$.

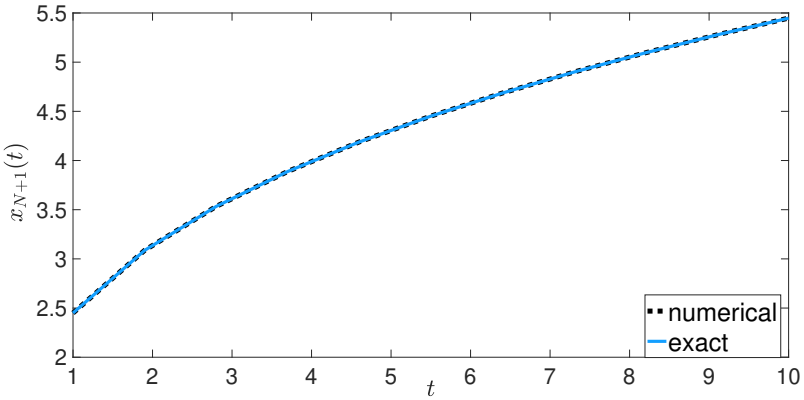

(b) The evolution of the boundary position for $t = 11$. The relative error at $x_{N+1}(10)$ is 2.45×10^{-6}.

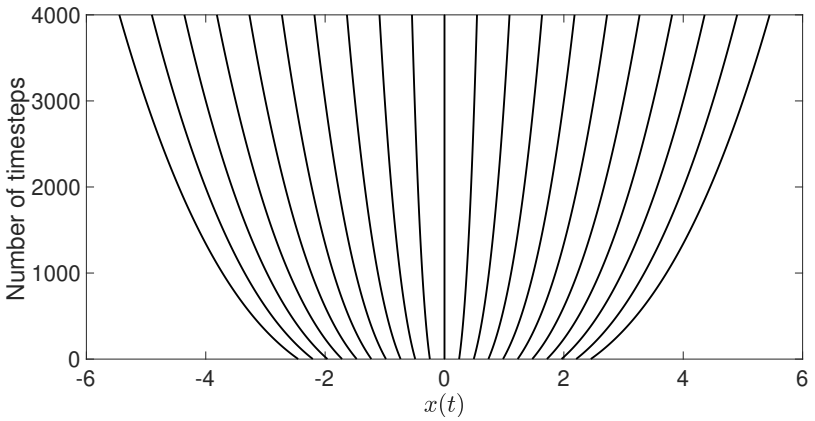

(c) The evolution of the mesh trajectory for $t = 11$.

Figure 5.2: The PME approximation with self-similar initial conditions with $N = 20$ and $\Delta t = 1/N^2 = 2.5 \times 10^{-3}$.

5.3.3 Convergence

In this section we examine the convergence of the finite difference moving mesh method as the number of nodes N increases while Δt decreases. We solve for $t \in [t^0, T]$ and compute results for $N = 10 \times 2^{\hat{N}-1}$, $\hat{N} = 1, \ldots, 6$. In order to compare the results for different values of $\hat{N}$, we denote the points of the mesh for a particular value $\hat{N}$ by $x_{i,\hat{N}}(t)$, $i = 0, \ldots, N$. We then compute both $x_{2^{\hat{N}-1}j,\hat{N}}(t)$ and $u_{2^{\hat{N}-1}j,\hat{N}}(t) \approx u(x_{2^{\hat{N}-1}j,\hat{N}}(t), t)$ for each $j = 0, \ldots, 10$ as $\hat{N}$ increases. This new notation allows comparison of $x_{i,\hat{N}}$ and $u_{i,\hat{N}}$ at eleven different points, determined by $i = 2^{\hat{N}-1}j$, $j = 1, \ldots, 10$, for various N. We have denoted the boundary position at each case by $x_{N+1}(t) = b(t)$.

Let us denote exact solution by $\bar{u}_{2^{\hat{N}-1}j,\hat{N}}(t)$ at the calculated mesh points and $\bar{x}_{N+1}(t) = \bar{b}(t)$ the boundary position. In order to balance the spatial and temporal error and recall the Euler time-stepping is used, we take $\Delta t = \mathcal{O}\left(\frac{1}{N^2}\right)$ anticipating that the errors $\mid \bar{u}_{2^{\hat{N}-1}j,\hat{N}}(t) - u_{2^{\hat{N}-1}j,\hat{N}}(t) \mid$ and $\mid \bar{b}(t) - b(t) \mid$ will decrease as $\hat{N}$ increases, for each $j = 0, \ldots, 10$.
For ease of exposition, we set $2^{\hat{N}-1} = \kappa$.

We measure the relative errors by calculating the ℓ_2 norms of u_i, $i = 0, \ldots, N$ and the maximum normal of b, i.e.,

$$E_N(u) = \sqrt{\frac{\sum_{i=0}^{N}(\bar{u}_{\kappa j}(T) - u_{\kappa j}(T))^2}{\sum_{i=0}^{N}(\bar{u}_{\kappa j}(T))^2}}$$

and

$$E_N(b) = \frac{\bar{b}(T) - b(T)}{\bar{b}(T)},$$

for $\hat{N} = 1, \ldots, 6$, $N = 10, 20, 40, 80, 160, 320$ where $\kappa = 2^{\hat{N}-1}$.

We may examine the order of convergence with respect to space and time by looking at the rate at which the differences between successive errors decrease.

We assume

$$E_N = \mathsf{A}(\Delta x)^q + \mathsf{B}(\Delta t)^p,$$

where the E_N is the error for each N, A and B are constants and q and p are the rates of convergence in respect to space and time, respectively. Since we are only accounting for the spatial errors and by halving Δx, we have

$$E_N = \mathsf{A}(\Delta x)^q \quad \text{and} \quad E_{2N} = \mathsf{A}(\Delta x/2)^q.$$

To eliminate A we divide E_{2N} by E_N,

$$\log_2\left(\frac{E_{2N}}{E_N}\right) = q\ \log_2\left(\frac{1}{2}\right)$$

giving the following expression for q

$$q = -\log_2\left(\frac{E_{2N}}{E_N}\right).$$

Therefore, the order of convergence of the approximated solution u and the boundary node b are calculated respectively by,

$$q_1 = -\log_2\left(\frac{E_{2N}(u)}{E_N(u)}\right) \quad \text{and} \quad q_2 = -\log_2\left(\frac{E_{2N}(b)}{E_N(b)}\right).$$

Since each step of our scheme is second-order in space and first-order in time, and recalling that $\Delta t = \mathcal{O}(1/N^2)$ we expect to observe $q_1, q_2 \approx 2$.

We solve for $t \in [1, 10]$ and compute results for $N = 10 \times 2^{\hat{N}-1}$ for $\hat{N} = 1, \ldots, 6$ using the time-step value of $\Delta t = 0.04(4^{-\hat{N}})$. Initially, the mesh nodes are equi-spaced for all cases.

The self-similar initial conditions, at $t = 1$, are the ones derived in Section 5.2.1. More precisely the initial self-similar solutions are

$$u(x, 1) = 1 - \frac{x^2}{6}, \qquad b(1) = \sqrt{6}. \tag{5.25}$$

The exact solution is obtained using similarity, i.e.,

$$\bar{u}(x, t) = \frac{1}{t^{1/3}}\left(1 - \frac{x^2}{b(t)^2}\right), \tag{5.26}$$

cf. (5.9), and the exact position of the boundary can be obtained by setting $u = 0$ in (5.26),

$$\bar{x}_{N+1} = \bar{b}(t) = t^{1/3}\sqrt{6},$$

cf. (5.8).
The convergence results are shown in Table 5.1. We observe a decrease in the relative errors $E_N(u)$ and $E_N(b)$ as N increases and an order of convergence which tends to approximately 2 as N tends to infinity.

N	$E_N(u)$	q_1	$E_N(b)$	q_2
10	3.76×10^{-4}		2.42×10^{-4}	
20	8.38×10^{-5}	2.16	6.06×10^{-5}	2.00
40	1.97×10^{-5}	2.09	1.51×10^{-5}	2.00
80	4.78×10^{-6}	2.04	3.78×10^{-6}	2.00
160	1.18×10^{-6}	2.02	9.46×10^{-7}	2.00
320	2.92×10^{-7}	2.01	2.37×10^{-7}	2.00

Table 5.1: Relative errors $E_N(u)$ and $E_N(b)$ with the corresponding rates of convergence q_1 and q_2 for the porous medium equation using $\Delta t = 0.04(4^{-\hat{N}})$.

5.3.4 Illustrations of the properties of the PME

In this section, we illustrate the capability of the numerical method to imitate some of the properties of the PME relevant to population dynamics, e.g. mass conservation and the convergence to the self-similar solution [161].

In Figure 5.3 we show that the similarity solution is an attractor. We have plotted in blue dotted lines the two approximated solutions, $u_1(x,t)$ and $u_2(x,t)$, using the non-self similar initial conditions against the exact solution $\bar{u}(x,t)$ using the self-similar solutions denoted by the black solid line. The initial conditions used for the self-similar solutions are the ones denoted in (5.25) where the non-self-similar initial conditions used for the simulation shown in Figure 5.3 are

$$\begin{aligned}
u_1(x,0) &= 0.1361(x-1)(-5-x), && (-5 \le x \le -2.04)\\
u_1(x,0) &= 1.224(1+x)(-3-x), && (-2 \le x \le -1)\\
u_2(x,0) &= 1.224(1-x)(3-x), && (1 \le x \le 2)\\
u_2(x,0) &= 0.1361(x+1)(5-x), && (2.04 \le x \le 5).
\end{aligned}$$

Initially, the three curves are set to have equal areas. As shown above, since the PME conserves the mass (i.e., the area under the curve) during the evolution, we would expect the three curves to retain their equal mass for all times and since the non-self similar solutions will approach the exact solution, it is expected that the three curves will meet at later times. We can clearly see in Figure 5.3 that as time passes the non-self-similar results converge to the self-similar solution where at $t = 100000$ the three curves almost completely overlap.

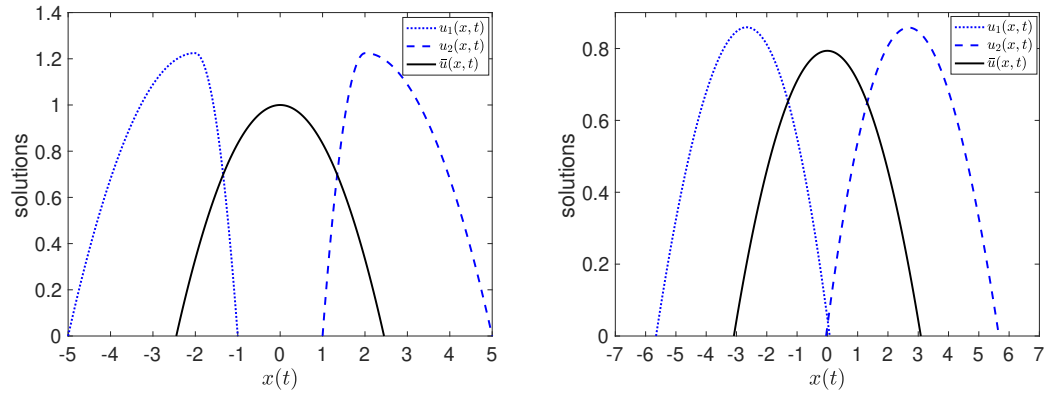

(a) $t = 1$ (b) $t = 2$

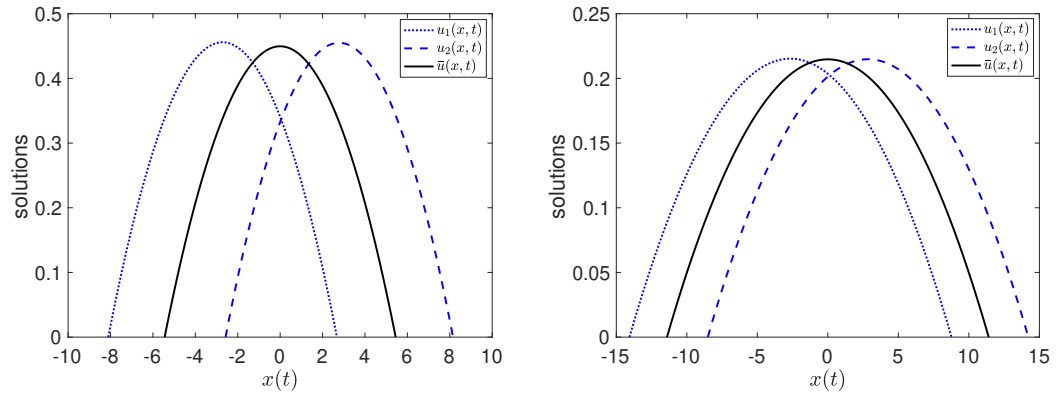

(c) $t = 10$ (d) $t = 100$

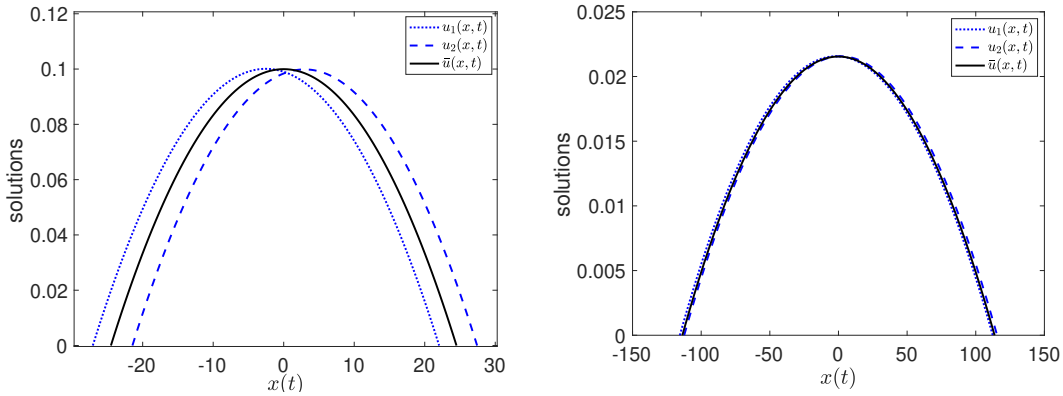

(e) $t = 1000$ (f) $t = 100000$

Figure 5.3: The PME solutions with non self-similar initial conditions $u_1(x, 0)$ and $u_2(x, 0)$ and the exact solution $\bar{u}(x, t)$ using the self-similar initial conditions for $m = 1$, $N = 100$, $\Delta t = 1/N^2 = 10^{-4}$. All curves have the same enclosed area.

So far we have demonstrated how the Porous Medium equation can be derived from a simple population model and discussed and proved some of its properties. Moreover, we showed the application of the MMFDM based on mass conservation for the PME and observe the convergence of the numerical results. In the following section, we introduce a two-cluster population model with density-dependent diffusion. The system is numerically solved using the moving mesh finite difference method based on mass conservation.

5.4 A Moving Mesh Finite Difference Method for a One-Dimensional Two-Cluster Population Model with Density-Dependent Diffusion

Now let us consider two clusters of the same population initially occupying distinct spatial regions. We denote the population densities of each cluster at space point x and time t by $u_1(x,t)$ and $u_2(x,t)$. The equation for the rate of change of each cluster population density is given by

$$\frac{\partial u_p}{\partial t} = \frac{\partial}{\partial x}\left(u_p \frac{\partial u_p}{\partial x}\right) + \alpha\, u_p(1 - \frac{u_p}{K}), \tag{5.27}$$

with $p = 1, 2$, (*cf.* (5.5)). The reaction term is the logistic growth presented by Verhulst in 1845 [162] where α represents the population rate of growth and K is the carrying capacity. The boundary conditions of each cluster are defined at the edge of the support,

$$u_p = 0 \quad \text{at} \quad x = a_p(t),\ b_p(t), \quad t > 0, \tag{5.28}$$

where $a_1(t), b_1(t)$ $a_2(t), b_2(t)$ describe the boundaries of the population densities u_1 and u_2 respectively.

Each cluster is initially assigned a unique mesh which corresponds to the spatial region each cluster occupies. Then the moving mesh finite difference method is applied to each cluster individually up to the time point where the two groups overlap. Once the populations intersect, then a new problem is formed with new compact support. For better understanding imagine two water drops on a flat surface. The two drops initially expand until they intersect forming a joined, bigger drop. The new drop has different properties, for example, greater mass and hence different velocity by which the drop is expanding on the surface.

5.4.1 Mass conserving problem

Setting α in (5.27) to zero leads back to the global mass conserving example given in (5.15). Hence, following the theory of partial mass conservation as described in Section 5.3.1, the numerical solution for each equation in the system (5.27) using the moving mesh method is as follows.
The constant total mass is given by

$$\theta = \int_{a(t)}^{b(t)} u(x,t)\ \mathrm{d}x.$$

Here the density u is general and represents both u_1 and u_2. To proceed with solving a mass conserving problem first consider a mesh given by x_i, $i = 1, \ldots, N+1$ such that

$$a(t) = x_1(t) < x_2(t) \ldots\ldots < x_N(t) < x_{N+1} = b(t). \tag{5.29}$$

As described in Section 5.3.1, for mass conserving problems, the moving mesh method is based on the conservation of partial masses, supposing that the mesh nodes are moving in such a manner that the mass within node intervals is constant, i.e.,

$$\int_{a(t)}^{\tilde{x}_i(t)} u(x,t)\ \mathrm{d}x = u_\eta \Delta\tilde{x}_\eta = \gamma_\eta, \tag{5.30}$$

where η is the interval $(a(t), \tilde{x}_i(t))$ and $\tilde{x}_i$ represents the $N+1$ mesh nodes which coincide instantaneously with x and vary with time.

Note that the integral in equation (5.18) is between two neighbouring points while in equation (5.30) η is the interval between the left-hand-side moving boundary and any inner node. The partial masses in the intervals of both equations are constant in time, therefore the theory of mass conservation applies in both cases. Also, later on in Section 5.3.1 (equation (5.20)) we set one of the nodes $\tilde{x}_1$ and $\tilde{x}_2$ to denote the anchor point.

To update the density u using equation (5.30), we require the updated node positions. Therefore equation for the mesh velocity is needed. We define the velocity at a node i to be

$$w(\tilde{x}_i(t), t) = \tilde{w}_i(t) = \frac{d\tilde{x}_i}{dt}.$$

Hence, for a given mesh $\tilde{x}_i(t)$ and solution $\tilde{u}_i(t) = u(\tilde{x}_i, t)$, we compute the mesh velocity $\tilde{w}_i(t) = w(\tilde{x}_i, t)$, and subsequently the updated mesh, to ultimately recover the updated solution on the new mesh.
Details are given below.

Determining the mesh velocity

We obtain an expression for the mesh velocity by differentiating (5.30) with respect to time and applying the Leibniz integral rule, giving

$$\int_{a(t)}^{\tilde{x}_i(t)} \frac{\partial u}{\partial t}\, \mathrm{d}x + \tilde{u}_i(t)\tilde{w}_i(t) - \tilde{u}_1(t)\tilde{w}_1(t) = 0.$$

Using the boundary conditions (5.28)

$$\tilde{w}_i(t) = -\frac{1}{\tilde{u}_i(t)} \int_{a(t)}^{\tilde{x}_i(t)} \frac{\partial u}{\partial t}\, \mathrm{d}x \tag{5.31}$$

where $\frac{\partial u}{\partial t}$ is given by the PDE (5.27). Thus, the velocity of the interior nodes where $\tilde{u}_i > 0$ is given by (5.31) and the boundary node velocities $\tilde{w}_1(t), \tilde{w}_{N+1}(t)$ can be evaluated from extrapolation.

Advancing the nodal positions in time

We choose a time step values Δt where $t^n = n\Delta t$ for $\Delta t > 0$, $n = 0, 1, \ldots$, with the approximations $x_i^n \approx \tilde{x}_i(t^n)$, $u_i^n \approx \tilde{u}_i(t^n)$, $w_i^n \approx \tilde{w}_i(t^n)$. Knowing the mesh positions x_i^n and having evaluated the mesh velocity w_i^n, use a time-stepping scheme to update the mesh x_i^{n+1}, like the first-order Euler time-stepping scheme (5.23).

Recovering the solution

To approximate the solution u_i^{n+1} using the updated node locations use equation (5.30), as in (5.24) for the interior nodes. The solution at the boundaries u_1^{n+1} and u_{N+1}^{n+1} is determined by the boundary conditions (5.28).

5.4.2 Moving mesh finite difference solution for equation (5.27) when $\alpha = 0$

For the solution of equation (5.27) when $\alpha = 0$ we follow the theory described in Section 5.3.1 for u_1 and u_2 independently until the two clusters overlap. Then, we consider the new mass of the population density u_3 at a specific location to be the combined mass of the densities u_1 and u_2 and the nodal velocities are constructed by supposing that fractions of the mass are held constant in time, i.e.,

$$(u_1 + u_2)_\eta \Delta\tilde{x}_\eta = (u_3)_\eta \Delta\tilde{x}_\eta = \gamma_\eta,$$

where η here defines the interval between two nodes in the x_3 mesh.
The PDE which describes the rate at which the population density u_3 changes in time can be found using (5.27), by setting $u_p = u_2 + u_1$ when $\alpha = 0$, giving

$$\frac{\partial u_3}{\partial t} = \frac{\partial}{\partial x}\left(u_3 \frac{\partial u_3}{\partial x}\right).$$

Here, we consider that regions for which u_1 and u_2 are non-zero are disjoint.

The algorithm for solving (5.27) when $\alpha = 0$ is as follows.

Algorithm

For each equation of u_p $(p = 1, 2)$:
Create a unique mesh under each compact support and choose the initial node positions $x^n_{p(i)}$ of each mesh, with corresponding approximate solution values $u^0_{p(i)} > 0$ (see Figure 5.4). For all time steps that the populations occupy district regions (i.e., $x_{1(N+1)} < x_{2(1)}$) we proceed at each time-step by

1. Calculating the velocity at each node $w^n_{p(i)}$, $i = 2, \ldots, N$ by (5.31) by substituting $\frac{\partial u}{\partial t}$ from (5.27) and performing the integration of the l.h.s

$$w^n_{p(i)} = -\frac{1}{u_p}\left(u_p \frac{\partial u_p}{\partial x}\right)\Big|_{x^n_{p(i)}} = -\frac{\partial u_p}{\partial x}\Big|_{x^n_{p(i)}}, \quad (i = 2, \ldots, N)$$

   The outer moving boundary velocities $w^n_{p(1)}$ and $w^n_{p(N+1)}$ are extrapolated.

2. The new mesh is obtained by the explicit Euler time-stepping scheme given in (5.23).

3. Finally, having updated the new node positions, we can recover the solution $u^{n+1}_{p(i)}$ using (5.24).

The algorithm above is carried out up to the time-step that the two clusters intersect (i.e., $x_{1(N+1)} > x_{2(1)}$). Then we proceed with the algorithm concerning the combined mass of the two clusters:

Set the new mesh $x_{3(i)}$ of the joined masses to be from $x_{1(1)}$ to $x_{2(N+1)}$ (see Figure 5.5) and set $a_3(t)$ and $b_3(t)$ to be the two edges of the u_3 support. Then, interpolate both u_1 and u_2 solutions on the new mesh $x_{3(i)}$ (see Figure 5.5). The u_3 initial condition is the sum of the densities u_1 and u_2 on the x_3 mesh. Having defined u_3 and x_3, at each time-step we proceed with the steps presented in the algorithm but now $p = 3$.

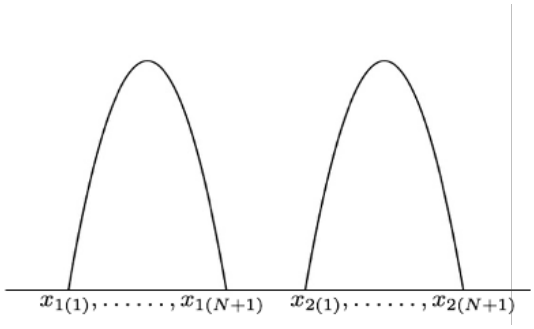

Figure 5.4: Mesh when $x_{1(N+1)} < x_{2(1)}$.

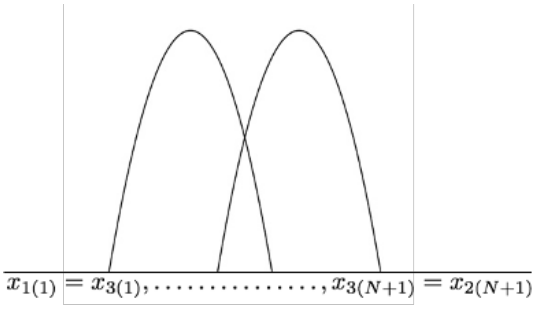

Figure 5.5: Mesh when $x_{1(N+1)} \geq x_{2(1)}$.

Results

For the following set of results, we have set both clusters to have the same mass but occupy distinct regions initially. The cluster with population density u_1 is located, at $t = 0$, in the region $a_1(0) = -5$ to $b_1(0) = -1$ and population two with density u_2 occupies the region $a_2(0) = 1$ to $b_2(0) = 5$. The initial conditions for u_1 and u_2 are shown in Figure 5.6 with the solid green and red colour respectively. Figure 5.6 shows the evolution of u_1 (green) and u_2 (red) from the initial conditions ($t = 0$) up to the time point where the two meshes overlap, i.e., $x_1(N + 1) > x_2(1)$. Then the new population density u_3 (blue) is created by adding the two population densities u_1 and u_2. Figure 5.7 shows the evolution of the u_3 (blue) solution plotted together with the evolution of the self-similar solution (exact) $\overline{u}$ (black), while at later times, the approximate solution u_3 approaches the exact solution $\overline{u}$, as shown in Figure 5.8.

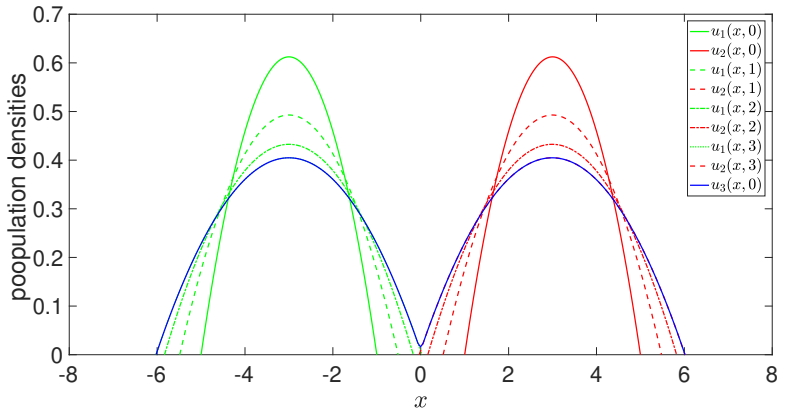

Figure 5.6: The evolution of u_1 (green) and u_2 (red) in time and the formation of u_3 (blue).

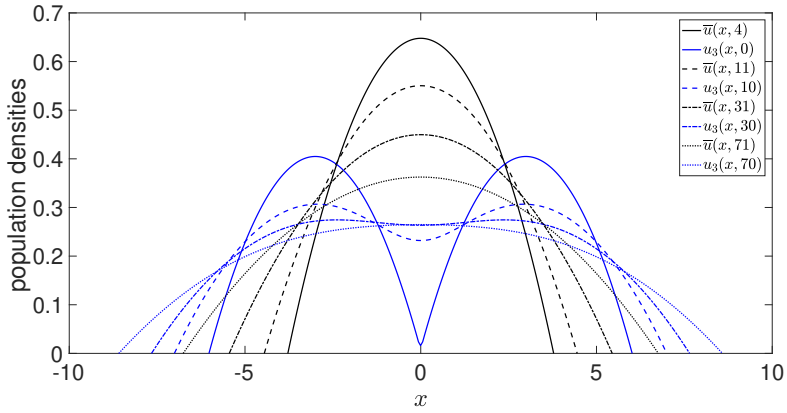

Figure 5.7: The evolution of u_3 (blue) and the self-similar solution $\overline{u}$ (black).

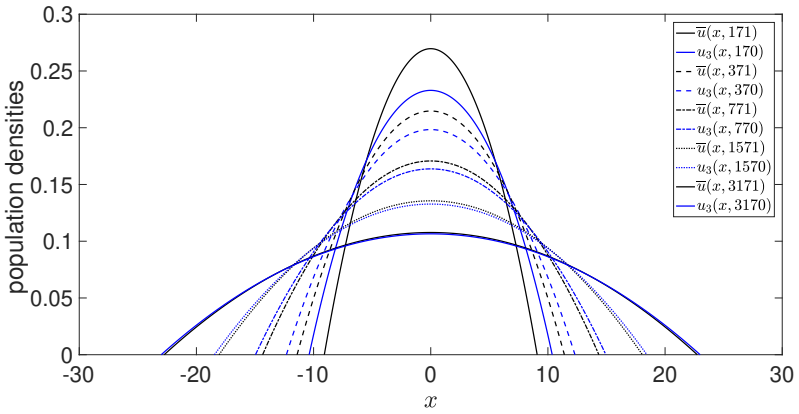

Figure 5.8: At later times the two solutions, u_3 (blue) and $\overline{u}$ (black), almost completely overlap.

5.4.3 Non-mass conserving problem

For non-mass conserving problems ($\alpha \neq 0$ in equation (5.27)), the theory for the moving mesh method relies on the assumption that normalised or partial mass fractions are conserved in time. We use the same mesh definition given in Section 5.3.1 where the time-dependent variable $\tilde{x}(t)$ represents the nodes of the mesh. The conserved normalised partial masses are given by,

$$\frac{1}{\theta(t)} \int_{a(t)}^{\tilde{x}_i(t)} u(x,t)\ \mathrm{d}x = \gamma_\eta, \tag{5.32}$$

where γ_η remains constant in time with η describing the interval $(a(t), \tilde{x}_i(t))$.
The procedure is as follows.
After the discretization of the domain into $N+1$ nodes, given a mesh $\tilde{x}_i(t)$, and solution $\tilde{u}_i(t) = u(\tilde{x}_i(t), t)$, $i = 1, \ldots, N+1$ we evaluate the total mass $\theta(t)$ directly from the integral of the density under the whole compact support, i.e.,

$$\theta(t) = \int_{a(t)}^{b(t)} u(x,t)\ \mathrm{d}x. \tag{5.33}$$

To update the solution u at the forward time level using equation (5.32), it is required to know the updated value of the total mass θ and the new $\tilde{x}$ positions. Therefore, equations for the rate of change of the total mass $\dot{\theta}(t)$ and the velocity of the nodes $\tilde{w}_i(t)$ are required. Having found $\dot{\theta}(t)$ and $\tilde{w}_i(t)$ the mesh and total mass are updated simultaneously using a time-stepping scheme. This enables the recovery of the updated solution on the new mesh. A more detailed procedure is given below.

Determining the rate of change of the total mass

The equation for the rate of change of the total mass $\theta(t)$ can be obtained by differentiating (5.33) with respect to time and applying the Leibniz integral rule, giving

$$\dot{\theta} = \frac{d}{dt}\int_{a(t)}^{b(t)} u(x,t)\ \mathrm{d}x = \int_{a(t)}^{b(t)} \frac{\partial u}{\partial t}\ \mathrm{d}x + \tilde{u}_b(t)\,\tilde{w}_b(t) - \tilde{u}_a(t)\,\tilde{w}_a(t).$$

Using the boundary conditions (5.28),

$$\dot{\theta}(t) = \int_{a(t)}^{b(t)} \frac{\partial u}{\partial t}\ \mathrm{d}x, \tag{5.34}$$

where $\frac{\partial u}{\partial t}$ is given by (5.27) for u_1 and u_2.

Determining the mesh velocity

The equation for the mesh velocities $\tilde{w}_i(t)$ can be obtained by differentiating (5.32) with respect to time and applying the Leibniz integral rule, giving

$$\dot{\theta}(t)\gamma_\eta = \frac{d}{dt}\int_{a(t)}^{\tilde{x}_i(t)} u(x,t)\ \mathrm{d}x = \int_{a(t)}^{\tilde{x}_i(t)} \frac{\partial u}{\partial t}\mathrm{d}x + \tilde{u}_i(t)\,\tilde{w}_i(t) - \tilde{u}_0(t)\,\tilde{w}_0(t).$$

Here η refers to the interval $(a(t), \tilde{x}_i(t))$.
From the boundary conditions (5.28), the velocity of the interior nodes is given by

$$\tilde{w}_i(t) = \frac{1}{\tilde{u}_i(t)}\left(\dot{\theta}(t)\gamma_\eta - \int_{a(t)}^{\tilde{x}_i(t)} \frac{\partial u}{\partial t}\mathrm{d}x\right), \tag{5.35}$$

where $\frac{\partial u}{\partial t}$ is given by (5.27) for u_1 and u_2, provided that $\tilde{u}_i(t) \neq 0$. Equation (5.35) hold for the interior nodes $i = 2, \ldots, N$ while the velocity of the boundary nodes $\tilde{w}_1$ and $\tilde{w}_{N+1}$ can be extrapolated from the internal mesh velocities.

Advancing the nodal positions and the total mass

As in Section 5.4.2, we choose a time step value Δt where $t^n = n\Delta t$ for $\Delta t > 0$, $n = 0, 1, \ldots$, with the approximations $x_i^n \approx \tilde{x}_i(t^n)$, $u_i^n \approx \tilde{u}_i(t^n)$, $w_i^n \approx \tilde{w}_i(t^n)$, $\theta^n \approx \theta(t^n)$ and $\dot{\theta}^n \approx \dot{\theta}(t^n)$. Knowing θ^n and the mesh positions x_i^n and having evaluated the rate of change of total mass $\dot{\theta}^n$ and the mesh velocity w_i^n, use the Euler time-stepping scheme (5.23) to update the total mass θ^{n+1} and mesh x_i^{n+1}.

Recovering the solution

To approximate the solution u_i^{n+1}, equate (5.32) between two points $\tilde{x}_{i+1}$ and $\tilde{x}_{i-1}$ at time levels t^{n+1} and t^0. After a second-order approximation the solution for u_i^{n+1} is given by

$$\frac{1}{\theta^{n+1}}\left(x_{i+1}^{n+1}-x_{i-1}^{n+1}\right)u_i^{n+1}=\frac{1}{\theta^0}\left(x_{i+1}^0-x_{i-1}^0\right)u_i^0, \tag{5.36}$$

for $i=2,\ldots,N$. The solution at the boundaries u_1^{n+1} and u_{N+1}^{n+1} is determined by the boundary conditions (5.28).

5.4.4 Moving mesh finite difference solution for equation (5.27) when $\alpha \neq 0$

We follow the theory described above of the moving mesh method for non-mass conserving problems to solve equation (5.27) when $\alpha \neq 0$. We apply the theory on both u_1 and u_2 separately until the two clusters intersect. Then, for the non-mass conserving problem, we are considering the mass at a specific location to be the combined mass of the densities u_1 and u_2. In the conservation method, the nodal velocities are constructed by supposing that fractions of the corresponding normalised mass are held constant in time, i.e.,

$$\frac{1}{\theta_1+\theta_2}\int_{a(t)}^{b(t)}(u_1+u_2)\ \mathrm{d}x=\frac{1}{\theta_3(t)}\int_{a(t)}^{b(t)}u_3(t)\ \mathrm{d}x=\gamma_\eta,$$

where η describes the interval between two nodes in the x_3 mesh.
The PDE which describes the rate at which the population density u_3 changes in time can be found using (5.27), by setting $u_3=u_2+u_1$, giving

$$\frac{\partial u_3}{\partial t}=\frac{\partial}{\partial x}\left(u_3\frac{\partial u_3}{\partial x}\right)+\alpha u_3\left(1-\frac{u_3}{K}\right)$$

and the algorithm for solving (5.27) when $\alpha \neq 0$ is as follows.

Algorithm

For each equation of u_p $(p=1,2)$:
The two clusters are each assigned a unique mesh with initial node position $x_{p(i)}^0$, with corresponding approximate solution values $u_{p(i)}^0>0$ (see Figure 5.4). For all time-steps that the populations occupy district regions, i.e., $x_{1(N+1)}<x_{2(1)}$ (see Figure 5.4) we proceed at each time-step by

1. Compute $\dot{\theta}_p^n$ from (5.34) by substituting (5.27) and performing the integration on the left-hand side, giving,

$$\dot{\theta}_p^n = \left(u_p \frac{\partial u_p}{\partial x} \right) \Big|_{a_p^n}^{b_p^n} + \int_{a_p^n}^{b_p^n} \alpha u_p \left(1 - \frac{u_p}{K} \right) \, \mathrm{d}x,$$

for $p = 1, 2$, where the integral of the reaction terms can be evaluated using the trapezoidal rule.

2. Calculating the velocity at each node $w_{p(i)}^n$, $i = 2, \ldots, N$ by (5.35) by substituting $\frac{\partial u}{\partial t}$ from (5.27) and performing the integration of the l.h.s

$$w_{p(i)}^n = -\frac{1}{u_{p(i)}^n} \left(\dot{\theta}_p^n \gamma_\eta - u_p \frac{\partial u_p}{\partial x} \Big|_{x_{p(i)}^n} - \int_{a_p^n}^{x_{p(i)}^n} \alpha u_p \left(1 - \frac{u_p}{K} \right) \, \mathrm{d}x \right), \quad (i = 2, \ldots, N),$$

for $p = 1, 2$, where η describes the interval $(a^n, x_{p(i)}^n)$.
Again, the integral of the reaction terms can be evaluated using the trapezoidal rule and the outer moving boundary velocities $w_{p(1)}^n$ and $w_{p(N+1)}^n$ are extrapolated.

3. Update the new mesh and the total mass by (5.23).

4. Finally, having updated the new node positions, we can recover the solution $u_{p(i)}^{n+1}$ using (5.36).

The above algorithm is carried out up to the time-step that the two clusters intersect (i.e., $x_{1(N+1)} > x_{2(1)}$). Then we proceed with the algorithm concerning the combined mass of the two clusters:

Set the new mesh $x_{3(i)}$ of the joined masses to be from $x_{1(1)}$ to $x_{2(N+1)}$ (see Figure 5.5) and set $a_3(t)$ and $b_3(t)$ to be the two edges of the u_3 support. Then, interpolate both u_1 and u_2 solutions on the new mesh $x_{3(i)}$ (see Figure 5.5). The u_3 initial condition is the sum of the densities u_1 and u_2 on the x_3 mesh. Having defined u_3 and x_3, at each time-step we proceed with the steps presented in the algorithm but now $p = 3$.

Results

The initial conditions used for the following set of results are shown in both Figures 5.9 and 5.10 with solid green and red colour for u_1 and u_2, respectively. Population with density u_1 is set to initially occupy the region $a_1(0) = -3$ to

$b_1(0) = -1$ and u_2 is initially located at $a_2(0) = 1$ to $b_2(0) = 5$. For the following set of results, we have used $\alpha = 0.4$ and $K = 1$. Figure 5.9 shows the evolution of u_1 and u_2 in time until the two clusters intersect and the new population density u_3(blue) is formed. Figure 5.10 is an illustration of the evolution of u_3 in time. The population is expanding in the domain forming one uniform hump while its mass is getting greater in time due to the reaction terms. We observe a smooth transition between algorithm 1 and algorithm 2.

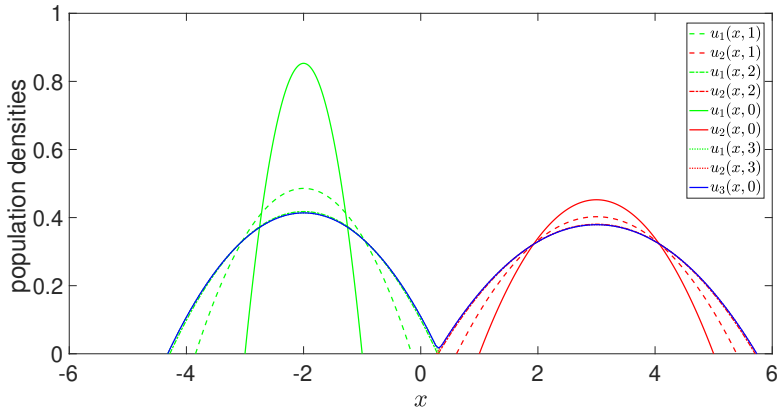

Figure 5.9: The evolution of u_1 (green) and u_2 (red) in time and the formation of u_3 (blue).

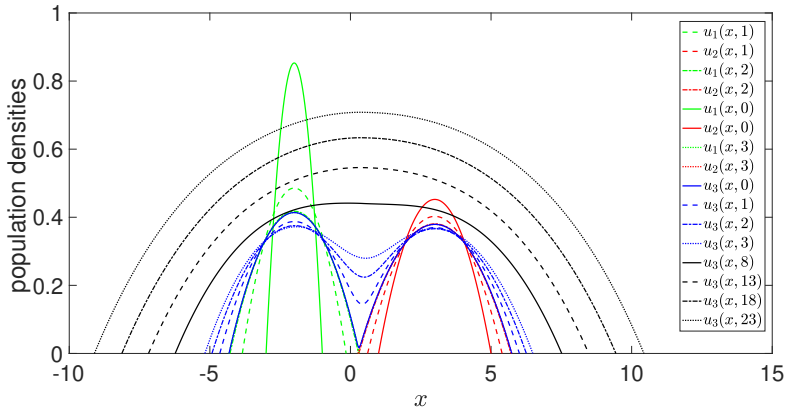

Figure 5.10: The evolution in time of u_3 (blue and black).

5.5 Summary

The PME is of great interest to both pure mathematicians and applied scientists and it is used to describe many other processes than diffusion including heat transfer and fluid flow.

The choice of the PME by many applied scientists is mainly due to its properties, which we have discussed in this chapter. Those properties make the moving mesh method a natural choice for the approximation solution of the PME as the mesh nodes follow the flow by the mass conservation.

The significance of the PME to population dynamics is that it shows that through nonlinear diffusion there are solutions with moving compact support that are conservative with a finite boundary velocity (unlike Fickian diffusion which requires infinite support). Also approximations can be computed with a moving mesh conservation method that imitates these properties. Moreover, source terms can be incorporated using relative conservation.

By the self-similar solution, we were able to compare the numerical solution with the exact solution and concluded that the moving mesh finite difference method is accurate. The numerical solution and the mesh appeared to have second-order convergence.

We have also demonstrated the application of the moving mesh method based on mass conservation to a two-cluster population system with non-linear diffusion initially occupying distinct domains. Since the two clusters are of the same species a natural way to solve the system is to use the combined mass of the clusters when the two groups overlap. We observed smooth stable results and the transition from unique masses to the combined was processed smoothly. The idea of combining the masses of the two clusters and hence solving the system on a single moving mesh gives the motivation for the new feature of the moving mesh method based on conservation which is presented in Chapter 7.

The subsequent population systems consider the standard Fickian diffusion to describe species diffusion, however, the non-linear density-dependent diffusion studied in this chapter is applied closely at the end of the thesis on an epidemic model.

The following chapter considers the application of the moving mesh finite difference method based on mass conservation on a system of two extremely competitive species. Due to the high competition, the two species are spatially segregated, and separated by a moving interface. Hence, each species occupies a distinct region in space and they annihilate each other by a moving interface.

The rest of the thesis is composed as a series of papers with Chapter 6 and Chapter 7 strongly based on the papers of Baines, M. J. and Christou, K., [11] and [15], respectively.

Chapter 6

A Moving-Mesh Finite-Difference Method for Segregated two-phase Competition-Diffusion

This chapter considers the application of the moving mesh finite difference method based on mass conservation described in Chapter 4, Section 4.2.5, on a system of two competitive species. Due to the high competition between the species, the two populations are segregated (i.e., cannot coexist in space) and separated in space by a moving interface.

This chapter, excluding the Summary Section 6.6, is strongly based on the paper: Baines, M.J.; Christou, K. A Moving-Mesh Finite-Difference Method for Segregated Two-Phase Competition-Diffusion. Mathematics 2021, 9, 386. The published paper can be found at https://doi.org/10.3390/math9040386.

6.1 Chapter Overview

A moving-mesh finite-difference solution of a Lotka-Volterra competition-diffusion model of theoretical ecology is described in which the competition is sufficiently strong to spatially segregate the two populations, leading to a two-phase problem with a coupling condition at the moving interface. A moving mesh approach preserves the identities of the two species in space and time, so that the parameters always refer to the correct population. The model is implemented numerically with a variety of parameter combinations, illustrating how the populations may evolve in time.

6.2 Introduction

Ecological competition is a widely studied concept in both theoretical and experimental ecology. In particular, interspecific competition has long been one of ecology's most prevailing pursuits as it is one of the factors that affect the evolution of species and can alter populations and community structure.

Many researchers have made efforts to develop models to investigate species competition from the viewpoint of mathematical ecology. For a theoretical understanding of spatial patterns arising in population dynamics for competitive species, several free boundary problems have been proposed [66, 65, 185, 170, 58] which provide useful theoretical results. Various numerical methods have been applied to solve such free boundary problems, for instance, in [110] the authors use a front-tracking approach and a front-fixing approach to a two-species competition-diffusion model with two free boundaries, whereas in [177] a moving mesh finite element method is used to solve a system of two competitive segregated species that cannot coexist in space.

Due to the complexity of the equations, a numerical approximation is useful both for extracting quantitative solutions and for achieving a qualitative understanding of the behaviour of the solution. However, special attention must be paid to the moving interface, whose location usually requires a higher resolution than the rest of the domain while the solution may exhibit singular behaviour there.

To avoid this difficulty adaptive methods have been used which modify the resolution of the domain as the solution evolves in response to changes in the dependent variable. Hence, greater precision can be achieved locally without having to increase the resolution everywhere in the domain, which would lead to a very computationally expensive scheme.

As we mentioned earlier in Chapter 4, in this thesis we are considering a particular velocity-based method which lies in the r-refinement category of mesh adaptive methods. In this method, the mesh is generated by one Eulerian conservation principle while the solution is determined algebraically from a Lagrangian form of conservation [14, 9, 103]. We first briefly describe the moving mesh method based on conservation.

We recall from Section 4.2.5 of Chapter 4 that the conservation method uses an integral to preserve a desired conserved quantity within each patch of elements from which the velocities are constructed. For a mass-conserving problem, in which the global mass is constant this quantity is the conserved local mass. However, for a non-mass-conserving problem, the theory uses the concept of relative mass. By the Leibniz integral rule, we can then construct an equation from which

the velocity of each node is derived. For a unique solution of that equation, the population density must be known at a node or a velocity must be applied to a node which may be thought of as an 'anchor' point.

The approach used in this chapter is similar to the finite difference method used in [103] which was ensued from the finite element versions of the velocity-based moving mesh approach of Baines, Hubbard and Jimack in [9] and [14] and by Baines, Hubbard, Jimack and Mahmood in [10].

In this chapter, we apply the moving mesh finite difference method based on conservation to a PDE system of the Lotka-Volterra competition model, first proposed by [75], which describes a two-phase segregated reaction-diffusion system with a high competition limit where the species are completely spatially segregated and only interact through an interface condition. It is shown in [75] that where the competition is strong enough to spatially segregate the two populations the Lotka-Volterra system can be reduced to a form similar to a Stefan problem in physics [67]. The two major differences are firstly, that there are additional logistic growth terms in the Lotka-Volterra model and secondly, there is a parameter in the Lotka-Volterra model of the interface condition (the equivalent of the latent heat coefficient of the Stefan problem) which is set equal to zero. Unlike the Stefan problem, one species does not transform into another which means that the competition system has an interface condition that specifies the interface velocity only implicitly.

In [47] the authors considered the segregation problem due to high competition with inhomogeneous Dirichlet boundary conditions while similar studies in the case of Neumann boundary conditions are presented in [49] and [74].

The system of equations presented in this chapter is suitable to describe concepts in ecology when two species with similar ecological niches cannot co-exist, known as the competitive exclusion principle [70]. One will always overcome the other, so the more competitive species will stay and the subordinate one will either adapt or be excluded by either emigration or extinction.

The layout of the chapter is as follows. Section 6.3 gives details of the Lotka-Volterra competition model with a highly competitive rate and describes the relative conservation principle approach and its finite difference implementation, together with the algorithm of the moving mesh finite difference method. In Section 6.4 illustrations are given for a variety of parameter combinations, observing the various behaviours that dominate as the species evolve through time. Finally, Section 6.5 gives a brief discussion of the results and potential research directions.

6.3 Materials and Methods

6.3.1 The Lotka-Volterra system

The Lotka-Volterra system is the two-component reaction-diffusion system

$$\frac{\partial u_1}{\partial t} = \delta_1 \frac{\partial^2 u_1}{\partial x^2} + f(u_1, u_2)u_1 \qquad x \in R_1(t), \quad t > 0 \tag{6.1}$$

$$\frac{\partial u_2}{\partial t} = \delta_2 \frac{\partial^2 u_2}{\partial x^2} + g(u_1, u_2)u_2 \qquad x \in R_2(t), \quad t > 0 \tag{6.2}$$

where $u_1(x,t)$ and $u_2(x,t)$ are the population densities of two competing species in abutting regions $R_1(t)$ and $R_2(t)$, the parameters δ_1, δ_2 are constant diffusion coefficients, and

$$f(u_1, u_2) = r_1 \left(1 - \frac{u_1 + k_1 u_2}{K_1}\right)$$

$$g(u_1, u_2) = r_2 \left(1 - \frac{u_2 + k_2 u_1}{K_2}\right)$$

are reaction terms in which k_1, k_2 are species-specific competition rates, K_1, K_2 are the carrying capacities of the species, and r_1, r_2 are reproductive rate parameters.
In [75] it is demonstrated that for two species completely segregated the reaction terms can be reduced to

$$f(u_1, u_2) = r_1(1 - u_1/K_1)$$

and

$$g(u_1, u_2) = r_2(1 - u_2/K_2)$$

so that equations (6.1) and (6.2) become

$$\frac{\partial u_1}{\partial t} = \delta_1 \frac{\partial^2 u_1}{\partial x^2} + \left\{ r_1 \left(1 - \frac{u_1}{K_1}\right) \right\} u_1 \qquad x \in R_1(t), \quad t > 0 \tag{6.3}$$

$$\frac{\partial u_2}{\partial t} = \delta_2 \frac{\partial^2 u_2}{\partial x^2} + \left\{ r_2 \left(1 - \frac{u_2}{K_2}\right) \right\} u_2 \qquad x \in R_2(t), \quad t > 0. \tag{6.4}$$

The resulting system represents the limit in which the carrying capacities K_1, K_2 values are very large, i.e., the competition rate is high enough that the two species cannot coexist in space and interact only through the interface boundary.

Initial conditions on u_1 and u_2 are selected such that one species is in growth and the other in decline. These are shown in Figure 6.1.

Zero Neumann boundary conditions $\partial u_1/\partial x = 0$ and $\partial u_2/\partial x = 0$ are applied at fixed external boundaries away from the interface.

6.3.2 The interface conditions

At the interface between the two species, there is a condition that gives the relationship between their fluxes. In essence, the species both flow into the interface and annihilate each other in a ratio determined by the competition coefficient μ. This condition is given by

$$\mu\delta_1\frac{\partial u_1}{\partial x} = -\delta_2\frac{\partial u_2}{\partial x}, \tag{6.5}$$

as shown in [75], where $\mu = k_2/k_1$ is the interspecies competition rate. Because the annihilation is complete we also have zero Dirichlet conditions $u_1 = u_2 = 0$ at the interface.

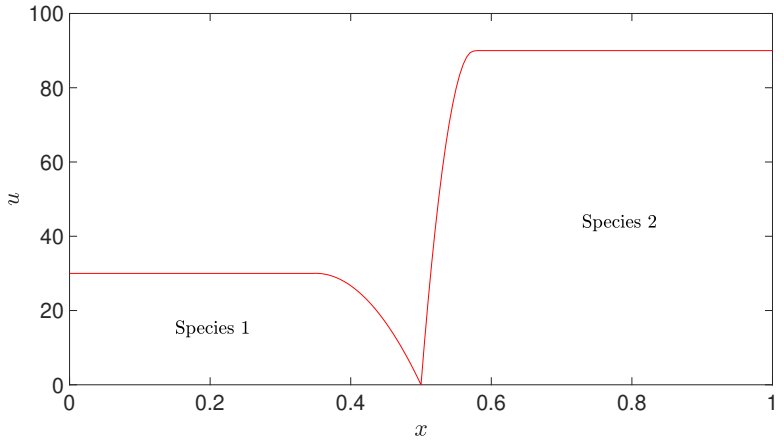

Figure 6.1: Initial conditions for the competition system, with population density u_1 of species 1 (on the left) and u_2 of species 2 (on the right). The interface node has zero population and must always satisfy the interface condition.

6.3.3 The MMFDM conservation method

A relative conservation principle

Define the total population of species p as

$$\theta_p(t) = \int_{R_p(t)} u_p(x,t)\ \mathrm{d}x,$$

$(p = 1, 2)$. Then by Leibniz integral rule,

$$\dot{\theta}_p = \frac{\mathrm{d}\theta_p}{\mathrm{d}t} = \frac{\mathrm{d}}{\mathrm{d}t}\int_{R_p(t)} u_p(x,t)\,\mathrm{d}x = \int_{R_p(t)} \frac{\partial u_p}{\partial t}\,\mathrm{d}x + \left[u_p w_p\right]_{R_p(t)}.$$

where w_p is the velocity of points of the domain.
The final term vanishes by the boundary and interface conditions, so

$$\dot{\theta}_p = \int_{R_p(t)} \frac{\partial u_p}{\partial t}\, \mathrm{d}x, \qquad (p = 1, 2).$$

From (6.3) and (6.4),

$$\dot{\theta}_p = \int_{R_p(t)} \left(\delta_p \frac{\partial^2 u_p}{\partial x^2} + \left\{ r_p \left(1 - \frac{u_p}{K_p} \right) \right\} u_p \right) \mathrm{d}x, \qquad (p = 1, 2) \tag{6.6}$$

which can be integrated in time to give θ_p.

We now suppose that population *fractions* $c(\Omega_p)$

$$c(\Omega_p) = \frac{1}{\theta_p(t)} \int_{\Omega_p(t)} u_p(x, t)\, \mathrm{d}x, \qquad (p = 1, 2) \tag{6.7}$$

in each moving subdomain $\Omega_p(t)$ are independent of time, so that $\theta_p(t)$ and $u_p(x, t)$ satisfy the *relative* conservation principle

$$c(\Omega_p) = \int_{\Omega_p(t)} \frac{1}{\theta_p(t)} u_p(x, t)\, \mathrm{d}x, \qquad (p = 1, 2). \tag{6.8}$$

Note that $\frac{u_p}{\theta_p}$ are conserved quantities.

Since the population fractions $c(\Omega_p)$ are constant in time, they are determined by the conditions at the initial time t^0, i.e.,

$$c(\Omega_p) = \frac{1}{\theta_p(t^0)} \int_{R_p(t^0)} u_p(x, t^0)\, \mathrm{d}x.$$

Writing (6.8) as

$$\int_{\Omega_p(t)} u_p(x, t)\, \mathrm{d}x = c(\Omega_p)\theta_p(t), \qquad (p = 1, 2) \tag{6.9}$$

and differentiating the left-hand side of (6.9) with respect to time using Leibnitz integral rule,

$$\frac{\mathrm{d}}{\mathrm{d}t} \left[\int_{\Omega_p(t)} u_p(x, t) \mathrm{d}x \right] = \int_{\Omega_p(t)} \left(\frac{\partial u_p}{\partial t} + \frac{\partial}{\partial x}(u_p w_p) \right) \mathrm{d}x, \qquad (p = 1, 2),$$

where w_p is the velocity of points of the domain. Therefore, by (6.9), given the population fractions $c(\Omega_p)$ of the total mass $\dot{\theta}_p$, the velocity w_p and u_p satisfy the equations

$$c(\Omega_p)\dot{\theta}_p - \int_{\Omega_p(t)} \frac{\partial}{\partial x}(u_p v_p)\mathrm{d}x = \int_{\Omega_p(t)} \frac{\partial u_p}{\partial t}\mathrm{d}x, \qquad (p = 1, 2),$$

where the $\dot{\theta}_p$ are given by (6.3) or (6.4), leading to

$$c(\Omega_p)\dot{\theta_p} - [u_p w_p]_{\Omega_p(t)} = \delta_p \left[\frac{\partial u_p}{\partial x}\right]_{\Omega_p(t)} + r_p \int_{\Omega_p(t)} u_p(x,t)\, \left(1 - \frac{u_p(x,t)}{K_p}\right) \mathrm{d}x. \tag{6.10}$$

We let the subdomains $\Omega_1(t)$ in the region $R_1(t)$ consist of the interval $(a, x(t))$ where a is a fixed boundary and let $x(t)$ be any point in the region $R_1(t)$. Similarly the subdomains $\Omega_2(t)$ in the region $R_2(t)$ consist of the interval $(x(t), b)$ where b is a fixed boundary and $x(t)$ is any point in the region $R_2(t)$.

The boundary conditions at the external boundaries $a = 0$ and $b = 1$ are $\partial u_1/\partial x = \partial u_2/\partial x = 0$, and also $w_1 = w_2 = 0$ because the boundaries are fixed. Together with the condition that $u_1 = u_2 = 0$ at the interface boundary, equations (6.10) for the velocities w_1 and w_2 and the rates of change in the total mass $\dot{\theta}_1$ and $\dot{\theta}_2$ satisfy

$$c_1(x)\dot{\theta_1} - (u_1 w_1)|_{x(t)} = \delta_1 \left.\frac{\partial u_1}{\partial x}\right|_{x(t)} + r_1 \int_a^{x(t)} u_1(x,t)\, \left(1 - \frac{u_1(x,t)}{K_1}\right) \mathrm{d}x \tag{6.11}$$

and

$$c_2(x)\dot{\theta_2} + (u_2 w_2)|_{x(t)} = -\delta_2 \left.\frac{\partial u_2}{\partial x}\right|_{x(t)} + r_2 \int_{x(t)}^b u_2(x,t)\, \left(1 - \frac{u_2(x,t)}{K_2}\right) \mathrm{d}x, \tag{6.12}$$

respectively, where

$$\theta_1 = \int_0^{x_m(t)} u(x,t)\,\mathrm{d}x, \qquad \theta_2 = \int_{x_m(t)}^1 u(x,t)\,\mathrm{d}x$$

and

$$c_1(x) = \frac{1}{\theta_1(t)} \int_0^{x(t)} u(x,t)\,\mathrm{d}x, \qquad c_2(x) = \frac{1}{\theta_2(t)} \int_{x(t)}^1 u(x,t)\,\mathrm{d}x.$$

From (6.6),

$$\dot{\theta}_1 = \delta_1 \left.\frac{\partial u_1}{\partial x}\right|_{x_m(t)} + r_1 \int_a^{x_m(t)} u_1(x,t)\, \left(1 - \frac{u_1(x,t)}{K_1}\right) \mathrm{d}x \tag{6.13}$$

and

$$\dot{\theta}_2 = -\delta_2 \left.\frac{\partial u_2}{\partial x}\right|_{x_m(t)} + r_2 \int_{x_m(t)}^b u_2(x,t)\, \left(1 - \frac{u_2(x,t)}{K_2}\right) \mathrm{d}x. \tag{6.14}$$

The interface condition

Since the population density $u = 0$ at the interface and the population densities on either side of the interface are positive, the density function is V-shaped at the interface.

From [75] the interface condition is given by (6.5). Whilst the interface velocity is not given explicitly by (6.5) this equation does determine the location of the interface implicitly. Thus, if we know $\partial u/\partial x$ adjacent to the interface in each region we may use the condition that $u = 0$ at the interface to infer an interface position such that the values of $\delta_p \partial u_p/\partial x$ either side of the interface are in the ratio $-\mu$.

We now describe a finite difference numerical method for the solution of the problem.

Numerical solution

Let the domain (a, b) be $(0, 1)$. At time level $t = t^n$ define time-dependent mesh points

$$0 = x_0 < x_1^n < \ldots < x_{m-1}^n < x_m^n < x_{m+1}^n < \ldots < x_N^n < x_{N+1}^n = 1,$$

where x_m^n is the node at the moving interface, and let u_i^n, $(0 \leq i \leq N + 1)$, approximate $u(x, t)$ by u_i^n at these points.

The total mass approximations $\theta_1^n \approx \theta_1(t)$ and $\theta_2^n \approx \theta_2(t)$ of (6.13) and (6.14) are estimated by the composite trapezium rule

$$\theta_1^n = \sum_{i=1}^{m} \frac{1}{2}(u_{i-1} + u_i)(x_i - x_{i-1}), \qquad \theta_2^n = \sum_{i=m}^{N} \frac{1}{2}(u_i + u_{i+1})(x_{i+1} - x_i), \quad (6.15)$$

and the constant-in-time relative masses $c_{1,i}$ and $c_{2,i}$ in the interval (x_{i-1}^n, x_i^n) by

$$c_{1,i} = \frac{1}{\theta_1}\frac{1}{2}(u_i^0 + u_{i+1}^0)(x_{i+1}^0 - x_i^0), \qquad (0 \leq i < m - 1), \quad (6.16)$$

$$c_{2,i} = \frac{1}{\theta_2}\frac{1}{2}(u_i^0 + u_{i-1}^0)(x_i^0 - x_{i-1}^0), \qquad (m + 1 < i \leq N + 1), \quad (6.17)$$

at the initial time $t = t^0$.

For the initial conditions we take the x_i^0 to be equally spaced and the u_i^0 pointwise

from an initial function

$$\begin{aligned}
&u(x,0) = 30, && (0 \le x \le 0.34)\\
&u(x,0) = (x-0.2)(0.5-x)\times 170\times 7.85, && (0.35 \le x \le 0.5)\\
&u(x,0) = 0, && (x = 0.51)\\
&u(x,0) = (x-0.65)(0.5-x)\times 170\times 94, && (0.52 \le x \le 0.58)\\
&u(x,0) = 90, && (0.59 \le x \le 1)
\end{aligned}$$

chosen to resemble the one in [177] (see Figure 6.1).

Rates of change of the total populations

The rates of change of the total populations $\dot{\theta}_1, \dot{\theta}_2$ of (6.6) are approximated by composite trapezium rules, in region 1 from (6.13),

$$\dot{\theta}_1 = \delta_1 \left(\frac{u_m^n - u_{m-1}^n}{x_m^n - x_{m-1}^n} \right)$$

$$+r_1 \sum_{i=1}^{m} \frac{1}{2} \left\{ u_{i-1}^n \left(1 - \frac{u_{i-1}^n}{K_1}\right) + u_i^n \left(1 - \frac{u_i^n}{K_1}\right) \right\} (x_i - x_{i-1}) \tag{6.18}$$

and in region 2, from (6.14),

$$\dot{\theta}_2 = -\delta_2 \left(\frac{u_{m+1}^n - u_m^n}{x_{m+1}^n - x_m^n} \right)$$

$$+r_2 \sum_{i=m}^{N} \frac{1}{2} \left\{ u_i^n \left(1 - \frac{u_i^n}{K_2}\right) + u_{i+1}^n \left(1 - \frac{u_{i+1}^n}{K_2}\right) \right\} (x_{i+1} - x_i). \tag{6.19}$$

Approximating the velocities

From (6.11), using the composite trapezium rule, the velocity w_i^n in region 1 satisfies,

$$c_{1,i}\dot{\theta}_1^n + u_i^n w_i^n = \delta_1 \left. \frac{\partial u}{\partial x} \right|_m^i$$

$$+r_1 \sum_{j=2}^{i} \frac{1}{2} \left\{ u_{j-1}^n \left(1 - \frac{u_{j-1}^n}{K_1}\right) + u_j^n \left(1 - \frac{u_j^n}{K_1}\right) \right\} (x_j - x_{j-1}), \quad (1 < i < m-1),$$

where we have taken the subdomain Ω_1^n to be the interval (x^n, x_m^n). Similarly, from (6.12),the velocity w_2^n in region 2 satisfies

$$c_{2,i}\dot{\theta}_2^n + u_i^n w_i^n = -\delta_2 \left.\frac{\partial u}{\partial x}\right|_m^i$$

$$+r_2 \sum_{j=i}^{N} \frac{1}{2}\left\{u_j^n\left(1-\frac{u_j^n}{K_2}\right) + u_{j+1}^n\left(1-\frac{u_{j+1}^n}{K_2}\right)\right\}(x_{j+1}-x_j), \quad (m+1<i<N),$$

where we have taken the subdomain Ω_2^n to be the interval (x_m^n, x^n).

Time-stepping

For the time integration we adopt an explicit Euler time-stepping approach. Given the u_i, we update the total masses θ_p from the equation $\dot{\theta}_p = \mathrm{d}\theta_p/\mathrm{d}t$, $(p = 1, 2)$ using (6.18) and (6.19) by

$$\theta_p^{n+1} = \theta_p^n + \Delta t\, \dot{\theta}_p^n, \tag{6.20}$$

$(p = 1, 2)$, where Δt is the time step, and the mesh points x_i^n are updated from the equation $\mathrm{d}x_i/\mathrm{d}t = w_i$ by

$$x_i^{n+1} = x_i^n + \Delta t\, w_i^n, \qquad (i \neq m). \tag{6.21}$$

The updates are first-order accurate in time and subject to limitations on the time step to preserve node ordering.

Note that in case of a zero velocity, there is the following well-known sufficient condition on a time step Δt in the explicit scheme to prevent the u_i^{n+1} (and hence the local mass in an interval) from going unstable,

$$\frac{\delta_p \Delta t}{(\Delta x_{min})^2} \leq \frac{1}{2}, \quad (p = 1, 2). \tag{6.22}$$

Here we take (6.22) as a guide for a safe time step in the moving mesh case.

The population densities

In order to determine the approximate population densities u_i at the new time step $t = t^{n+1}$ from the θ_p^{n+1} and x_i^{n+1} we approximate the relative conservation principle (6.8) as

$$\frac{1}{\theta_p}(x_{i+1}^{n+1} - x_{i-1}^{n+1})u_i^{n+1} = \overline{c}_{p,i}, \qquad (p = 1, 2), \tag{6.23}$$

where from (6.16) and (6.17) the constants

$$\overline{c}_{p,i} = \frac{1}{\theta_p^0}(x_{i+1}^0 - x_{i-1}^0)u_i^0, \qquad (p = 1, 2), \tag{6.24}$$

are dependent only on initial values.

Thus, once the x_i^{n+1} have been found, in region 1, the approximate population density u_i^{n+1} is given by

$$u_i^{n+1} = \frac{\overline{c}_{1,i}\theta_1^{n+1}}{(x_{i+1}^{n+1} - x_i^{n+1})}, \qquad (0 \le i \le m-1), \tag{6.25}$$

and in that region 2 by

$$u_i^{n+1} = \frac{\overline{c}_{2,i}\theta_2^{n+1}}{(x_i^{n+1} - x_{i-1}^{n+1})}, \qquad (m+1 \le i \le N+1) \tag{6.26}$$

while $u_m^{n+1} = 0$ from the interface condition.

Note that the values of $u_{m\pm1}^{n+1}$ determined by (6.23) depend on x_m^{n+1}, which is not yet known at t^{n+1}. This value can however be found using the one-sided approximations

$$u_{m-1}^{n+1} = \frac{c_1\theta_1}{\frac{1}{2}(x_{m-1}^{n+1} - x_{m-2}^{n+1})}, \qquad u_{m+1}^{n+1} = \frac{c_2\theta_2}{\frac{1}{2}(x_{m+2}^{n+1} - x_{m+1}^{n+1})}$$

where from (6.16) and (6.17))

$$c_1 = \frac{1}{2}u_{m-1}^0(x_{m-1}^0 - x_{m-2}^0), \quad c_2 = \frac{1}{2}u_{m+1}^0(x_{m+2}^0 - x_{m+1}^0).$$

Approximating the interface

The interface condition (6.5) is approximated by

$$\mu\delta_1\frac{u_m - u_{m-1}}{x_m - x_{m-1}} = -\delta_2\frac{u_{m+1} - u_m}{x_{m+1} - x_m}, \tag{6.27}$$

where the subscript m denotes the interface node and the $x_{m\pm1}, u_{m\pm1}$ are adjacent node positions and solution values. Since $u_m = 0$, from (6.27) an approximation to the position of the interface node x_m^{n+1} in terms of adjacent nodal values at $m \pm 1$ is

$$x_m^{n+1} = \left(\frac{\mu\delta_1 u_{m-1}^{n+1}x_{m+1}^{n+1} + \delta_2 u_{m+1}^{n+1}x_{m-1}^{n+1}}{\mu\delta_1 u_{m-1}^{n+1} + \delta_2 u_{m+1}^{n+1}}\right). \tag{6.28}$$

Thus, once the other x_i^{n+1}, u_i^{n+1} have been updated, x_m^{n+1} can be found from (6.28).

6.3.4 Algorithm

In summary, the moving mesh finite difference solution of the competition-diffusion problem given by equations (6.3) and (6.4) with the interface condition (6.5) on the moving mesh in 1-D generated by (6.8) is given by the following algorithm.

From the initial mesh and the initial condition compute the initial values $\theta_p(0)$, $(p = 1, 2)$ of the total populations of the species from (6.15) and the values of the relative masses $c_{p,i}$ and $\overline{c}_{p,i}$ from (6.16), (6.17) and (6.24).

Then for each time step:

1. Find the rates of change $\dot{\theta}_1, \dot{\theta}_2$ of the total masses from (6.18) and (6.19),
2. Calculate the nodal velocities v_i from (6.11) and (6.12),
3. Update θ_1 and θ_2 from $\dot{\theta}_1$ and $\dot{\theta}_2$ using the explicit Euler scheme (6.20),
4. Generate the nodes x_i at the next time-step from the w_i using the explicit Euler scheme (6.21),
5. Update the population densities u_i at the next time level in each region from (6.25) and (6.26),
6. Update the new position of the interface node x_m at the next time level from (6.28).

6.4 Results

We find that the model is stable and robust for a variety of parameter choices even when using the explicit Euler integration scheme when using a sufficiently small time step. We observe minimal oscillations affecting the smoothness of the results.

6.4.1 A parameter choice

In the body of work concerning Lotka-Volterra equations, there is a vast range of parameter values in use because there are so many varied but suitable examples of the type of competition that are described here. We select a conservatively representative set of parameters, chosen to demonstrate some of the behaviour that this model is able to describe.

For the first example, the parameter values are chosen followed by the ones used in [177] for consistency, namely $\delta_1 = \delta_2 = 0.01$, $K_1 = K_2 = 100$, $r_1 = r_2 = 1$ and $\mu = 3$ for the dimensional system in (6.3)-(6.5). The choice allowed the

comparison of the results using the moving mesh finite element of [177] and the moving mesh finite difference version used in this chapter. Even if species 2 makes territorial gains at early stages with the moving interface shifting towards the left, the rapid growth in the population of species 1 becomes its weapon to transform it from the inferior species to the superior one (Figure 6.2). The moving interface changes direction, moving towards the right at an approximately constant velocity where species 1 continues to increase in density with a rate that decreases as time progresses (Figure 6.3). As we approach the annihilation of species 2, the interface velocity increases again. This is due to the low mass of species 2 affecting its ability to grow (Figure 6.4). The movement of the interface is shown in Figure 6.5.

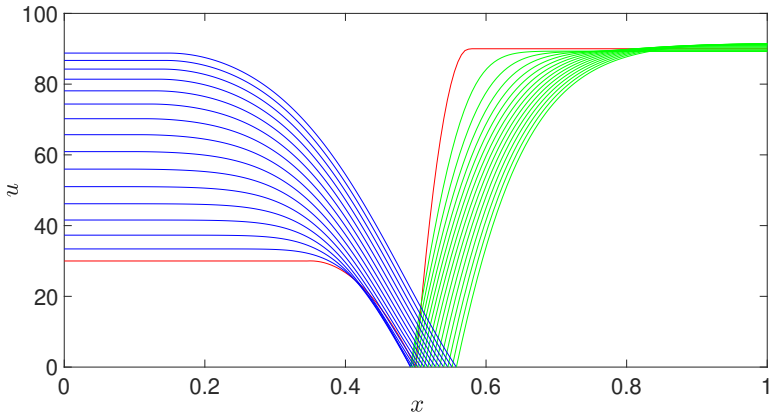

Figure 6.2: Result of competition model up to $t = 1.5$. Here we use $\delta_1 = \delta_2 = 0.01$, $k_1 = k_2 = 100$, $r_1 = r_2 = 1$ and $\mu = 3$. We run the model with a time step of 10^{-5} for 1.5×10^5 iterations and plot the results every 0.1.We see the internal dynamics of the species driving the population densities and interface fluxes, and the position of the interface responding to those fluxes. The initial conditions are shown in red, with species 1 in blue and species 2 in green.

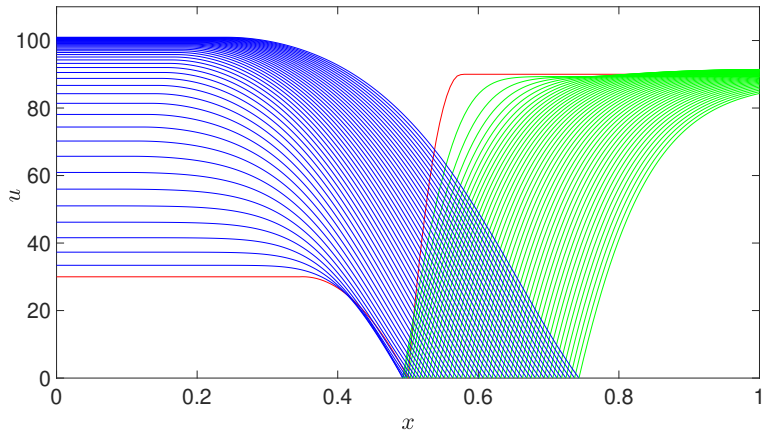

Figure 6.3: Result of competition model up to $t = 4.5$. Here we use $\delta_1 = \delta_2 = 0.01$, $K_1 = K_2 = 100$, $r_1 = r_2 = 1$ and $\mu = 3$. We run the model with a time step of 10^{-5} for 4.5×10^5 iterations and plot the results every 0.1. The interface continues to evolve and the masses of the species are now limited by the respective carrying capacities. The initial conditions are shown in red, with species 1 in blue and species 2 in green.

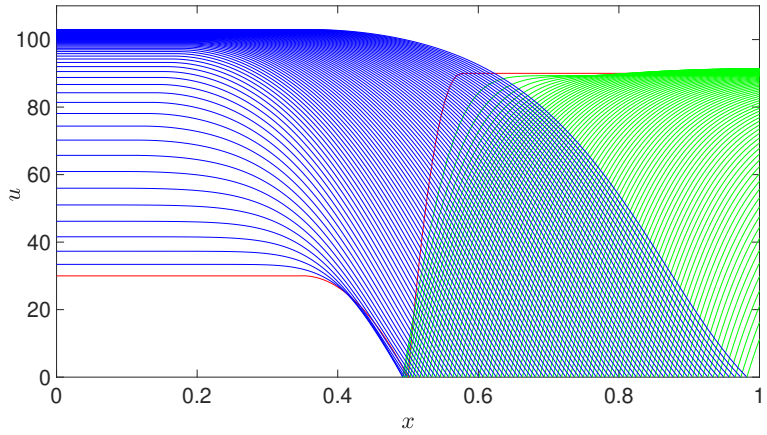

Figure 6.4: Result of competition model up to $t = 8$. Here we use $\delta_1 = \delta_2 = 0.01$, $K_1 = K_2 = 100$, $r_1 = r_2 = 1$ and $\mu = 3$. We run the model with a time step of 10^{-5} for 8×10^5 iterations and plot the results every 0.1. We observe that whilst species 2 initially grew in mass, it will now be wiped out by competition with species 1. The initial conditions are shown in red, with species 1 in blue and species 2 in green.

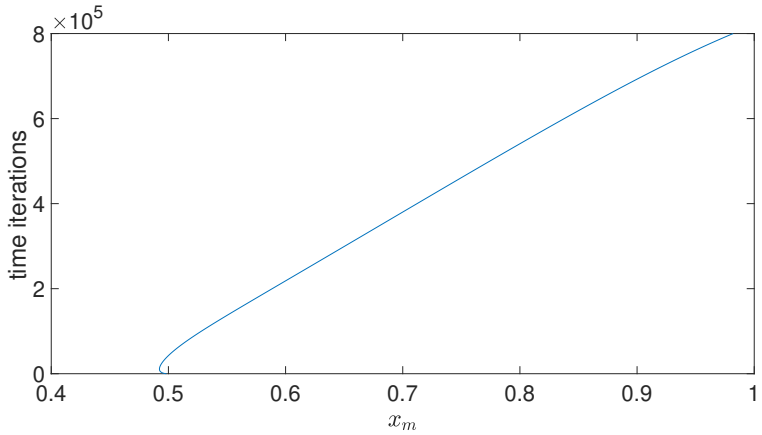

Figure 6.5: Movement of the interface position x_m for the competition model with parameters $\delta_1 = \delta_2 = 0.01$, $K_1 = K_2 = 100$, $r_1 = r_2 = 1$ and $\mu = 3$. We run the model with a time step of 10^{-5} for 8×10^5 iterations.

6.4.2 Other parameter choices

Carrying capacities

We now investigate other parameter choices. We restrict the growth of species 1 by lowering its carrying capacity and observe that in this scenario neither species is dominant, even though all the competition and diffusion characteristics are unchanged. Here we use $\delta_1 = \delta_2 = 0.01$, $K_1 = 50, K_2 = 150$, $r_1 = r_2 = 1$ and $\mu = 3$. With these differently chosen carrying capacities, we find that the interface position is approximately steady and the two species are in balance. This scenario is shown in Figure 6.6. Density dependence can affect the ability of a species to compete. In the case of decreasing the carrying capacity of species 1, we observe that species can both exist in space, still competing for common resources with none shifting towards other regions in space or in some cases becoming extinct.

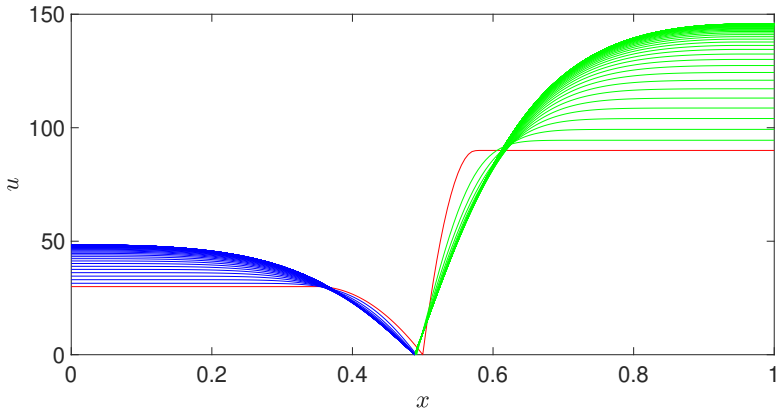

Figure 6.6: Result of competition model up to $t = 9$, considering the effect of altered carrying capacities. Here we use $\delta_1 = \delta_2 = 0.01$, $K_1 = 50, K_2 = 150$, $r_1 = r_2 = 1$ and $\mu = 3$. We run the model with a time step of 10^{-5} for 9×10^5 iterations and plot the results every 0.1. The figure shows the rapid territorial gains. The initial conditions are shown in red, with species 1 in blue and species 2 in green.

Diffusion characteristics

Alternatively, we may adjust the diffusion characteristics of the system. By allowing species 2 to diffuse at a higher rate, we observe that species 2 is able to make territorial gains due to this property alone (Figure 6.7). Here we use $\delta_1 = 0.01, \delta_2 = 0.05$, $K_1 = K_2 = 100$, $r_1 = r_2 = 1$ and $\mu = 3$. Due to the growth characteristics, we can see interesting temporal effects. Here the interface velocity has actually reversed directions as the system changes from diffusion dominated to growth dominated. We observe that species 2 is able to make territory gains initially due to its high diffusion rate, even though the competition rate is unaltered. However, as time goes on, the growth and competition characteristics become increasingly important. We see species 1 becoming more dominant over time so that the interface velocity actually reverses direction.

Figure 6.8 shows the evolution of the system up to $t = 11$ and Figure 6.9 shows the movement of the interface with the direction reversal.

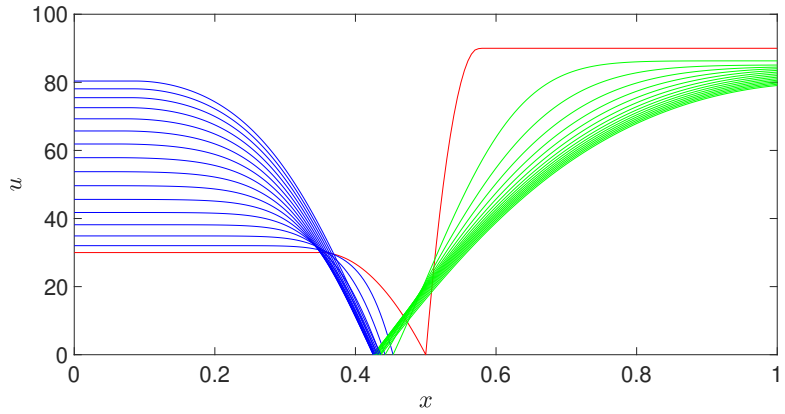

Figure 6.7: Result of competition model up to $t = 1.5$, considering the effect of an increased diffusion rate for species 2. Here we use $\delta_1 = 0.01, \delta_2 = 0.05$, $K_1 = K_2 = 100$, $r_1 = r_2 = 1$ and $\mu = 3$. We run the model with a time step of 10^{-5} for 1.5×10^5 iterations and plot the results every 0.1. The figure shows the rapid territorial gains of species 2 over species 1 due to its high diffusion rate. The initial conditions are shown in red, with species 1 in blue and species 2 in green.

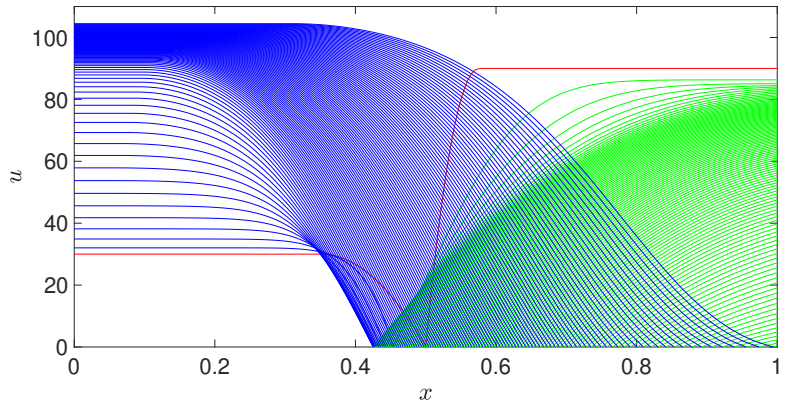

Figure 6.8: Result of competition model up to $t = 11$, considering the effect of an increased diffusion rate for species 2. Here we use $\delta_1 = 0.01, \delta_2 = 0.05$, $K_1 = K_2 = 100$, $r_1 = r_2 = 1$ and $\mu = 3$. We run the model with a time step of 10^{-5} for 1.1×10^5 iterations and plot the results every 0.1. We see that the initial diffusion-driven gains by species 2 are reversed and that the overall growth characteristics are dominating so that species 1 is gaining territory. The initial conditions are shown in red, with species 1 in blue and species 2 in green.

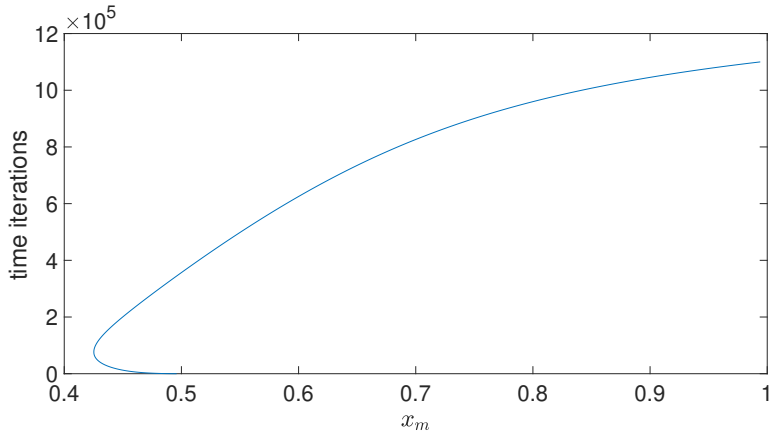

Figure 6.9: Position of the interface, x_m, showing interface movement for the competition model at up to $t = 11$, considering the effect of an increased diffusion rate for species 2. Here we use $\delta_1 = 0.01, \delta_2 = 0.05$, $K_1 = K_2 = 100$, $r_1 = r_2 = 1$ and $\mu = 3$. We run the model with a time step of 10^{-5} for 1.1×10^5 iterations. Here the interface velocity has actually reversed direction.

6.5 Discussion

In this chapter, we constructed a moving mesh finite difference method based on conservation for the Lotka-Volterra competition system with a high competition limit, such that the species are completely spatially segregated at an interface. The system of equations produced interesting behaviour. We were able to implement the model with a wide variety of parameter combinations and observed various effects dominating in turn as the populations evolve through time.

The illustrations presented above give confidence that the model and the moving mesh finite difference approach are likely to be able to satisfy the requirements of modelling a wide variety of competition systems and is numerically stable to a large choice of set-up parameters and are able to produce complex behaviours without problems.

For a set of parameters that favour species 1, we see an increasing interface velocity in the initial stages followed by a change in direction and a long steady phase where the interface velocity is approximately constant. Although the population of species 2 initially makes territorial gains it is eventually wiped out by the competition with species 1. As the annihilation of species 2 is approached, the interface velocity increases again. This is due to the low population of species 2 affecting its ability to compete with species 1.

If the growth of species 1 is restricted by lowering its carrying capacity, interestingly, we observe that neither species is dominant, even though all the competition and diffusion characteristics are unchanged. Therefore, density dependence can affect the competitive ability of a species.

In the case of increasing the diffusion rate for species 2, this species is able to make initial territorial gains, even though the competition rate is unaltered. However, as time goes on, growth and competition characteristics become increasingly important and species 1 becomes more dominant, so the interface velocity reverses direction.

A natural extension is to two dimensions along the lines described in [67], a first attempt appearing in reference [178] which foundered only on stability issues. In further work it would be interesting to compare the behaviour of the model against an empirical data set. The model lends itself to alterations to the logistic terms and changes to parameters without the need for any further development. The aim should be to understand the requirements from both a mathematical and quantitative perspective.

6.6 Summary

In this chapter, we illustrated a detailed application of the moving mesh finite difference method on a system of highly competitive species. The simulations were produced by choosing a range of different set-up parameters chosen to demonstrate some of the interesting behaviour that this model can explain. We explored the nature of the solution for various parameter values in relation to each other by varying one parameter value at a time. We found that the model is stable and robust. Even using the simplest Euler integration scheme, we observed no oscillations affecting the smoothness of results though a very small time step value was required.

The application of the moving mesh method based on conservation on systems such as the one presented in this chapter is quite straightforward as the equations are not coupled and each species occupies a distinct part of the domain. The application of the method gets more complicated when the system consists of coupled equations where species have overlapping domains. In such cases, the standard application of the method would involve the interpolation of the two meshes (of each population/species) at each time step in order to approximate the coupled terms, resulting in a very messy scheme.

In the following chapter, we present a new approach to approximating coupled systems using the moving mesh method which avoids the need of interpolation

as the entire system is solved on a single mesh.

Chapter 7

A Numerical Method for Multi-species Populations in a Moving Domain using Combined Masses

Motivated by the study of the highly competitive spatially segregated species of Chapter 6 we consider here a system of two coupled equations where species are still competing for common resources but coexist in space. We consider a new feature of the moving mesh method based on conservation for approximating coupled equations. This new approach considers the combined masses of the populations and the two species equations are solved on a single mesh. The combined mass process will form the substance of our study in the following chapters of the thesis where we aim to demonstrate its application on various coupled species systems including multi-species systems (consisting of more than two species).

This chapter, excluding Section 7.5 for the extension to the radially symmetric case and the Summary Section 7.7, is strongly based on the paper: Baines, M.J.; Christou, K. A Numerical Method for Multispecies Populations in a Moving Domain Using Combined Masses. Mathematics 2022, 10, 1124. The published paper can be found at https://doi.org/10.3390/math10071124.

7.1 Chapter Overview

This chapter concerns the numerical evolution of two interacting species satisfying coupled reaction-diffusion equations in one dimension which inhabit the same part of a moving domain. The domain has both moving external boundaries and moving interior interfaces where species may arise, overlap, or disappear. Numerically, a moving finite difference method is used in which node movement is generated by local mass preservation which includes a general combined mass strategy for species occupying overlapping domains. The method is illustrated by a test case on a one-dimensional domain in which a range of parameters is explored while we also extend our study to the two-dimensional radial case.

7.2 Introduction

Many simulation problems over a vast range of different sectors including physics, finance, biology and many more, can be described by partial differential equation models that exhibit a priori unknown sets such as interfaces, moving boundaries, shocks etc.

Moving or free boundary problems have emerged in increasing numbers over recent years, especially in ecology, for modelling species interactions and generally for gaining insights into population dynamics. Many theoretical results for general models in ecology including competition diffusion models are found in [94, 119, 171, 81, 66, 172] and references cited therein. While the theoretical analysis of free boundary problems in ecology is well represented in the literature there are fewer studies on the implementation of numerical methods for solving such problems, partly due to the presence of moving boundaries.

The approximate solution of free and moving boundary problems is challenging since a higher resolution is usually required in the vicinity of boundaries where a change in the slope of the solution is located, often occupying a central position within the domain.

In reference [110], the authors have used both front tracking and front fixing approaches to numerically solve competition-diffusion models with two free boundaries. The approach involves the use of a fixed grid to locate the position of the moving boundaries, which are then tracked explicitly. However, for solutions possessing sharp spatial transitions that move, such as free or moving boundaries, a fixed mesh method is generally considered inefficient since the very small spatial step required for the resolution of the boundary leads to an extremely small time step due to the stiffness of the system.

Over the years adaptive grid methods have been used successfully to solve free and moving boundary problems. Such methods automatically adjust the size of the space step to better approximate critical regions of high spatial activity without the use of a large number of nodes. Here we focus on a particular adaptive mesh method which describes the dynamic movement of existing nodes continuously in time to track the features of interest, known as moving mesh methods. For further details on adaptive mesh methods see also Chapter 4.

In particular, the moving mesh method used in this chapter is the conservation method in which an integral is used to preserve a desired conserved quantity, e.g., mass, within each patch of elements, from which node velocities are constructed. A moving mesh equation is extracted and solved in association with the PDE(s) [14, 9, 103].

More recently, the moving mesh finite difference method based on conservation of [103] was used in [11] (Chapter 6) for solving the competition diffusion system of [75] in which species are spatially segregated due to high competition and interact only through a moving interface. The results in [11] (Chapter 6) gave confidence that the method is numerically stable and robust for a wide choice of parameter values.

Even though moving mesh methods have proved to be efficient and reliable, they can be challenging when the system being solved includes coupled PDEs and the solution variables occupy distinct but overlapping domains.

Motivated by the work in [11] (Chapter 6), we apply the moving mesh finite difference method based on conservation for the general case of the competition-diffusion system of [75] where coupled species can coexist in space but still compete for common resources.

7.2.1 The competition-diffusion system of cohabiting species with moving boundaries

In order to demonstrate the features of the numerical method we have chosen the one-dimensional classical Lotka-Volterra system

$$\frac{\partial u}{\partial t} = \delta_1 \frac{\partial^2 u}{\partial x^2} + f(u,v)u \qquad x \in \mathcal{R}_1(t), \quad t > 0 \tag{7.1}$$

$$\frac{\partial v}{\partial t} = \delta_2 \frac{\partial^2 v}{\partial x^2} + g(u,v)v \qquad x \in \mathcal{R}_2(t) \quad t > 0, \tag{7.2}$$

where $f(u,v) = r_1\left(1 - \frac{u+k_1 v}{K_1}\right)$ and $g(u,v) = r_2\left(1 - \frac{v+k_2 u}{K_2}\right)$. Here u and v are the densities of two competing species that move by diffusion in space, δ_p is the

diffusion rate, r_p is the intrinsic growth rate, K_p is the carrying capacity and k_p is the competition rate ($p = 1, 2$). All the parameters are positive constants. The domains $\mathcal{R}_1(t)$ and $\mathcal{R}_2(t)$ are occupied by species u and v respectively, and partly overlap (see Figure 7.1).

Boundary conditions
A zero Neumann boundary condition is imposed, i.e.,

$$\frac{\partial u}{\partial x} = 0 \quad t > 0, \quad x = 0$$

on u at the fixed left-hand boundary ($x = 0$) of the whole domain $\mathcal{R}_1(t) \cup \mathcal{R}_2(t)$, (see Figure 7.1), which implies that there is no migration across the left-hand boundary. In other words, the zero Neumann condition implies a zero net inward flux, say q, at the boundary $x = 0$.

Interface conditions
The dynamics of the two inner-moving boundaries $H(t)$ and $Z(t)$, from a continuity of net flux, are

$$\frac{\mathrm{d}H}{\mathrm{d}t} = -\frac{\delta_1}{k_1} \left(\frac{\partial u}{\partial x} \right) \Bigg|_{x=H} \tag{7.3}$$

and

$$\frac{\mathrm{d}Z}{\mathrm{d}t} = -\frac{\delta_2}{k_2} \left(\frac{\partial v}{\partial x} \right) \Bigg|_{x=Z} . \tag{7.4}$$

We impose $u(H(t), t) = 0$ and $v(Z(t), t) = 0$.

Free boundary condition
Lastly, the right-hand side boundary $S(t)$ of species 2 is taken to be a free boundary which is assigned the condition

$$\frac{\mathrm{d}S}{\mathrm{d}t} = -\frac{\delta_2}{\mu} \left(\frac{\partial v}{\partial x} \right) \Bigg|_{x=S} , \tag{7.5}$$

where μ is inversely proportional to the preferred population density at the spreading front. For the ecological background of free and moving boundary conditions refer to [33].

The difference between the model in [75] and this one is that here the species are only partly segregated initially with a region in the middle of the domain where species coexist, as shown in Figure 7.1.

By contrast, in [11] the application of the moving mesh method to the two-species problem is straightforward as there is no coupling between the equations. The non-linear reaction terms in each equation depend only on the local species and

not on that of the competitor. Moreover, each species occupies a separate part of the domain.

The aim of this chapter is to solve the above system of competitive species using a moving mesh finite difference method based on the conservation of mass and a known net inward flux $q(t)$ at $x = 0$.

The layout of the chapter is as follows. In Section 7.3.1 we recall the basics of the conservation method and state algorithms for solving mass and non-mass conserving problems using the moving mesh finite difference based on mass balance. In Section 7.3.2 we introduce a combined mass approach in which the competition-diffusion system (7.1) and (7.2) is solved on a single mesh, thus avoiding interpolation to approximate f and g at each time-step. The essential difference in the approach is the use of the combined mass in overlapped domains. Following the algorithm of Section 7.3.1 and the use of a combined mass approach of 7.3.2 we provide a detailed solution for approximating the competition system (7.1) and (7.2). Section 7.4 provides illustrations for a variety of parameter combinations and in 7.5 we show that the new feature of the moving mesh conservation method can be easily extended to approximate the two-dimensional radial case of the competitive system. Finally, Section 7.6 gives a brief discussion of the method, the results, and potential research directions.

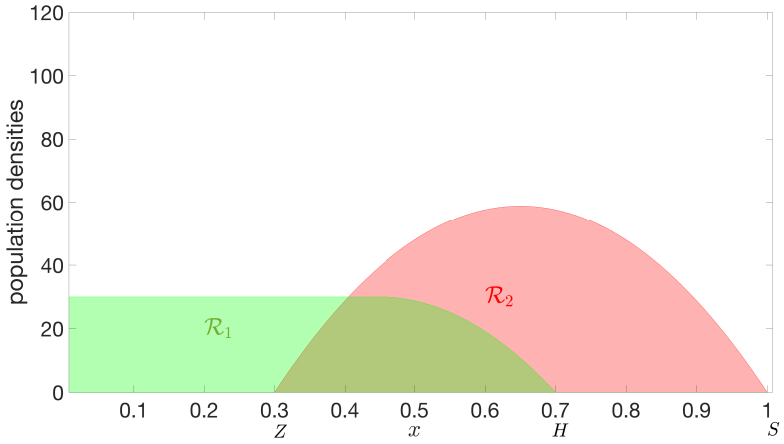

Figure 7.1: Initial conditions for the competition system, with population density u of species 1 in green and v of species 2 in red. The outer boundaries are $x = 0$ (fixed) and $x = S(t)$ (free) while the interfaces are at $x = Z(t)$ and $x = H(t)$.

7.3 Materials and Methods

7.3.1 A solution based on the conservation method

In what follows m refers to an interval and j or i refers to a node.
We introduce a time-dependent space coordinate $\tilde{x}(x,t)$, abbreviated to $\tilde{x}(t)$ at a specific x, which coincides instantaneously with the fixed coordinate x in the domain $(a(t), b(t))$. Let $\Delta\tilde{x}$ denote the interval between adjacent *moving* nodes. We follow an interval $\Delta\tilde{x}_m$ possessing a density $u_m(\tilde{x},t)$. The mass in the interval is approximated by

$$\theta_m(t) = u_m(t)\Delta\tilde{x}_m, \tag{7.6}$$

and the total mass in the moving domain $(a(t), b(t))$ is

$$\theta(t) = \sum_m u_m(t)\Delta\tilde{x}_m, \tag{7.7}$$

say.

By mass balance the rate of change of the mass $\theta_m(t)$ in the interval m is given by the inward flux $q(\tilde{x},t)$ through the interval boundaries together with the flux due to movement, i.e.,

$$[q(\tilde{x},t)]_m + [u(\tilde{x},t)w(\tilde{x},t)]_m,$$

where the notation $[\cdot]_m$ denotes the jump in the argument across the interval m. Since $w(\tilde{x},t) = \Delta\tilde{x}/\Delta t$ to first order in Δt it follows from mass balance that

$$\frac{\mathrm{d}}{\mathrm{d}t}(u_m\Delta\tilde{x}_m) = -[q(\tilde{x},t) + u(\tilde{x},t)w(\tilde{x},t)]_m, \tag{7.8}$$

where $[w(\tilde{x},t)]_m$ denotes a velocity associated with the interval m, i.e., the velocities at the boundaries of the interval m.
The flux $q(\tilde{x},t)$ is the mass increment within the interval m due to the inward/outward fluxes and the source/sink terms, as provided by the problem.
The overall rate of change of mass in the moving domain $(a(t), b(t))$ is

$$\frac{\mathrm{d}}{\mathrm{d}t}\sum_m u_m\Delta\tilde{x}_m = -[q(\tilde{x},t) + u(\tilde{x},t)w(\tilde{x},t)]_{a(t)}^{b(t)},$$

where $q(\tilde{x},t) = \int_{a(t)}^{b(t)} \frac{\partial u}{\partial t}\mathrm{d}x$ and $[u(\tilde{x},t)w(\tilde{x},t)]_{a(t)}^{b(t)}$ is the flux jump across the boundaries of the moving domain.

A method based on preservation of relative masses

The conservation of mass fractions (CMF) method for those problems that conserve the total mass of the solution, i.e., for which $\theta(t)$ remains constant for all $t \geq t^0$, is based on the preservation of partial masses by supposing that $\tilde{x}$ moves in such a way that the mass in any interval is independent of time, i.e.,

$$u_m(t)\Delta\tilde{x}_m(t) = c_m \tag{7.9}$$

is constant in time.
Then both sides of (7.8) are zero and the nodal velocities may be constructed from the zero right-hand side. New $\tilde{x}$ positions are determined by a time integration scheme using the evaluated nodal velocities and the new $u(\tilde{x}, t + \Delta t)$ is obtained by equation (7.6) using the new node locations.

For more general problems that do not conserve mass such as the one in Section 7.2.1, the total mass $\theta(t)$ varies with time. Therefore, it is inconsistent to suppose that the mass (7.6) in each interval is constant in time. However, the relative density, defined as $u(\tilde{x}, t)/\theta(t)$, has a total relative mass

$$\int_{a(t)}^{b(t)} \frac{u(\tilde{x}, t)}{\theta(t)} \, \mathrm{d}x$$

which equals unity. It is therefore consistent to suppose that the local relative mass,

$$\int_m \frac{u(\tilde{x}, t)}{\theta(t)} \, \mathrm{d}x \tag{7.10}$$

in a cell m is conserved in time. The conservation of the relative mass in each subinterval can therefore be used to generate fluxes and velocities to move the nodes. The approach requires the total mass to be given as part of the problem.

The relative CMF method can be described as follows. Define a relative density

$$\widehat{u}_m = \frac{u_m}{\theta(t)}, \tag{7.11}$$

where $\theta(t)$ is the current total mass. Then by (7.10) the relative mass in cell m can be written

$$\int_m \widehat{u}_m(x, t) \, \mathrm{d}x = \gamma_m, \tag{7.12}$$

say, constant in time. Summing γ_m over m gives 1. Also, by conservation of the relative mass (*cf.* 7.9), the relative flux jump across cell m is

$$[\widehat{q} + \widehat{u}\widehat{w}]_m = 0, \tag{7.13}$$

where $\widehat{q}$ is a modified flux. Summing (7.13) over all intervals m, leads to $[\widehat{q} + \widehat{u}\widehat{w}]_a^b = 0$. If the argument vanishes at one end of the domain, then $\widehat{q} + \widehat{w}\widehat{u}$ is zero at all nodes and

$$\widehat{w} = -\frac{\widehat{q}}{\widehat{u}}$$

is the relative velocity (provided that $\widehat{u} \neq 0$).
The CMF equations for a mass-conserving problem consist of the local conservation of mass equation (7.12) together with the flux balance equation (7.13). We remark here that equations (7.12) and (7.13) are equivalent to the Lagrangian and Eulerian conservation laws respectively which are coincident for small times. We relate $\widehat{q}$ to the static $\partial u/\partial t$ which is known from the statement of the problem in Section 7.2.1. Differentiating (7.12) and using the Leibniz integral rule for the relative mass,

$$\frac{\mathrm{d}}{\mathrm{d}t}\int_m \widehat{u}(x,t)\ \mathrm{d}x = 0 = \int_m \frac{\partial \widehat{u}}{\partial t}\mathrm{d}x + [\widehat{u}\widehat{w}]_m.$$

By the relative mass balance equation (7.13),

$$0 = [\widehat{q}]_m + [\widehat{u}\widehat{w}]_m \tag{7.14}$$

yielding

$$[\widehat{q}]_m = \int_m \frac{\partial \widehat{u}}{\partial t}\,\mathrm{d}x. \tag{7.15}$$

Hence if u, θ (therefore $\widehat{u}$) are known, $[\widehat{q}]$ can be determined from $\frac{\partial u}{\partial t}$. Since by (7.11)

$$\frac{\partial \widehat{u}}{\partial t} = \frac{\partial}{\partial t}\Big(\frac{u}{\theta}\Big) = \frac{1}{\theta}\frac{\partial u}{\partial t} - \frac{\dot{\theta}}{\theta^2}u,$$

where $\dot{\theta} = d\theta/dt$, then from (7.15)

$$[\widehat{q}]_m = \frac{1}{\theta}\int_m \frac{\partial u}{\partial t}\,\mathrm{d}x - \frac{\dot{\theta}}{\theta^2}\int_m u(x,t)\ \mathrm{d}x$$

and by (7.12)

$$[\widehat{q}]_m = \frac{1}{\theta}\Big(\int_m \frac{\partial u}{\partial t}\,\mathrm{d}x - \dot{\theta}\gamma_m\Big), \tag{7.16}$$

where $\partial u/\partial t$ is known from the statement of the problem and the time-independent γ_m are given by (7.12), leading to

$$[\widehat{u}\widehat{w}]_m = -\frac{1}{\theta}\Big(\int_m \frac{\partial u}{\partial t}\,\mathrm{d}x - \gamma_m\dot{\theta}\Big) \tag{7.17}$$

by equation (7.14). If m denotes the interval between two successive nodes, e.g. (x_i, x_{i+1}), the left-hand side of (7.17) can be written $(\widehat{u}\widehat{w})_{i+1} - (\widehat{u}\widehat{w})_i$. For a unique solution of $\widehat{u}\widehat{w}$, the flux $[\widehat{u}\widehat{w}]$ must be imposed at one point which may be thought of as an 'anchor' point. A common choice of an anchor point is at the boundary of the region, such as x_0^n, where the value $\widehat{u}\widehat{w}$ is known. Summing from a fixed point at node x_0 to $\tilde{x}_i$ gives

$$(uw)_i - (uw)_0 = -\Big(\int_m \frac{\partial u}{\partial t}\, \mathrm{d}x - \Gamma_i \dot{\theta} \Big) \tag{7.18}$$

since $[\widehat{u}\widehat{w}]_m \theta = [uw]_m$, where $\Gamma_i = \sum_{j=0}^{i} \gamma_j$.
The rate of change $\dot{\theta}(t)$ of the total mass $\theta(t)$ can be evaluated using the original PDE. By mass balance, the rate of change of the total mass equals the flux $q(\tilde{x}, t)$ (inward/outward fluxes and reaction terms) plus the flux due to motion, i.e.,

$$\frac{\mathrm{d}\theta}{\mathrm{d}t} = \int_{a(t)}^{b(t)} \frac{\partial u}{\partial t}\, \mathrm{d}x + [uw]_{a(t)}^{b(t)}, \tag{7.19}$$

where $[uw]_{a(t)}^{b(t)}$ in (7.19) is given by the boundary conditions of the problem.
Example
As an example related to the equations (7.1) and (7.2), consider u such that

$$\frac{\partial u}{\partial t} = \delta \frac{\partial^2 u}{\partial x^2} + s(x, t), \tag{7.20}$$

where δ is the diffusion coefficient and $s(x, t)$ denotes the source terms.
Substituting equation (7.20) into equations (7.18) and (7.19), we can calculate $\hat{w}_m$ and $\frac{\partial \theta}{\partial t}$ by integration of the diffusion term, together with the boundary conditions.
The equation for $\frac{d\theta}{dt}$ using (7.19) and (7.20) is

$$\frac{\mathrm{d}\theta}{\mathrm{d}t} = \int_{a(t)}^{b(t)} \Big(\delta \frac{\partial^2 u}{\partial x^2} + s \Big)\, \mathrm{d}x + [uw]_{a(t)}^{b(t)} = \int_{a(t)}^{b(t)} s\, \mathrm{d}x + \left[\delta \frac{\partial u}{\partial x} + uw \right]_{a(t)}^{b(t)} \tag{7.21}$$

and the equation for the velocity w_i of a node x_i is given from (7.18) and (7.20) as

$$w_i = \frac{1}{u_i} \left(\Gamma_i \dot{\theta} - \int_m \Big(\delta \frac{\partial^2 u}{\partial x^2} + s \Big)\, \mathrm{d}x + uw|_0 \right) \quad = \frac{1}{u_i} \left(\Gamma_i \dot{\theta} - \int_m s\, \mathrm{d}x - \delta \left[\frac{\partial u}{\partial x} \right]_m \right), \tag{7.22}$$

where the anchor point is taken to be the fixed node x_0 (i.e., $w_0 = 0$), m is the interval (x_0, x_i) and Γ_i denotes the summation of all the γ_m from $m = 0$ to i.

Note that $\dot{\theta}$ is known from (7.21).
The example ends here.
Once the velocity w has been found it can be integrated to move the nodes

$$\frac{\mathrm{d}\tilde{x}}{\mathrm{d}t} = w,$$

while the new total mass is found by integrating

$$\frac{\mathrm{d}\theta}{\mathrm{d}t} = Q, \tag{7.23}$$

where Q is the known rate of increase of mass.
Finally, having the new positions of $\tilde{x}$ and the new θ we can use equations (7.11) and (7.12) to update $u(\tilde{x}, t)$ from,

$$\int_m u_m(\tilde{x}, t)\ \mathrm{d}x = \gamma_m \theta(t) \tag{7.24}$$

where m denotes an interval. A first-order-in-time finite-difference algorithm based on this theory is as follows.

Finite difference method

Given a time-step $\Delta t > 0$ and a fixed number N of spatial nodes, choose discrete times $t^n = n\Delta t, (n = 0, 1, \dots)$ and discretise the domain at each time using the nodes $\tilde{x}_i^n = \tilde{x}(x_i, t^n)$, $i = 0, 1, \dots, N+1$, for which $a(t^n) = x_0^n < x_1^n < \dots < x_{N+1}^n = b(t^n)$. Let m denote the intervals between the nodes, i.e., $m = 1, \dots, N+1$ (see Figure 7.2). Also define the approximations at the nodes $u_i^n \approx u(\tilde{x}, t^n)$, $w_i^n \approx w(\tilde{x}, t^n)$, $\theta^n \approx \theta(t^n)$ and $\dot{\theta}^n \approx \dot{\theta}(t^n)$. Having defined the notation, we proceed to the initial conditions required for the approximate solution.

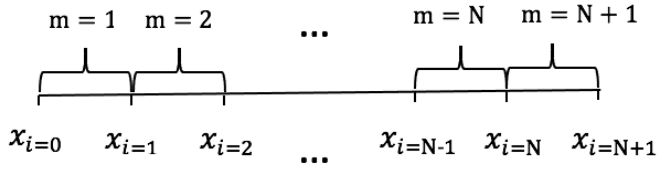

Figure 7.2: Domain discretisation.

Time-stepping

Time-stepping x_i
A first-order-in-time explicit time-stepping scheme for $\tilde{x}_i^{n+1}$ is

$$\tilde{x}_i^{n+1} = \tilde{x}_i^n + \Delta t\, w_i^n. \tag{7.25}$$

Another first-order-in-time explicit time-stepping scheme for (7.23) that preserves the sign of $\Delta\tilde{x}_m$ (thus avoiding mesh tangling) for any positive Δt is, [12]

$$\Delta\tilde{x}_m^{n+1} = \Delta\tilde{x}_m^n \exp\Big(\Delta t \frac{\Delta w_m^n}{\Delta\tilde{x}_m^n}\Big) \tag{7.26}$$

which is equivalent to (7.25) to first order in Δt.
Then, given $\tilde{x}_i^{n+1}$ at one point, in this case taken to be the fixed node $\tilde{x}_0$, we update the location of the nodes using $\Delta\tilde{x}_i^{n+1}$ by

$$\tilde{x}_i^{n+1} = \tilde{x}_0 + \sum_{i=0}^{i} \Delta\tilde{x}_m^{n+1}, \quad i = m = 1, ..., N+1 \tag{7.27}$$

Time-stepping $\theta(t)$
In updating the total mass $\theta(t)$, it is important to ensure that θ^{n+1} will remain positive so that the condition $u > 0$ will not be violated. In the same manner as (7.26), the exponential time-integration scheme may be used to update θ, i.e.,

$$\theta^{n+1} = \theta^n \exp\Big(\Delta t \frac{\dot{\theta}^n}{\theta^n}\Big), \tag{7.28}$$

ensuring that $\theta^{n+1} > 0$. More details on the exponential time-stepping scheme for updating $\tilde{x}$ can be found in [12].

Initial conditions

Choose initial node positions $\tilde{x}_i^0, (i = 0, 1, .., N+1)$ with corresponding initial u_i^0. From the initial conditions derive Δx_i^0 and compute the initial value θ^0 of the total mass θ, given by the composite trapezoidal scheme applied to (7.7),

$$\theta^0 = \frac{1}{2}\sum_{i=0}^{N-1} \Big(\tilde{x}_{i+1}^0 - \tilde{x}_i^0\Big)(u_i^0 + u_{i+1}^0). \tag{7.29}$$

Given θ^0 we can compute the approximate relative masses γ_m of (7.12) by a first-order-in-space shift to the end of the interval, i.e.,

$$\gamma_m = \frac{1}{\theta^0}(\tilde{x}_i^0 - \tilde{x}_{i-1}^0)u_i^0, \quad (i = m = 1, \ldots, N+1). \tag{7.30}$$

Then at time t^n for $n = 1, 2, \ldots$, given θ^n, $\tilde{x}_i^n$ and u_i^n we calculate θ^{n+1}, $\tilde{x}_i^{n+1}$ and u_i^{n+1} as follows:

Algorithm

At each time step n,

1. Evaluate the rate of change of the total mass $\dot{\theta}^n$ by discretising (7.19) as the boundary influx, source terms and flux due to motion as

$$\left(\frac{\mathrm{d}\theta}{\mathrm{d}t}\right)^n = \int_{\tilde{x}_0^n}^{\tilde{x}_N^n} \frac{\partial u(x,t^n)}{\partial t}\,\mathrm{d}x + w_{\tilde{x}_N}^n u_{\tilde{x}_N}^n - w_{\tilde{x}_0}^n u_{\tilde{x}_0}^n.$$

   The integral is calculated from the governing PDE where the derivative terms are evaluated by one-sided approximation and the integration of the reaction terms by the trapezoidal rule.

2. Evaluate the discrete velocity at interior points from (7.18), specifying an anchor point, say x_0, so that the equations for the velocity are given by

$$w_i^n = \frac{u_0^n w_0^n - \int_{\tilde{x}_0^n}^{\tilde{x}_i^n} \frac{\partial u(s,t^n)}{\partial t}\,\mathrm{d}x + \Gamma_i \dot{\theta}}{u_i^n}, \quad (i = 1, \ldots, N+1), \tag{7.31}$$

   where $\Gamma_i = \sum_{j=0}^{i} \gamma_j$.
   At the boundaries extrapolate the velocity from interior values. Derive Δw_m^n for all intervals.

3. Update the new $\Delta \tilde{x}_m^{n+1}$ using the exponential time-stepping scheme (7.26).

4. Update θ^{n+1} by the exponential time-stepping scheme (7.28).

5. Recover the solution u_m^{n+1} at the interior points from (7.24) in the form

$$u_m^{n+1} = \frac{\gamma_m \theta^{n+1}}{\Delta \tilde{x}_m^{n+1}}, \quad (m = 1, \ldots, N+1) \tag{7.32}$$

   and determine u_i^{n+1} $(i = 1, \ldots, N)$ by one-sided approximation with u_0^{n+1} and u_N^{n+1} being updated either from given boundary conditions or by extrapolation, depending on the nature of the problem.

We now apply the theory and methodology of the moving mesh based on mass conservation given by the algorithm above to approximate the competition-diffusion system studied in this chapter. We also introduce a new feature of the conservation method which considers the combined mass of the species.

7.3.2 Numerical solution for a competition-diffusion system with two interfaces and a moving boundary

We divide the domain into three regions separated by the two interfaces ($Z(t)$ and $H(t)$) as shown in Figure 7.3. Denote by $\mathcal{R}_L$ the region on the left-hand-side

of the moving boundary $Z(t)$, and by $\mathcal{R}_R$ the region on the right-hand-side of the moving boundary $H(t)$. The region in the middle bounded by both moving boundaries $Z(t)$ and $H(t)$ is denoted by $\mathcal{R}_M$. Note that $v(t) = 0$ in $\mathcal{R}_L(t)$ and $u(t) = 0$ in $\mathcal{R}_R(t)$.

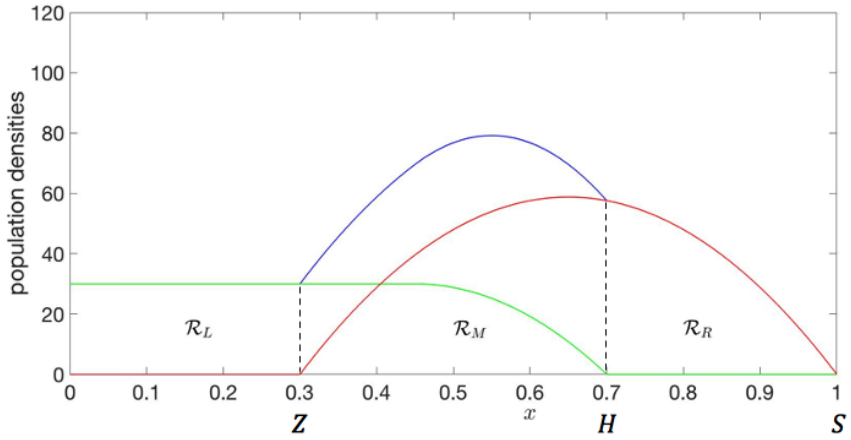

Figure 7.3: Initial conditions for the competition system, with population density u of species 1 in green and v of species 2 in red. The blue shows the initial combined population density $(u+v)$. The outer boundaries are $x = 0$ (fixed) and $x = S(t)$ (free) while the interfaces are at $x = Z(t)$ (green/blue) and $x = H(t)$ (blue/red). The two interfaces are indicated by dotted lines and separate the domain into the three regions $\mathcal{R}_L, \mathcal{R}_M$ and $\mathcal{R}_R$.

As discussed above, we are considering the mass at a specific location to be the combined mass of the densities u and v. In the conservation method, the nodal velocities are constructed by supposing that fractions of the corresponding relative mass are held constant in time.
For ease of exposition, we drop the *tilde* (˜) for the rest of the chapter.

At time level $t = t^n$ define time-dependent mesh points

$$0 = x_0 < x_1^n < \ldots < x_\zeta^n < \ldots < x_\eta^n < \ldots < x_{N+1}^n = x_\sigma^n,$$

where x_ζ^n is the node at the moving interface $Z(t)$, x_η^n is the node at the moving interface $H(t)$. Let u_i^n and v_i^n $(0 \le i \le N+1)$, approximate $u(x,t)$ and $v(x,t)$ by u_i^n and v_i^n respectively at these points.

For the initial conditions (at $n = 0$) we take the x_i^0 to be equally spaced and the u_i^0 and v_i^0 pointwise from an initial function

$$
\begin{aligned}
u(x,0) &= 30, && (0 \le x \le 0.46)\\
u(x,0) &= 480(x-0.2)(0.7-x), && (0.46 \le x \le 0.7)\\
u(x,0) &= 0, && (0.7 \le x \le 1)\\
v(x,0) &= 0, && (0 \le x \le 0.3)\\
v(x,0) &= 480(x-1)(0.3-x), && (0.3 \le x \le 1)
\end{aligned}
$$

as shown in Figure 7.3.
The initial values θ_L^0, θ_M^0 and θ_R^0 of the total masses θ in the intervals $\mathcal{R}_L, \mathcal{R}_M, \mathcal{R}_R$ respectively, of (7.29) are estimated by the composite trapezium rule. We also use the approximations $\theta_L^n \approx \theta_L(t^n)$, $\theta_M^n \approx \theta_M(t^n)$ and $\theta_R^n \approx \theta_R(t^n)$ for the total masses in each region at forward times. The constant-in-time relative masses $\gamma_{L,i}$, $\gamma_{M,i}$ and $\gamma_{R,i}$ in the interval (x_{i-1}^n, x_i^n) from (7.30). Then, at each time step, we proceed with the following calculations as indicated by the algorithm in section 7.3.1.

Having defined the initial conditions of u and v and the initial nodal positions we proceed by calculating the mesh velocity. We first evaluate the velocities at the moving boundaries from the boundary conditions given in the problem.

7.3.3 Velocities at the moving boundaries

In order to evaluate the nodal velocities at the moving interfaces and the outer boundary, we apply one-sided approximation to the derivative terms of equations (7.3), (7.4) and (7.5) for η, ζ and σ respectively,

$$\frac{\mathrm{d}\eta}{\mathrm{d}t} = -\frac{\delta_1}{k_1}\Big(\frac{u(\eta) - u(\eta^-)}{x(\eta) - x(\eta^-)}\Big), \tag{7.33}$$

where η^- is the node immediately to the left of η.

$$\frac{\mathrm{d}\zeta}{\mathrm{d}t} = -\frac{\delta_2}{k_2}\Big(\frac{v(\zeta^+) - v(\zeta)}{x(\zeta^+) - x(\zeta)}\Big), \tag{7.34}$$

where ζ^+ is the node immediately to the right of ζ.

$$\frac{\mathrm{d}\sigma}{\mathrm{d}t} = -\frac{\delta_2}{\mu}\Big(\frac{v(\sigma) - v(\sigma^-)}{x(\sigma) - x_(\sigma^-)}\Big) \tag{7.35}$$

where σ^- is the node immediately to the left of σ.

Given the boundary velocities, we then solve for the velocities of the inner nodes by setting the boundary nodes as the anchor points. The procedure is as follows.

7.3.4 Approximating the velocities and the rates of change of the total populations

From (7.31), by setting the anchor point x_0, the velocity w_i^n in region $\mathcal{R}_L$ satisfies,

$$w_i^n u_i^n = u_0^n w_0^n - \int_{x_0^n}^{x_i^n} \frac{\partial u(s,t^n)}{\partial t}\, \mathrm{d}x + \Gamma_{L,i}\dot{\theta}_L \quad (x_i \in \mathcal{R}_L),$$

where $\Gamma_{L,i} = \sum_{j=0}^{i} \gamma_{L,j}$ for $i = 1, \ldots \zeta - 1$.
By substituting the original PDE (7.1) and applying the boundary condition $w_0 = 0$, the equation for the node velocities in the region $\mathcal{R}_L$ is

$$w_i^n = \frac{1}{u_i^n}\left(\Gamma_{L,i}\dot{\theta}_L^n - \int_{x_0^n}^{x_i^n} \left(\delta_1 \frac{\partial^2 u}{\partial x^2} + r_1 u\Big(1 - \frac{u}{K_1}\Big)\right) \mathrm{d}x\right), \tag{7.36}$$

provided that $u_i^n \neq 0$, since $v = 0$ in $\mathcal{R}_L$.
Performing the integration and the Neumann boundary condition at x_0 the equation (7.36) becomes,

$$w_i^n = \frac{1}{u_i^n}\left(\Gamma_{L,i}\dot{\theta}_L^n - \delta_1 \left.\frac{\partial u}{\partial x}\right|_i - \Phi_i^n\right), \quad (1 \leq i \leq \zeta - 1), \tag{7.37}$$

where the derivative term is approximated by one-sided approximation as in section 2.8.1. Φ_i denotes the integral of the reaction terms of equation (7.1) approximated by the composite trapezium rule which has summation over $j = 0$ and i ($i = 1, \ldots, \zeta - 1$). In order to evaluate w_i^n in (7.37) we require $\dot{\theta}_L^n$.
By setting $x_i^n = x_\zeta^n$ in (7.36), due to the boundary conditions and the known velocity at the moving boundary x_ζ^n, we can obtain an equation for $\dot{\theta}^n$ in the region $\mathcal{R}_L$, i.e.,

$$\dot{\theta}_L^n = \delta_1 \left.\frac{\partial u}{\partial x}\right|_\zeta + \Phi^n + uw|_\zeta \tag{7.38}$$

since summing $\gamma_{L,j}$ over $j = 0$ to ζ gives 1. The summation of the composite trapezoidal rule approximation Φ^n is over $j = 0$ and $i = \zeta$.

Similarly, from (7.31) by taking the anchor point to be x_ζ^n, the velocity w^n in region $\mathcal{R}_M$ for the combined masses of u and v satisfies

$$w_i^n(u_i^n + v_i^n) = (u_\zeta^n + v_\zeta^n)w_\zeta^n - \int_{x_\zeta^n}^{x_i^n} \left(\frac{\partial u(s,t^n)}{\partial t} + \frac{\partial v(s,t^n)}{\partial t}\right) \mathrm{d}x + \Gamma_{M,i}\dot{\theta}_M, \quad (x_i \in \mathcal{R}_M),$$

where $\Gamma_{M,i} = \sum_{j=\zeta}^{i} \gamma_{M,j}$ for $i = \zeta + 1, \ldots \eta - 1$.
By substituting the original PDEs (7.1) and (7.2) and applying the boundary conditions, the equation for the node velocities in the region $\mathcal{R}_M$ is

$$w_i^n = \frac{1}{(u_i^n + v_i^n)} \Bigg(\Gamma_{M,i} \dot{\theta}_M^n$$

$$- \int_{x_\zeta^n}^{x_i^n} \left(\delta_1 \frac{\partial^2 u}{\partial x^2} + \delta_2 \frac{\partial^2 v}{\partial x^2} + r_1 u \Big(1 - \frac{u + k_1 v}{K_1} \Big) + r_2 v \Big(1 - \frac{v + k_2 u}{K_2} \Big) \right) \mathrm{d}x + (u+v) w|_\zeta \Bigg), \tag{7.39}$$

provided that $u_i^n + v_i^n \neq 0$.
Performing the integration, equation (7.39) becomes,

$$\begin{aligned} w_i^n = & \frac{1}{(u_i^n + v_i^n)} \Bigg(\Gamma_{M,i} \dot{\theta}_M^n - \delta_1 \left. \frac{\partial u}{\partial x} \right|_\zeta^i - \delta_2 \left. \frac{\partial v}{\partial x} \right|_\zeta^i \\ & - \Psi_i^n - \Upsilon_i^n + (u+v) w|_\zeta \Bigg), \quad (\zeta + 1 \leq i \leq \eta - 1), \end{aligned} \tag{7.40}$$

where Ψ_i^n and Υ_i^n denote the composite trapezoidal rule approximations for the reaction terms of (7.1) and (7.2) respectively with summation from $j = \zeta$ to i $(i = \zeta + 1, \ldots, \eta - 1)$.
By setting $i = \eta$ and since summing $\gamma_{M,j}$ over $j = \zeta$ to η gives 1, the equation for $\dot{\theta}^n$ in region $\mathcal{R}_M$ is given by

$$\dot{\theta}_M^n = \delta_1 \left. \frac{\partial u}{\partial x} \right|_\zeta^\eta + \delta_2 \left. \frac{\partial v}{\partial x} \right|_\zeta^\eta + \Psi^n + \Upsilon^n + (u+v) w|_\zeta^\eta. \tag{7.41}$$

Here the composite trapezoidal rule approximations Ψ^n and Υ^n with summation from $j = \zeta$ to $i = \eta$.
Finally from (7.31) by taking the anchor point x_η^n, the velocity w^n in region $\mathcal{R}_R$ where only v exists is given by

$$w_i^n v_i^n = v_\eta^n w_\eta^n - \int_{x_\eta^n}^{x_i^n} \frac{\partial v(s, t^n)}{\partial t} \, \mathrm{d}x + \Gamma_{R,i} \dot{\theta}_R, \quad (x_i \in \mathcal{R}_R),$$

where $\Gamma_{R,i} = \sum_{j=\eta}^{i} \gamma_{R,j}$ for $i = \eta + 1, \ldots \sigma - 1$.
By substituting the original PDE (7.2), the equation for the node velocities in the region $\mathcal{R}_R$ is

$$w_i^n = \frac{1}{v_i^n} \left(\Gamma_{R,i} \dot{\theta}_R^n - \int_{x_\eta^n}^{x_i^n} \left(\delta_2 \frac{\partial^2 v}{\partial x^2} + r_2 v \Big(1 - \frac{v}{K_2} \Big) \right) \mathrm{d}x + v w|_\eta \right) \tag{7.42}$$

since $u = 0$ in $\mathcal{R}_R$, provided that $v_i^n \neq 0$.
Performing the integration, equation (7.42) becomes,

$$w_i^n = \frac{1}{v_i^n}\left(\Gamma_{R,i}\dot{\theta}_R^n - \delta_2 \left.\frac{\partial v}{\partial x}\right|_\eta^i - \Xi_i^n + vw|_\eta\right), \quad (\eta + 1 \leq i \leq \sigma - 1). \tag{7.43}$$

Ξ_i^n is the composite trapezoidal rule approximation of the reaction terms of equation (7.2) with summation from $j = \eta$ to i $(i = \eta + 1, \ldots \sigma - 1)$.
The equation for $\dot{\theta}^n$ in region $\mathcal{R}_R$ is obtain from equation (7.42) by setting $i = \sigma$, i.e.,

$$\dot{\theta}_R^n = \delta_2 \left.\frac{\partial v}{\partial x}\right|_\eta^\sigma + \Xi^n + vw|_\sigma - vw|_\eta, \tag{7.44}$$

where the composite trapezoidal rule approximation Ξ^n with summation from $j = \eta$ to $i = \sigma$.
Having found the velocities for all the nodes in the domain we update the nodal positions.

7.3.5 Time-stepping

As discussed in Section 7.3.1, a first-order exponential scheme is used to update both the node positions of x_i^{n+1}, i.e.,

$$\Delta x_i^{n+1} = \Delta x_i^n \exp\left(\Delta t \frac{\Delta w_i^n}{\Delta x_i^n}\right). \tag{7.45}$$

Although the above exponential time stepping scheme is a first-order scheme as the explicit Euler scheme, it ensures a positive value of Δx_i^{n+1} and hence avoids node tangling.
In a similar manner, the new θ^{n+1} is updated by

$$\theta^{n+1} = \theta^n \exp\left(\Delta t \frac{\dot{\theta}^n}{\theta^n}\right). \tag{7.46}$$

7.3.6 The population densities

Having found the new positions of the nodes, all that is left now is to determine the approximate population densities u and v at the moved nodes at the new time $t = t^{n+1}$.

Once the x_i^{n+1} have been found, we find an approximation solution for the population densities u^{n+1} and v^{n+1}. Instead of using the conservation principle as

follows by the algorithm in 7.3.1, equation (7.32), we use the mass balance equations for the u and v local masses to update u and v individually throughout the domain. The rate of change of the mass equals the augmented flux (i.e., inward/outward flux and the flux due to motion) and the reaction terms. Thus, using the velocities and the updated x-positions found above, we can update u and v individually throughout the domain using the Leibniz integral rule or the Arbitrary Lagrangian equation [52] in the following form

$$\frac{\mathrm{d}}{\mathrm{d}t}\int_{x_{i-1}}^{x_i} u \,\mathrm{d}x = \int_{x_{i-1}}^{x_i} \frac{\partial u}{\partial t}\,\mathrm{d}x + \int_{x_{i-1}}^{x_i} \frac{\partial}{\partial x}(uw)\,\mathrm{d}x, \quad (i = 1, \ldots, \eta - 1) \tag{7.47}$$

$$\frac{\mathrm{d}}{\mathrm{d}t}\int_{x_i}^{x_{i+1}} v \,\mathrm{d}x = \int_{x_i}^{x_{i+1}} \frac{\partial v}{\partial t}\,\mathrm{d}x + \int_{x_i}^{x_{i+1}} \frac{\partial}{\partial x}(vw)\,\mathrm{d}x, \quad (i = \zeta + 1, \ldots, N). \tag{7.48}$$

Note that $u_i = 0$ for $i = \eta, .., N + 1$ and $v_i = 0$ for $i = 0, \ldots, \zeta$.
In detail, substituting equations (7.1) and (7.2) into the right hand sides of (7.47) and (7.48) gives,

$$\begin{aligned}\frac{\mathrm{d}}{\mathrm{d}t}\int_{x_{i-1}}^{x_i} u \,\mathrm{d}x = \int_{x_{i-1}}^{x_i} \delta_1\frac{\partial^2 u}{\partial x^2}\,\mathrm{d}x + \int_{x_{i-1}}^{x_i} r_1 u\Big(1 - \frac{u + k_1 v}{K_1}\Big)\,\mathrm{d}x \\ + \int_{x_{i-1}}^{x_i} \frac{\partial}{\partial x}(uw)\,\mathrm{d}x, \qquad (i = 1, \ldots, \eta - 1)\end{aligned}$$

$$\begin{aligned}\frac{\mathrm{d}}{\mathrm{d}t}\int_{x_i}^{x_{i+1}} v \,\mathrm{d}x = \int_{x_i}^{x_{i+1}} \delta_2\frac{\partial^2 v}{\partial x^2}\,\mathrm{d}x + \int_{x_i}^{x_{i+1}} r_2 v\Big(1 - \frac{v + k_2 u}{K_2}\Big)\,\mathrm{d}x \\ + \int_{x_i}^{x_{i+1}} \frac{\partial}{\partial x}(vw)\,\mathrm{d}x, \qquad (i = \zeta + 1, \ldots, N).\end{aligned}$$

Performing the integration on the right-hand side,

$$\begin{aligned}\frac{\mathrm{d}}{\mathrm{d}t}\int_{x_{i-1}}^{x_i} u \,\mathrm{d}x = \delta_1\frac{\partial u}{\partial x}\Big|_{i-1}^{i} + \int_{x_{i-1}}^{x_i} r_1 u\Big(1 - \frac{u + k_1 v}{K_1}\Big)\,\mathrm{d}x \\ + uw|_{i-1}^{i}, \qquad (i = 1, \ldots, \eta - 1)\end{aligned}$$

$$\begin{aligned}\frac{\mathrm{d}}{\mathrm{d}t}\int_{x_i}^{x_{i+1}} v \,\mathrm{d}x = \delta_2\frac{\partial v}{\partial x}\Big|_{i}^{i+1} + \int_{x_i}^{x_{i+1}} r_2 v\Big(1 - \frac{v + k_2 u}{K_2}\Big)\,\mathrm{d}x \\ + vw|_{i}^{i+1}, \qquad (i = \zeta + 1, \ldots, N).\end{aligned}$$

Now integrate in time,

$$u_i^{n+1} = \frac{1}{x_i^{n+1} - x_{i-1}^{n+1}} \Big(u_i^n (x_i^n - x_{i-1}^n) + \Delta t \Big(\delta_1 \frac{\partial u^n}{\partial x} \Big|_{i-1}^{i} + \int_{x_{i-1}^n}^{x_i^n} r_1 u^n \Big(1 - \frac{u^n + k_1 v^n}{K_1} \Big) \, \mathrm{d}x + u^n w^n |_{i-1}^{i} \Big) \Big), \quad (i = 1, \ldots, \eta - 1) \quad (7.49)$$

$$v_i^{n+1} = \frac{1}{x_{i+1}^{n+1} - x_i^{n+1}} \Big(v_i^n (x_{i+1}^n - x_i^n) + \Delta t \Big(\delta_2 \frac{\partial v^n}{\partial x} \Big|_{i}^{i+1} - \int_{x_i^n}^{x_{i+1}^n} r_2 v^n \Big(1 - \frac{v^n + k_2 u^n}{K_2} \Big) \, \mathrm{d}x + v^n w^n |_{i}^{i+1} \Big) \Big), \quad (i = \zeta + 1, \ldots, N). \quad (7.50)$$

Note that $v_{N+1}^n = 0$ and u_0^n can be found by (7.12) by a first-order-in-space shift to the end of the interval and since the relative masses γ_m are constant in time the value of u_0^n can be evaluated by

$$\frac{1}{\theta_L^0}(x_1^0 - x_0^0) u_0^0 = \frac{1}{\theta_L^n}(x_1^n - x_0^n) u_0^n. \quad (7.51)$$

and hence

$$u_0^n = \frac{\theta_L^n}{\theta_L^0} \frac{(x_1^0 - x_0^0)}{(x_1^n - x_0^n)} u_0^0. \quad (7.52)$$

The algorithm in this chapter for the approximate solution of the Lotka-Volterra competition diffusion system of cohabiting species (7.1) and (7.2) using the moving mesh finite difference method based on conservation and the combined mass procedure can be summarised as follows.

7.3.7 Algorithm for the competition-diffusion system

First evaluate the combined mass θ_L, θ_M and θ_R by (7.29), noting that $u = 0$ in $\mathcal{R}_R$ and $v = 0$ in $\mathcal{R}_L$ and calculate γ_m in each interval m, for each region by (7.30).

Then, at each time step we proceed with the following calculations:

1. Evaluate the rate of change of mass in each region $\dot{\theta}_L^n$, $\dot{\theta}_M^n$ and $\dot{\theta}_R^n$ by (7.38), (7.41) and (7.44) respectively.

2. Evaluate the velocities at the two interfaces by (7.33) and (7.34) and at the free boundary by (7.35). Calculate the nodal velocities w_i^{n+1} in each region by (7.37), (7.40) and (7.43). For $\mathcal{R}_L$ the anchor point is taken at x_0, in region $\mathcal{R}_M$ is taken at x_ζ and in region $\mathcal{R}_R$ at x_η.

3. Update the new nodal positions x_i^{n+1} and the new masses θ_L^{n+1}, θ_M^{n+1} and θ_R^{n+1} by the exponential time-stepping scheme ((7.45) and (7.46)).

4. Recover the solutions u_i^{n+1} for $i = 0, \ldots, \eta - 1$ and v_i^{n+1} for $i = \zeta + 1, \ldots, N$ by the use of the mass balance equations and the updated nodal positions x_i^{n+1} from equations (7.49) and (7.50) respectively.

In order to check whether the procedure of using a single mesh for the combined mass is reliable for solving the two-component Lotka-Volterra competition-diffusion model, we first compared our results against the standard, well-established, moving mesh finite difference method of [11, 103], where each species' equation was solved on a unique mesh and coupling terms were approximated using interpolation.

7.4 Results

The scheme is found to be stable and robust for a variety of parameter choices. Even though the use of the exponential time-stepping scheme ensured that no tangling would occur, it remains an explicit scheme. Therefore, the time step was restricted by stability considerations. For this reason, the time-step value was set at $\Delta t = 0.0005$.

7.4.1 Symmetrical case

In order to check whether the procedure of using a single mesh for the combined mass is reliable for solving the two-component Lotka-Volterra competition-diffusion model, we experimented with the symmetrical problem of (7.1) and (7.2). Species are allocated with equal value parameters as well as the same initial conditions, symmetrical by $x = 0.5$, as shown by Figure 7.4. The nodal velocity condition of the left-end node of the domain, $x = \xi(t)$, is set to have the same form as the one on the right-end but depending on the gradient of u i.e., $\frac{d\xi}{dt} = -\frac{\delta_1}{\mu}\left(\frac{\partial u}{\partial x}\right)\Big|_{x=\xi}$ (*cf.* (7.5)). If the method of combined masses is able to maintain the properties of the model as well as the geometry, it's an indication that the method is well grounded. Figure 7.5 shows how the population densities evolve through time with the parameters $\delta_1 = \delta_2 = 0.001$, $K_1 = K_2 = 100$, $k_1 = k_2 = 1$, $r_1 = r_2 = 1$. The population densities of the species are symmetrical about the axis of symmetry $x = 0.5$ and the velocities of the nodes are equal in

magnitude but opposite in signs. We observe a symmetrical spread of the nodes, without mesh tangling.

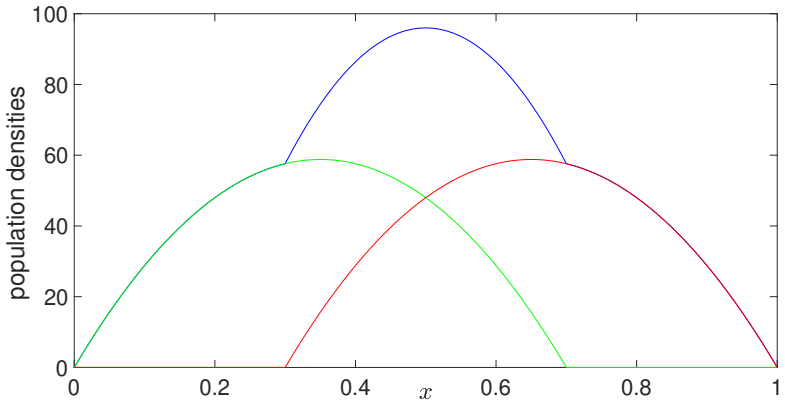

Figure 7.4: Symmetrical (around $x = 0.5$) initial conditions for the competition-diffusion system, with population densities u, v and $(u + v)$ shown in green, red and blue colour respectively.

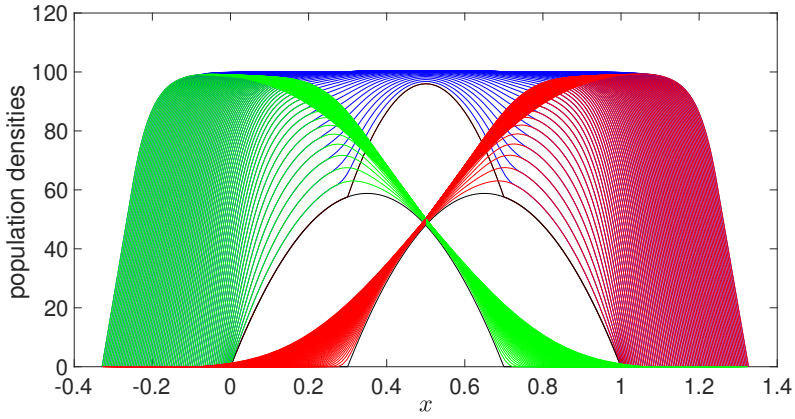

Figure 7.5: The approximated solution evolution through time of the symmetrical case at $t = 20$ with parameter values $\delta_1 = \delta_2 = 0.001$, $K_1 = K_2 = 100$, $k_1 = k_2 = 1$, $r_1 = r_2 = 1$. Initial conditions are shown in black colour.

7.4.2 Parameter choices

For the following examples, we have used the initial conditions illustrated in Figure 7.3. The mass of species 2 is set initially to be greater than species 1 and species 2 can escape the overlapping region through the outer right moving

boundary. Species 1 is restricted by the left-hand-side stationary boundary where we have imposed a zero Neumann boundary condition which implies no migration. The default variables used for the simulations, $\delta_1 = \delta_2 = 0.001$, $K_1 = K_2 = 100$, $r_1 = r_2 = 1$ and $\mu = 50$, are similar to the ones used in [11] and [177] for the extreme case of the competition-diffusion system (7.1) and (7.2), presented in [75], where the competition parameters k_1 and k_2 are very large to spatially segregate the two populations. Here, we instead use the competition parameters $k_1 = k_2 = 1$ to model a system where species are competing for common resources but they can coexist in space. A sensitivity analysis was carried out by varying one parameter at a time to test the robustness of the results which showed that the model and the numerical method produce stable results for each parameter change. A selection of results is presented below which indicates that the method is likely to be able to satisfy the requirements of modelling a wide variety of competition systems.

In the following figures, the initial conditions are shown in black while green, blue and red indicate respectively how the population densities u, $u + v$ and v evolve over time. All results are run with a time step 0.0005 and we plot the results for every step of 0.25.

Figure 7.6 shows the evolution of the populations as time progresses using $\delta_1 = \delta_2 = 0.001$, $K_1 = K_2 = 100$, $k_1 = k_2 = 1$, $r_1 = r_2 = 1$ and $\mu = 50$. The two populations have both reached their maximum carrying capacities and individuals are spreading throughout the domain through the moving boundaries.

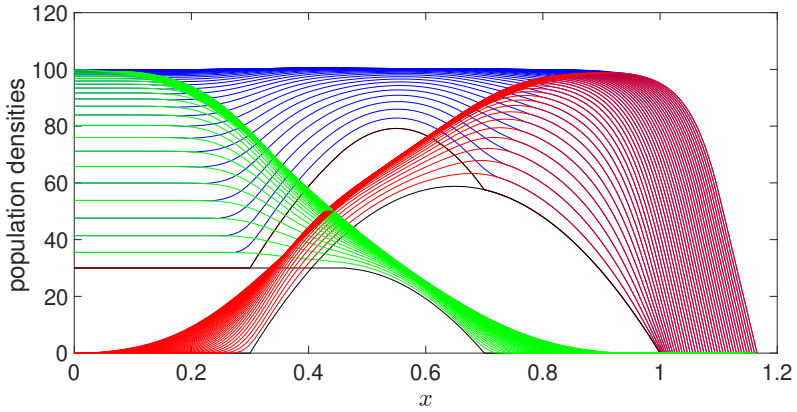

Figure 7.6: Result of competition-diffusion model at $t = 10$. Here we use $\delta_1 = \delta_2 = 0.001$, $K_1 = K_2 = 100$, $k_1 = k_2 = 1$, $r_1 = r_2 = 1$ and $\mu = 50$. Both species have reached their maximum carrying capacities (K_1 and K_2) and diffuse in the domain through the moving boundaries.

We investigate other parameter choices. We have selected a conservatively representative set of parameters, chosen to demonstrate some of the interesting behaviours that this model is able to describe.

Decreasing the carrying capacity K_2

For Figure 7.7 we have used the same parameter values as the example above except for the carrying capacity of species 2 which is set to be lower ($K_2 = 60$ instead of $K_2 = 100$). We restrict the growth of species 2 by lowering its carrying capacity and in comparison, to Figure 7.6, we observe that the decrease in the carrying capacity has caused the population to disperse less through the moving boundaries. Species 1 on the other hand is being benefitted from the restriction of species 2 to increase its mass, and species 1 disperses faster in the domain through the moving boundary, taking over most of the domain.

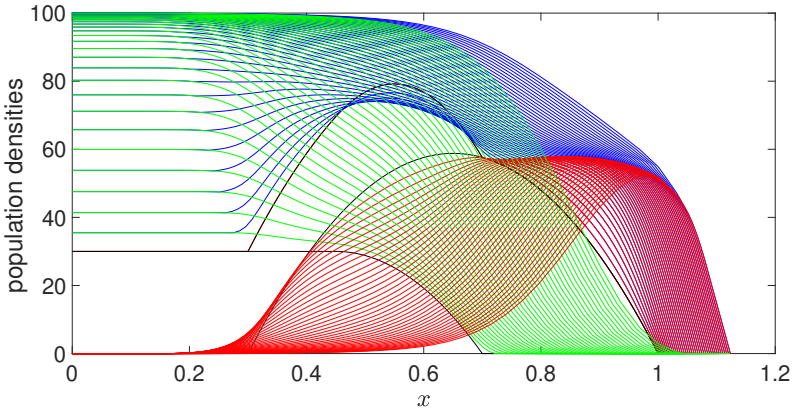

Figure 7.7: Result of competition-diffusion model at $t = 10$. Here we use $\delta_1 = \delta_2 = 0.001$, $k_1 = k_2 = 1$, $K_1 = 100, K_2 = 60$, $r_1 = r_2 = 1$ and $\mu = 50$. The restriction on the carrying capacity of species 2 has caused the inability to increase its mass resulting in species 1 taking over most of the domain.

Increasing the competition rate k_2

The following result in Figure 7.8 is focused on the effect of changing the competition parameter. We have increased the competition parameter of species 2 (k_2) by a factor of 5. As shown in Figure 7.8, due to the high competition of species 2, the population of species 2 is shifting towards the right-hand side of the domain, away from the overlapping region.

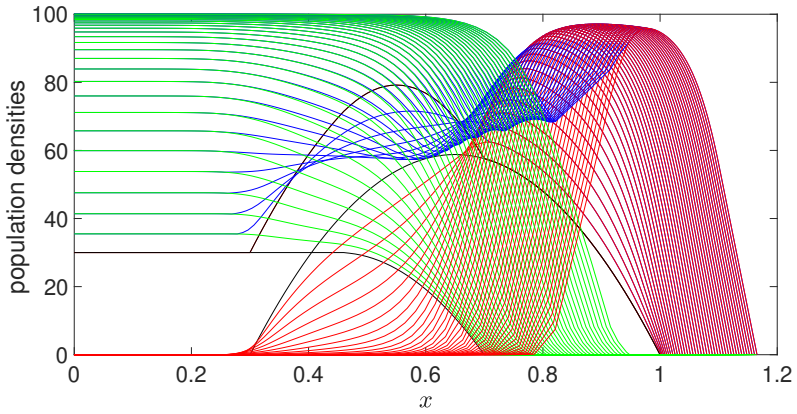

Figure 7.8: Result of competition-diffusion model at $t = 10$. Here we use $\delta_1 = \delta_2 = 0.001$, $k_1 = 1, k_2 = 5$, $K_1 = K_2 = 100$, $r_1 = r_2 = 1$ and $\mu = 50$. Due to the high competition rate of species 1, species 2 is unable to compete.

Decreasing the diffusion coefficient δ_1

In Figure 7.9 we have decreased the diffusion coefficient of species 1 by a factor of 10. As expected, that has restricted the ability of species 1 to disperse in the domain compared to Figure 7.6.

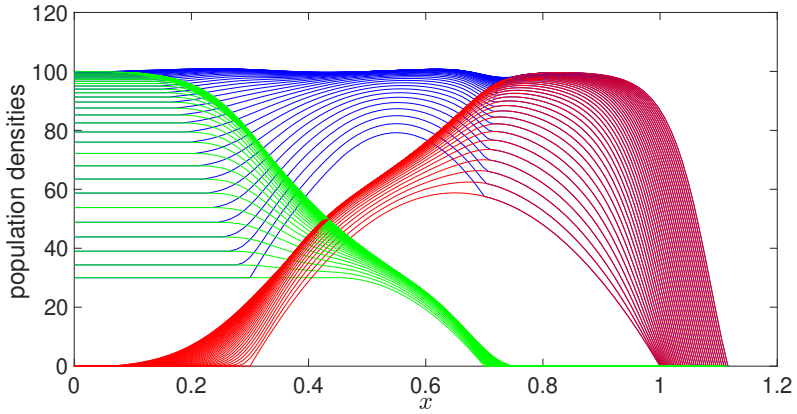

Figure 7.9: Result of competition-diffusion model at $t = 8$. Here we use $\delta_1 = 0.0001, \delta_2 = 0.001$, $k_1 = k_2 = 1$, $K_1 = K_2 = 100$, $r_1 = r_2 = 1$ and $\mu = 50$.

Decreasing the parameter μ

Lastly, in Figure 7.10 we are investigating the μ parameter in the boundary condition at the right-hand side outer moving boundary. We set $\mu = 1$ instead

of $\mu = 50$ as used before. In [33] is shown that μ is inversely proportional to the preferred population density at the spreading front. Thus increasing $\frac{1}{\mu}$ causes the population to disperse more through the moving boundary in its effort to increase the population density, as shown in Figure 7.10. We can also observe that the velocity of the right-hand-side outer moving boundary is increasing at earlier times and remains constant for the rest of the time.

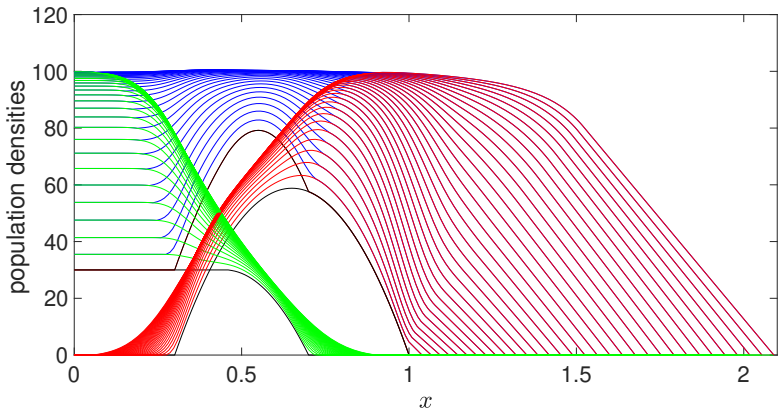

Figure 7.10: Result of competition-diffusion model at $t = 10$. Here we use $\delta_1 = \delta_2 = 0.001$, $k_1 = k_2 = 1$, $K_1 = K_2 = 100$, $r_1 = r_2 = 1$ and $\mu = 1$. Decreasing μ has caused the population to disperse more through the boundary and the velocity of the moving boundary is slightly increasing at earlier times and remains constant for the rest of the time.

We have given details of applying the moving mesh method based on the combined mass approach to the one-dimensional competition-diffusion system. We now demonstrate that the same method can be applied to the two-dimensional radially symmetric case of the system.

7.5 The Two-Dimensional Radially Symmetric Competition-Diffusion System of Cohabiting Species with Moving Boundaries

We use the moving mesh method based on the combined approach described in Section 7.3.1 to approximate the radial case of (7.1) and (7.2) in two dimensions,

$$\frac{\partial u}{\partial t} = \frac{1}{\mathsf{r}}\frac{\partial}{\partial \mathsf{r}}\left(\delta_1 \mathsf{r}\frac{\partial u}{\partial \mathsf{r}}\right) + \frac{1}{\mathsf{r}^2}\frac{\partial}{\partial \phi}\left(\delta_1 \frac{\partial u}{\partial \phi}\right) + r_1 u\left(1 - \frac{u + k_1 v}{K_1}\right) \quad \mathsf{r} \in \mathcal{R}_1,\ t > 0 \tag{7.53}$$

$$\frac{\partial v}{\partial t} = \frac{1}{\mathsf{r}}\frac{\partial}{\partial \mathsf{r}}\left(\delta_2 \mathsf{r}\frac{\partial v}{\partial \mathsf{r}}\right) + \frac{1}{\mathsf{r}^2}\frac{\partial}{\partial \phi}\left(\delta_2 \frac{\partial v}{\partial \phi}\right) + r_2 v\left(1 - \frac{v + k_2 u}{K_2}\right) \quad \mathsf{r} \in \mathcal{R}_2,\ t > 0. \tag{7.54}$$

The domains $\mathcal{R}_1$ and $\mathcal{R}_2$ are occupied by species u and v respectively, and partly overlap.

When a two-dimensional problem in cylindrical or spherical co-ordinates possesses circular symmetry (i.e., no ϕ dependence), then $\frac{\partial^2 u}{\partial \phi^2} = \frac{\partial^2 v}{\partial \phi^2} = 0$, and equations (7.53) and (7.54) simplify to

$$\frac{\partial u}{\partial t} = \frac{1}{\mathsf{r}}\frac{\partial}{\partial \mathsf{r}}\left(\delta_1 \mathsf{r}\frac{\partial u}{\partial \mathsf{r}}\right) + r_1 u\left(1 - \frac{u + k_1 v}{K_1}\right) \quad \mathsf{r} \in \mathcal{R}_1,\ t > 0 \tag{7.55}$$

and

$$\frac{\partial v}{\partial t} = \frac{1}{\mathsf{r}}\frac{\partial}{\partial \mathsf{r}}\left(\delta_2 \mathsf{r}\frac{\partial v}{\partial \mathsf{r}}\right) + r_2 v\left(1 - \frac{v + k_2 u}{K_2}\right) \quad \mathsf{r} \in \mathcal{R}_2,\ t > 0, \tag{7.56}$$

respectively, with the boundary condition on the left-hand-side stationary boundary,

$$\frac{\partial u}{\partial \mathsf{r}} = 0 \quad t > 0, \quad \mathsf{r} = 0. \tag{7.57}$$

where the conditions at the inner interfaces $\eta(t)$ and $\zeta(t)$ are

$$\frac{\mathrm{d}\eta}{\mathrm{d}t} = -\frac{\delta_1}{K_1}\left(\frac{\partial u}{\partial \mathsf{r}}\right)\bigg|_{\mathsf{r}=\eta} \quad \text{and} \quad u(\eta(t), t) = 0 \tag{7.58}$$

and

$$\frac{\mathrm{d}\zeta}{\mathrm{d}t} = -\frac{\delta_2}{K_2}\left(\frac{\partial v}{\partial \mathsf{r}}\right)\bigg|_{\mathsf{r}=\zeta} \quad \text{and} \quad v(\zeta(t), t) = 0, \tag{7.59}$$

respectively.
Lastly, for the free boundary on the right-hand side, the assigned conditions are

$$\frac{\mathrm{d}\sigma}{\mathrm{d}t} = -\frac{\delta_2}{\mu}\left(\frac{\partial v}{\partial \mathsf{r}}\right)\bigg|_{\mathsf{r}=\sigma} \quad \text{and} \quad v(\sigma(t), t) = 0. \tag{7.60}$$

7.5.1 Numerical solution for the radial coordinates case

We slightly vary the notation from Section 7.3.1 such that the space variable x is replaced by r and w replaced by z. We use $\tilde{\mathsf{r}}_i(t^n) \approx \mathsf{r}_i^n$, $i = 0, 1, \ldots, N$, to denote the i^{th} node along the radius of the mesh, at time $n\Delta t$, $n = 0, 1, \ldots$. The corresponding solutions notation is $u(\tilde{\mathsf{r}}_i, t^n) = \tilde{u}_i(t^n) \approx u_i^n$ and $v(\tilde{\mathsf{r}}_i, t^n) = \tilde{v}_i(t^n) \approx v_i^n$,and the velocity of each node is $z(\tilde{\mathsf{r}}_i, t^n) = \tilde{z}_i(t) = \frac{d\tilde{\mathsf{r}}_i}{dt}$.

We use a similar procedure to the one given carried out in Section 7.3.1, to show that, given a mesh along a radius $\tilde{\mathsf{r}}_i(t^n)$, with corresponding solution $\tilde{u}_i(t^n)$ (or $\tilde{v}_i(t^n)$), the updated mesh along a radius $\tilde{\mathsf{r}}_i(t^{n+1})$ and solution $\tilde{u}_i(t^{n+1})$ (or $\tilde{v}_i(t^{n+1})$) can be found by computing a mesh velocity $\tilde{z}_i(t^n)$.
The mass in the interval m is

$$\theta_m(t) = \tilde{\mathsf{r}}_m(t)\tilde{u}_m(t)\Delta\tilde{\mathsf{r}}_m.$$

Having divided the domain into three regions namely $\mathcal{R}_L$, $\mathcal{R}_M$ and $\mathcal{R}_R$, separated by the two inner interfaces η and ζ, we then evaluate the initial values θ_L^0, θ_M^0 and θ_R^0 of the total masses θ in each region, by (7.61) using the composite trapezium rule, (*cf.* (7.29))

$$\theta^0 = \frac{1}{4}\sum_{i=0}^{N-1}\Big(\mathsf{r}_{i+1}^0 - \mathsf{r}_i^0\Big)(\mathsf{r}_i^0 + \mathsf{r}_{i+1}^0)(u_i^0 + u_{i+1}^0). \tag{7.61}$$

The constant-in-time relative masses $\gamma_{L,i}$, $\gamma_{M,i}$ and $\gamma_{R,i}$ in the interval $(\mathsf{r}_{i-1}^n, \mathsf{r}_i^n)$ is given by, (*cf.* (7.30))

$$\int_m u_m(\tilde{\mathsf{r}}, t)\tilde{\mathsf{r}}_m(t)\ \mathrm{d}\mathsf{r} = \gamma_m$$

$$\gamma_m = \frac{1}{\theta^0}(\mathsf{r}_i^0 - \mathsf{r}_{i-1}^0)\mathsf{r}_i^0 u_i^0, \quad (i = m = 1, \ldots, N). \tag{7.62}$$

7.5.2 Approximating the mesh velocities and the rates of change of the total populations

As with the one-dimensional case, we seek a mesh velocity by differentiating a relative mass $\hat{u}$ in an interval m with respect to time, using the Leibniz integral rule and the relative mass balance, i.e., (*cf.* (7.31))

$$\frac{d}{dt}\int_m \tilde{\mathsf{r}}(t)\hat{u}(\tilde{\mathsf{r}}, t)\ \mathrm{d}\mathsf{r} = \int_m \tilde{\mathsf{r}}(t)\frac{\partial\hat{u}(\tilde{\mathsf{r}}, t)}{\partial t}\ \mathrm{d}\mathsf{r} + [\tilde{\mathsf{r}}(t)\hat{u}(\tilde{\mathsf{r}}, t)\hat{z}(\tilde{\mathsf{r}}, t)]_m = 0$$

$$= \frac{1}{\theta}\left(\int_m \tilde{\mathsf{r}}(t)\frac{\partial u(\tilde{\mathsf{r}},t)}{\partial t}\ \mathrm{d}\mathsf{r} - \gamma_m\dot{\theta}\right) + [\tilde{\mathsf{r}}\hat{\tilde{u}}\hat{\tilde{z}}]_m = 0$$

giving,

$$[\tilde{\mathsf{r}}\hat{\tilde{u}}\hat{\tilde{z}}]_m = -\frac{1}{\theta}\left(\int_m \tilde{\mathsf{r}}(t)\frac{\partial u(\tilde{\mathsf{r}},t)}{\partial t}\ \mathrm{d}\mathsf{r} - \gamma_m\dot{\theta}\right).$$

Since $\hat{\tilde{u}}\hat{\tilde{z}}$ denote the relative masses, $[\tilde{\mathsf{r}}\hat{\tilde{u}}\hat{\tilde{z}}]_m\theta = [\tilde{\mathsf{r}}\tilde{u}\tilde{z}]_m$ yielding to

$$\tilde{\tilde{z}}_m = \frac{1}{\tilde{\mathsf{r}}_m\tilde{u}_m}\left(\gamma_m\dot{\theta} - \int_m \tilde{\mathsf{r}}(t)\frac{\partial u(\tilde{\mathsf{r}},t)}{\partial t}\ \mathrm{d}\mathsf{r}\right). \tag{7.63}$$

For the region $\mathcal{R}_L$, by taking the anchor point at $\mathsf{r}=0$, from (7.63), the velocity z_i^n satisfies,

$$\mathsf{r}_i^n u_i^n z_i^n = \mathsf{r}_0^n u_0^n z_0^n - \int_{\mathsf{r}_0^n}^{\mathsf{r}_i^n} \mathsf{r}\frac{\partial u}{\partial t}\ \mathrm{d}\mathsf{r} + \gamma_{L,i}\dot{\theta}_L, \quad (\mathsf{r}_i \in \mathcal{R}_L),$$

since $v=0$ in $\mathcal{R}_L$.
Substituting for $\frac{\partial u}{\partial t}$ from (7.53), evaluating the integral, and cancelling terms due to the boundary condition (7.57) gives, (*cf.* (7.37))

$$z_i^n = \frac{1}{\mathsf{r}_i^n u_i^n}\left(\gamma_{Li}\dot{\theta}_L^n - \delta_1\mathsf{r}_i^n\frac{\partial u}{\partial \mathsf{r}}\Big|_i - \int_{\mathsf{r}_0^n}^{\mathsf{r}_i^n} \mathsf{r}\ r_1 u\left(1-\frac{u}{K_1}\right)\ \mathrm{d}\mathsf{r}\right), \quad (1\le i\le \zeta-1), \tag{7.64}$$

provided that $u_i^n \neq 0$.
By setting $\mathsf{r}_i = \mathsf{r}_\zeta$ in (7.64), we can obtain an equation for $\dot{\theta}^n$ in region $\mathcal{R}_L$, i.e., (*cf.* (7.38))

$$\dot{\theta}_L^n = \delta_1\mathsf{r}_\zeta^n\frac{\partial u}{\partial x}\Big|_\zeta + \int_{\mathsf{r}_0^n}^{\mathsf{r}_\zeta^n} \mathsf{r}\ r_1 u\left(1-\frac{u}{K_1}\right)\ \mathrm{d}\mathsf{r} + \mathsf{r}^n u^n z^n|_\zeta. \tag{7.65}$$

Similarly, for the velocity z_i^n in region $\mathcal{R}_M$ we take the anchor point to be $\mathsf{r}=\zeta$, therefore by (7.63)

$$\mathsf{r}_i^n(u_i^n+v_i^n)z_i^n = \mathsf{r}_\zeta^n(u_\zeta^n+v_\zeta^n)z_\zeta^n -$$
$$\int_{\mathsf{r}_\zeta^n}^{\mathsf{r}_i^n} \mathsf{r}\left(\frac{\partial u(\mathsf{r},t^n)}{\partial t} + \frac{\partial v(\mathsf{r},t^n)}{\partial t}\right)\mathrm{d}\mathsf{r} + \gamma_{M,i}\dot{\theta}_M, \quad (\mathsf{r}_i\in\mathcal{R}_M).$$

By substituting the original PDEs (7.55) and (7.56) and applying the boundary conditions in (7.58) and (7.59), the equation for the node velocities in region $\mathcal{R}_M$ is (*cf.* (7.40))

$$z_i^n = \frac{1}{\mathsf{r}_i^n(u_i^n+v_i^n)}\Bigg(\gamma_{M,i}\dot{\theta}_M^n - \delta_1\left[\mathsf{r}^n\frac{\partial u}{\partial \mathsf{r}}\right]_\zeta^i + \delta_2\left[\mathsf{r}^n\frac{\partial v}{\partial \mathsf{r}}\right]_\zeta^i$$

$$+\int_{\mathsf{r}_\zeta^n}^{\mathsf{r}_i^n} \mathsf{r}\left(r_1 u\left(1-\frac{u+k_1 v}{K_1}\right)+r_2 v\left(1-\frac{v+k_2 u}{K_2}\right)\right)\,\mathrm{d}\mathsf{r}$$

$$+\,\mathsf{r}^n(u^n+v^n)z^n|_\zeta\Bigg), \tag{7.66}$$

provided that $u_i^n \neq 0$ and $v_i^n \neq 0$.
Setting $\mathsf{r}_i = \mathsf{r}_\eta$ gives the equation for $\dot{\theta}^n$ in region $\mathcal{R}_M$, i.e., (*cf.* (7.41))

$$\dot{\theta}_M^n = \delta_1\left[\mathsf{r}^n\frac{\partial u}{\partial x}\right]_\zeta^\eta + \delta_2\left[\mathsf{r}^n\frac{\partial v}{\partial x}\right]_\zeta^\eta$$

$$-\int_{r_\zeta^n}^{r_\eta^n}\mathsf{r}\left(r_1 u\left(1-\frac{u+k_1 v}{K_1}\right)+r_2 v\left(1-\frac{v+k_2 u}{K_2}\right)\right)\mathrm{d}\mathsf{r} - [\mathsf{r}^n(u^n+v^n)z^n]_\zeta^\eta\,. \tag{7.67}$$

Finally for region $\mathcal{R}_R$, from (7.63), by taking η to be the anchor point $x=\eta$, the velocity z^n is given by

$$\mathsf{r}_i^n u_i^n z_i^n = \mathsf{r}_\eta^n u_\eta^n z_\eta^n - \int_{\mathsf{r}_\eta^n}^{\mathsf{r}_i^n}\mathsf{r}\frac{\partial v}{\partial t}\,\mathrm{d}\mathsf{r} + \gamma_{R,i}\dot{\theta}_R, \quad (r_i \in \mathcal{R}_R),$$

since $u=0$ in $\mathcal{R}_R$.
We substitute the original PDE (7.56) and the boundary conditions to get the equation for the node velocities in region $\mathcal{R}_R$ (*cf.* (7.43))

$$z_i^n = \frac{1}{\mathsf{r}_i^n v_i^n}\left(\gamma_{R,i}\dot{\theta}_R^n - \delta_2\left[\mathsf{r}^n\frac{\partial v}{\partial \mathsf{r}}\right]_\eta^i + \int_{\mathsf{r}_\eta^n}^{\mathsf{r}_i^n}\mathsf{r}\left(r_2 v\left(1-\frac{v}{K_2}\right)\right)\mathrm{d}\mathsf{r} + \mathsf{r}^n v^n z^n|_\eta\right), \tag{7.68}$$

provided that $v_i^n \neq 0$.
The equation for $\dot{\theta}^n$ in region $\mathcal{R}_R$ is obtain from equation (7.68) by setting $i=\sigma$, i.e., (*cf.* (7.44))

$$\dot{\theta}_R^n = \delta_2\left[\mathsf{r}^n\frac{\partial v}{\partial \mathsf{r}}\right]_\eta^\sigma + \int_{\mathsf{r}_\eta^n}^{\mathsf{r}_\sigma^n}\mathsf{r}\left(r_2 v\left(1-\frac{v}{K_2}\right)\right)\mathrm{d}\mathsf{r} + [\mathsf{r}^n v^n z^n]_\eta^\sigma\,. \tag{7.69}$$

7.5.3 The velocities of the moving interfaces and the free boundary

In order to evaluate the nodal velocities at the moving interfaces η, ζ and the outer boundary σ, we apply one-sided approximation to the derivative terms of equations (7.58), (7.59) and (7.60) for x_η, x_ζ and x_σ respectively,

$$\frac{d\eta}{dt} = -\frac{\delta_1}{K_1}\Big(\frac{u(\eta)-u(\eta^-)}{\mathsf{r}(\eta)-\mathsf{r}(\eta^-)}\Big), \tag{7.70}$$

where η^- is the node immediately to the left of η,

$$\frac{d\zeta}{dt} = -\frac{\delta_2}{K_2}\Big(\frac{v(\zeta^+) - v(\zeta)}{\mathsf{r}(\zeta^+) - \mathsf{r}(\zeta)}\Big), \tag{7.71}$$

where ζ^+ is the node immediately to the right of ζ and

$$\frac{d\sigma}{dt} = -\frac{\delta_2}{\mu}\Big(\frac{v(\sigma) - v(\sigma^-)}{\mathsf{r}(\sigma) - \mathsf{r}_(\sigma^-)}\Big), \tag{7.72}$$

where σ^- is the node immediately to the left of σ.

7.5.4 Time-stepping

As in Section 7.3.5 using the evaluated nodal velocities we use the first-order exponential scheme to update the node positions r_i^{n+1} and the new θ^{n+1}, i.e.,

$$\Delta\mathsf{r}_i^{n+1} = \Delta\mathsf{r}_i^n \exp\left(\Delta t \frac{\Delta z_i^n}{\Delta\mathsf{r}_i^n}\right) \tag{7.73}$$

and

$$\theta^{n+1} = \theta^n \exp\left(\Delta t \frac{\dot\theta^n}{\theta^n}\right). \tag{7.74}$$

Having found the new nodal positions and the new θ we can approximate the population densities u and v at the new time t^{n+1}.

7.5.5 The population densities

We could update the population densities $\hat u(\tilde{\mathsf{r}}, t)$ and $\hat v(\tilde{\mathsf{r}}, t)$ by the use of the ALE equation as in Section 7.3.6. However, since the combined population density $(u(\tilde{\mathsf{r}}, t) + v(\tilde{\mathsf{r}}, t))$ only exists in the middle section $\mathcal{R}_M$ we only use the ALE to update each population in this region. For the regions $\mathcal{R}_L$ and $\mathcal{R}_R$ we can update $\hat u(\tilde{\mathsf{r}}, t)$ and $\hat v(\tilde{\mathsf{r}}, t)$, respectively by (*cf.* (7.24))

$$\int_m u_m(\tilde{\mathsf{r}}, t)\tilde{\mathsf{r}}\ \mathrm{d}\mathsf{r} = \gamma_m\theta(t)$$

and

$$\int_m v_m(\tilde{\mathsf{r}}, t)\tilde{\mathsf{r}}\ \mathrm{d}\mathsf{r} = \gamma_m\theta(t).$$

Hence, in region $\mathcal{R}_L$ we approximate u^{n+1} by

$$u_i^{n+1} = \frac{\gamma_i\theta_L^{n+1}}{\mathsf{r}_i^{n+1}(\mathsf{r}_{i+1}^{n+1} - \mathsf{r}_i^{n+1})}, \qquad (0 \le i \le \zeta - 1), \tag{7.75}$$

$$u_i^{n+1} = \frac{\gamma_i \theta_L^{n+1}}{\mathsf{r}_i^{n+1}(\mathsf{r}_i^{n+1} - \mathsf{r}_{i-1}^{n+1})}, \qquad (i = \zeta), \tag{7.76}$$

and in region $\mathcal{R}_R$ we approximate the population density v^{n+1} by

$$v_i^{n+1} = \frac{\gamma_i \theta_R^{n+1}}{\mathsf{r}_i^{n+1}(\mathsf{r}_i^{n+1} - \mathsf{r}_{i-1}^{n+1})}, \qquad (\sigma + 1 \leq i \leq N + 1) \tag{7.77}$$

and

$$v_i^{n+1} = \frac{\gamma_i \theta_R^{n+1}}{\mathsf{r}_i^{n+1}(\mathsf{r}_{i+1}^{n+1} - \mathsf{r}_i^{n+1})}, \qquad (i = \sigma). \tag{7.78}$$

Lastly, to get update the population densities u^{n+1} and v^{n+1} in the middle region $\mathcal{R}_M$, as in Section 7.3.6, the mass balance equations are used together with the Leibniz integral rule, i.e., (*cf.* (7.47) & (7.48))

$$\frac{d}{dt}\int_{\mathsf{r}_i^n}^{\mathsf{r}_{i+1}^n} u \; \mathrm{d}\mathsf{r} = \int_{\mathsf{r}_i^n}^{\mathsf{r}_{i+1}^n} \mathsf{r}\frac{\partial u}{\partial t} \; \mathrm{d}\mathsf{r} + \int_{\mathsf{r}_i^n}^{\mathsf{r}_{i+1}^n} \frac{\partial}{\partial \mathsf{r}}(\mathsf{r}uz) \; \mathrm{d}\mathsf{r}, \quad (i = \zeta, .., \eta - 1)$$

$$\frac{d}{dt}\int_{\mathsf{r}_i^n}^{\mathsf{r}_{i+1}^n} v \; \mathrm{d}\mathsf{r} = \int_{\mathsf{r}_i^n}^{\mathsf{r}_{i+1}^n} \mathsf{r}\frac{\partial v}{\partial t} \; \mathrm{d}\mathsf{r} + \int_{\mathsf{r}_i^n}^{\mathsf{r}_{i+1}^n} \frac{\partial}{\partial \mathsf{r}}(\mathsf{r}vz) \; \mathrm{d}\mathsf{r}, \quad (i = \zeta, .., \eta - 1).$$

Substituting equations (7.55) and (7.56) and performing the integration gives,

$$\frac{d}{dt}\int_{\mathsf{r}_i^n}^{\mathsf{r}_{i+1}^n} u \; \mathrm{d}\mathsf{r} = \delta_1 \left[\mathsf{r}^n \frac{\partial u}{\partial \mathsf{r}}\right]_i^{i+1} + \int_{\mathsf{r}_i^n}^{\mathsf{r}_{i+1}^n} \mathsf{r} \; r_1 u\Big(1 - \frac{u - k_1 v}{K_1}\Big) \; \mathrm{d}\mathsf{r} + [\mathsf{r}^n u^n z^n]_i^{i+1}$$

$$\frac{d}{dt}\int_{\mathsf{r}_i^n}^{\mathsf{r}_{i+1}^n} v \; \mathrm{d}\mathsf{r} = \delta_2 \left[\mathsf{r}^n \frac{\partial v}{\partial x}\right]_i^{i+1} + \int_{\mathsf{r}_i^n}^{\mathsf{r}_{i+1}^n} \mathsf{r} \; r_2 v\Big(1 - \frac{v - k_2 u}{K_2}\Big) \; \mathrm{d}\mathsf{r} + [\mathsf{r}^n v^n z^n]_i^{i+1}.$$

By integrating in time

$$u_i^{n+1} = \frac{1}{\mathsf{r}_i^{n+1}(\mathsf{r}_{i+1}^{n+1} - \mathsf{r}_i^{n+1})}\Big(u_i^n \mathsf{r}_i^n(\mathsf{r}_{i+1}^n - \mathsf{r}_i^n) + \Delta t\Big(\delta_1 \left[\mathsf{r}^n \frac{\partial u}{\partial \mathsf{r}}\right]_i^{i+1} + \int_{\mathsf{r}_i^n}^{\mathsf{r}_{i+1}^n} \mathsf{r} \; r_1 u\Big(1 - \frac{u - k_1 v}{K_1}\Big) \; \mathrm{d}\mathsf{r} + [\mathsf{r}^n u^n z^n]_i^{i+1}\Big)\Big) \tag{7.79}$$

for $i = \zeta, .., \eta - 1$, and

$$u_i^{n+1} = \frac{1}{\mathsf{r}_i^{n+1}(\mathsf{r}_i^{n+1} - \mathsf{r}_{i-1}^{n+1})}\Big(u_i^n \mathsf{r}_i^n(\mathsf{r}_i^n - \mathsf{r}_{i-1}^n) + \Delta t\Big(\delta_1 \left[\mathsf{r}^n \frac{\partial u}{\partial \mathsf{r}}\right]_{i-1}^{i} + \int_{\mathsf{r}_{i-1}^n}^{\mathsf{r}_i^n} \mathsf{r}\ r_1 u\Big(1 - \frac{u - k_1 v}{K_1}\Big)\ \mathrm{d}\mathsf{r} + [\mathsf{r}^n u^n z^n]_{i-1}^{i}\Big)\Big) \tag{7.80}$$

for $i = \eta$.

Likewise for the equation of v,

$$v_i^{n+1} = \frac{1}{\mathsf{r}_i^{n+1}(\mathsf{r}_{i+1}^{n+1} - \mathsf{r}_i^{n+1})}\Big(v_i^n \mathsf{r}_i^n(\mathsf{r}_{i+1}^n - \mathsf{r}_i^n) + \Delta t\Big(\delta_2 \left[\mathsf{r}^n \frac{\partial v}{\partial \mathsf{r}}\right]_{i}^{i+1} - \int_{\mathsf{r}_i^n}^{\mathsf{r}_{i+1}^n} \mathsf{r}\ r_2 v\Big(1 - \frac{v - k_2 u}{K_2}\Big)\ \mathrm{d}\mathsf{r} + [\mathsf{r}^n v^n z^n]_{i}^{i+1}\Big)\Big) \tag{7.81}$$

for $i = \zeta, .., \eta - 1$ and

$$v_i^{n+1} = \frac{1}{\mathsf{r}_i^{n+1}(\mathsf{r}_i^{n+1} - \mathsf{r}_{i-1}^{n+1})}\Big(v_i^n \mathsf{r}_i^n(\mathsf{r}_i^n - \mathsf{r}_{i-1}^n) + \Delta t\Big(\delta_2 \left[\mathsf{r}^n \frac{\partial v}{\partial \mathsf{r}}\right]_{i-1}^{i} + \int_{\mathsf{r}_{i-1}^n}^{\mathsf{r}_i^n} \mathsf{r}\ r_2 v\Big(1 - \frac{v - k_2 u}{K_2}\Big)\ \mathrm{d}\mathsf{r} + [\mathsf{r}^n v^n z^n]_{i-1}^{i}\Big)\Big) \tag{7.82}$$

for $i = \eta$.

The algorithm for the Lotka-Volterra competition diffusion system of cohabiting species (7.55) and (7.56) in radial coordinates using the moving mesh finite difference method together with the combined mass approach is as follows.

7.5.6 Algorithm for the competition-diffusion system in radial coordinates

First evaluate the combined mass θ_L, θ_M and θ_R by (7.80), noting that $u = 0$ in $\mathcal{R}_R$ and $v = 0$ in $\mathcal{R}_L$ and calculate γ_m in each interval m, for each region by (7.62).
Then, at each time step we proceed with the following calculations:

1. Evaluate the rate of change of mass in each region $\dot{\theta}_L^n$, $\dot{\theta}_M^n$ and $\dot{\theta}_R^n$ by (7.65), (7.67) and (7.69) respectively.

2. Evaluate the velocities at the two interfaces by (7.70) and (7.71) and at the free boundary by (7.72). Calculate the nodal velocities z_i^{n+1} in each region

by (7.64), (7.66) and (7.68). For $\mathcal{R}_L$ the anchor point is taken at r_0, in region $\mathcal{R}_M$ is taken at r_ζ and in region $\mathcal{R}_R$ at r_η.

3. Update the new nodal positions r_i^{n+1} and the new masses θ_L^{n+1}, θ_M^{n+1} and θ_R^{n+1} by the exponential time-stepping scheme ((7.73) and (7.74)).

4. Recover the solution u_i^{n+1} in region $\mathcal{R}_L$ by equation (7.75) and v_i^{n+1} in region $\mathcal{R}_R$ by equation (7.77). u_i^{n+1} at $i = \zeta$ is calculated by (7.76) and v_i^{n+1} at $i = \eta$ by equation (7.78).

5. Obtain u_i^{n+1} and v_i^{n+1} in region $\mathcal{R}_M$ by the use of the mass balance equations and the updated nodal positions r_i^{n+1} from equations (7.79) and (7.81) respectively. The u_i^{n+1} and the v_i^{n+1} at $i = \eta$ are evaluated by (7.80) and (7.82).

7.5.7 Results

The moving mesh method for the radial case solves the L-V competition diffusion system along a line $0 \leq \mathsf{r} \leq \mathsf{r}_N$ and then uses radial symmetry to give the solution over a complete circle, see Figure 7.11b. We use the same set of parameter choices as in the one-dimensional Cartesian coordinates case and the mesh is constructed initially with $N = 100$ equispaced nodes. We use the same time step value $\Delta t = 0.5 \times 10^{-3}$ for all the simulations.

Throughout the runs, in the one-dimensional representation of the results (over the line $0 \leq \mathsf{r} \leq \mathsf{r}_N$) u, v and $u+v$ are shown in green, red and blue colour respectively where in the two-dimensional representation (over the complete circle) the half torus shape in red colour on the outer region depicts the v population where the shape in green colour in the middle of the graph represents the population u.

Initial conditions

Figure 7.11 illustrates the initial conditions of populations u, v and $u+v$ which have been used for all the examples presented in this section. Initial conditions are shown over the line $0 \leq \mathsf{r} \leq \mathsf{r}_N$ and over the complete circle in Figures 7.11a and 7.11b, respectively.

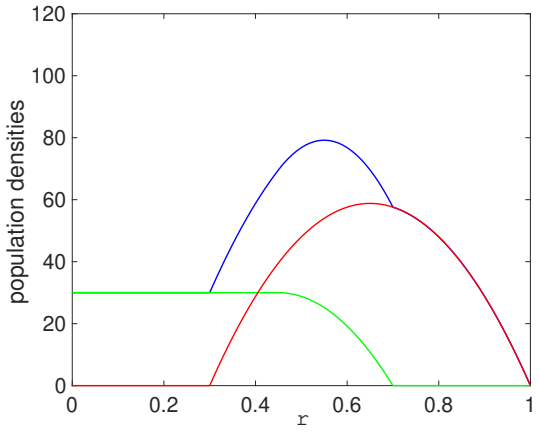

(a) The initial conditions of the populations u (green), v (red) and $u+v$ (blue) along the line $0 \leq \mathsf{r} \leq \mathsf{r}_N$.

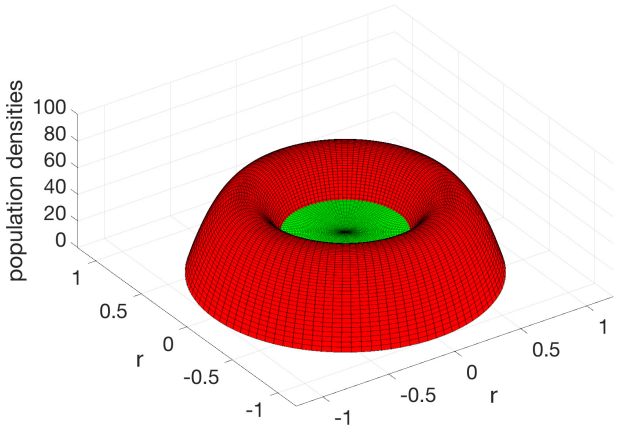

(b) The 2-dimensional radial L-V competition diffusion model initial conditions of u and v.

Figure 7.11: Initial conditions.

Approximated solution at $t = 5$

The first set of parameter values, $\delta_1 = \delta_2 = 0.001$, $k_1 = k_2 = 1$, $K_1 = K_2 = 100$, $r_1 = r_2 = 1$ and $\mu = 50$, gives the results in Figures 7.12a and 7.12b . The results in Figure 7.12a shows the results along the line $0 \leq \mathsf{r} \leq \mathsf{r}_N$, plotted for every 0.2 time-steps up to $t = 5$. We observe very similar results when comparing the approximated solution in Figure 7.12a with the results of the one-dimensional case (Figure 7.6). Figure 7.12b shows the results at $t = 5$ over the complete circle.

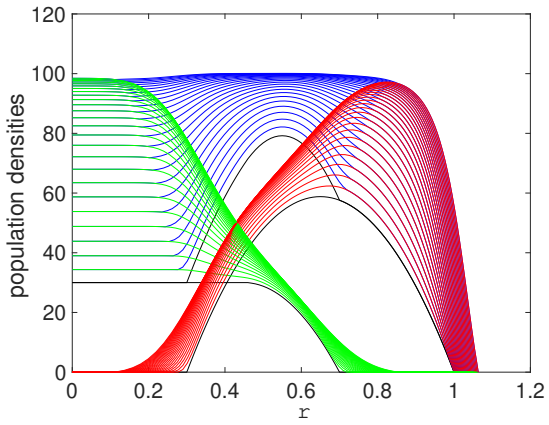

(a) The approximated solutions u (green), v (red) and $u + v$ (blue) plotted for every 0.20 time steps with final time $t = 5$.

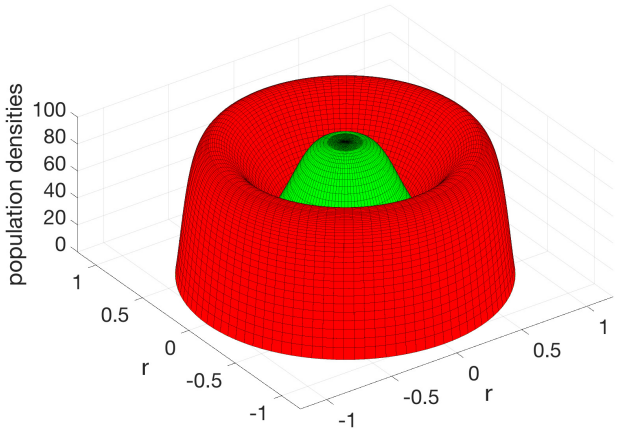

(b) The approximated solutions of u and v at $t = 5$ of the 2-dimensional radial L-V competition diffusion model.

Figure 7.12: The result of the competition-diffusion model at $t = 5$. Here we use $\delta_1 = \delta_2 = 0.001$, $k_1 = k_2 = 1$, $K_1 = K_2 = 100$, $r_1 = r_2 = 1$ and $\mu = 50$.

Mesh evolution through time

Figure 7.13a shows the smooth trajectories of the mesh nodes and the direction of the inner interfaces and the moving boundary. The black bold lines represent the nodes at the inner interfaces $\mathsf{r} = \eta$ and $\mathsf{r} = \zeta$ and the node at the free boundary $\mathsf{r} = \sigma$, starting from the left-hand side, respectively. Figure 7.13b shows the final node positions at $t = 5$ over the complete circle.

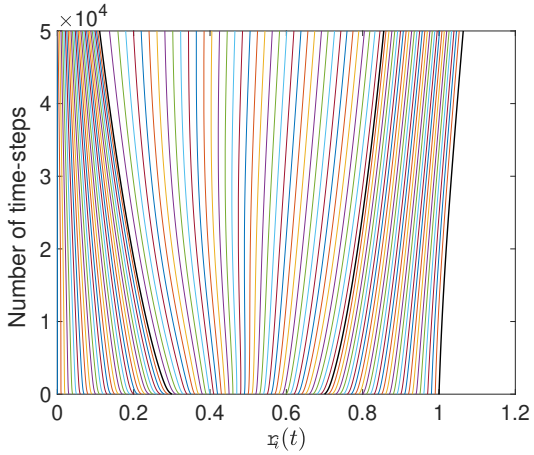

(a) The mesh trajectory.

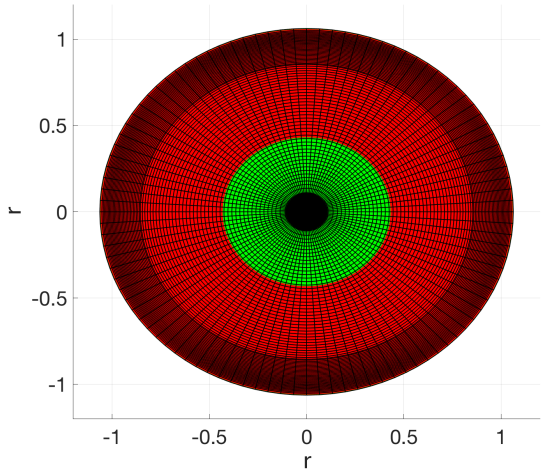

(b) The mesh for the two-dimensional, radial L-V competition diffusion model.

Figure 7.13: The mesh evolution for the radial case of the competition-diffusion model at $t = 5$ with parameter values $\delta_1 = \delta_2 = 0.001$, $k_1 = k_2 = 1$, $K_1 = 100, K_2 = 100$, $r_1 = r_2 = 1$ and $\mu = 50$.

Different parameter choices

We investigate different parameter sets by varying one parameter each time. For the first set of parameters, we have chosen to decrease the carrying capacity of species 2 to $K_2 = 60$, instead of $K_2 = 100$ used in the previous set. In the second set of parameters, we set the competition rate of species 2 to be 5 times higher than before ($k_2 = 5$ instead of $k_2 = 1$). Figures 7.14 and 7.15 show the results at time $t = 8$ for each set of parameters, respectively. Figures 7.14a and 7.15a show how the solutions evolve in time on the line $0 \leq \mathsf{r} \leq \mathsf{r}_N$ while Figures 7.14b and 7.15b show the final results at $t = 5$ over the complete circle. The model and the method used have proven to produce biologically relevant results in response to the parameter being altered and the results are matching the ones from the one-dimensional Cartesian coordinates case. We observe that the variation in the parameter values are affecting both the Cartesian coordinate and the radially symmetric cases in a similar manner. We notice a smooth spread of the nodes, without any tangling in both cases.

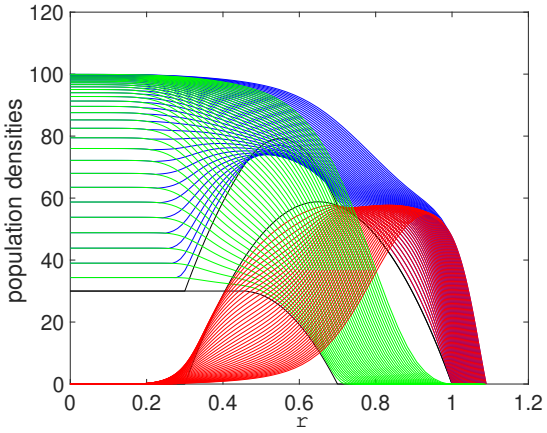

(a) The approximated solutions u (green), v (red) and $u+v$ (blue) plotted for every 0.20 time steps with final time $t = 8$.

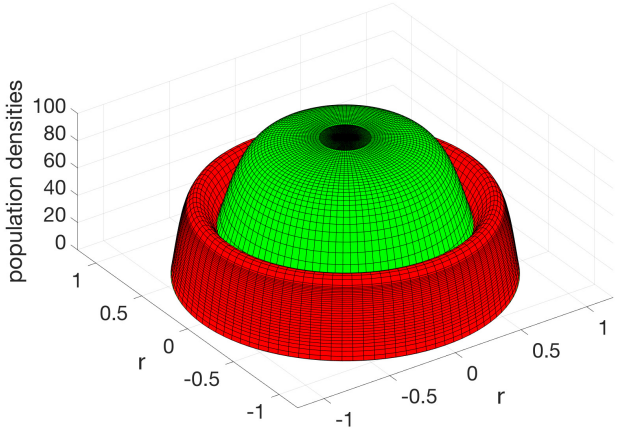

(b) The approximated solutions of u and v at $t = 8$ of the 2-dimensional radial L-V competition diffusion model.

Figure 7.14: The result of the competition-diffusion model at $t = 8$ with $\delta_1 = \delta_2 = 0.001$, $k_1 = k_2 = 1$, $K_1 = 100$, $K_2 = 60$, $r_1 = r_2 = 1$ and $\mu = 50$.

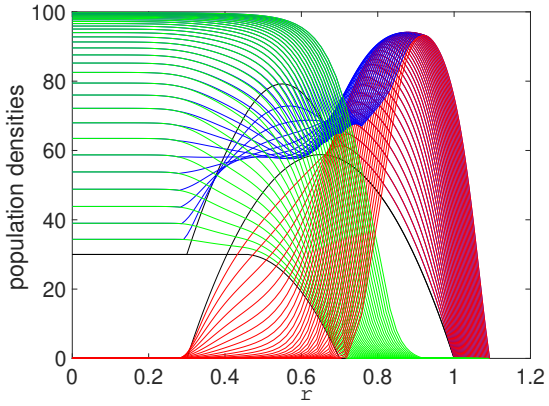

(a) The approximated solutions u (green), v (red) and $u+v$ (blue) plotted for every 0.20 time steps with final time $t = 7$.

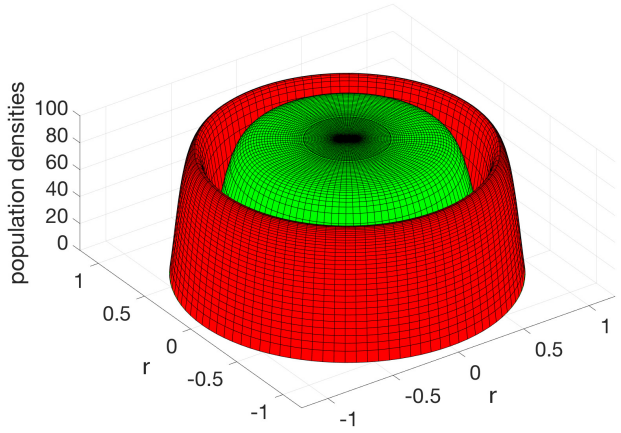

(b) The approximated solutions of u and v at $t = 7$ of the 2-dimensional radial L-V competition diffusion model.

Figure 7.15: The result of the competition-diffusion model at $t = 7$. Here we use $\delta_1 = \delta_2 = 0.001$, $k_1 = 1$, $k_2 = 5$, $K_1 = K_2 = 100$, $r_1 = r_2 = 1$ and $\mu = 50$.

7.6 Discussion

In this chapter, we have described a one-dimensional moving mesh finite difference numerical method based on local mass conservation for the approximate solution of a two-species Lotka-Volterra (L-V) competition system with a free boundary and moving internal interfaces.

The system consists of two species governed by coupled Lotka-Volterra equa-

tions in one dimension, partially coexisting in space and competing for common resources. The domain has a moving outer boundary and there are moving interfaces in the interior where species arise, overlap or disappear. We therefore considered an L-V model with distinct moving regions in which species are smooth, separated by interfaces with interface conditions.

Numerically, rather than allocate a separate mesh to each species (which would have led to the need for interpolation and a generally messy scheme), we used a single moving mesh for both species and adjusted the solution using the Arbitrary Lagrangian Euler (ALE) equations. The mesh is generated by preserving the total sum of local densities (therefore masses) at a point in time. We called this the combined mass approach, which allows the use of a single moving mesh in overlapping regions and handles moving interfaces. The combined mass procedure is general and can be applied to other overlapping situations.

We used a method to move the nodes based on the preservation of relative densities (i.e., those normalised by the total mass) since relative masses are conserved. Once the nodes had been moved, the local densities of each species were computed from ALE schemes. Throughout the chapter, we used an exponential time integrating scheme for nodal intervals which produces non-tangling meshes and is stable for sufficiently small time steps.

First, we solved the system using symmetrical initial conditions to ensure that the combined mass approach will maintain the symmetric properties of the problem, i.e., symmetric node velocities and solution. Then we implemented the model for a number of parameter combinations and observed a variety of scenarios. We have altered one parameter at a time from the initial set of parameters and observed various effects dominating in turn as the populations evolve through time. The illustrations indicate that the method is stable for a variety of different set-up parameters and can be applied to many other competition problems.

We also demonstrated that our moving mesh method with the combined mass approach can easily be extended to the radially symmetric two-dimensional case. However, when using finite differences, the two-dimensional case must be radially symmetric, which is not a limitation when using the finite element method. An advantage of using finite elements for the general two-dimensional case (instead of the radial case) is that the method can be applied to more general domains.

This chapter is proof-of-concept rather than exhaustive and can be refined in a number of ways. Also, the time step can be made semi-implicit, allowing larger time steps, albeit at the risk of losing accuracy.

We conclude that the approach can be used on a variety of ecological models involving multi-species populations and moving boundaries, and is capable of

simulating complex behaviour.

Future work will also include the adaptation of the parameters for use on empirical data sets and comparison of results against observations.

7.7 Summary

In this chapter we provided a detailed description of the new combined mass approach for approximating coupled equations with overlapping domains with moving interfaces and free boundaries by the moving mesh method based on conservation.

The combined mass approach was applied to a system involving the coupled equations of two competitive species with overlapping domains. The simulations for the one-dimensional Cartesian coordinate system were derived for different initial data and parameter values while we also demonstrated that the combined mass approach can also be easily applied to the radial case (2-D) as well. The illustrations presented give confidence that the new approach is suitable for approximating such coupled systems and provides a more neat, efficient and less computationally expensive process as it avoids the interpolation of the meshes at each time step. The results of this chapter indicate that the methodology can be generalised for more complex equations that are able to more realistically describe the species' behaviour and evolution through time.

In certain ecological contexts, reaction-diffusion models may not adequately describe how organisms move and disperse through space. Besides the classical Laplacian diffusion of Chapters 6 and 7 and the non-linear diffusion of Chapter 5, ecological modellers have included an advection term, as the one in Chapter 3 to describe the ability of living organisms to sense the stimulating signals in the environment and adjust movements accordingly [112]. Many authors have modelled the directed movements of species either through motion along gradients (taxis) or through cross/self-diffusion terms [48, 188].

This is the incentive for the study of the SIR (susceptible-infected-recovered) model in the following chapter. The SIR system includes self- and cross-diffusion which describe self-isolation and social distancing of individuals where the spread of the disease in the domain is modelled by a moving boundary.

In the next chapter we apply the concept of combined masses, as described in Chapter 7, to an epidemic SI(R) model with Fickian diffusion while later on, we apply the method to a system of multi-sub-populations (susceptible-infected-recovered-vaccinated) with density-dependent non-linear diffusion as the one presented in Chapter 5.

Chapter 8

Numerical Solution of a Reaction-Diffusion-Advection Epidemic Model with a Moving Boundary

This chapter considers the application of the moving mesh finite difference method based on mass conservation using the combined mass approach, as described in Chapter 7, for an epidemic model with Fickian diffusion describing the random motion of the sub-populations. Bias velocity is also incorporated in the model by the use of cross- and self-diffusion reflecting the effect of social distancing and self-isolation applied by individuals. The spread of the disease through the domain is modelled in the system by a moving boundary. We extend our study of the SI(R) (Susceptible-Infected-(Recovered)) system to a multi-species model consisting of four sub-populations (SIRV) (Susceptible-Infected-Recovered-Vaccinated) and demonstrate the application of the method on this multi-species system with non-linear density-dependent diffusion as described in Chapter 5.

8.1 Chapter Overview

Mathematical modelling is an effective tool for dealing with the evolution of disease outbreaks. This work outlines the importance of a particular SI(R) model with cross- and self-diffusion terms which describe the physical distancing and self-isolation applied by individuals. The motive is to gain useful predictions in the context of the impact of intervention in decreasing the number of infected-susceptible incidence rates and avoiding the risk of a rapid increase in demand

for medical services and, ultimately, the exhaustion of hospital resources and space. The most significant feature of the models discussed in this chapter is the moving, inner boundary, which describes the spread of the virus. A moving mesh finite difference method is used in which the node movement is based on the local mass preservation of the sub-populations combined mass. Illustrations reveal that social interactions play a vital role in disease transmission: in the spread of the disease through the domain and in the number of infections. We also demonstrate that the initially infected radius h_0 is also important in the spreading of the disease. Even if the reproductive parameter $R_e > 0$ the disease will not spread in the whole area if h_0 is sufficiently small. The method is also applied to a system of multi-sub-populations (SIRV) and the results give confidence that the combined mass approach is also suitable for systems consisting of more than two species (as illustrated so far).

8.2 Introduction

Mathematical models have long been used in epidemiology to provide quantitative information on the spread of diseases and to provide useful guidelines to outbreak management.

In particular, epidemic models have attracted great attention lately in mathematical ecology due to the outbreak of pneumonia caused by a novel coronavirus (COVID-19) [46, 5, 138, 41, 156, 114]. The well-known SIR models which are based on ordinary differential equations have been widely used in the past to describe the quantitative epidemic evolution dynamics of many diseases [108, 25, 180]. Such models classify the population into three subgroups namely 'susceptible' (S), 'infected' (I) and 'recovered' (R). In [46] authors used a simple prototype of a SIR model, first proposed by Kermack and McKendrick [93], to model the spread of COVID-19 in different communities. One can describe the population evolution through time by the following system of ordinary differential equations

$$\frac{dS}{dt} = -\beta S(t)I(t),$$

$$\frac{dI}{dt} = \beta S(t)I(t) - \alpha I(t) - \lambda I(t),$$

$$\frac{dR}{dt} = \lambda I(t),$$

where $\beta > 0$ is the infection rate, $\lambda > 0$ is the recovery rate and α is the rate of death due to the disease.
We can easily observe that for an epidemic to occur the number of infected should increase over time, i.e.,

$$\frac{dI}{dt} > 0$$

implying that

$$\beta SI - \alpha I - \lambda I > 0$$

giving

$$\frac{\beta S}{\alpha + \lambda} = R_e > 1,$$

where R_e is defined to be the basic reproductive rate as the fate of the evolution of the disease depends upon it. The value of R_e can determine whether the disease will lead to an epidemic or if it will die out quickly, e.g., if $\frac{dI}{dt} < 0 \implies R_e < 1$ the infected population will decrease monotonically to zero and if $\frac{dI}{dt} > 0 \implies R_e > 1$ will increase.

Even though results are shown to be useful both quantitatively and qualitatively, the model does not include many real-time complexities associated with the spread of the virus. A crucial drawback of such models is that they describe only spatially homogeneous dynamics.

A key issue in epidemic modelling is the formation of spatial patterns. Accounting for the spatial dynamics of the model can alter the outcome and the spread of the epidemic, especially in the case of COVID-19 where no vaccines were available for over a year after the outbreak of the pandemic and the isolation of the diagnosed infected and social distancing were the only measures available to combat the spread of the virus.

Therefore, disease-spreading theories such as the SIR model, have been extended to reaction-diffusion equations [57, 43, 19, 173]. These models, however, are based on the assumption that individuals disperse with a random diffusion, based on the Brownian motion, which does not incorporate general physical distancing and self-isolation applied by individuals. In general, reaction-diffusion systems in the context of population modelling only account for the interactions of individuals through the reaction terms and do not account for the influence of species interactions on the individuals' movement.

In certain ecological contexts, reaction-diffusion models may not adequately describe how organisms move and disperse through space [139]. Hence, many ecological and biological studies have examined a variety of other dispersal mechanisms,

especially those including density-dependent dispersal, in order to better model the motion of individuals beyond purely random movement [157].

When it comes to modelling living organisms one of the characteristic features is their ability to sense the stimulating signals in the environment and adjust movements accordingly. Species may be either completely ignorant of the surrounding environment nor will their movement perfectly track regions with better environmental conditions. More realistically, species should be modelled as a combination of both random and biased conditions. For instance, adding some amount of random motion to a purely directed movement dispersal strategy could help an individual escape a local environmental trap to find some distant but better sources [6]. This can be achieved by the addition of an advection term. Shigesada et al. [148] proposed cross-diffusion models to either describe species' tendency to avoid overcrowding or to model the directed movement of species towards better recourses. Over the past few decades, ecological modellers have included directed movements of species either through motion along gradients (taxis) or through cross/self-diffusion terms [92, 48, 63, 188, 109, 130].

The use of cross-diffusion to model the avoidance of the infected population by the susceptible is presented in [150] where in [22] authors suggested a spatially two-dimensional reaction-diffusion system for modelling the susceptible and infected populations when the spatial pattern formation is driven by cross-diffusion. They set the non-linear cross diffusion term (by which the susceptible population avoids the infected) to depend on the number of infected individuals, as awareness increases when there is an increase in infections. In [155] a two-dimensional SIR model is presented with a dynamical density functional theory to incorporate both self-isolation and social distancing. Most prior work related to disease transmission has focused on understanding the disease dynamic in the fixed domain.

In [95] and [105] authors studied the reaction-diffusion SIR model with one and two free boundaries, respectively, and provided useful theoretical results regarding the existence and uniqueness of results together with the sufficient conditions for the disease vanishing or spreading. Although these studies investigate the characteristics of the disease spreading in a moving area the work is still very limited for numerical methods approximating such free boundary problems.

In this chapter, a particular r-refinement adaptive scheme is described for the solution of one-dimensional epidemic models on moving domains with additional cross- and self-diffusion terms to model the effects of social distancing and self-isolation on the disease spreading. The work we present here preserves mass (or relative mass as appropriate), causing the mesh to naturally refine where the solution has high relative density. This is particularly useful for solutions

with blow-up, or (as demonstrated here) moving free boundaries. In particular, we apply the moving mesh finite difference method based on mass conservation [14, 103, 9] with the combined mass approach demonstrated in [15](Chapter 7) for a system of competitive species. An attractive aspect of the combined mass approach is that the entire system is approximated on a single mesh and hence no interpolation of the meshes is required to approximate the coupled equations. Only one mesh velocity is needed to update the nodal positions hence the approach of combined masses, compared to the standard application of the MMFDM, where each equation is assigned a unique mesh, is considered to be neater and less computationally expensive.

The structure of the chapter is as follows. Section 8.3 gives the description of the SIR model on a free boundary with advection terms in detail. A general description of the moving mesh method follows together with a relative conservation principle approach and the finite difference implementation. A MMFDM algorithm based on relative mass conservation is provided which is then used together with the combined mass approach to approximately solve the reaction-diffusion-advection SIR equations with a free boundary. In Section 8.8 illustrations are given for a variety of parameter choices observing the effects of social interactions on the spreading of the disease as well as various factors affecting the vanishing and spreading of the disease. The multi-species SIRV (susceptible-infected-recovered-vaccinated) model is presented in Section 8.6 and the application of the MMFDM based on the combined mass approach follows which allows the approximation of the system where illustrations of the results are shown in Section 8.8. Section 8.9 gives a brief discussion of the results and a potential future research direction.

8.3 Materials and Methods

8.3.1 The reaction-diffusion-advection SI(R) model with a moving boundary

We are considering a reaction-diffusion-advection SIR epidemic model with a free boundary which describes the spreading front of the disease as presented in [95]. We are also incorporating self- and cross-diffusion, similar to the ones in [22] but with constant coefficients, to model the effects of social distancing and self-isolation on the spread of the disease in a domain. The system below assumes that births and deaths due to other causes (apart from the disease) are balanced out and that the recovered individuals are assumed to be immune to the disease and can no longer transmit the virus to the susceptible ones. Therefore, we exclude the particular equation regarding the recovered ones from our model since the

main scope is to model the spread of the virus through the front.

Therefore, the extended version of the reaction-diffusion-advection SI(R) system with self- and cross-diffusion with a moving boundary can be described as

$$\frac{\partial z}{\partial t} = \delta \frac{\partial^2 z}{\partial x^2} + \frac{\partial}{\partial x}\left(z\left(\kappa_{si}\frac{\partial u}{\partial x} + \kappa_{sd}\frac{\partial z}{\partial x}\right)\right) - \beta z u \qquad x \in \mathcal{R}, t > 0 \tag{8.1}$$

$$\frac{\partial u}{\partial t} = \delta \frac{\partial^2 u}{\partial x^2} + \frac{\partial}{\partial x}\left(u\left(\kappa_{si}\frac{\partial u}{\partial x} + \kappa_{si}\frac{\partial z}{\partial x}\right)\right) + \beta z u - \lambda u - \alpha u \tag{8.2}$$

$$x \in \mathcal{R}_u(t), t > 0$$

where z and u denote the susceptible and the infected subpopulation densities respectively. All the variables and the parameters are described in Table 8.1. We set the total domain to be denoted by $\mathcal{R}$ while $\mathcal{R}_u(t)$ is a sub-region in $\mathcal{R}$. Susceptibles are initially set to occupy the whole domain $\mathcal{R}$ while in $\mathcal{R}_u(t)$ both sub-populations co-exist.

Variable/Parameter	Description
t	time
x	space
z	the susceptible population density
u	the infected population density
δ	Diffusion parameter
β	Risk of infection
α	Virus-induced average fatality rate
λ	Recovery rate of infectious individuals
μ	Interface condition parameter
κ_{si}	cross diffusion pressure due to self-isolation
κ_{sd}	self-diffusion pressure due to social distancing

Table 8.1: Description of the variables and parameters used in the model.

Inner free boundary conditions
The infected population is spreading through the domain by a moving front which is denoted by $h(t)$. The infected population density is zero at the moving front and the equation governing the free boundary corresponds to the well-known Stefan condition. These two conditions are expressed by

$$u(x,t) = 0 \qquad x \geq h(t),\ t \geq 0$$

and

$$\frac{dh}{dt} = -\delta\mu\frac{\partial u}{\partial x}(h(t),t) \qquad t \geq 0. \tag{8.3}$$

The parameter μ is proportional to the preferred population density at the spreading front. For the ecological background of free and moving boundary conditions refer to [53].

External boundary conditions
For the two external fixed boundaries of the domain $\mathcal{R}$ which are denoted by $x = a$ and $x = b$ (i.e., $[a, b]$) we use homogeneous Neumann boundary conditions that imply that the above system is self-contained and there is no migration across the boundaries, i.e.,

$$\frac{\partial u}{\partial x} = 0 \qquad x = a \quad t \geq 0 \tag{8.4}$$

and

$$\frac{\partial z}{\partial x} = 0 \qquad x = a, x = b \quad t \geq 0. \tag{8.5}$$

Cross and self-diffusion
The avoidance of the infected sub-population by the susceptible is incorporated into the model by the use of a positive non-linear cross-diffusion term $\frac{\partial}{\partial x}\left(\kappa_{si} z \frac{\partial u}{\partial x}\right)$. This term directs the flow of the susceptible in the direction opposite to the gradient of u. This, however, does not incorporate general physical distancing also between the susceptible individuals (which is required if infected persons cannot generally be identified as such). The repulsion within the susceptible subgroup is considered by the positive non-linear self-diffusion term $\frac{\partial}{\partial x}\left(\kappa_{sd} z \frac{\partial z}{\partial x}\right)$ where the flow is into the opposite direction of the gradient $\frac{\partial z}{\partial x}$. The directed motion of infected species in the opposite direction of $\frac{\partial u}{\partial x}$ and $\frac{\partial z}{\partial x}$ is described by similar terms as in the equation of the susceptible. The constant κ_{si} is the pressure/interaction strength due to the isolation of the infected whereas the κ_{sd} is the self-diffusion pressure due to the social distancing applied by the susceptible individuals.

We use a velocity-based moving mesh finite difference method based on conservation with the combined mass approach as described in [15] for the numerical treatment of the above reaction-diffusion-advection SI(R) system with a moving boundary. The procedure is described below.

8.3.2 Conservation-based moving mesh methods

We introduce a time-dependent space coordinate $\tilde{x}(x,t)$ which coincides instantaneously with the fixed coordinate x. Consider two such coordinates, $\tilde{x}(x_1,t)$

and $\tilde{x}(x_2, t)$, in $(a(t), b(t))$, abbreviated to $\tilde{x}_1(t)$ and $\tilde{x}_2(t)$.
The rate of change of the mass in the sub-interval $(\tilde{x}_1(t), \tilde{x}_2(t))$ is given by Leibniz integral rule in the form

$$\frac{d}{dt}\int_{\tilde{x}_1(t)}^{\tilde{x}_2(t)} u(\varsigma, t)\ \mathrm{d}\varsigma = \int_{\tilde{x}_1(t)}^{\tilde{x}_2(t)} \left(\frac{\partial u(\varsigma, t)}{\partial t} + \frac{\partial}{\partial \varsigma}\left(u(\varsigma, t) w(\varsigma, t)\right)\right)\ \mathrm{d}\varsigma,$$

where

$$w(x, t) = \left.\frac{d\tilde{x}}{dt}\right|_{\tilde{x}=x} \tag{8.6}$$

is a local velocity.
We denote the total mass in the domain $(a(t), b(t))$ by

$$\theta(t) = \int_{a(t)}^{b(t)} u(x, t)\ \mathrm{d}x \tag{8.7}$$

and the mass in the interval $(\tilde{x}_1(t), \tilde{x}_2(t))$ by

$$\theta_m(t) = \int_{\tilde{x}_1(t)}^{\tilde{x}_2(t)} u(\varsigma, t)\ \mathrm{d}\varsigma,$$

where m specifies the interval $(\tilde{x}_1(t), \tilde{x}_2(t))$. We recall that for problems conserving the total (global) mass, i.e., $\frac{d\theta}{dt} = \dot{\theta}(t) = 0$, the theory of moving mesh based on mass conservation is constructed by supposing that partial masses within any spatial interval is conserved in time, i.e., $\dot{\theta}_m(t) = 0$.

For more general problems that do not conserve mass, $\theta(t)$ (defined by (8.7)) varies with time hence such an assumption is unreasonable. In such cases, the theory uses the normalised function $u(\tilde{x}, t)/\theta(t)$ which gives the relative density $\hat{u}$.

For example, the total relative mass is given by

$$\int_{a(t)}^{b(t)} \frac{u(\tilde{x}, t)}{\theta(t)}\ \mathrm{d}x$$

which equals unity making it compatible to suppose that the local relative mass given by

$$\int_{\tilde{x}_1(t)}^{\tilde{x}_2(t)} \frac{u(\varsigma, t)}{\theta(t)}\ \mathrm{d}\varsigma$$

is conserved in time.
Therefore,

$$\int_{\tilde{x}_1(t)}^{\tilde{x}_2(t)} \frac{u(\varsigma, t)}{\theta(t)}\ \mathrm{d}\varsigma = \int_{\tilde{x}_1(t)}^{\tilde{x}_2(t)} \hat{u}(\varsigma, t)\ \mathrm{d}\varsigma = \gamma(\tilde{x}_1(t), \tilde{x}_2(t)) \tag{8.8}$$

is constant in time.
We now make use of the Leibniz integral rule applied to the relative density $\hat{u}$

$$\frac{d}{dt}\int_{\tilde{x}_1(t)}^{\tilde{x}_2(t)} \hat{u}(\varsigma,t)\ \mathrm{d}\varsigma = \int_{\tilde{x}_1(t)}^{\tilde{x}_2(t)} \left(\frac{\partial \hat{u}(\varsigma,t)}{\partial t} + \frac{\partial}{\partial \varsigma}\left(\hat{u}(\varsigma,t)\hat{w}(\varsigma,t)\right)\right)\ \mathrm{d}\varsigma. \tag{8.9}$$

The left hand side of (8.9) is zero and the term $\frac{\partial \hat{u}(s,t)}{\partial t}$ is given by

$$\frac{\partial \hat{u}}{\partial t} = \frac{\partial}{\partial t}\left(\frac{u}{\theta}\right) = \frac{1}{\theta}\frac{\partial u}{\partial t} - \frac{\dot{\theta}}{\theta^2}u,$$

where $\dot{\theta} = d\theta/dt$.
Then (8.9) becomes

$$\int_{\tilde{x}_1(t)}^{\tilde{x}_2(t)} \left(\frac{1}{\theta}\frac{\partial u}{\partial t} - \frac{\dot{\theta}}{\theta^2}u\right)\ \mathrm{d}\varsigma + [\hat{u}\hat{w}]_{\tilde{x}_1}^{\tilde{x}_2} = 0$$

and by (8.8),

$$\int_{\tilde{x}_1(t)}^{\tilde{x}_2(t)} \left(\frac{\partial u}{\partial t}\right)\ \mathrm{d}\varsigma - \dot{\theta}\gamma\left(\tilde{x}_1(t),\tilde{x}_2(t)\right) + \theta[\hat{u}\hat{w}]_{\tilde{x}_1}^{\tilde{x}_2} = 0,$$

leading to

$$[uw]_{\tilde{x}_1}^{\tilde{x}_2} = -\left(\int_{\tilde{x}_1(t)}^{\tilde{x}_2(t)} \left(\frac{\partial u}{\partial t}\right)\ \mathrm{d}\varsigma - \dot{\theta}\gamma\left(\tilde{x}_1(t),\tilde{x}_2(t)\right)\right), \tag{8.10}$$

since $\theta[\hat{u}\hat{w}]_{\tilde{x}_1}^{\tilde{x}_2} = [uw]_{\tilde{x}_1}^{\tilde{x}_2}$.

Equation (8.10) can be used to obtain the nodal velocities uniquely at all interior points, provided the flux $[uw]$ is known at a point and that $u(x,t) > 0$ in the interior of the domain.
To evaluate $\dot{\theta}$ we integrate (8.9) from $a(t)$ to $b(t)$, assuming that $u(x,t)$ and $w(x,t)$ are continuous up to the boundary, yielding

$$\dot{\theta} = \int_{a(t)}^{b(t)} \left(\frac{\partial u}{\partial t}\right)\ \mathrm{d}x + [uw]_{a(t)}^{b(t)}. \tag{8.11}$$

Then, given $\dot{\theta}$ and w, the updated value of θ and the new position of the points $\tilde{x}(x,t)$ can be evaluated respectively using a time integration scheme, such as the explicit Euler, which are then used to recover the solution of $u(\tilde{x}(t),t)$ by (8.8), i.e.,

$$\int_{\tilde{x}_1(t)}^{\tilde{x}_2(t)} \frac{u(\varsigma,t)}{\theta(t)}\ \mathrm{d}\varsigma = \int_{\tilde{x}_1(0)}^{\tilde{x}_2(0)} \frac{u(\varsigma,0)}{\theta(0)}\ \mathrm{d}\varsigma$$

implying that

$$\int_{\tilde{x}_1(t)}^{\tilde{x}_2(t)} u(\varsigma, t)\ \mathrm{d}\varsigma = \theta(t)\gamma(\tilde{x}_1(0), \tilde{x}_2(0)),$$

where the constant γ is given by (8.8) using the initial data $u(x, 0)$ and $\theta(0)$. Applying a one-point quadrature approximation leads to

$$u(x, t) = \frac{\theta(0)\gamma(\tilde{x}_1(0), \tilde{x}_2(0))}{\tilde{x}_2(t) - \tilde{x}_1(t)}. \tag{8.12}$$

Finite Difference method

We now define a finite difference method based on this theory, with the following notation. Given a time step $\Delta t > 0$ and a fixed number $N + 1$ of spatial nodes, choose discrete times $t^n = n\Delta t$, $n = 0, 1, ...$, and discretize the interval at each discrete time t^n using the nodal points $\tilde{x}_i^n = \tilde{x}_i(t^n)$, $i = 0, 1, \ldots, N$, for which $a = \tilde{x}_0^n < \tilde{x}_1^n < \ldots < \tilde{x}_N^n = b$.

Also define approximations $u_i^n \approx u(\tilde{x}_i, t^n)$, $z_i^n \approx z(\tilde{x}_i, t^n)$, $w_i^n \approx w(\tilde{x}_i, t^n)$, $\theta^n \approx \theta(t^n)$ and $\dot{\theta}^n \approx \dot{\theta}(t^n)$.

Before proceeding further to the general algorithm of the moving mesh based on conservation as given above, we discuss some considerations regarding the time integration schemes and stability remarks.

Time-stepping and stability remarks

Time-stepping $x_i(t)$ In numerical approximation schemes, the size of the time step is often associated with stability considerations depending on the numerical method used. A further issue that arises concerning moving mesh methods is mesh overtaking which occurs when the order of the nodes changes due to the poor discretization of the problem. Thus, time steps are sought that preserve the order of the nodes in the case of moving mesh methods and to prevent the numerical approximations from exhibiting unstable behaviour for both moving and fixed mesh methods.

For the time integration, the most common choice is an explicit Euler time-stepping approach which is often used to update the nodal positions at each time by

$$\tilde{x}_i^{n+1} = \tilde{x}_i^n + \Delta t w_i^n. \tag{8.13}$$

However, it does not imply that the order of the nodes will be preserved. A sufficient condition to prevent node overtaking can be derived from (8.13). For example, assume that at time n the order of the nodes is preserved, then in order for the nodes $i+1$ and i to remain ordered after a further time step the inequality

$$\tilde{x}_{i+1}^{n+1} > \tilde{x}_i^{n+1} \tag{8.14}$$

must hold.
Using the explicit Euler scheme (8.13) the inequality (8.14) becomes,

$$\tilde{x}_{i+1}^n + \Delta t w_{i+1}^n > \tilde{x}_i^n + \Delta t w_i^n. \tag{8.15}$$

Rearranging (8.15) to determine a restriction for Δt gives,

$$\Delta t < \frac{\tilde{x}_{i+1}^n - \tilde{x}_i^n}{w_i^n - w_{i+1}^n}. \tag{8.16}$$

For node crossing to occur the inequality $w_i^n > w_{i+1}^n$ must hold which implies that $w_i^n - w_{i+1}^n > 0$. The inequality (8.16) only holds if node crossing occurs and leads us to a restriction in the size of Δt given

$$\Delta t < \frac{\tilde{x}_{i+1}^n - \tilde{x}_i^n}{w_i^n - w_{i+1}^n} \qquad \text{if} \quad w_i^n > w_{i+1}^n, \tag{8.17}$$

and no restriction otherwise.

Even though the condition (8.16) ensures that no node crossing will occur there are some drawbacks to using the above condition. The first issue that arises with this requirement of the time step is that it does not guarantee that the time step will not approach zero and stop the method from proceeding. If for example the node $\tilde{x}_{i+1}$ is stationary and $\tilde{x}_i$ moves with a constant velocity w_i, as $\tilde{x}_i$ is approaching $\tilde{x}_{i+1}$, the time step will be approaching zero. Another drawback is that even though node crossing is avoided, the condition (8.16) does not imply stability. Equation (8.16) ensures that $\tilde{x}_{i+1}^n - \tilde{x}_i^n > 0$ but it does not specify a limit on how small this interval can be. If for example, we apply a simple quadrature to the relative conservation principle (8.8) giving

$$\frac{1}{\theta}(\tilde{x}_{i+1}^n - \tilde{x}_i^n) u_i^n = \gamma_i, \tag{8.18}$$

where if the $\tilde{x}_{i+1}^n - \tilde{x}_i^n$ is arbitrarily small then u_i^n can grow arbitrarily large. Therefore, even if $\Delta\tilde{x}_i$ $(\tilde{x}_{i+1}^n - \tilde{x}_i^n)$ remains positive, non-smooth behaviour (e.g., oscillations) can occur when Δx_i is vanishingly small due to build-up of errors. Moreover, the consequent behaviour of u_i^n is then also non-smooth due to the use of conservation, equation (8.18), to get u_i^n and there is no mechanism for controlling oscillations in u_i^n.
However, there are other time-integration schemes which are not restricted by

the condition (8.17) in the time step size to prevent nodes from overtaking. Such schemes allow the use of a larger Δt, still preserving the order of the nodes, but as in the explicit Euler scheme they do not prevent oscillations in u_i^n (i.e., when $\tilde{x}_{i+1}^n - \tilde{x}_i^n$ is very small).
For example, in [12] Baines proposed an alternative scheme for preserving the node order which has the same order of accuracy as the explicit Euler scheme. He focused on the differences between the nodal positions $\tilde{x}_{i+1}$ and $\tilde{x}_i$ denoted as $\Delta\tilde{x}_i$ and the differences between the nodal velocities w_{i+1} and w_i denoted as Δw_i. He introduced the following scheme which uses an amplification factor in the form of an exponential

$$\Delta\tilde{x}_i^{n+1} = \Delta\tilde{x}_i^n \exp\left(\Delta t \frac{\Delta w_i^n}{\Delta\tilde{x}_i^n}\right). \tag{8.19}$$

As shown above, the only way mesh overtaking will occur is if $\tilde{x}_i > \tilde{x}_{i+1}$ and therefore having a negative Δw_i. As the exponential is always positive the sign of $\Delta\tilde{x}_i$ is unchanged in a time step regardless of the sign of Δw_i, thus preserving the ordering of the nodes. Therefore, given $\tilde{x}_i^{n+1}$ at one point we can update the nodal positions using the differences $\Delta\tilde{x}_i^{n+1}$, i.e.,

$$\tilde{x}_i^{n+1} = \tilde{x}_0^{n+1} + \sum_{i=0}^{i} \Delta\tilde{x}_i^{n+1}, \qquad (i = 1, \ldots, N-1). \tag{8.20}$$

Again, even if the scheme ensures no mesh tangling, there is no restriction on the size of $\Delta\tilde{x}_i^{n+1}$, i.e., how small $\Delta\tilde{x}_i^{n+1}$ can be.

Time-stepping $\theta(t)$ In updating the total mass $\theta(t)$, it is important to ensure that θ^{n+1} will remain positive so that the condition $u > 0$ will not be violated. An explicit Euler scheme, like the one in (8.13), for updating θ does not imply that θ^{n+1} will remain positive. For example, if $\dot{\theta} < 0$ the explicit Euler scheme can lead to a negative θ^{n+1} for large Δt.

In order to preserve the positive sign of θ even if $\dot{\theta}$ is negative, we also use the exponential time stepping scheme of (8.19). For example, the first-order exponential time-stepping scheme for updating θ is

$$\theta^{n+1} = \theta^n \exp\left(\Delta t \frac{\dot{\theta}^n}{\theta^n}\right). \tag{8.21}$$

Hence, our finite difference moving mesh algorithm for non-mass-conserving problems is as follows.

Algorithm

Choose initial node positions $\tilde{x}_i^0$, $i = 0, 1, \ldots N$ with corresponding approximate solution values $u_i^0 > 0$, $i = 0, 1, \ldots, N$ and derive $\Delta\tilde{x}_i^0$. Then calculate the approximate relative masses of (8.8) within each interval by,

$$\gamma_i = \frac{1}{\theta^0}(\tilde{x}_i^0 - \tilde{x}_{i-1}^0)u_i^0, \qquad (i = 1, \ldots, N), \tag{8.22}$$

where θ^0, the initial value of θ is given from (8.7) by

$$\theta^0 = \frac{1}{2}\sum_i (\tilde{x}_{i+1}^0 - \tilde{x}_i^0)(u_i^0 + u_{i+1}^0). \tag{8.23}$$

Then at time t^n for $n = 1, 2, \ldots$, given θ^n, $\tilde{x}_i^n$ and u_i^n we compute θ^{n+1}, $\tilde{x}_i^{n+1}$ and u_i^{n+1} as follows:

1. Evaluate the rate of change of the total mass $\dot{\theta}^n$ from (8.11) in the form

$$\dot{\theta}^n = \int_{\tilde{x}_0^n}^{\tilde{x}_N^n} \frac{\partial u}{\partial t}\, \mathrm{d}s + u_N^n w_N^n - u_0^n w_0^n.$$

2. Evaluate the discrete velocity at interior points from (8.10) by specifying an anchor point, say $\tilde{x}_0$,

$$w_i^n = \frac{u_0^n w_0^n - \int_{\tilde{x}_0^n}^{\tilde{x}_i^n} \frac{\partial u}{\partial t}\, \mathrm{d}s + \dot{\theta}\gamma(\tilde{x}_0, \tilde{x}_i)}{u_i^n}, \quad (i = 1, \ldots, N-1). \tag{8.24}$$

   The equation above can be solved by substituting the governing PDE where the derivative terms are evaluated by a one-sided approximation and the integral of the reaction terms by the trapezium rule over the summation $\sum_{j=0}^{i}$. In order to evaluate $\gamma(\tilde{x}_0, \tilde{x}_i)$ we are summing all γ_i over the interval $(\tilde{x}_0, \tilde{x}_i)$.
   The velocities at the moving boundaries can be extrapolated from the velocity of the interior values. Then we derive Δw_i^n for all the intervals.

3. Evolve both the nodal positions $\tilde{x}_i^n$, $i = 1, \ldots, N-1$, and the total mass θ^n from t^n to time t^{n+1} by the exponential time-stepping schemes (8.19) and (8.21) respectively.

4. Recover the solution u_i^n at the interior points from (8.8) by

$$u_i^{n+1} = \frac{\gamma_i \theta^{n+1}}{\Delta\tilde{x}_i^{n+1}}, \quad (i = 1, \ldots, N-1)$$

with the approximated solution at the boundaries of the domain u_0^{n+1} and u_{N+1}^{n+1} being updated either from given boundary conditions or by extrapolation, depending on the nature of the problem.

The theory and method described above are general and can be applied to a large range of partial differential equations including equations involving fluid flow, heat transfer or diffusion as well as equations in mathematical biology and in other fields.
In the following section, we apply the method described in Section 8.3.1 to the SI(R) model in epidemiology with a moving boundary ((8.1) and (8.2)).

8.3.3 Numerical solution for a SI(R) system with the disease spreading front

Since each population occupies a different part of the domain, therefore having a unique mesh, interpolation would be needed at each time step for each mesh to approximate both the advection and reaction terms of (8.1) and (8.2). Therefore we make use of the combined mass approach for the moving mesh method as presented in [15] (Chapter 7) by considering the combined mass of the two populations in regions of species coexistence. This will allow us to solve the entire system on a single mesh.
Therefore we are considering the mass at a specific location to be the combined mass of the densities u and z $(u + z)$ and we move the mesh by supposing that the fractions of the relative mass are preserved in time.
For ease of exposition, we drop *tilde*($\tilde{}$) for the rest of the chapter.

We start by dividing the domain into two parts $\mathcal{R}_-$ and $\mathcal{R}_+$ separated by the disease front $h(t)$ which is initially located at $x = 0.3$ (see Figure 8.1). $\mathcal{R}_-$ denotes the overlapping region on the left-hand side of $h(t)$ and $\mathcal{R}_+$ depicts the region on the right-hand side of $h(t)$. Note here that $u = 0$ in $\mathcal{R}_+$.
We create a mesh with $N+1$ equally spaced time-dependent nodes. At time level $t = t^n$ the mesh points are defined by

$$0 = x_0 < x_1^n < \ldots < x_h^n < \ldots < x_N = 1,$$

where the node x_h^n depicts the disease front $h(t)$. Note that from the boundary conditions, the velocity of the end nodes of the domain is zero. We approximate the population densities $u(x,t)$ and $z(x,t)$ by u_i^n and z_i^n, and the velocity $w(x,t)$ by w_i^n. We also define the approximations for $\theta(t)$ and $\dot{\theta}(t)$ by θ^n and $\dot{\theta}^n$, respectively.
The initial values θ_-^0 and θ_+^0 of the total masses θ in each region $\mathcal{R}_-$ and $\mathcal{R}_+$, respectively, are estimated from (8.7) using the combined mass of the sub-populations,

i.e.,

$$\theta(t) = \int_{x_0}^{x_h} (u(x,t) + z(x,t)) \, \mathrm{d}x \tag{8.25}$$

and by the composite trapezium rule (*cf.* (8.23))

$$\theta_-^0 = \frac{1}{2} \sum_{i=0}^{h^-} (x_{i+1}^0 - x_i^0)(u_i^0 + z_i^0) \tag{8.26}$$

Similarly for region $\mathcal{R}_+$ where only z exists

$$\theta_+^0 = \frac{1}{2} \sum_{i=h^+}^{N} (x_i^0 - x_{i-1}^0) z_i^0, \tag{8.27}$$

where the constant-in-time relative masses γ_i are approximated by (8.8), (*cf.*. (8.22))

$$\gamma_i = \frac{1}{\theta_-^0} (x_{i+1}^0 - x_i^0)(u_i^0 + z_i^0), \quad (i = 0, \ldots, h^-) \tag{8.28}$$

and

$$\gamma_i = \frac{1}{\theta_+^0} (x_i^0 - x_{i-1}^0) z_i^0, \quad (i = h^+, \ldots, N), \tag{8.29}$$

where h^- and h^+ denote the nodes immediately on the left and on the right of h, respectively.
Then, at each time-step following the algorithm in Section 8.3.2 we proceed as follows.

8.3.4 Approximating the interface velocity

We use one-sided approximation for the derivative term of (8.3) to evaluate the velocity at the boundary $h(t)$,

$$\frac{\mathrm{d}h}{\mathrm{d}t} = -\delta\mu \left(\frac{u(h) - u(h^-)}{x(h) - x(h^-)} \right) \tag{8.30}$$

with h^- being the node immediately on the left of h.

8.3.5 Approximating the velocity of the interior points

Starting with region $\mathcal{R}_-$ and setting the anchor point to be $x = 0$, by (8.10), the velocity w_i^n can be evaluated by, (*cf.* (8.24))

$$w_i^n(u_i^n + z_i^n) = w_0^n(u_0^n + z_0^n) - \int_{x_0^n}^{x_i^n} \left(\frac{\partial z(\varsigma, t^n)}{\partial t} + \frac{\partial u(\varsigma, t^n)}{\partial t} \right) \, \mathrm{d}\varsigma + \gamma_m \dot{\theta}_-^n, \quad (8.31)$$

where m denotes the interval (x_0^n, x_i^n).
By substituting (8.1) and (8.2) in (8.31) and since $w_0^n = 0$ the velocity equation for the nodes in region $\mathcal{R}_-$ is,

$$\begin{aligned} w_i^n = & \frac{1}{(u_i^n + z_i^n)} \Bigg(\gamma_m \dot{\theta}_-^n \\ & - \int_{x_0^n}^{x_i^n} \left(\delta \frac{\partial^2 z}{\partial x^2} + \frac{\partial}{\partial x} \left(z \left(\kappa_{si} \frac{\partial u}{\partial x} + \kappa_{sd} \frac{\partial z}{\partial x} \right) \right) + u(x,t) \left(\beta z(x,t) - \alpha - \lambda \right) \right) \, \mathrm{d}\varsigma \\ & - \int_{x_0^n}^{x_i^n} \left(\delta \frac{\partial^2 u}{\partial x^2} + \frac{\partial}{\partial x} \left(\kappa_{si} u \left(\frac{\partial u}{\partial x} + \frac{\partial z}{\partial x} \right) \right) - \beta z(x,t) u(x,t) \right) \, \mathrm{d}\varsigma \Bigg), \end{aligned}$$

provided $u_i^n + z_i^n \neq 0$.
Finally, by performing the integration and the zero Neumann boundary conditions for the node x_0^n,

$$\begin{aligned} w_i^n = \frac{1}{(u_i^n + z_i^n)} \Bigg(& \gamma_m \dot{\theta}_-^n - \delta \frac{\partial z}{\partial x}\bigg|_{x_i^n} - \delta \frac{\partial u}{\partial x}\bigg|_{x_i^n} - z \left(\kappa_{si} \frac{\partial u}{\partial x} + \kappa_{sd} \frac{\partial z}{\partial x} \right) \bigg|_{x_i^n} \\ & - \kappa_{si} u \left(\frac{\partial u}{\partial x} + \frac{\partial z}{\partial x} \right) \bigg|_{x_i^n} - \int_{x_0^n}^{x_i^n} \left(-\alpha u(x,t) - \lambda u(x,t) \right) \, \mathrm{d}\varsigma, \quad (8.32) \end{aligned}$$

where the derivatives are approximated by one-sided approximation and the integration of the reaction terms by the trapezium rule over the summation $\sum_{j=0}^{i=1,\ldots,h^-}$. The constant γ_m is evaluated by summing all γ_i over the interval m, $\gamma(x_0^n, x_i^n) = \sum_{j=0}^{i} \gamma_j$ for $i = 1, \ldots, h^-$.
In the same way, we can obtain the velocity equation for the interior nodes of the region $\mathcal{R}_+$ from (8.10), by setting the anchor point $x = h$.
So, the velocity w_i^n in $\mathcal{R}_+$ satisfies

$$w_i^n(z_i^n) = w_h^n(z_h^n) + \int_{x_h^n}^{x_i^n} \left(\frac{\partial z(\varsigma, t^n)}{\partial t} \right) \, \mathrm{d}\varsigma - \gamma_m \dot{\theta}_+^n, \tag{8.33}$$

where m denotes the interval (x_h^n, x_i^n).
We then substitute (8.1) in (8.33) giving,

$$w_i^n = \frac{1}{z_i^n} \left(w_h^n(z_h^n) + \int_{x_h^n}^{x_i^n} \left(\delta \frac{\partial^2 z}{\partial x^2} + \frac{\partial}{\partial x} \left(z \left(\kappa_{si} \frac{\partial u}{\partial x} + \kappa_{sd} \frac{\partial z}{\partial x} \right) \right) \right) \, \mathrm{d}\varsigma - \gamma_m \dot{\theta}_+^n \right), \tag{8.34}$$

since $u = 0$ in $\mathcal{R}_+$, provided $z_i^n \neq 0$.
By performing the integration,

$$w_i^n = \frac{1}{z_i^n} \left(\delta \frac{\partial z}{\partial x} \Bigg|_{x_h^n}^{x_i^n} + z \left(\kappa_{si} \frac{\partial u}{\partial x} + \kappa_{sd} \frac{\partial z}{\partial x} \right) \Bigg|_{x_h^n}^{x_i^n} - \gamma_m \dot{\theta}_+^n \right), \tag{8.35}$$

since $u = 0$ in $\mathcal{R}_+$ the reaction term of equation (8.1) is zero. The derivative terms can be now approximated by one-sided approximation where γ_m here is evaluated by summing all γ_i over the interval m, i.e., $\gamma(x_h^n, x_i^n) = \sum_{j=h}^{i} \gamma_j$ for $i = h^+, \ldots, i$.

8.3.6 Approximating the rates of change of the populations

The rates of change of the total populations in each region can be evaluated by (8.32) and (8.35) in the region $\mathcal{R}_-$ and $\mathcal{R}_+$, respectively, by setting x_i^n in $\mathcal{R}_-$ at $x_i = x_h$ and for the region $\mathcal{R}_+$ at $x_i = x_N$. A more detailed calculation follows.
In $\mathcal{R}_{h^-}$, by setting $x_i = x_h$ equation (8.32) becomes,

$$w_h^n(u_h^n + z_h^n) = w_0^n(u_0^n + z_0^n) - \int_{x_0^n}^{x_h^n} \left(\frac{\partial z(\varsigma, t^n)}{\partial t} + \frac{\partial u(\varsigma, t^n)}{\partial t} \right) \, \mathrm{d}\varsigma + \gamma_m \dot{\theta}_-^n,$$

where m is the interval (x_0^n, x_h^n).
Substituting equations (8.1) and (8.2) and performing the integration and the boundary conditions the equation for $\dot{\theta}^n$ in $\mathcal{R}_-$ is

$$\dot{\theta}_{-}^{n} = \delta \frac{\partial z}{\partial x}\bigg|_{x_h^n} + \delta \frac{\partial u}{\partial x}\bigg|_{x_h^n} + z\left(\kappa_{si}\frac{\partial u}{\partial x} + \kappa_{sd}\frac{\partial z}{\partial x}\right)\bigg|_{x_h^n} + \kappa_{si}u\left(\frac{\partial u}{\partial x} + \frac{\partial z}{\partial x}\right)\bigg|_{x_h^n} + \int_{x_0^n}^{x_h^n} \left(-\alpha u(x,t) - \lambda u(x,t)\right)\, \mathrm{d}\varsigma. \quad (8.36)$$

Note that summing γ_m over the interval (x_0^n, x_h^n) gives 1. Again, we approximate the derivative terms by one-sided approximation and the integration of the reaction terms by the trapezium rule over the summation $\sum_{j=0}^{i=h}$. Finally, in $\mathcal{R}_+$, by setting $x_i = x_N$ equation (8.35) becomes,

$$w_N^n z_N^n = w_h^n z_h^n - \int_{x_h^n}^{x_N^n} \frac{\partial z(\varsigma, t^n)}{\partial t}\, \mathrm{d}\varsigma + \gamma_m \dot{\theta}_{+}^{n}, \quad (8.37)$$

where m here denotes the interval (x_h^n, x_N^n).
Since $w_N^n = 0$,

$$\gamma_m \dot{\theta}_{+}^{n} = \int_{x_h^n}^{x_N^n} \frac{\partial z(\varsigma, t^n)}{\partial t}\, \mathrm{d}\varsigma - w_h^n z_h^n. \quad (8.38)$$

Substituting (8.1) in (8.38), performing the integration and applying the zero Neumann boundary condition at the right-end boundary gives,

$$\dot{\theta}_{+}^{n} = -\delta \frac{\partial z}{\partial x}\bigg|_{x_h^n} - z\left(\kappa_{si}\frac{\partial u}{\partial x} + \kappa_{sd}\frac{\partial z}{\partial x}\right)\bigg|_{x_h^n} - w_h^n z_h^n, \quad (8.39)$$

since summing over γ_m over the interval (x_h^n, x_N^n) gives 1.
The new mesh is obtained at time $t^{n+1} = t^n + \Delta t$ by the exponential time-stepping scheme (8.20). Likewise for the new masses in each region by (8.21). For example, the equation for updating the new node position is given by

$$x_i^{n+1} = x_0^{n+1} + \sum_{j=0}^{i} \Delta x_i^{n+1}, \qquad (i = 1, \ldots, N-1), \quad (8.40)$$

where the equation for updating the masses in each region $\mathcal{R}_-$ and $\mathcal{R}_+$, respectively is

$$\theta_{-}^{n+1} = \theta_{-}^{n} \exp\left(\Delta t \frac{\dot{\theta}_{-}^{n}}{\theta_{-}^{n}}\right) \quad (8.41)$$

and

$$\theta_+^{n+1} = \theta_+^n \exp\left(\Delta t \frac{\dot{\theta}_+^n}{\theta_+^n}\right). \tag{8.42}$$

Having found the new location of the nodes and the new masses in each region, we can now update the population densities u and z in each region at the new time t^{n+1}.

To get u and z individually in the region $\mathcal{R}_-$ we can use the Leibniz integral rule using the updated x-positions in the form

$$\left(\frac{d}{dt}\right)\int_{x_i^n}^{x_{i+1}^n} u \, \mathrm{d}\varsigma = \int_{x_i^n}^{x_{i+1}^n} \left(\frac{\partial u}{\partial t} + \frac{\partial}{\partial \varsigma}(uw)\right) \, \mathrm{d}\varsigma \quad (i = 1, \ldots, h^-) \tag{8.43}$$

and

$$\left(\frac{d}{dt}\right)\int_{x_i^n}^{x_{i+1}^n} z \, \mathrm{d}\varsigma = \int_{x_i^n}^{x_{i+1}^n} \left(\frac{\partial z}{\partial t} + \frac{\partial}{\partial \varsigma}(zw)\right) \, \mathrm{d}\varsigma \quad (i = 1, \ldots, h^-). \tag{8.44}$$

Substituting equations (8.1) and (8.2) into the right-hand sides of (8.43) and (8.44) and performing integration on the right-hand side gives,

$$\begin{aligned}\left(\frac{d}{dt}\right)\int_{x_i^n}^{x_{i+1}^n} u \, \mathrm{d}\varsigma =& \delta \frac{\partial u}{\partial x}\Big|_i^{i+1} + \kappa_{si} u \left(\frac{\partial u}{\partial x} + \frac{\partial z}{\partial x}\right)\Big|_i^{i+1} \\ &+ \int_{x_i^n}^{x_{i+1}^n} (\beta u z - \alpha u - \lambda u) \, \mathrm{d}\varsigma \; + \; uw|_i^{i+1}\end{aligned}$$

and

$$\begin{aligned}\left(\frac{d}{dt}\right)\int_{x_i^n}^{x_{i+1}^n} z \, \mathrm{d}\varsigma =& \delta \frac{\partial z}{\partial x}\Big|_i^{i+1} + z \left(\kappa_{si}\frac{\partial u}{\partial x} + \kappa_{sd}\frac{\partial z}{\partial x}\right)\Big|_i^{i+1} \\ &+ \int_{x_i^n}^{x_{i+1}^n} (\beta u z) \, \mathrm{d}\varsigma \; + \; zw|_i^{i+1}.\end{aligned}$$

Through time integration,

$$\begin{aligned}u_i^{n+1} = \frac{1}{x_{i+1}^{n+1} - x_i^{n+1}} \Bigg(& u_i^n (x_{i+1}^n - x_i^n) + \Delta t \Big(\delta \frac{\partial u}{\partial x}\Big|_i^{i+1} + \kappa_{si} u \left(\frac{\partial u}{\partial x} + \frac{\partial z}{\partial x}\right)\Big|_i^{i+1} \\ & + \int_{x_i^n}^{x_{i+1}^n} (\beta u z - \alpha u - \lambda u) \, \mathrm{d}\varsigma \; + \; uw|_i^{i+1} \Big) \Bigg), \quad (i = 1, \ldots, h^-)\end{aligned} \tag{8.45}$$

with $u_h = 0$ (for all times) from the boundary conditions and

$$z_i^{n+1} = \frac{1}{x_{i+1}^{n+1} - x_i^{n+1}} \left(u_i^n (x_{i+1}^n - x_i^n) + \Delta t \Big(\delta \frac{\partial z}{\partial x}\Big|_i^{i+1} + z \left(\kappa_{si} \frac{\partial u}{\partial x} + \kappa_{sd} \frac{\partial z}{\partial x} \right) \Big|_i^{i+1} + \int_{x_i^n}^{x_{i+1}^n} (\beta u z) \ \mathrm{d}\varsigma \ + \ z w |_i^{i+1} \Big) \right), \quad (i = 1, \ldots, h^-). \tag{8.46}$$

To update z at the node x_h we use,

$$z_i^{n+1} = \frac{1}{x_i^{n+1} - x_{i-1}^{n+1}} \left(u_i^n (x_i^n - x_{i-1}^n) + \Delta t \Big(\delta \frac{\partial z}{\partial x}\Big|_{i-1}^{i} + z \left(\kappa_{si} \frac{\partial u}{\partial x} + \kappa_{sd} \frac{\partial z}{\partial x} \right) \Big|_{i-1}^{i} + \int_{x_{i-1}^n}^{x_i^n} (\beta u z) \ \mathrm{d}\varsigma \ + \ z w |_{i-1}^{i} \Big) \right), \quad (i = h). \tag{8.47}$$

The integrals in (8.45), 8.46) and (8.47) are approximated using the trapezoidal rule.
Lastly, to update z in region $\mathcal{R}_+$ we use the updated x-positions and θ_+^{n+1} in equation (8.47) i.e.,

$$z_i^{n+1} = \frac{\gamma_i \theta_+^{n+1}}{(x_{i+1}^{n+1} - x_i^{n+1})}, \qquad (h_+ \leq i \leq N-1). \tag{8.48}$$

The algorithm for the approximate solution of the reaction-diffusion-advection SI(R) model with a free or moving boundary (8.1) and (8.2) using the moving mesh finite difference method based on relative mass conservation and the combined mass procedure can be summarised as follows.

8.3.7 Algorithm for the SI(R) system

First evaluate the combined mass θ_- and θ_+ by (8.26) and (8.27) and γ_i by (8.28) and (8.29) for each region $\mathcal{R}_-$ and $\mathcal{R}_+$.

Then, at each time step, we proceed with the following calculations:

1. Evaluate the rate of change of mass in each region $\dot{\theta}_-^n$ and $\dot{\theta}_+^n$ by (8.36) and (8.39) respectively.
2. Evaluate the velocity of the interface by (8.30). Calculate the nodal velocities v_i^{n+1} in each region by (8.32) and (8.35). For $\mathcal{R}_-$ the anchor point is taken at x_0 and in region $\mathcal{R}_+$ at x_h.

3. Update the new nodal positions x_i^{n+1} and the new masses θ_-^{n+1} and θ_+^{n+1} by the exponential time-stepping scheme (8.40) for the x-positions and (8.41) for θ_-^{n+1} and (8.42) for θ_+^{n+1} .

4. Obtain u_i^{n+1} and z_i^{n+1} in the region $\mathcal{R}_-$ by the use of the Leibniz integral rule and the updated nodal positions x_i^{n+1} from equations (8.45) and (8.46) respectively. The z_i^{n+1} at $i = h$ is evaluated by (8.47).

5. Recover the solution z_i^{n+1} in region $\mathcal{R}_+$ by equation (8.48).

8.4 Results

Table 8.1 shows the definition of each model parameter and variable.

The relevant control parameters are κ_{si} and κ_{sd} which define the strength of social interactions and are taken to be greater or equal to zero which corresponds to repulsive interactions.
The default variables for the simulations given here are

$$\begin{aligned} \delta_u &= 0.01, \\ \delta_z &= 0.01, \\ \beta &= 0.75, \\ \lambda &= 0.20, \\ \alpha &= 0.035, \\ \mu &= 3, \\ \kappa_{si} &= 0.02, \\ \kappa_{sd} &= 0.002. \end{aligned} \tag{8.49}$$

Let us consider the above parameter values as a base so as to analyse the results by varying some of them.

The model has been encoded on a 1-D domain defined by $0 \leq x \leq 1$. At the initial time, the infected sub-population is set to occupy only a part of the domain defined by $0 \leq x \leq 0.3$ with $x = 0.3$ being the moving interface, and the susceptible sub-population to exist throughout the domain $[0, 1]$. We initially created a mesh with 101 uniformly spaced nodes. We have used a small time-step value of $\Delta t = 0.0001$ to avoid oscillations and ensure the smoothness of the results.

At the outset of an epidemic there are no recovered individuals and nearly everyone is susceptible as the initial infected population is very small compared to

the whole population. Hence, we initially set the susceptible population number to approximately equal the number of the total population ($S \approx S + I + R$). We have chosen to present the sub-populations as a fraction of the total population so we can say that $S \approx 1$ at $t = 0$. Therefore we set the sub-population density z to be constant throughout the domain at $z = 1$. Note that we use S and z to distinguish sub-population numbers from sub-population densities: S is the total number of susceptibles, while z is the number of susceptibles per unit area, i.e., the area under the graph of z at $t = 0$ as shown in Figure 8.1 equals the number of the susceptible population S. The same applies to the infected subgroup with I and u, respectively.
The default parameter values represent an epidemic situation where the disease has the potential to spread throughout the domain as $R_e = \beta S/(\alpha+\lambda) \approx 3.2 > 1$. The initial conditions shown in Figure 8.1 are described by the following functions

$$\begin{aligned}
u(x,0) &= 0.012, && (0 \leq x \leq 0.15)\\
u(x,0) &= (x)(0.3 - x) \times 0.53, && (0.15 \leq x \leq 0.30)\\
u(x,0) &= 0, && (x = 0.3)\\
z(x,0) &= 1, && (0 \leq x \leq 1).
\end{aligned}$$

Figure 8.1 shows the initial conditions used for the following simulations with the sub-populations u and z in green and red colours, respectively. The vertical dashed line at $x = 0.3$ separates (initially) the two regions $\mathcal{R}_-$ and $\mathcal{R}_+$.

The colours green, red and blue were used in all the following illustrations to present u, z and $u+z$, respectively. The black lines in the next illustrations show the result of each sub-population at the final time of the simulation.

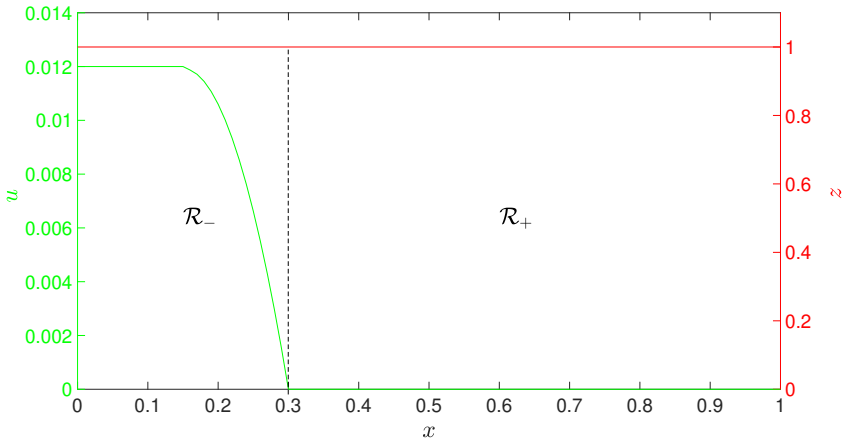

Figure 8.1: The initial conditions. Note the different scales on the y-axes.

We ran the simulations up to $t = 10$ and plotted the results for every 6000 time step. The sub-population time evolution is shown in Figure 8.2 where the black colour lines indicate the final densities at time $t = 10$. We can clearly observe the increase in the total mass of I, i.e., the number of I individuals, and the spread of the infected ones in the domain through the moving front. The total number of susceptible individuals is decreasing as time progresses as well as the total population.

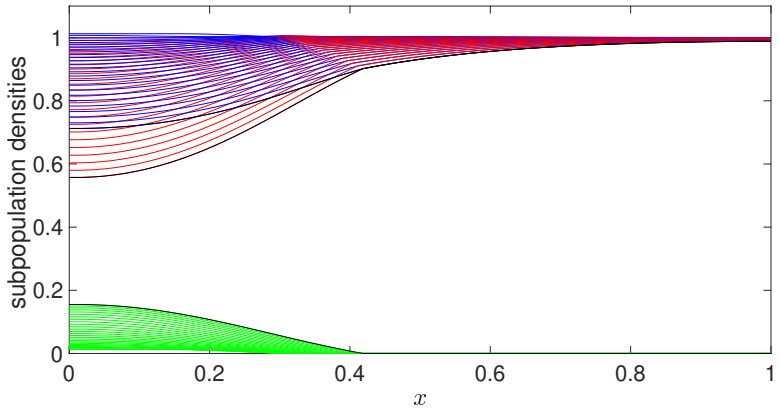

Figure 8.2: The evolution through time of the approximated solutions u (green), z (red) and $u + z$ (blue) plotted for every 6000 time steps up to $t = 10$. The results at $t = 10$ are marked with black colour.

Figures 8.3 show the evolution of the populations at the forward times $t = 20$

and $t = 40$ in Figures 8.3a and 8.3b, respectively. Interestingly we can observe in Figure 8.3a a decrease in the rate of increase of the infected sub-population (the green lines are closer together at final times). This is due to the reduction in the number of susceptibles causing the reproductive parameter of the disease R_e to decrease, i.e., the number of R_e is approximately 2.2 compared to the initial value of $R_e \approx 3.2$. This effect is clearer in Figure 8.3b where the susceptible sub-population is stationary for multiple time steps up to $t = 40$.

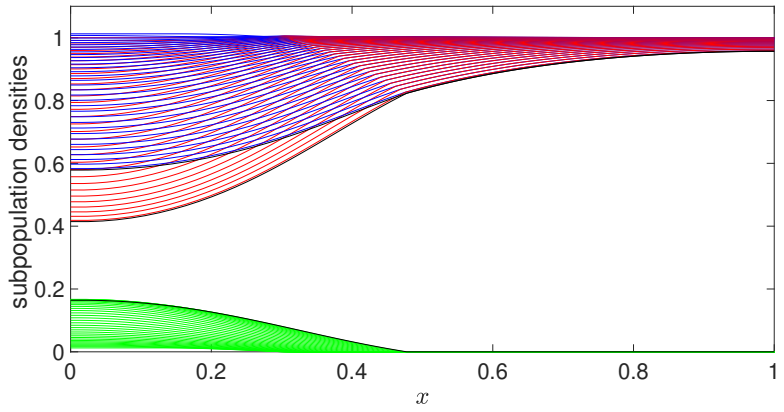

(a) The approximated solution up to $t = 20$.

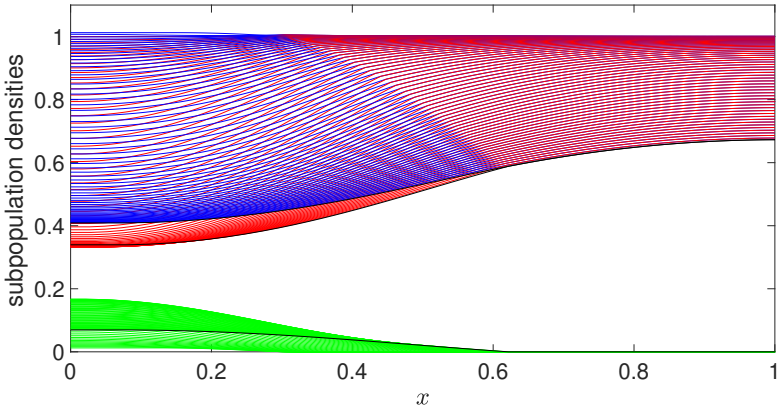

(b) The approximated solution up to $t = 40$.

Figure 8.3: The evolution of the approximated solution plotted for every 6000 time steps up tp $t = 20$ (a) and $t = 40$ (b). The sub-population densities u, z and $u + z$ are marked with green, red and blue colour, respectively, where the results at $t = 20$ and $t = 40$ are shown in black colour.

Figures 8.4 show the results up to $t = 100$ with (8.4a) and without (8.4b) the

social interaction terms. This set of results allows us to see the effect of social distancing and self-isolation over the course of time. We ran the results without including the social interaction terms (cross- and self-diffusion), therefore random diffusion is the only dispersal mechanism in both equations, the results of which are shown in Figure 8.4b. The final sub-populations are shown in black dotted lines. At $t = 100$ the infected population (green) approaches zero and the disease has attenuated while the susceptible and the total population (red and blue) are now stabilised at a constant population density throughout the domain at approximately $u + z \approx z \approx 0.3$. Comparing the two graphs we notice that in the case of the inclusion of social interaction terms (Figure 8.4a), the infected population is more contained regarding both the size of the infected population and the infected radius (spread of the disease through the domain). At the final time $t = 100$, the susceptible population which has not been infected is higher in Figure 8.4a compared to Figure 8.4b.

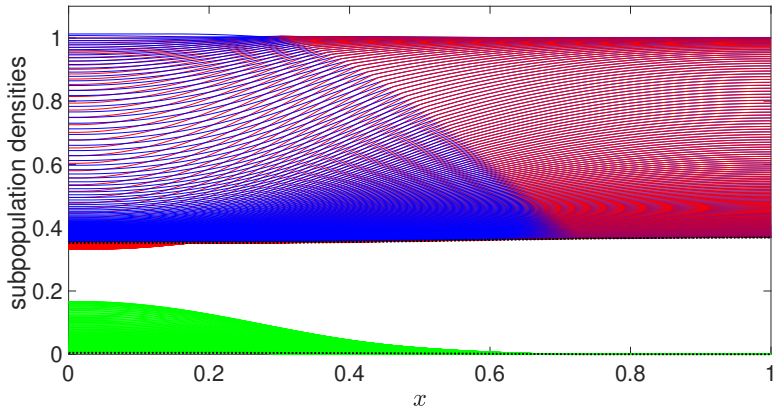

(a) The approximated solution **with** the social interaction terms up to $t = 100$.

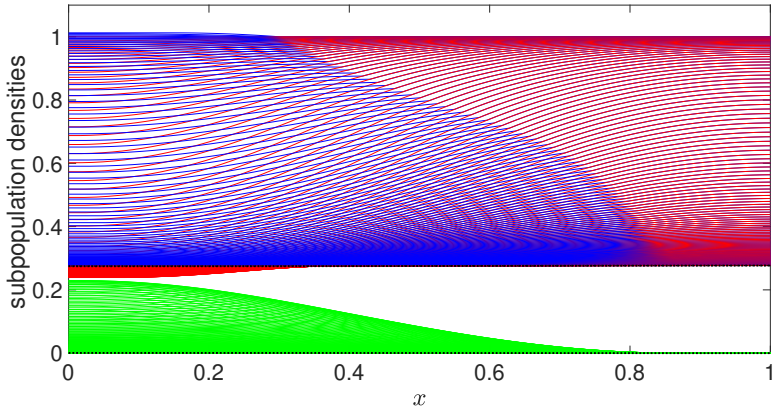

(b) The approximated solution **without** the social interaction terms up to $t = 100$.

Figure 8.4: The evolution of the approximated solutions with (a) and without (b) the social interaction terms, plotted for every 6000 time steps up to $t = 100$. The sub-population densities u, z and $u + z$ are marked with green, red and blue colours respectively where the results at $t = 100$ are shown in black dotted lines.

We also ran the program with various values of κ_{si} while keeping κ_{sd} constant. With κ_{sd} kept at 0.002 we set κ_{si} to take values so that $\kappa_{si} = 2\kappa_{sd}$, $\kappa_{si} = 4\kappa_{sd}$, $\kappa_{si} = 6\kappa_{sd}$, $\kappa_{si} = 8\kappa_{sd}$ and $\kappa_{si} = 10\kappa_{sd}$. We ran the model up to $t = 15$ with all other parameters kept at their values as shown in (8.49). In Figure 8.5b we plotted the results to see the effect of different κ_{si} values on the disease front position and in Figure 8.5a the effect of κ_{si} on the final mass of the infected population θ_I. The results demonstrate that social distancing and self-isolation

cannot change the fate of the disease but can slow its spread.

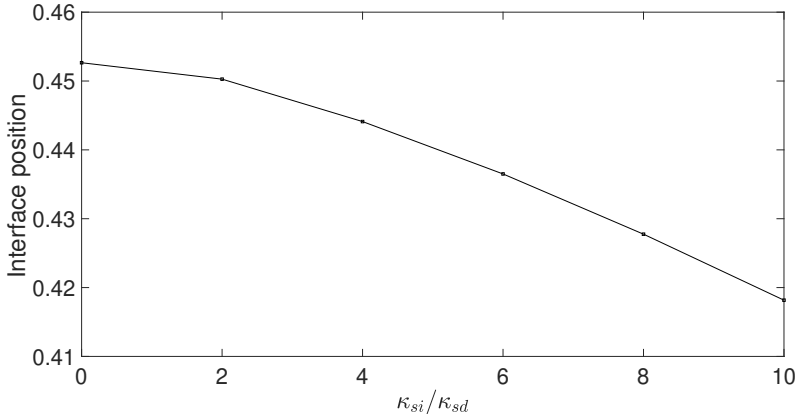

(a) The interface position with different values of κ_{si}/κ_{sd}.

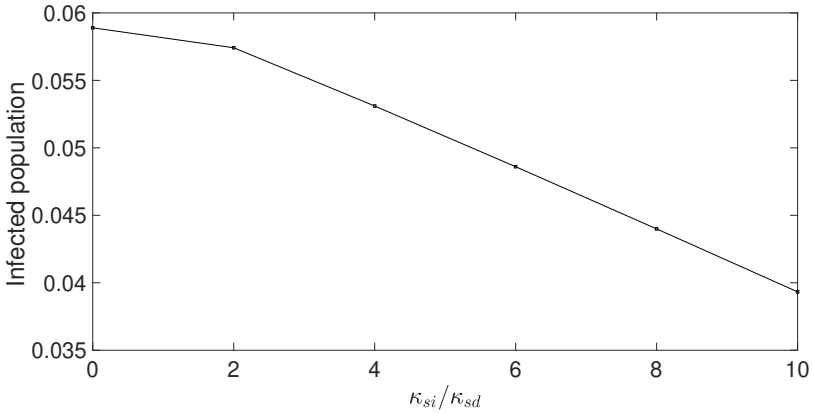

(b) The infected sub-population with different values of κ_{si}/κ_{sd}.

Figure 8.5: The effect of different values of κ_{si}/κ_{sd} on the interface position and the infected sub-population.

Other parameter choices We ran a sensitivity analysis by varying one parameter at a time to test the robustness of the results and to increase the understanding of the relationships between the input parameters and their effect on the system. For the first simulation, we ran the program setting $\mu = 0.4$ instead of 0.3. The results are illustrated in Figures 8.6a and 8.6b for $t = 20$ and $t = 40$ respectively. Comparing the result with Figures 8.3a and 8.3b where $\mu = 0.3$ we can clearly observe the increase in the infected sub-population density in the case of $\mu = 0.4$. Apart from the overall increase in the density of the infected, the virus has spread to almost the whole domain with $h \approx 0.9$ at $t = 40$.

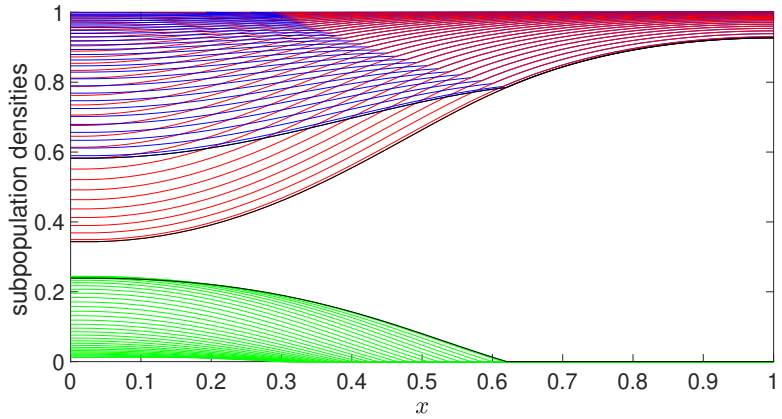

(a) The approximated solution up to $t = 20$ with $\mu = 4$.

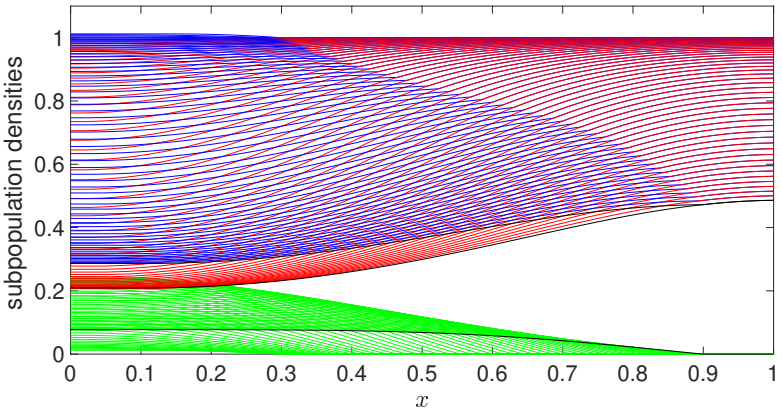

(b) The approximated solution up to $t = 40$ with $\mu = 4$.

Figure 8.6: The evolution of the approximated solution with μ parameter at $\mu = 0.4$ plotted for every 6000 time steps for $t = 20$ (a) and $t = 40$ (b). The subpopulation densities u, z and $u+z$ are marked with green, red and blue colours respectively where the results at $t = 20$ and $t = 40$ are shown in black colour.

The second simulation of which the results are illustrated in Figure 8.7, includes the variation of the infected rate $\beta = 1$ instead of 0.75 (Figure 8.3a). Therefore the reproductive parameter of the disease is initially at approximately 4.3 instead of 3.2. The results in Figure 8.7 reflect the effect of the increased R_e with an overall increase in infected mass. Moreover, the final position of the disease front is at $h \approx 0.7$ instead of $h \approx 0.46$, as observed in Figure 8.3a.

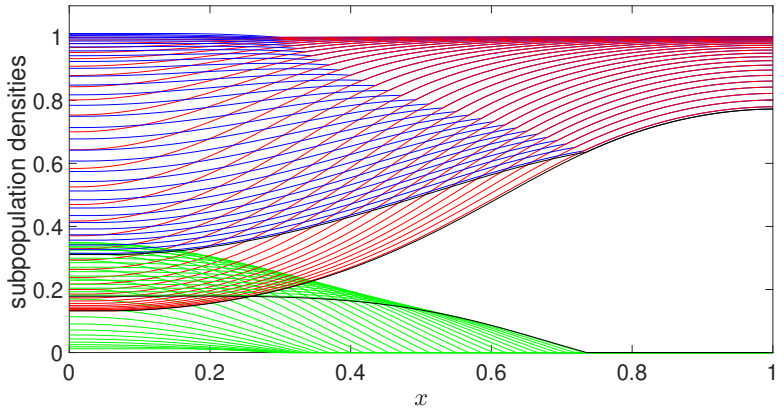

Figure 8.7: The evolution through time of the approximated solutions u (green), z (red) and $u+z$ (blue) with $\beta = 1$ plotted for every 6000 time steps up to $t = 20$. The results at $t = 20$ are marked with black colour.

Figure 8.8 shows the results of setting $\lambda = 0.4$ instead of 0.2 ran up to $t = 40$. The infected overall mass is much less than the one in the results of 8.3b. This is because the infected ones are recovering fast enough affecting the pace by which the sub-population is increasing. Hence, the susceptible population density is higher compared to the results in Figure 8.3b.

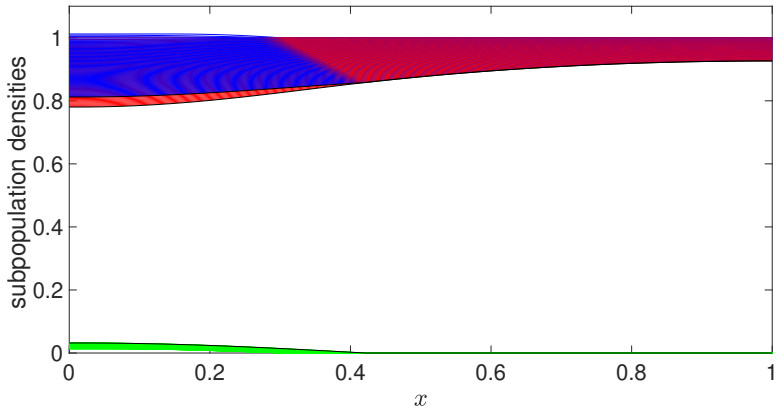

Figure 8.8: The evolution through time of the approximated solutions u (green), z (red) and $u + z$ (blue) with $\lambda = 0.4$ plotted for every 6000 time steps up to $t = 40$. The results at $t = 40$ are marked with black colour.

From the results in Figures 8.6, 8.7 and 8.8, we are able to conclude that our model and the numerical method produce similar results to what we were expecting to obtain according to the parameter values being altered.
We also perform a sensitivity analysis to examine how different values of the varied parameter at each simulation affects the solution. We conclude that small changes in the parameter (i.e., varying the parameter value by 5% or 10%) resulted in small changes in the results and vice-versa for big changes in the parameter (i.e., doubling the parameter value) which resulted in big changes in the results. All the parameters in the reaction terms of our model are of great importance as the reproductive parameter of the disease R_e depends upon them.

The simulation with a small infected radius. Figure 8.9 shows the result of the model without the social interaction terms with the initial position of the moving boundary at 0.05. The initial data are shown in Figure 8.9a. The spatial discretization for this example differs from the previous results. We initially divided the domain by 300 equally spaced nodes. The results are shown in Figure 8.9b, plotted for every 6000 time-steps up to t=20 with $\Delta t = 0.0001$. The black lines show the final sub-population densities at $t = 20$. The population density of the infected, u, is approaching zero while the sub-population density of the susceptibles has stabilised throughout the domain at approximately $z = 0.99$. Interestingly, even if the susceptible sub-population density in the region enclosed by the moving boundary is sufficiently large and the reproductive parameter $R_e > 1$, the infected sub-population density decreases as time advances. Therefore, apart from the reproductive parameter which plays a vital role in the spreading

or vanishing of a disease, an important role is also played by the initial position of the moving boundary. As shown in the paper of Kwang Ik Kim et. al [95], the disease will not spread to the whole area if the basic reproduction number $R_e < 1$ or the initially infected radius h is sufficiently small even if $R_e > 1$.

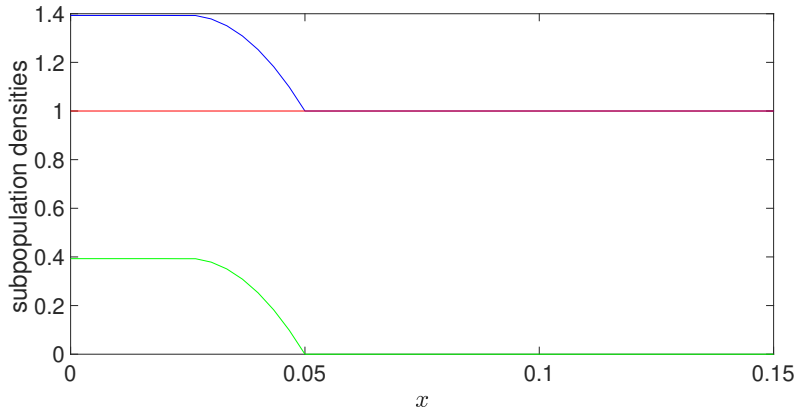

(a) The initial conditions for u in green, z in red and $u+z$ in blue colour.

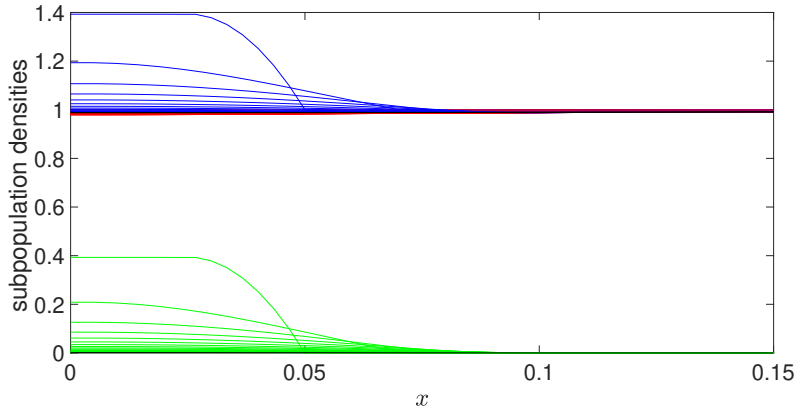

(b) The approximated solution up to $t = 20$.

Figure 8.9: The simulation with the small initial infected radius. Both graphs have been plotted with space range $0 \leq x \leq 0.15$ so that the results are more visible. The results at $t = 20$ are marked with black colour.

8.5 Convergence

We begin by examining the convergence of the finite difference moving mesh method as the number of nodes N increases while keeping Δt constant for all the simulations. We solve for $t = 20$ and compute results for $N = 50 \times 2^{\hat{N}-1}$, $\hat{N} =$

$1, \ldots, 4$. In order to compare the results for different values of $\hat{N}$, we denote the points of the mesh for a particular value of $\hat{N}$ by $x_{i,\hat{N}}$, $i = 0, \ldots, (50 \times 2^{\hat{N}-1})$. We then compute both $x_{2^{\hat{N}-1}j,\hat{N}}$ and the sub-population densities $(u_{2^{\hat{N}-1}j,\hat{N}}, z_{2^{\hat{N}-1}j,\hat{N}})$ at $t = 20$ for each $j = 0, \ldots, 50$ as $\hat{N}$ increases. We have denoted the boundary position by $x_{h_{\hat{N}},\hat{N}}$ where $h_{\hat{N}} = (2^{\hat{N}-1} \times 15) + 1$. The new notation gives the approximation to the values of $x_i(20)$, $u_i(20)$ and $z_i(20)$ at fifty different points for various N determined by $i = 2^{\hat{N}-1}j$. Since an exact solution is not available, we consider the numerical outcome of $\hat{N} = 5$ as the exact as it is supposed to be the more accurate one. Let us denote outcome of the case $\hat{N} = 5$ by $\bar{u}_{2^{\hat{N}-1}j,\hat{N}}$ and $\bar{z}_{2^{\hat{N}-1}j,\hat{N}}$ at the calculated mesh points and $\bar{x}_{h_{\hat{N}},\hat{N}}$ the boundary position, at $t = 20$. We anticipate that the errors $\mid \bar{u}_{2^{\hat{N}-1}j,\hat{N}} - u_{2^{\hat{N}-1}j,\hat{N}} \mid$, $\mid \bar{z}_{2^{\hat{N}-1}j,\hat{N}} - z_{2^{\hat{N}-1}j,\hat{N}} \mid$ and $\mid \bar{x}_{h_{\hat{N}},\hat{N}} - x_{h_{\hat{N}},\hat{N}} \mid$ will decrease as $\hat{N}$ increases, for each $i = 0, \ldots, 50$. We measure the relative errors by calculating the 2-norms of the population densities u_i and z_i and the maximum normal of x_h. For example, the calculation of u_i and x_h error is of the following forms

$$E_N(u) = \sqrt{\frac{\sum_{i=0}^{50}(\bar{u}_{2^{\hat{N}-1}j,\hat{N}} - u_{2^{\hat{N}-1}j,\hat{N}})^2}{\sum_{i=0}^{50}(\bar{u}_{2^{\hat{N}-1}j,\hat{N}})^2}}$$

and

$$E_N(x_h) = \frac{\bar{x}_{h_{\hat{N}},\hat{N}} - x_{h_{\hat{N}},\hat{N}}}{\bar{x}_{h_{\hat{N}},\hat{N}}},$$

for $\hat{N} = 1, \ldots, 5$, $N = 50, 100, 200, 400$. We may examine the order of convergence with respect to space. When Δx is varied with Δt held constant, we expect a fixed non-zero component of the temporal error, so we may estimate the order of convergence by looking at the rate at which the differences between successive errors decrease.

We assume

$$E_N = \mathsf{A}(\Delta x)^p + \mathsf{B}(\Delta t)^q,$$

where the E_N are the errors for each N, A and B are constants and p and q are the rates of convergence with respect to space and time, respectively. Since we are only accounting for spatial errors and with Δx halving, we have

$$E_N = \mathsf{A}(\Delta x)^p \quad \text{and} \quad E_{2N} = \mathsf{A}(\Delta x/2)^p.$$

To eliminate A we divide E_{2N} by E_N, giving the following expression for p

$$p = -\log_2 \left(\frac{E_{2N}}{E_N} \right). \tag{8.50}$$

The Table below 8.2 shows the convergence of the approximate solutions u, z and $u + z$ and the position of the moving boundary x_h where we halved Δx for each simulation while keeping Δt constant. $E_N(u)$ and $E_N(z)$ denote the error of the approximate solutions u and z while $E_N(x_h)$ is the error of the moving boundary position.

N	Error		p
50	$E_N(u)$	4.2×10^{-2}	-
	$E_N(z)$	5.2×10^{-2}	-
	$E_N(x_h)$	2.6×10^{-2}	-
100	$E_N(u)$	1.7×10^{-2}	1
	$E_N(z)$	2.3×10^{-2}	1
	$E_N(x_h)$	1.2×10^{-2}	1
200	$E_N(u)$	5.9×10^{-3}	2
	$E_N(z)$	9.8×10^{-3}	1
	$E_N(x_h)$	5.3×10^{-3}	1
400	$E_N(u)$	1.9×10^{-3}	2
	$E_N(z)$	3.3×10^{-3}	2
	$E_N(x_h)$	1.8×10^{-3}	2

Table 8.2: Relative errors for u, z and x_h with rates of convergence using the exponential time-stepping scheme observed by halving Δx while keeping Δt constant.

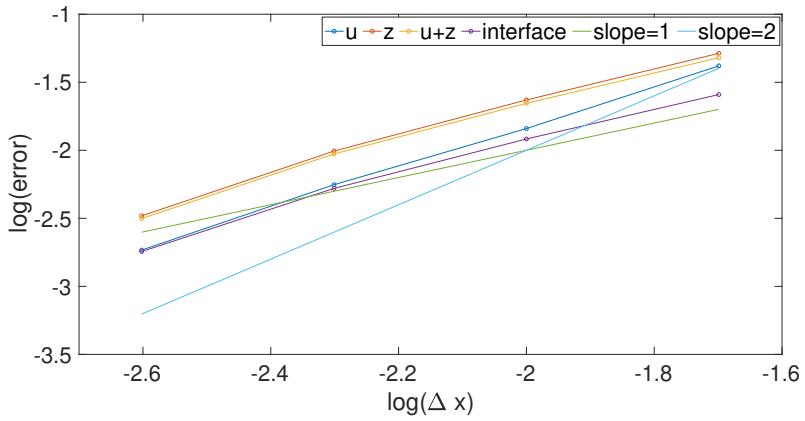

Figure 8.10: Comparison of l^2 errors in the solution and the magnitudes of the errors in the interface node position for the SI(R) in one space dimension, at $T = 20$ for a constant value of Δt in all simulations.

From Table 8.2 we observe that $E_N(u)$, $E_N(z)$ and $E_N(x_h)$ decrease as the number of nodes (N) increases for the moving mesh finite difference method. This suggests that as the number of nodes increases, both the solutions $u_i(t)$ and $z_i(t)$ and the boundary position $x_h(t)$ are converging to the exact solution (approximation solution with $N = 400$). Figure (8.10) shows the convergence of the errors of the approximated solutions u and z as well as the error of the interface position at $t = 20$ as the mesh resolution is increased. The slopes of orders 1 and 2 are plotted for reference. The p values indicate that the rate of convergence increase for both the numerical solution and numerical boundary position in effect to the increase in spatial nodes.

To check our results we have also examined the convergence of the finite difference moving mesh method for the above SI(R) reaction-diffusion-advection equation by halving Δx while adjusting Δt accordingly so that in Case 1 the value of $\Delta t/\Delta x^2$ is kept constant and in Case 2 the value of $\Delta t/\Delta x$ is kept constant for all the simulations. The exact procedure was carried out as the one described above. We examined the order of convergence by (8.50).
The tables 8.3 and 8.4 show the results of Case 1 ($\Delta t/\Delta x^2$) and Case 2 ($\Delta t/\Delta x$), respectively which allow the inspection of how the error varies as N increases and the convergence, given by (8.50), of the approximate solutions u and z and the position of the moving boundary x_h.

N	Error		p
50	$E_N(u)$	4.5×10^{-2}	-
	$E_N(z)$	5.3×10^{-2}	-
	$E_N(x_h)$	2.8×10^{-2}	-
100	$E_N(u)$	1.8×10^{-2}	1
	$E_N(z)$	2.3×10^{-2}	1
	$E_N(x_h)$	1.2×10^{-2}	1
200	$E_N(u)$	6.0×10^{-3}	2
	$E_N(z)$	1.0×10^{-2}	1
	$E_N(x_h)$	5.7×10^{-3}	1
400	$E_N(u)$	1.9×10^{-3}	2
	$E_N(z)$	3.4×10^{-3}	2
	$E_N(x_h)$	1.9×10^{-3}	2

Table 8.3: Case 1: Relative errors for u, z and x_h with rates of convergence using the exponential time-stepping scheme observed by keeping $\Delta t/\Delta x^2$ constant.

N	Error		p
50	$E_N(u)$	4.1×10^{-2}	-
	$E_N(z)$	5.2×10^{-2}	-
	$E_N(x_h)$	2.6×10^{-2}	-
100	$E_N(u)$	1.5×10^{-2}	1
	$E_N(z)$	2.3×10^{-2}	1
	$E_N(x_h)$	1.2×10^{-2}	1
200	$E_N(u)$	6.7×10^{-3}	1
	$E_N(z)$	9.9×10^{-3}	1
	$E_N(x_h)$	5.3×10^{-3}	1
400	$E_N(u)$	2.1×10^{-3}	2
	$E_N(z)$	3.3×10^{-3}	2
	$E_N(x_h)$	1.9×10^{-3}	2

Table 8.4: Case 2: Relative errors for u, z and x_h with rates of convergence using the exponential time-stepping scheme observed by keeping $\Delta t/\Delta x$ constant.

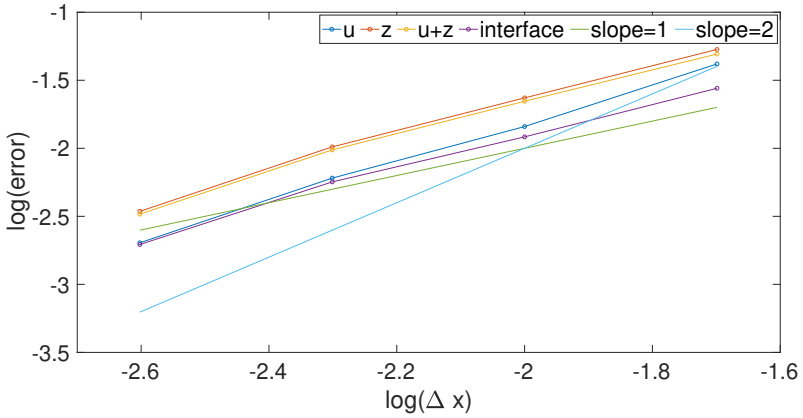

Figure 8.11: Comparison of l^2 errors in the solution and the magnitudes of the errors in the interface node position for the SI(R) in one space dimension, at $T = 20$ for a constant value of $\Delta t/\Delta x^2$ for all simulations.

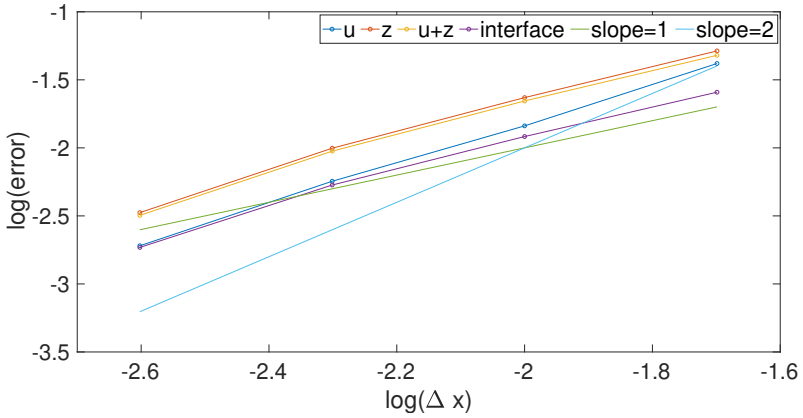

Figure 8.12: Comparison of l^2 errors in the solution and the magnitudes of the errors in the interface node position for the SI(R) in one space dimension, at $T = 20$ for a constant value of $\Delta t/\Delta x$ for all simulations.

We ran three different cases to examine the system's convergence with the numerical method by accounting only for spatial errors. In the first one, we ran the simulations by halving Δx while keeping Δt constant. Moreover, we checked the results by halving Δx while keeping $\Delta t/\Delta x^2$ constant, and finally, for the last case, we kept the value of $\Delta t/\Delta x$ constant for all the simulations while halving Δx. In all three cases, we see that the approximations converge to the exact solution (approximation solution with $N = 400$) as the number of nodes in the

domain increase. Moreover, we observe an increase in the convergence rate as N increases. Comparing Figure 8.11, and 8.10 as well as the values of p in the Tables 8.2, 8.3 and 8.4, we observe approximately the same order of convergence in all three results.

8.6 The reaction-diffusion-advection SIRV system with cross- and self-diffusion on a moving domain

We now consider a mathematical model that focuses on the dynamics of a multi-sub-populations system. Multi-species communities are the subject of significant interest in the ecological literature but have been largely neglected by mathematical modellers. The increased complexity of such systems and the difficulties associated with the solution and analysis of the corresponding models are partially responsible for this neglect. However, considering a system of more than two species gives insights into the possible direct and indirect impacts species have on one another in a multi-species assemblage.

In particular, we wish to consider a multi-sub-populations system comprising the susceptible, infected, recovered and vaccinated subgroups with an alternative choice of diffusion term other than the standard Fickian diffusion.

We recall from Chapter 3 equation (2.13) that the representation of the species velocity by the Fickian diffusion is unreasonable as it leads to a diffusion velocity that tends to infinity as the population density goes to zero.

In the following example of a multi-sub-populations system comprising of the susceptible, infected, recovered and vaccinated subgroups we have chosen to use a simple case of the general density-dependent diffusion, as in Chapter 5 equation (5.2), also referred to as the Porous medium equation. The system presented here assumes that births and deaths from other causes other than the disease are balanced out and there are no re-infections.
Therefore the equations for the susceptible, infected, recovered and vaccinated subgroups respectively, with a density-dependent diffusion, are

$$\begin{aligned}\frac{\partial z}{\partial t} =& \frac{\partial}{\partial x}\left(z\left(\frac{\partial z}{\partial x}+\kappa_{si}\frac{\partial u}{\partial x}+\kappa_{sd}\left(\frac{\partial r}{\partial x}+\frac{\partial z}{\partial x}+\frac{\partial v}{\partial x}\right)\right)\right) \\ & -\beta z u-\rho z \qquad\qquad x\in\mathcal{R}, t>0\end{aligned} \tag{8.51}$$

$$\begin{aligned}\frac{\partial u}{\partial t} =& \frac{\partial}{\partial x}\left(u\left(\frac{\partial u}{\partial x}+\kappa_{si}\left(\frac{\partial u}{\partial x}+\frac{\partial z}{\partial x}+\frac{\partial r}{\partial x}+\frac{\partial v}{\partial x}\right)\right)\right) \\ &+\beta z u-\lambda u-\alpha u+\epsilon\beta v u \qquad\qquad x\in\mathcal{R}_u, t>0\end{aligned} \tag{8.52}$$

$$\begin{aligned}\frac{\partial r}{\partial t} =& \frac{\partial}{\partial x}\left(r\left(\frac{\partial r}{\partial x}+\kappa_{si}\frac{\partial u}{\partial x}+\kappa_{sd}\left(\frac{\partial r}{\partial x}+\frac{\partial v}{\partial x}+\frac{\partial z}{\partial x}\right)\right)\right) \\ &+\lambda u \qquad\qquad x\in\mathcal{R}, t>0\end{aligned} \tag{8.53}$$

$$\begin{aligned}\frac{\partial v}{\partial t} =& \frac{\partial}{\partial x}\left(v\left(\frac{\partial v}{\partial x}+\kappa_{si}\frac{\partial u}{\partial x}+\kappa_{sd}\left(\frac{\partial r}{\partial x}+\frac{\partial v}{\partial x}+\frac{\partial z}{\partial x}\right)\right)\right) \\ &+\rho z-\epsilon\beta v u \qquad\qquad x\in\mathcal{R}, t>0\end{aligned} \tag{8.54}$$

where

$$u(x,t)=0 \qquad x\geq h(t),\ t\geq 0$$

and

$$h'(t)=-\mu\frac{\partial u}{\partial x}(h(t),t) \qquad t\geq 0 \tag{8.55}$$

and with outer boundary conditions

$$\begin{aligned}\frac{\partial u}{\partial x}&=0 \qquad x=a,\quad t\geq 0\\ \frac{\partial z}{\partial x}=\frac{\partial r}{\partial x}=\frac{\partial v}{\partial x}&=0 \qquad x=a, x=b,\quad t\geq 0.\end{aligned} \tag{8.56}$$

Here z, u, r and v denote the susceptible, infected, recovered and vaccinated population densities, respectively, ρ is the vaccination rate and ϵ is the vaccine inefficacy or efficacy ($0\leq\epsilon\leq 1$). So $1-\epsilon$ represents the vaccine efficacy. If $\epsilon=0$, the vaccine offers 100% protection against the disease. The notation of the rest of the parameters is the same as the ones used for the SI(R) system of which the description can be seen in Table 8.1.

Again, the system is defined on a domain $[a,b]$ ($a=0$ and $b=1$) with zero Neumann boundary conditions (8.56) on the two boundaries which indicates no immigration across the boundaries. The individuals of the population densities z, r and v are dispersing throughout the domain while u individuals are spreading in the domain by the moving interface h of which the condition is given by (8.55). The region enclosed by the moving interface, where initially all population subgroups exist, is defined by $\mathcal{R}_u(t)$ while $\mathcal{R}$ defines the whole domain.

8.7 MMFDM method for the SIRV system with a moving boundary

We proceed to the numerical approximation of the susceptible-infected-recovered-vaccinated system using the moving mesh finite difference method based on relative mass conservation using the combined mass approach.

We divide our domain into two regions separated by the moving interface. In such a way we can consider the mass at a specific location to be the combined mass of the densities z, u, r, and v $(z + u + r + v)$ and we move the mesh by supposing that the fractions of the relative mass are preserved in time. The region enclosed by the moving interface is denoted by $\mathcal{R}_-$ where the region on the right of the moving interface is defined by $\mathcal{R}_+$.

The discretizations given in Section (8.3.2) are augmented by the additional approximations $r_i^n \approx r(x,t)$ and $v_i^n \approx v(x,t)$ and then our finite difference moving mesh algorithm for the reaction-diffusion-advection SIRV system with a moving interface is as follows.

We choose the same initial conditions as the ones in Section 8.4, presented by Figure 8.1. The initial condition of the recovered and vaccinated population densities are zero throughout $[0,1]$, i.e., $r(x,0) = v(x,0) = 0,\ (0 \le x \le 1)$.

The initial values θ_-^0 and θ_+^0, approximated by $\theta_- \approx \theta_-(t^n)$ and $\theta_+ \approx \theta_+(t^n)$, of the total masses θ in each region $\mathcal{R}_-$ and $\mathcal{R}_+$ respectively, are evaluated by, (*cf.* (8.26) and (8.27))

$$\theta_-^0 = \frac{1}{2}\sum_{i=0}^{h^-}(x_{i+1}^0 - x_i^0)(u_i^0 + z_i^0 + r_i^0 + v_i^0)$$

and

$$\theta_+^0 = \frac{1}{2}\sum_{i=h^+}^{N}(x_i^0 - x_{i-1}^0)(z_i^0 + r_i^0 + v_i^0),$$

where the constant-in-time relative masses γ_i are approximated by, (*cf.* (8.28) and (8.29))

$$\gamma_i = \frac{1}{\theta_-^0}(x_{i+1}^0 - x_i^0)(u_i^0 + z_i^0 + r_i^0 + v_i^0), \quad (i = 0, \ldots, h^-) \tag{8.57}$$

and

$$\gamma_i = \frac{1}{\theta_+^0}(x_i^0 - x_{i-1}^0)(z_i^0 + r_i^0 + v_i^0), \quad (i = h^+, \ldots, N), \tag{8.58}$$

where h^- and h^+ denote the nodes immediately on the left and on the right of h, respectively.

8.7.1 Approximating the interface velocity

The interface velocity is calculated by equation (8.30).

8.7.2 Approximating the velocity of the interior points

The velocity w_i^n in $\mathcal{R}_-$ can be evaluated from (8.10) by setting the anchor point to be $x = 0$, (*cf.*(8.31))

$$\begin{aligned} w_i^n(z_i^n + u_i^n + r_i^n + v_i^n) &= w_0^n(z_0^n + u_0^n + r_0^n + v_0^n) \\ &- \int_{x_0^n}^{x_i^n} \left(\frac{\partial z(\varsigma, t^n)}{\partial t} + \frac{\partial u(\varsigma, t^n)}{\partial t} + \frac{\partial r(\varsigma, t^n)}{\partial t} + \frac{\partial v(\varsigma, t^n)}{\partial t} \right) \mathrm{d}\varsigma + \gamma_m \dot{\theta}_-^n, \end{aligned} \tag{8.59}$$

where m denotes the interval (x_0^n, x_i^n).
By substituting (8.51), (8.52), (8.53) and (8.54) in (8.59) and since $w_0^n = 0$ the velocity equation for the nodes in region $\mathcal{R}_-$ is,

$$
\begin{aligned}
w_i^n =& \frac{1}{(z_i^n + u_i^n + r_i^n + v_i^n)} \Bigg(\gamma_m \dot{\theta}_-^n \\
& - \int_{x_0^n}^{x_i^n} \left(\frac{\partial}{\partial x} \left(z \left(\frac{\partial z}{\partial x} + \kappa_{si} \frac{\partial u}{\partial x} + \kappa_{sd} \left(\frac{\partial z}{\partial x} + \frac{\partial r}{\partial x} + \frac{\partial v}{\partial x} \right) \right) \right) \right. \\
& \left. - \beta z(x,t) u(x,t) - \rho z(x,t) \right) \, \mathrm{d}\varsigma \\
& - \int_{x_0^n}^{x_i^n} \left(\frac{\partial}{\partial x} \left(u \left(\frac{\partial u}{\partial x} + \kappa_{si} \left(\frac{\partial u}{\partial x} + \frac{\partial z}{\partial x} + \frac{\partial r}{\partial x} + \frac{\partial v}{\partial x} \right) \right) \right) \right. \\
& \left. + \beta z(x,t) u(x,t) - \alpha u(x,t) - \lambda u(x,t) + \epsilon \beta u(x,t) v(x,t) \right) \, \mathrm{d}\varsigma \\
& - \int_{x_0^n}^{x_i^n} \left(\frac{\partial}{\partial x} \left(r \left(\frac{\partial r}{\partial x} + \kappa_{si} \frac{\partial u}{\partial x} + \kappa_{sd} \left(\frac{\partial z}{\partial x} + \frac{\partial r}{\partial x} + \frac{\partial v}{\partial x} \right) \right) \right) \right. \\
& \left. + \lambda u(x,t) \right) \, \mathrm{d}\varsigma \\
& - \int_{x_0^n}^{x_i^n} \left(\frac{\partial}{\partial x} \left(v \left(\frac{\partial v}{\partial x} + \kappa_{si} \frac{\partial u}{\partial x} + \kappa_{sd} \left(\frac{\partial z}{\partial x} + \frac{\partial r}{\partial x} + \frac{\partial v}{\partial x} \right) \right) \right) \right. \\
& \left. + \rho z(x,t) - \epsilon \beta u(x,t) v(x,t) \right) \, \mathrm{d}\varsigma \Bigg),
\end{aligned}
$$

provided that $z_i^n + u_i^n + r_i^n + v_i^n \neq 0$.
Then, by performing the integration and the zero Neumann boundary conditions for the node x_0^n and cancelling out the reaction terms, (*cf.*(8.32))

$$
\begin{aligned}
w_i^n =& \frac{1}{(z_i^n + u_i^n + r_i^n + v_i^n)} \Bigg(\gamma_m \dot{\theta}_-^n \\
& - z_i^n \left(\frac{\partial z}{\partial x} + \kappa_{si} \frac{\partial u}{\partial x} + \kappa_{sd} \left(\frac{\partial z}{\partial x} + \frac{\partial r}{\partial x} + \frac{\partial v}{\partial x} \right) \right)_i \\
& - u_i^n \left(\frac{\partial u}{\partial x} + \kappa_{si} \left(\frac{\partial u}{\partial x} + \frac{\partial z}{\partial x} + \frac{\partial r}{\partial x} + \frac{\partial v}{\partial x} \right) \right)_i \\
& - r_i^n \left(\frac{\partial r}{\partial x} + \kappa_{si} \frac{\partial u}{\partial x} + \kappa_{sd} \left(\frac{\partial z}{\partial x} + \frac{\partial r}{\partial x} + \frac{\partial v}{\partial x} \right) \right)_i \\
& - v_i^n \left(\frac{\partial v}{\partial x} + \kappa_{si} \frac{\partial u}{\partial x} + \kappa_{sd} \left(\frac{\partial z}{\partial x} + \frac{\partial r}{\partial x} + \frac{\partial v}{\partial x} \right) \right)_i - \int_{x_0^n}^{x_i^n} \left(-\alpha u(x,t) \right) \, \mathrm{d}\varsigma \Bigg),
\end{aligned}
\tag{8.60}
$$

where the derivative can be approximated by one-sided approximation and the integration of the reaction term by the trapezium rule. γ_m is evaluated by summing all γ_i over the interval m, $\gamma(x_0^n, x_i^n) = \sum_{j=0}^{i} \gamma_j$ for $i = 1, \ldots, h^-$.

In region $\mathcal{R}_+$ we can evaluate the velocity of the interior nodes of from (8.10) by setting the anchor point $x = h$, (*cf.* (8.33))

$$w_i^n(z_i^n + r_i^n + v_i^n) = w_h^n(z_h^n + r_h^n + v_h^n) + \int_{x_h^n}^{x_i^n} \left(\frac{\partial z(\varsigma, t^n)}{\partial t} + \frac{\partial r(\varsigma, t^n)}{\partial t} + \frac{\partial v(\varsigma, t^n)}{\partial t} \right) \, \mathrm{d}\varsigma - \gamma_m \dot{\theta}_+^n, \tag{8.61}$$

where m denotes the interval (x_h^n, x_i^n).
We then substitute (8.51), (8.53) and (8.54) in (8.61) giving,

$$\begin{aligned} w_i^n = & \frac{1}{(z_i^n + r_i^n + v_i^n)} \Bigg(w_h^n(z_h^n + r_h^n + v_h^n) - \gamma_m \dot{\theta}_+^n \\ & + \int_{x_h^n}^{x_i^n} \frac{\partial}{\partial x} \left(z \left(\frac{\partial z}{\partial x} + \kappa_{si} \frac{\partial u}{\partial x} + \kappa_{sd} \left(\frac{\partial z}{\partial x} + \frac{\partial r}{\partial x} + \frac{\partial v}{\partial x} \right) \right) \right) \\ & - \beta u(x,t) z(x,t) - \rho z(x,t) \, \mathrm{d}\varsigma \\ & + \int_{x_h^n}^{x_i^n} \frac{\partial}{\partial x} \left(r \left(\frac{\partial r}{\partial x} + \kappa_{si} \frac{\partial u}{\partial x} + \kappa_{sd} \left(\frac{\partial z}{\partial x} + \frac{\partial r}{\partial x} + \frac{\partial v}{\partial x} \right) \right) \right) \\ & - \lambda u(x,t) \, \mathrm{d}\varsigma \\ & + \int_{x_h^n}^{x_i^n} \frac{\partial}{\partial x} \left(v \left(\frac{\partial v}{\partial x} + \kappa_{si} \frac{\partial u}{\partial x} + \kappa_{sd} \left(\frac{\partial z}{\partial x} + \frac{\partial r}{\partial x} + \frac{\partial v}{\partial x} \right) \right) \right) \\ & + \rho z(x,t) - \epsilon \beta u(x,t) z(x,t) \, \mathrm{d}\varsigma \Bigg), \end{aligned}$$

since $u = 0$ in $\mathcal{R}_+$. Provided $z_i^n + r_i^n + v_i^n \neq 0$ is not equal to zero.
By performing the integration,

$$\begin{aligned} w_i^n = & \frac{1}{(z_i^n + r_i^n + v_i^n)} \Bigg(w_h^n(z_h^n + r_h^n + v_h^n) - \gamma_m \dot{\theta}_+^n \\ & + \left[z \left(\frac{\partial z}{\partial x} + \kappa_{si} \frac{\partial u}{\partial x} + \kappa_{sd} \left(\frac{\partial z}{\partial x} + \frac{\partial r}{\partial x} + \frac{\partial v}{\partial x} \right) \right) \right]_{x_h^n}^{x_i^n} \\ & + \left[r \left(\frac{\partial r}{\partial x} + \kappa_{si} \frac{\partial u}{\partial x} + \kappa_{sd} \left(\frac{\partial z}{\partial x} + \frac{\partial r}{\partial x} + \frac{\partial v}{\partial x} \right) \right) \right]_{x_h^n}^{x_i^n} \\ & + \left[v \left(\kappa_{si} \frac{\partial u}{\partial x} + \kappa_{sd} \left(\frac{\partial z}{\partial x} + \frac{\partial r}{\partial x} + \frac{\partial v}{\partial x} \right) \right) \right]_{x_h^n}^{x_i^n} \Bigg), \end{aligned} \tag{8.62}$$

since $u = 0$ in $\mathcal{R}_+$ the reaction terms are equal to zero. The derivative terms are now approximated by a one-sided approximation and γ_m is evaluated by summing all γ_i over the interval m, $\gamma(x_h^n, x_i^n) = \sum_{j=h}^{i} \gamma_j$ for $i = h^+, \ldots, i$.

8.7.3 Approximating the rates of change of the populations

The rates of change of the total populations in each region can be evaluated by (8.60) and (8.62) in the region $\mathcal{R}_-$ and $\mathcal{R}_+$, respectively, by setting x_i^n in $\mathcal{R}_-$ at $x_i = x_h$ and for the region $\mathcal{R}_+$ at $x_i = x_N$. A more detailed calculation follows. In $\mathcal{R}_{h^-}$, by setting $x_i = x_h$ equation (8.59) becomes,

$$\begin{aligned} w_h^n(u_h^n + z_h^n + r_h^n + v_h^n) &= w_0^n(u_0^n + z_0^n + r_0^n + v_0^n) \\ &- \int_{x_0^n}^{x_h^n} \left(\frac{\partial z(\varsigma, t^n)}{\partial t} + \frac{\partial u(\varsigma, t^n)}{\partial t} + \frac{\partial r(\varsigma, t^n)}{\partial t} + \frac{\partial v(\varsigma, t^n)}{\partial t} \right) \, \mathrm{d}\varsigma + \gamma_m \dot{\theta}_-^n, \end{aligned} \tag{8.63}$$

where m is the interval (x_0^n, x_h^n).
Substituting equations (8.51), (8.52), (8.53) and (8.54) and performing the integration and the boundary conditions the equation for $\dot{(\theta)}^n$ in $\mathcal{R}_-$ is

$$\begin{aligned} \dot{\theta}_-^n =& z_h^n \left(\frac{\partial z}{\partial x} + \kappa_{si} \frac{\partial u}{\partial x} + \kappa_{sd} \left(\frac{\partial z}{\partial x} + \frac{\partial r}{\partial x} + \frac{\partial v}{\partial x} \right) \right)_h \\ &+ u_h^n \left(\frac{\partial u}{\partial x} + \kappa_{si} \left(\frac{\partial u}{\partial x} + \frac{\partial z}{\partial x} + \frac{\partial r}{\partial x} + \frac{\partial v}{\partial x} \right) \right)_h \\ &+ r_h^n \left(\frac{\partial r}{\partial x} + \kappa_{si} \frac{\partial u}{\partial x} + \kappa_{sd} \left(\frac{\partial z}{\partial x} + \frac{\partial r}{\partial x} + \frac{\partial v}{\partial x} \right) \right)_h \\ &+ v_h^n \left(\frac{\partial v}{\partial x} + \kappa_{si} \frac{\partial u}{\partial x} + \kappa_{sd} \left(\frac{\partial z}{\partial x} + \frac{\partial r}{\partial x} + \frac{\partial v}{\partial x} \right) \right)_h + \int_{x_0^n}^{x_h^n} (-\alpha u(\varsigma, t)) \, \mathrm{d}\varsigma. \end{aligned} \tag{8.64}$$

Note that summing γ_m over the interval (x_0^n, x_h^n) gives 1. Again, we approximate the derivative terms by one-sided approximation and the integration of the reaction terms by the trapezium rule.
Finally, in $\mathcal{R}_+$, by setting $x_i = x_N$ equation (8.61) becomes,

$$\begin{aligned} w_N^n(z_N^n + r_N^n + v_N^n) &= w_h^n(z_h^n + r_h^n + v_h^n) \\ &- \int_{x_h^n}^{x_N^n} \left(\frac{\partial z(\varsigma, t^n)}{\partial t} + \frac{\partial r(\varsigma, t^n)}{\partial t} + \frac{\partial v(\varsigma, t^n)}{\partial t} \right) \, \mathrm{d}\varsigma + \gamma_m \dot{\theta}_+^n, \end{aligned}$$

where m here denotes the interval (x_h^n, x_N^n).
Since $v_N^n = 0$ and by substituting (8.51), (8.53) and (8.54) and applying the integration gives,

$$\begin{aligned}\dot{\theta}_+^n = &- z_i^n \left(\frac{\partial z}{\partial x} + \kappa_{si}\frac{\partial u}{\partial x} + \kappa_{sd}\left(\frac{\partial z}{\partial x} + \frac{\partial r}{\partial x} + \frac{\partial v}{\partial x}\right)\right)_h \\ &- r_h^n \left(\frac{\partial r}{\partial x} + \kappa_{si}\frac{\partial u}{\partial x} + \kappa_{sd}\left(\frac{\partial z}{\partial x} + \frac{\partial r}{\partial x} + \frac{\partial v}{\partial x}\right)\right)_h \\ &- v_h^n \left(\frac{\partial v}{\partial x} + \kappa_{si}\frac{\partial u}{\partial x} + \kappa_{sd}\left(\frac{\partial z}{\partial x} + \frac{\partial r}{\partial x} + \frac{\partial v}{\partial x}\right)\right)_h - w_h^n(z_h^n + r_h^n + v_h^n).\end{aligned} \tag{8.65}$$

Note that summing γ_m over the interval (x_h^n, x_N^n) gives 1 and we have a zero Neumann boundary condition at the right end boundary.
The new nodal positions and the new total masses in each region can be found using the exponential time-stepping scheme as in (8.40), (8.41) and (8.42).
Having found the new location of the nodes and the new masses in each region, we can now update the population densities u, z, r and v at the new time t^{n+1}.

To get u, z, r and v individually in the domain we can simply use the Leibniz integral rule using the updated x-positions in the form.

For example, the population z can be updated by,

$$\left(\frac{d}{dt}\right)\int_{x_i}^{x_{i+1}} z \, \mathrm{d}\varsigma = \int_{x_i}^{x_{i+1}} \left(\frac{\partial z}{\partial t} + \frac{\partial}{\partial \varsigma}(zw)\right) \, \mathrm{d}\varsigma, \quad (i = 1, \ldots, N-1).$$

Substituting equation (8.51) into the right-hand side and performing the integration on the right-hand side gives,

$$\begin{aligned}\left(\frac{d}{dt}\right)\int_{x_i}^{x_{i+1}} z \, \mathrm{d}\varsigma = &\delta\frac{\partial z}{\partial x}\bigg|_i^{i+1} + z\left(\kappa_{si}\frac{\partial u}{\partial x} + \kappa_{sd}\left(\frac{\partial z}{\partial x} + \frac{\partial r}{\partial x} + \frac{\partial v}{\partial x}\right)\right)\bigg|_i^{i+1} \\ &+ \int_{x_i}^{x_{i+1}} (\beta u z) \, \mathrm{d}\varsigma \; + \; zw|_i^{i+1}, \quad (i = 1, \ldots, N-1).\end{aligned}$$

Through time integration,

$$
\begin{aligned}
z_i^{n+1} =& \frac{1}{x_{i+1}^{n+1} - x_i^{n+1}} \Bigg(u_i^n (x_{i+1}^n - x_i^n) \\
&+ \Delta t \Big(\delta \frac{\partial z}{\partial x} \Big|_i^{i+1} + z \left(\kappa_{si} \frac{\partial u}{\partial x} + \kappa_{sd} \left(\frac{\partial z}{\partial x} + \frac{\partial r}{\partial x} + \frac{\partial v}{\partial x} \right) \right) \Big|_i^{i+1} \\
&+ \int_{x_i}^{x_{i+1}} (\beta u z) \ \mathrm{d}\varsigma \ + \ z w |_i^{i+1} \Big) \Bigg), \quad (i = 1, \ldots, N-1).
\end{aligned} \tag{8.66}
$$

The same procedure applies for updating u, r and v throughout the domain by using (8.52), (8.53) and (8.54), respectively.

8.7.4 Algorithm for the SIRV system

Choose initial node positions x_i^0, $i = 0, 1, \ldots, N$ with corresponding approximate solution values z_i^0, u_i^0, r_i^0 and v_i^0 and use them to determine the approximate masses θ_+^0 and θ_-^0 by (8.63) and (8.64). Having found the total masses in each region, we proceed with approximating the relative masses γ_i of (8.57) and (8.58) in each region.

Since we have evaluated the required approximations using the initial data, we proceed at each time step with the following calculations

1. Calculate the rate of change of the total mass in each region $\mathcal{R}_-$ and $\mathcal{R}_+$ by (8.64) and (8.65) respectively.
2. Evaluate the velocity of the interface h by (8.30) and proceed with the velocity of the interior nodes in each region by (8.60) and (8.62).
3. Update the x-positions (x_i^{n+1}) and the new θ_-^{n+1} and θ_+^{n+1} by (8.40), (8.41) and (8.42) respectively.
4. Update the population densities z_i^{n+1}, u_i^{n+1}, r_i^{n+1} and v_i^{n+1} in each region by the use of Leibniz Integral rule and the update nodal positions. i.e., (8.66). The population densities at the outer boundaries z_i^{n+1}, u_i^{n+1}, r_i^{n+1} and v_i^{n+1}, $i = 0$ or $i = N$, can be evaluated by the given boundary conditions.

8.8 Results

We apply the same discretization of the space and time domains as in Section 8.4 (101 equally spaced nodes, $\Delta t = 0.0001$). The same initial conditions were used as in Section 8.4 for z and u with the additional zero initial data for r and v,

$$\begin{aligned}
u(x,0) &= 0.012, && (0 \leq x \leq 0.15)\\
u(x,0) &= (x)(0.3-x) \times 0.53, && (0.15 \leq x \leq 0.30)\\
u(x,0) &= 0, && (x = 0.3)\\
z(x,0) &= 1, && (0 \leq x \leq 1)\\
r(x,0) &= 0, && (0 \leq x \leq 1)\\
v(x,0) &= 0, && (0 \leq x \leq 1).
\end{aligned}$$

The reproductive rate of the disease for the SIVR model in Section 8.6 takes the form $R_e = \frac{\beta(z+\epsilon v)}{\lambda+\alpha}$.
For the following simulations, we use the parameter values stated in (8.49) with the additional parameter values $\rho = 0.06$ and $\epsilon = 0.8$.

We run the simulations at different times to observe the evolution of the disease through the domain. Figure 8.13a shows the results at $t = 10$, Figure 8.13b at $t = 20$ while the results at $t = 40$ can be seen in Figure 8.14. In 8.14a we observe the time evolution of each sub-population at different times and in Figure 8.14b the population densities at time $t = 40$. In all results, the evolution of the population densities through time is shown in blue for the total population, red for the susceptible, in turquoise is the evolution of the vaccinated, and in green and pink is the time evolution of the infected and recovered, respectively. The black lines in Figures 8.13a, 8.13b and 8.14a show the final population densities for each time simulation. Initially, we observe an increase in the population density of the infected(green), recovered(pink) and vaccinated(turquoise) while we see a decrease in the density of the susceptible(red) group and in the total population(blue) density. In Figure 8.13b we see that the vaccinated population density has remained constant for a few time simulations and has now started to decrease. At $t = 40$, as shown in Figure 8.14b we observe a decrease in the infected population density while the susceptible population density is levelling off at around 0.03 throughout the space domain. The total population is now consisting of mostly recovered and vaccinated individuals. The results give confidence that the combined mass feature of the moving mesh method based on conservation can successfully handle systems comprising more than two equations.

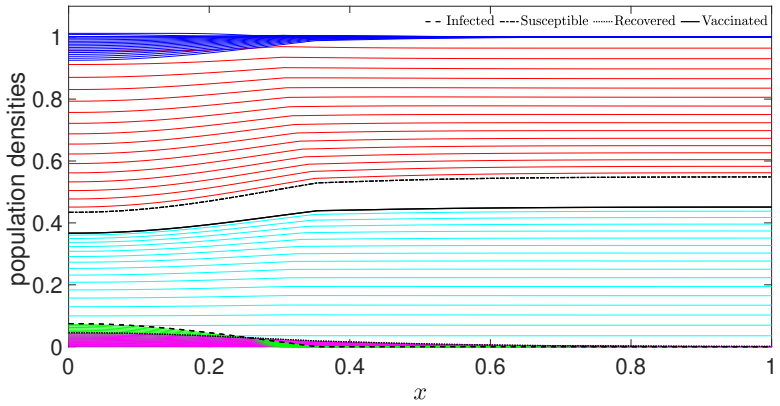

(a) The evolution of the approximated solution up to $t = 10$.

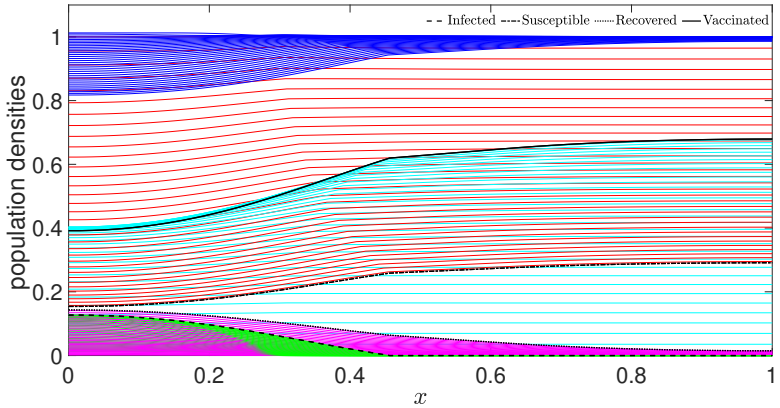

(b) The evolution of the approximated solution up to $t = 20$.

Figure 8.13: The evolution through time of the approximated solution at $t = 10$ (a) and $t = 20$ (b). The total population is shown in blue while red, turquoise, green and pink colours show the population densities of the susceptible, vaccinated, infected and recovered, respectively. Black lines show the final solution for each time.

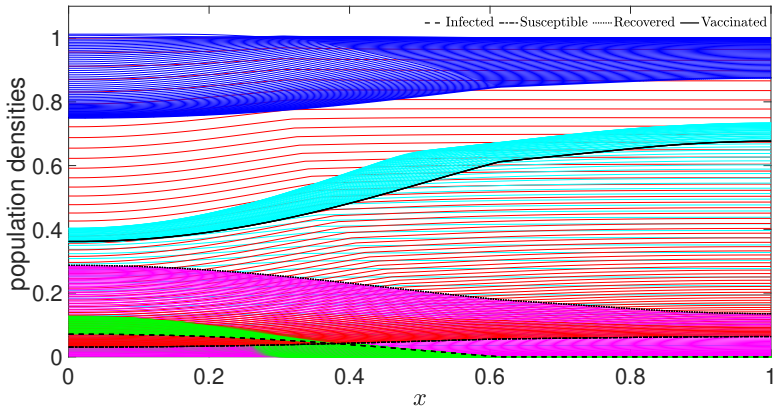

(a) The evolution of the approximated solution up to $t = 40$.

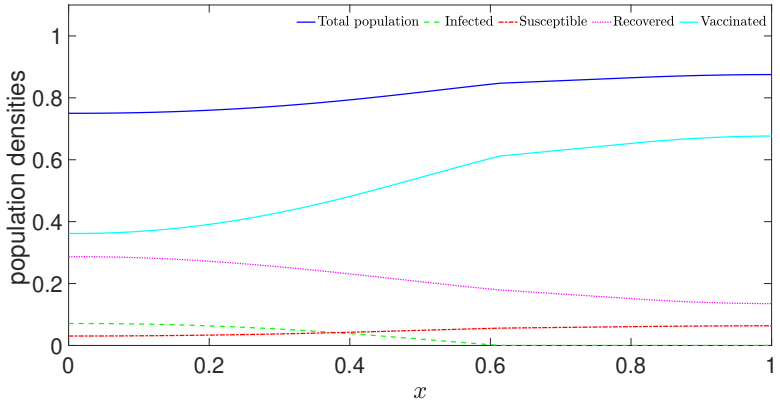

(b) The approximated solution at the time $t = 40$.

Figure 8.14: The results at $t = 40$. The evolution of the approximated population densities through time is shown in (a) where the total population is shown in blue colour while red, turquoise, green and pink colours show the population densities of the susceptible, vaccinated, infected and recovered, respectively and the black lines show the final population densities at $t = 40$. A clearer representation of the final solutions of the population densities can be seen in (b).

8.9 Discussion

In this chapter, we have presented a reaction-diffusion-advection form of the SIR model with a moving boundary which depicts the spreading of the disease in the domain. Self- and cross-diffusion which correspond to social distancing and self-isolation of individuals were examined. Assuming that the recovered individuals are immune to the disease and can no longer transmit the virus implies that the spreading of the disease is not being affected by the recovered ones. Hence, we have only modelled the infected and susceptible sub-populations.

Moving mesh finite difference based on relative mass conservation with a combined mass approach was used to approximate the solution of the SI(R) system. The combined mass approach allows both equations (susceptible and infected) to be modelled on a single mesh by considering the mass at a specific location to be the total mass of the two subgroups. Then, the mesh is generated by conserving the total sum of local densities at that point.

Since the relative masses are conserved, we suppose that the relative densities are also preserved by which theory the equations for the nodal velocities are being constructed and the nodal location is updated at each time. Following the generation of the new mesh, the new local densities for each species separately can be obtained by the use of ALE equations. The time integration is accomplished by the use of the exponential time-stepping scheme which prevents nodes from overtaking, a property which is not provided by the explicit Euler scheme.

The inclusion of self- and cross-diffusion in the modelling of disease allows the consideration of interactions of individuals other than through the reaction terms. The results in Figures 8.4 and 8.5 showed that social distancing and self-isolation could modify the spread of a disease through the area and the number of infections. In the case of a disease outbreak, the priority is to decrease the number of infections and slow the spread of the disease so that the healthcare system can take care of all the cases.

The results of the sensitivity analysis (Figures 8.6, 8.7 and 8.8) by varying one parameter at a time, either by a small or large factor, indicate that the system and the numerical method can produce reasonable behaviour both in terms of the biological meaning of each parameter and the mathematical modelling aspect.

Many factors can affect the spreading or vanishing of a disease. An obvious factor is the reproductive parameter R_e, where the disease vanishes if $R_e < 1$ and spreads over the whole domain if $R_e > 1$. We have shown in Figure 8.9 that another parameter affecting the dominance of the disease is the initial position of the moving boundary. Even if $R_e > 1$, if the initially infected radius h is

sufficiently small, the disease will die out.

Mathematical modelling theories are effective tools for dealing with the time and space evolution of disease outbreaks. They provide us with useful predictions in the context of the impact of intervention in decreasing the number of infected-susceptible incidence rates.

Apart from the infected-susceptible interactions, it is crucial to observe the effect of other sub-populations such as the vaccinated ones, which have a huge impact on the disease evolution. Therefore, we have also approximated a SIRV system (susceptible-infected-recovered-vaccinated) by the use of the moving mesh finite difference based on relative mass conservation with a combined mass approach. The result illustrations indicate that the method is suitable for modelling multi-species communities with great success.

Apart from the extension of the model to a two-dimensional domain, more sophisticated models than the standard SIR model can also be considered, allowing to incorporate, for example, different age groups or seasonal diseases.

8.10 Summary

In this chapter, we used the moving mesh finite difference method based on the conservation of the combined masses of the populations considered in the system. The numerical method allowed us to approximate the solution of a SI(R) model with a moving boundary on a single mesh. The efficiency of this particular approach, the combined mass, includes the use of only one velocity equation to update the node locations as the whole system is approximated on a single mesh instead of assigning a mesh to each sub-population. This also prevents the need for interpolation of the various meshes at each time step to approximate the coupled terms in each equation.

The numerical results provided as illustrations in the chapter, allowed us to observe the impact of social distancing and self-isolation on the spread of the disease which has been included in the model by the use of cross and self-diffusion terms.

We also demonstrated the application of the numerical method on a SIRV model, proving that the new approach based on the conservation of the combined masses can be used to approximate multi-species systems and efficiently deal with systems composed of more than two species (as used before).

Some future extensions of the SIRV model considered in this chapter could be the inclusion of the following:

- Incubation period: A susceptible that comes in contact with an infectious will not automatically move to the infected cluster as it takes some amount of time to display symptoms. How does the inclusion of the incubation period alter the spread of the disease?
- Age-structured populations: A limitation of the model presented above is that the rate of infection is average since the model does not consider pre-existing health conditions, poor quality of healthcare or age. An obvious adaptation of the model to a more updated and realistic system is the addition of age-structured populations reflecting the susceptibility to the disease of the more vulnerable groups, i.e., the old adult group.
- Vaccination efficiency: Now that vaccines are available, UK's government has let its hope on the vaccination of individuals and measures such as social distancing and wearing masks are not compulsory anymore. Is the vaccination alone able to regulate or stop the spread of SARS-CoV-2? How many people need to get vaccinated and how are the results affected by the efficiency of the vaccine?
- Vaccination of children: There were debates in the UK focused on whether to expand the use of SARS-CoV-2 vaccines in children aged 12 years and over. Even though there is very good evidence that children who have SARS-CoV-2 are much less likely to develop severe symptoms and much less likely to die from the disease than adults, a crucial yet unanswered question is how the non-vaccination of children could affect the community as a whole.

In the next chapter, we summarise the work and conclusions of this thesis, and suggest ideas for future work.

Chapter 9

Conclusion

This thesis examined the application of numerical methods for the approximation of various partial differential equations in population dynamics. In particular, the thesis began by considering a reaction-diffusion-advection parasitoid-host system with temperature dependence that was numerically solved using a standard fixed mesh method in two dimensions. The central aim of this investigation was to observe the effect of global warming on the spatial distribution of the interacting species and community formation. Hence, results were derived using the maximum reported temperatures of the years 1950 and 2020 and the maximum temperature predictions for the year 2050 which are shown to be correlated with the insights gained from the model stability analysis. Although such numerical techniques have been successfully used in the literature to approximate various PDEs, their efficacy is limited by accuracy considerations when the solution exhibits a high degree of spatial activity such as a near discontinuity, e.g., at the top or base of a very vertical part of the solution graph. The challenge is even greater if such regions of rapid variation in the solution are moving. To resolve this, it might be better to set a moving point at the discontinuity and replace the PDE with a jump condition at that point leading to the so-called moving boundary.

Reaction-diffusion equations for population dynamics with moving boundaries have been intensively studied analytically in recent years, however, very little numerical work has been done in this field due to numerical challenges in tracking free boundaries. Existing work is mostly focused on the stability analysis of the models while studies on the numerical approximation of such models are very limited.

Mesh adaptation methods for accurately tracking moving boundaries have evolved

considerably over recent years, becoming a versatile tool to accurately simulate a wide range of problems. The application of such methods has concentrated mainly on the numerical approximation of problems in physics such as heat transfer, gas or fluid dynamics, propagation in water waves or the two-phase Stefan problem.

In the thesis, we discussed one method which lies in the broad class of mesh adaptation methods and more specifically in the moving mesh methods. The key advantage of a moving mesh is its ability to adjust its distribution to focus on areas of interest such as a moving boundary, inner interface or blow-up. Increasing the resolution around these features of high activity allows the increase of the accuracy of the solution. The strategy associated with the particular method used here, the conservation method, is to use an integral of the underlying solution of the PDE to preserve a desired quantity, such as mass (i.e., the total number of individuals in a population as used in the thesis), within each patch of elements from which the mesh velocity is constructed. This strategy is related to the GCL method and was first introduced by Baines, Hubbard and Jimack [14] in the context of the finite element framework and later used in [104] using the finite difference method where the method was applied to numerically solve problems describing physical phenomena.

Apart from the standard application of the moving mesh method based on mass conservation as used in [14] and [104], a new feature of the method is presented in this work which is referred to as the combined mass approach. In this approach, the quantity which is preserved within each patch of elements and hence produces the velocity equation for the mesh nodes is the sum of the local densities of all the species involved in the system. Hence the name combined mass. This approach is efficient and neat when dealing with coupled equations with overlapping domains. Instead of assigning a mesh to each species equation, the whole system is solved on a single mesh where the mesh is generated by conserving the total sum of local densities at that point. The attractive aspect of the approach is that avoids the constant interpolation of the meshes at each time step to approximate the coupled terms and hence it is considered to be more accurate and less computationally expensive. Following the generation of the new mesh, the new local densities for each species separately can be obtained by the use of ALE equations.

In this thesis, we studied and numerically solved various reaction-diffusion-advection multi-species models describing different ecological phenomena such as predation, competition or disease models with moving outer or inner boundaries and interfaces where species arise, overlap, or disappear. The strategy followed for each system was first to understand the biological phenomenon we want to model and the species interactions associated with each relationship. Then the models were constructed using similar, existing models in the literature. In cases where the pa-

rameter values were not available from existing studies, we carried out a stability analysis of the model to get an insight into the parameter values required to produce biologically meaningful results by looking at the different equilibrium points of the system. We then applied the appropriate numerical technique according to the nature of the problem, i.e., the fixed or moving mesh method. The strongest indicator of which method is the most suitable one is whether the problem being solved involves any sharp moving features like inner or outer moving fronts or interfaces, hence the use of a moving mesh method is required to accurately approximate these regions. All simulations were carried out in MATLAB without the use of any existing packages. For all systems, we carried out a sensitivity analysis by varying one parameter value by a very small factor to check the effect on the results. We can conclude that small changes in the parameters resulted in small changes in the results. We have also reported illustrations of the results for various parameter choices concluding that the model and the numerical method produce reasonable biological results in the effect of the parameter value being altered.

The main scope of the thesis was to examine the application of numerical methods to approximate systems regarding population dynamics though great attention has been given to the models in particular. We studied models which answer questions of great attention lately in mathematical and biological modelling. For example, we looked at a parasitoid-prey model with climate influence which can be used in any predator-prey framework to observe the impact of global warming on species interactions and their distribution in space. Moreover, due to the outbreak of COVID-19, epidemic models have attracted great attention. In the thesis, we provided a SIRV model with cross and self-diffusion describing the effect of social distancing and self-isolation on the spread of the virus through the domain.

Systems of competitive species were also extensively studied here. For example, we looked at a system of two highly competitive species which are spatially segregated and separated by a moving interface. A version of this model was also considered where the competition between the species is not extremely high to spatially segregate them. Species coexist in space but still compete for common resources. In an effort to create more realistic population models, we also considered a range of advection terms to describe the directed movement of species. The advection terms presented in the thesis take the form of a cross- and self-diffusion which describe the attraction or repulsion between individuals of the same or different populations. Moreover, we looked at an advection term based on a fecundity gradient which describes the tendency of species to move towards more favourable parts of the domain which accounts for both environmental conditions and species interactions. Lastly, we also looked at a non-linear density-

dependent diffusion which can more suitably describe species dispersal compared to the classical Fickian diffusion, especially for very high or very low population densities.

From a numerical perspective, we conclude that the moving mesh finite difference based on conservation and the novel combined mass approach can be used on a variety of ecological models involving multi-species populations and moving boundaries, and the methods are capable of simulating complex behaviour. The results of this thesis are considered proof-of-concept rather than exhaustive and can be refined in several ways and directions.

9.0.1 Further work

The generalisation of the one-dimensional spatial domain models presented in the thesis together with the extension of the moving mesh technique to fully two-dimensional is a priority for future work. The explicit and exponential time-stepping schemes used are proven to be accurate for a range of problems and produced stable results, with no mesh tangling, provided that sufficiently small time steps were taken. We note, however, that when solving real-world problems, it may be desirable to apply a semi-implicit time-stepping scheme since the solution over a larger time may be required.

The population models and simulations in the thesis are novel and are suitable to realistically describe many ecological relationships and real-world situations. Following on from the acquaintance with the background and formulation of differential models of real-world problems and numerical techniques, future work should include the testing and comparison of the behaviour of such models against empirical data sets and explore how findings and predictions can inform and advise on different actions that need to be taken to address various ecological issues.

In doing so, the first step would be to adapt the models' parameters and domains in regard to the situation we wish to model. The models in the thesis are already deployed and are suitable for tackling certain questions, such as how changes in the resource space and changes in the environment might alter behaviour. A first attempt to adapt the model in a realistic domain is shown in Chapter 3 where the model is applied to the Spanish and Portuguese spatial domain and real values of the average maximum temperatures are used.

The next consideration would be to validate existing models. It would be very interesting to compare the behaviour of the models against empirical data sets. The models easily lend themselves to adaptions in the sizes and shapes of the domains and alterations and changes in parameter values without requiring further

calculations. This adaptability means there is a wide range of potential biological and ecological systems on which we could now test the models.

The applications of the models presented in the thesis are limitless and can be proven to be powerful tools that not only provide us with information on current situations but also allow us to predict the future evolution of species accounting for many key factors affecting it. The models and the methods used here can be easily converted into user-friendly software which can be used by experts within different research fields such as ecologists, epidemiologists or even by the policy sector where they could input predefined parameters in order to get meaningful conclusions.

Bibliography

[1] Adjerid, S., & Flaherty, J. E. (1986). A moving finite element method with error estimation and refinement for one-dimensional time dependent partial differential equations. *SIAM Journal on Numerical Analysis, 23*(4), 778-796.

[2] Ahamadi, M., & Harlen, O. G. (2008). A Lagrangian finite element method for simulation of a suspension under planar extensional flow. *Journal of Computational Physics, 227*(16), 7543-7560.

[3] Alan Pounds, J., Bustamante, M. R., Coloma, L. A., Consuegra, J. A., Fogden, M. P., Foster, P. N., ... & Young, B. E. (2006). Widespread amphibian extinctions from epidemic disease driven by global warming. *Nature, 439*(7073), 161-167.

[4] Amarasekare, P., & Nisbet, R. M. (2001). Spatial heterogeneity, source-sink dynamics, and the local coexistence of competing species. *The American Naturalist, 158*(6), 572-584.

[5] Anand, N., Sabarinath, A., Geetha, S., & Somanath, S. (2020). Predicting the Spread of COVID-19 Using SIR Model Augmented to Incorporate Quarantine and Testing. *Transactions of the Indian National Academy of Engineering, 5*(2), 141-148.

[6] Armsworth, P. R., Roughgarden, J. E. (2005). The impact of directed versus random movement on population dynamics and biodiversity patterns. *The American Naturalist, 165*(4), 449-465.

[7] Audusseau, H., Nylin, S., & Janz, N. (2013). Implications of a temperature increase for host plant range: predictions for a butterfly. *Ecology and Evolution, 3*(9), 3021-3029.

[8] Baer, T. A., Cairncross, R. A., Schunk, P. R., Rao, R. R., & Sackinger, P. A. (2000). A finite element method for free surface flows of incompressible

fluids in three dimensions. Part II. Dynamic wetting lines. *International Journal for Numerical Methods in Fluids, 33*(3), 405-427.

[9] Baines, M. J., Hubbard, M. E., & Jimack, P. K. (2011). Velocity-based moving mesh methods for nonlinear partial differential equations. *Communications in Computational Physics, 10*(3), 509-576.

[10] Baines, M. J., Hubbard, M. E., Jimack, P. K., & Mahmood, R. (2009). A moving-mesh finite element method and its application to the numerical solution of phase-change problems. *Communications in Computational Physics, 6*(3), 595-624.

[11] Baines, M. J.,& Christou, K. (2021). A moving-mesh finite-difference method for segregated two-phase competition-diffusion. *Mathematics, 9*(4), 386.

[12] Baines, M. J. (2015). Explicit time-stepping for moving meshes. *Journal of Mathematical Study, 48*(2), 93-105.

[13] Baines, M.J. (1994) *Moving Finite Elements*. Oxford University Press.

[14] Baines, M. J., Hubbard, M. E., & Jimack, P. K. (2005). A moving mesh finite element algorithm for the adaptive solution of time-dependent partial differential equations with moving boundaries. *Applied Numerical Mathematics, 54*(3-4), 450-469.

[15] Baines, M. J., & Christou, K. (2022). A numerical method for multispecies populations in a moving domain using combined masses. *Mathematics, 10*(7), 1124.

[16] Barenblatt, G. I., & Isaakovich, B. G. (1996). *Scaling, self-similarity, and intermediate asymptotics: dimensional analysis and intermediate asymptotics* (No. 14). Cambridge University Press.

[17] Barlow, A. J. (2008). A compatible finite element multi-material ALE hydrodynamics algorithm. *International journal for numerical methods in fluids, 56*(8), 953-964.

[18] Beckett, G., & Mackenzie, J. A. (2001). On a uniformly accurate finite difference approximation of a singularly perturbed reaction–diffusion problem using grid equidistribution. *Journal of computational and applied mathematics, 131*(1-2), 381-405.

[19] Belik, V., Geisel, T., & Brockmann, D. (2011). Natural human mobility patterns and spatial spread of infectious diseases. *Physical Review X, 1*(1), 011001.

[20] Bellard, C., Bertelsmeier, C., Leadley, P., Thuiller, W., & Courchamp, F. (2012). Impacts of climate change on the future of biodiversity. *Ecology letters, 15*(4), 365-377.

[21] Berg, M. P., Kiers, E. T., Driessen, G., Van Der Heijden, M., Kooi, B. W., Kuenen, F., ... & Ellers, J. (2010). Adapt or disperse: understanding species persistence in a changing world. *Global Change Biology, 16*(2), 587-598.

[22] Berres, S., & Ruiz-Baier, R. (2013). Simulation of an epidemic model with nonlinear cross-diffusion. *Numerical methods for hyperbolic equations: theory and applications*, 331-338.

[23] Berteaux, D., Réale, D., McAdam, A. G., & Boutin, S. (2004). Keeping pace with fast climate change: can arctic life count on evolution?. *Integrative and Comparative Biology, 44*(2), 140-151.

[24] Bertsch, M., & Hilhorst, D. (1986). A density dependent diffusion equation in population dynamics: stabilization to equilibrium. *SIAM Journal on Mathematical Analysis, 17*(4), 863-883.

[25] Bjørnstad, O. N., Finkenstädt, B. F., & Grenfell, B. T. (2002). Dynamics of measles epidemics: estimating scaling of transmission rates using a time series SIR model. *Ecological monographs, 72*(2), 169-184.

[26] Boussinesq, J. (1904). Recherches théoriques sur l'écoulement des nappes d'eau infiltrées dans le sol et sur le débit des sources. *Journal de mathématiques pures et appliquées, 10*, 5-78.

[27] Brackbill, J. U., & Saltzman, J. S. (1982). Adaptive zoning for singular problems in two dimensions. *Journal of Computational Physics, 46*(3), 342-368.

[28] Brackbill, J. U. (1993). An adaptive grid with directional control. *Journal of Computational Physics, 108*(1), 38-50.

[29] Bretagnolle, V., & Gillis, H. (2019). Predator-prey interactions and climate change.P.O. Dunn, A.P. Moller (Eds.), *Effects of climate change on birds*, Oxford University Press, 199-220.

[30] Brown, J. H. (1991). New approaches and methods in ecology. *Foundations of ecology*. University of Chicago Press, Chicago, Illinois, USA, 445-455.

[31] Budd, C. J., & Williams, J. F. (2009). Moving mesh generation using the parabolic Monge–Ampère equation. *SIAM Journal on Scientific Computing, 31*(5), 3438-3465.

[32] Budd, C. J., Huang, W., & Russell, R. D. (2009). Adaptivity with moving grids. *Acta Numerica, 18*, 111-241.

[33] Bunting, G., Du, Y., & Krakowski, K. (2012). Spreading speed revisited: analysis of a free boundary model. *Networks Heterogeneous Media, 7*(4), 583.

[34] Burgers, J. M. (1948). A mathematical model illustrating the theory of turbulence. *Advances in applied mechanics, 1*, 171-199.

[35] Cairncross, R. A., Schunk, P. R., Baer, T. A., Rao, R. R., & Sackinger, P. A. (2000). A finite element method for free surface flows of incompressible fluids in three dimensions. Part I. Boundary fitted mesh motion. *International journal for numerical methods in fluids, 33*(3), 375-403.

[36] Cantrell, R. S.,& Cosner, C. (2004). *Spatial ecology via reaction-diffusion equations*. John Wiley Sons.

[37] Cao, W., Huang, W., & Russell, R. D. (2003). Approaches for generating moving adaptive meshes: location versus velocity. *Applied Numerical Mathematics, 47*(2), 121-138.

[38] Cao, W., Huang, W.,& Russell, R. D. (2002). A moving mesh method based on the geometric conservation law. *SIAM Journal on Scientific Computing, 24*(1), 118-142.

[39] Cao, W., Huang, W., & Russell, R. D. (1999). Anr-adaptive finite element method based upon moving mesh PDEs. *Journal of Computational physics, 149*(2), 221-244.

[40] Caramana, E. J., & Shashkov, M. J. (1998). Elimination of artificial grid distortion and hourglass-type motions by means of Lagrangian subzonal masses and pressures. *Journal of Computational Physics, 142*(2), 521-561.

[41] Carcione, J. M., Santos, J. E., Bagaini, C., & Ba, J. (2020). A simulation of a COVID-19 epidemic based on a deterministic SEIR model. *Frontiers in public health*, 230.

[42] Chan, T. F. (1984). Stability analysis of finite difference schemes for the advection-diffusion equation. *SIAM journal on numerical analysis, 21*(2), 272-284.

[43] Chinviriyasit, S., & Chinviriyasit, W. (2010). Numerical modelling of an SIR epidemic model with diffusion. *Applied Mathematics and Computation, 216*(2), 395-409.

[44] Conway, E. D., & Smoller, J. A. (1977). Diffusion and the predator-prey interaction. *SIAM Journal on Applied Mathematics, 33*(4), 673-686.

[45] Conway, E. D., & Smoller, J. A. (1977). A comparison technique for systems of reaction-diffusion equations. *Communications in Partial Differential Equations, 2*(7), 679-697.

[46] Cooper, I., Mondal, A., & Antonopoulos, C. G. (2020). A SIR model assumption for the spread of COVID-19 in different communities. *Chaos, Solitons Fractals, 139*, 110057.

[47] Crooks, E. C., Dancer, E. N., Hilhorst, D., Mimura, M., & Ninomiya, H. (2004). Spatial segregation limit of a competition-diffusion system with Dirichlet boundary conditions. *Nonlinear Analysis: Real World Applications, 5*(4), 645-665.

[48] Dai, F., & Liu, B. (2020). Global solution for a general cross-diffusion two-competitive-predator and one-prey system with predator-taxis. *Communications in Nonlinear Science and Numerical Simulation, 89*, 105336.

[49] Dancer, E. N., Hilhorst, D., Mimura, M., & Peletier, L. A. (1999). Spatial segregation limit of a competition–diffusion system. *European Journal of Applied Mathematics, 10*(2), 97-115.

[50] Dawes, J. H. P., & Souza, M. (2013). A derivation of Holling's type I, II and III functional responses in predator–prey systems. *Journal of theoretical biology, 327*, 11-22.

[51] DeAngelis, D. L., & Zhang, B. (2014). Effects of dispersal in a non-uniform environment on population dynamics and competition: a patch model approach. *Discrete and Continuous Dynamical Systems-B, 19*(10), 3087.

[52] Donea, J., Huerta, A., Ponthot, J. P., & Rodríguez-Ferran, A. (2004). Arbitrary Lagrangian–Eulerian Methods. *Encyclopedia of computational mechanics*.

[53] Du, Y., & Lin, Z. (2010). Spreading-vanishing dichotomy in the diffusive logistic model with a free boundary. *SIAM Journal on Mathematical Analysis, 42*(1), 377-405.

[54] Dubey, B., Das, B., & Hussain, J. (2001). A predator–prey interaction model with self and cross-diffusion. *Ecological Modelling, 141*(1-3), 67-76.

[55] Dvinsky, A. S. (1991). Adaptive grid generation from harmonic maps on Riemannian manifolds. *Journal of Computational Physics, 95*(2), 450-476.

[56] Fan, M., & Kuang, Y. (2004). Dynamics of a nonautonomous predator–prey system with the Beddington–DeAngelis functional response. *Journal of Mathematical Analysis and applications, 295*(1), 15-39.

[57] Gai, C., Iron, D., & Kolokolnikov, T. (2020). Localized outbreaks in an SIR model with diffusion. *Journal of Mathematical Biology, 80*(5), 1389-1411.

[58] Gardner, R. A. (1982). Existence and stability of travelling wave solutions of competition models: a degree theoretic approach. *Journal of Differential equations, 44*(3), 343-364.

[59] Garduno, F. S., & Maini, P. K. (1994). An approximation to a sharp type solution of a density-dependent reaction-diffusion equation. *Applied Mathematics Letters, 7*(1), 47-51.

[60] Gentleman, W., Leising, A., Frost, B., Strom, S., & Murray, J. (2003). Functional responses for zooplankton feeding on multiple resources: a review of assumptions and biological dynamics.*Deep Sea Research Part II: Topical Studies in Oceanography, 50*(22-26), 2847-2875.

[61] Gretchko, S., Marley, J., & Tyson, R. C. (2018). The Effects of Climate Change on Predator-Prey Dynamics. *arXiv preprint arXiv:1805.11816*.

[62] Grindrod, P. (1991). Patterns and waves: The theory and applications of reaction-diffusion equations. *Oxford University Press*.

[63] Grindrod, P. (1988). Models of individual aggregation or clustering in single and multi-species communities. *Journal of Mathematical Biology, 26*(6), 651-660.

[64] Gui-Quan, S., Zhen, J., Quan-Xing, L., & Li, L. (2008). Pattern formation induced by cross-diffusion in a predator–prey system. *Chinese Physics B, 17*(11), 3936.

[65] Guo, J. S., & Wu, C. H. (2012). On a free boundary problem for a two-species weak competition system. *Journal of Dynamics and Differential Equations, 24*(4), 873-895.

[66] Guo, J. S., & Wu, C. H. (2014). Dynamics for a two-species competition–diffusion model with two free boundaries. *Nonlinearity, 28*(1), 1.

[67] Gupta, S. C. (2017). *The classical Stefan problem: basic concepts, modelling and analysis with quasi-analytical solutions and methods*, (Vol. 45), Elsevier.

[68] Gurney, W. S., & Nisbet, R. M. (1975). The regulation of inhomogeneous populations. *Journal of Theoretical Biology, 52*(2), 441-457.

[69] Gurtin, M. E., & MacCamy, R. C. (1977). On the diffusion of biological populations. *Mathematical biosciences, 33*(1-2), 35-49.

[70] Hardin, G. (1960). The Competitive Exclusion Principle: An idea that took a century to be born has implications in ecology, economics, and genetics. *science, 131*(3409), 1292-1297.

[71] Harlen, O. G., Rallison, J. M., & Szabo, P. (1995). A split Lagrangian-Eulerian method for simulating transient viscoelastic flows. *Journal of non-newtonian fluid mechanics, 60*(1), 81-104.

[72] Hastings, A. (2013). Population dynamics. Levin Simon A. (Ed.), *Encyclopedia of Biodiversity* (second ed.), Academic Press, Waltham (2013), 175-181.

[73] Heil, M. (2004). An efficient solver for the fully coupled solution of large-displacement fluid–structure interaction problems. *Computer Methods in Applied Mechanics and Engineering, 193*(1-2), 1-23.

[74] Hilhorst, D., Iida, M., Mimura, M., & Ninomiya, H. (2001). A competition-diffusion system approximation to the classical two-phase Stefan problem. *Japan journal of industrial and applied mathematics, 18*(2), 161-180.

[75] Hilhorst, D., Mimura, M., & Schätzle, R. (2003). Vanishing latent heat limit in a Stefan-like problem arising in biology. *Nonlinear analysis: real world applications, 4*(2), 261-285.

[76] Hindmarsh, A. C., Gresho, P. M., & Griffiths, D. F. (1984). The stability of explicit Euler time-integration for certain finite difference approximations of the multi-dimensional advection–diffusion equation.*International journal for numerical methods in fluids, 4*(9), 853-897.

[77] Holling, C. S. (1959). Some characteristics of simple types of predation and parasitism. *The canadian entomologist, 91*(7), 385-398.

[78] Holling, C. S. (1959). The components of predation as revealed by a study of small-mammal predation of the European Pine Sawfly1. *The Canadian Entomologist, 91*(5), 293-320.

[79] Holmes, E. E., Lewis, M. A., Banks, J. E., & Veit, R. R. (1994). Partial differential equations in ecology: spatial interactions and population dynamics. *Ecology, 75*(1), 17-29.

[80] Holt, R. D., McPeek, M. A. (1996). Chaotic population dynamics favors the evolution of dispersal. *The American Naturalist, 148*(4), 709-718.

[81] Huang, H., & Wang, M. (2015). The reaction-diffusion system for an SIR epidemic model with a free boundary. *Discrete Continuous Dynamical Systems-B, 20*(7), 2039.

[82] Huang, W.,& Russell, R. D. (2001). Adaptive mesh movement—the MMPDE approach and its applications. *Journal of Computational and Applied Mathematics, 128*(1-2), 383-398.

[83] Huang, W., & Russell, R. D. (1998). Moving mesh strategy based on a gradient flow equation for two-dimensional problems. *SIAM Journal on Scientific Computing, 20*(3), 998-1015.

[84] Huang, W., Ren, Y., & Russell, R. D. (1994). Moving mesh methods based on moving mesh partial differential equations. *Journal of Computational Physics, 113*(2), 279-290.

[85] Huang, W., Ren, Y., & Russell, R. D. (1994). Moving mesh partial differential equations (MMPDES) based on the equidistribution principle. *SIAM Journal on Numerical Analysis, 31*(3), 709-730.

[86] Huang, W., & Russell, R. D. (1998). A high-dimensional moving mesh strategy. *Applied Numerical Mathematics, 26*(1-2), 63-76.

[87] Hughes, T. J. (2012). *The finite element method: linear static and dynamic finite element analysis*. Courier Corporation.

[88] Hwang, T. W. (2003). Global analysis of the predator–prey system with Beddington–DeAngelis functional response. *Journal of Mathematical Analysis and Applications, 281*(1), 395-401.

[89] Ivlev, V.S. (1961) *Experimental Ecology of the Feeding of Fish*. Yale University Press, New York, 302.

[90] Jeschke, J. M., Kopp, M., & Tollrian, R. (2002). Predator functional responses: discriminating between handling and digesting prey. *Ecological Monographs, 72*(1), 95-112.

[91] Johnson, T., & Bennett, A. (1995). The thermal acclimation of burst escape performance in fish: an integrated study of molecular and cellular physiology and organismal performance. *The Journal of Experimental Biology, 198*(10), 2165-2175.

[92] Kareiva, P., & Odell, G. (1987). Swarms of predators exhibit" preytaxis" if individual predators use area-restricted search. *The American Naturalist, 130*(2), 233-270.

[93] Kermack, W. O., & McKendrick, A. G. (1927). A contribution to the mathematical theory of epidemics. *Proceedings of the royal society of london. Series A, Containing papers of a mathematical and physical character, 115*(772), 700-721.

[94] Kim, K., Lin, Z., & Ling, Z. (2010). Global existence and blowup of solutions to a free boundary problem for mutualistic model. *Science China Mathematics, 53*(8), 2085-2095.

[95] Kim, K. I., Lin, Z., & Zhang, Q. (2013). An SIR epidemic model with free boundary. *Nonlinear Analysis: Real World Applications, 14*(5), 1992-2001.

[96] Kingsolver, J. G., & Pfennig, D. W. (2007). Patterns and power of phenotypic selection in nature. *Bioscience, 57*(7), 561-572.

[97] Knupp, P. (1995). Mesh generation using vector fields. *Journal of Computational Physics, 119*(1), 142-148.

[98] Knupp, P. M., & Robidoux, N. (2000). A framework for variational grid generation: conditioning the Jacobian matrix with matrix norms. *SIAM Journal on Scientific Computing, 21*(6), 2029-2047.

[99] Ko, W., & Ryu, K. (2008). On a predator–prey system with cross-diffusion representing the tendency of prey to keep away from its predators. *Applied mathematics letters, 21*(11), 1177-1183.

[100] Ko, W., & Ryu, K. (2006). Qualitative analysis of a predator–prey model with Holling type II functional response incorporating a prey refuge. *Journal of Differential Equations, 231*(2), 534-550.

[101] Kuhl, E., Hulshoff, S., & De Borst, R. (2003). An arbitrary Lagrangian Eulerian finite-element approach for fluid–structure interaction phenomena. *International journal for numerical methods in engineering, 57*(1), 117-142.

[102] Kurowski, L., Krause, A. L., Mizuguchi, H., Grindrod, P., & Van Gorder, R. A. (2017). Two-species migration and clustering in two-dimensional domains. *Bulletin of mathematical biology, 79*(10), 2302-2333.

[103] Lee, T. E., Baines, M. J., & Langdon, S. (2015). A finite difference moving mesh method based on conservation for moving boundary problems. *Journal of Computational and Applied Mathematics, 288*, 1-17.

[104] Lee, T. E. (2011). Modelling time-dependent partial differential equations using a moving mesh approach based on conservation (Doctoral dissertation, University of Reading).

[105] Lei, C., Kim, K., & Lin, Z. (2014). The spreading frontiers of avian-human influenza described by the free boundary. *Science China Mathematics, 57*(5), 971-990.

[106] Li, S. B., Xiao, Y., & Dong, Y. (2021) Diffusive predator-prey models with fear effect in spatially heterogeneous environment, *Electronic Journal of Differential Equations*, no. 70, 1-31.

[107] Li, W. T., & Wu, S. L. (2008). Traveling waves in a diffusive predator–prey model with Holling type-III functional response. *Chaos, Solitons Fractals, 37*(2), 476-486.

[108] Li, Z., Teng, Z., & Miao, H. (2017). Modeling and control for HIV/AIDS transmission in China based on data from 2004 to 2016. *Computational and mathematical methods in medicine*.

[109] Li, C. (2016). Global existence of classical solutions to the cross-diffusion three-species model with prey-taxis. *Computers Mathematics with Applications, 72*(5), 1394-1401.

[110] Liu, S., & Liu, X. (2018). Numerical methods for a two-species competition-diffusion model with free boundaries. *Mathematics, 6*(5), 72.

[111] Lotka, A. J. (1920). Analytical note on certain rhythmic relations in organic systems. *Proceedings of the National Academy of Sciences, (67)*, 410-415.

[112] Lou, Y., Zhao, X. Q., Zhou, P. (2019). Global dynamics of a Lotka–Volterra competition–diffusion–advection system in heterogeneous environments. *Journal de Mathématiques Pures et Appliquées, 121*, 47-82.

[113] Ma, T., & Meng, X. (2022). Global analysis and Hopf-bifurcation in a cross-diffusion prey-predator system with fear effect and predator cannibalism. *Mathematical Biosciences and Engineering, 19*(6), 6040-6071.

[114] Marinov, T. T., & Marinova, R. S. (2020). Dynamics of COVID-19 using inverse problem for coefficient identification in SIR epidemic models. *Chaos, Solitons Fractals: X*, 5, 100041.

[115] Meiss, J. D. (2007). Differential dynamical systems. *Society for Industrial and Applied Mathematics*.

[116] Mendes, P. A., & Branco, F. A. (1999). Analysis of fluid–structure interaction by an arbitrary Lagrangian–Eulerian finite element formulation. *International Journal for Numerical Methods in Fluids, 30*(7), 897-919.

[117] Miller, K. (1981). Moving finite elements. II. *SIAM Journal on Numerical Analysis, 18*(6), 1033-1057.

[118] Miller, K., & Miller, R. N. (1981). Moving finite elements. I. *SIAM Journal on Numerical Analysis, 18*(6), 1019-1032.

[119] Mimura, M., Yamada, Y., & Yotsutani, S. (1987). Free boundary problems for some reaction-diffusion equations. *Hiroshima mathematical journal, 17*(2), 241-280.

[120] Mimura, M. (1981). Stationary pattern of some density-dependent diffusion system with competitive dynamics. *Hiroshima Mathematical Journal, 11*(3), 621-635.

[121] Morton, K. W., & Mayers, D. F. (2005). *Numerical solution of partial differential equations: an introduction*. Cambridge University press.

[122] Murray, J. D. (2002). *Mathematical biology: I. An introduction*. Springer-Verlag, Berlin.

[123] Muskat, M. (1938). The flow of homogeneous fluids through porous media. *Soil Science, 46*(2), 169.

[124] Okubo, A., & Levin, S. A. (2001). *Diffusion and ecological problems: modern perspectives* (Vol. 14). New York: Springer.

[125] Paaijmans, K. P., Heinig, R. L., Seliga, R. A., Blanford, J. I., Blanford, S., Murdock, C. C., & Thomas, M. B. (2013). Temperature variation makes ectotherms more sensitive to climate change. *Global change biology, 19*(8), 2373-2380.

[126] Parmesan, C. (2007). Influences of species, latitudes and methodologies on estimates of phenological response to global warming. *Global change biology, 13*(9), 1860-1872.

[127] Pearce, I. G., Chaplain, M. A., Schofield, P. G., Anderson, A. R., & Hubbard, S. F. (2006). Modelling the spatio-temporal dynamics of multi-species host–parasitoid interactions: heterogeneous patterns and ecological implications. *Journal of Theoretical Biology, 241*(4), 876-886.

[128] Petchey, O. L., McPhearson, P. T., Casey, T. M., & Morin, P. J. (1999). Environmental warming alters food-web structure and ecosystem function. *Nature, 402*(6757), 69-72.

[129] Peterson, R. C., Jimack, P. K., & Kelmanson, M. A. (1999). The solution of two-dimensional free-surface problems using automatic mesh generation. *International journal for numerical methods in fluids, 31*(6), 937-960.

[130] Pettet, G. J., McElwain, D. L. S., & Norbury, J. (2000). Lotka-Volterra equations with chemotaxis: walls, barriers and travelling waves. *Mathematical Medicine and Biology: A Journal of the IMA, 17*(4), 395-413.

[131] Piggott, M. D., Gorman, G. J., Pain, C. C., Allison, P. A., Candy, A. S., Martin, B. T., & Wells, M. R. (2008). A new computational framework for multi-scale ocean modelling based on adapting unstructured meshes. *International Journal for Numerical Methods in Fluids, 56*(8), 1003-1015.

[132] Poggiale, J. C., & Auger, P. (2004). Impact of spatial heterogeneity on a predator-prey system dynamics. *Comptes rendus biologies, 327*(11), 1058-1063.

[133] Press, W. H., Teukolsky, S. A., Vetterling, W. T., & Flannery, B. P. (2007). *Numerical recipes 3rd edition: The art of scientific computing*. Cambridge university press.

[134] Rall, B. C., Vucic-Pestic OL., Ehnes, R. B., Emmerson, M., & Brose, U. (2010). Temperature, predator–prey interaction strength and population stability. *Global Change Biology, 16*(8), 2145-2157.

[135] Réale, D., McAdam, A. G., Boutin, S., & Berteaux, D. (2003). Genetic and plastic responses of a northern mammal to climate change. *Proceedings of the Royal Society of London. Series B: Biological Sciences, 270*(1515), 591-596.

[136] Ren, G., & Liu, B. (2022). Global existence and convergence to steady states for a predator-prey model with both predator-and prey-taxis. *Discrete & Continuous Dynamical Systems, 42*(2), 759.

[137] Robinson, R. C. (2012). An introduction to dynamical systems: continuous and discrete (Vol. 19). *American Mathematical Soc.*

[138] Rojas, S. (2020). *The epidemiological SIR model on coronavirus COVID-19 pandemic data.* Physics Department, University Simón Bolivar, Caracas, Venezuela.

[139] Rowell, J. T. (2009). The limitation of species range: a consequence of searching along resource gradients. *Theoretical Population Biology, 75*(2-3), 216-227.

[140] Saksono, P. H., Dettmer, W. G., & Perić, D. (2007). An adaptive remeshing strategy for flows with moving boundaries and fluid–structure interaction. *International Journal for Numerical Methods in Engineering, 71*(9), 1009-1050.

[141] Schmidt, A. (1996). Computation of three dimensional dendrites with finite elements. *Journal of Computational Physics, 125*(2), 293-312.

[142] Sekerci, Y. (2020). Climate change effects on fractional order prey-predator model. *Chaos, Solitons & Fractals, 134*.

[143] Sekerci, Y., & Petrovskii, S. (2015). Mathematical modelling of plankton–oxygen dynamics under the climate change. *Bulletin of mathematical biology, 77*(12), 2325-2353.

[144] Sheridan, J. A., Bickford, D. (2011). Shrinking body size as an ecological response to climate change. *Nature climate change, 1*(8), 401-406.

[145] Skalski, G. T., & Gilliam, J. F. (2001). Functional responses with predator interference: viable alternatives to the Holling type II model. *Ecology, 82*(11), 3083-3092.

[146] Snyder, R. E., & Chesson, P. (2004). How the spatial scales of dispersal, competition, and environmental heterogeneity interact to affect coexistence. *The American Naturalist, 164*(5), 633-650.

[147] Soulaimani, A., & Saad, Y. (1998). An arbitrary Lagrangian-Eulerian finite element method for solving three-dimensional free surface flows. *Computer methods in applied mechanics and engineering, 162*(1-4), 79-106.

[148] Shigesada, N., Kawasaki, K., & Teramoto, E. (1979). Spatial segregation of interacting species. *Journal of theoretical biology, 79*(1), 83-99.

[149] Sugie, J., Kohno, R., & Miyazaki, R. (1997). On a predator-prey system of Holling type. *Proceedings of the American Mathematical Society, 125*(7), 2041-2050.

[150] Sun, G. Q., Jin, Z., Liu, Q. X., & Li, L. (2009). Spatial pattern in an epidemic system with cross-diffusion of the susceptible. *Journal of Biological Systems, 17*(01), 141-152.

[151] Szabo, P., & Hassager, O. (1995). Simulation of free surfaces in 3-D with the arbitrary Lagrange–Euler method. *International journal for numerical methods in engineering, 38*(5), 717-734.

[152] Szabó, B., & Babuška, I. (2021). Finite Element Analysis: Method, Verification and Validation.

[153] Tang, T. (2005). Moving mesh methods for computational fluid dynamics. *Contemporary mathematics, 383*(8), 141-173.

[154] Taylor, N. P., Kim, H., Krause, A. L., & Van Gorder, R. A. (2020). A non-local cross-diffusion model of population dynamics I: emergent spatial and spatiotemporal patterns. *Bulletin of Mathematical Biology, 82*(8), 1-40.

[155] Te Vrugt, M., Bickmann, J., & Wittkowski, R. (2020). Effects of social distancing and isolation on epidemic spreading modeled via dynamical density functional theory. *Nature communications, 11*(1), 1-11.

[156] Thompson, R. N. (2020). Epidemiological models are important tools for guiding COVID-19 interventions. *BMC medicine, 18*(1), 1-4.

[157] Travis, J. M., Murrell, D. J., & Dytham, C. (1999). The evolution of density–dependent dispersal. *Proceedings of the Royal Society of London. Series B: Biological Sciences, 266*(1431), 1837-1842.

[158] Turchin, P. (2013). Complex population dynamics. *In Complex Population Dynamics*. Princeton university press.

[159] Van Grunsven, R. H., Van Der Putten, W. H., Bzemer, T. M., Tamis, W. L., Berendse, F., & Veenendaal, E. M. (2007). Reduced Plant-Soil Feedback of Plant Species Expanding Their Range as Compared to Natives. *Journal of Ecology*, 1050-1057.

[160] Vázquez, J. L. (2007). *The porous medium equation: mathematical theory*. Oxford University Press on Demand.

[161] Vázquez, J. L. (1992). An introduction to the mathematical theory of the porous medium equation. *In Shape optimization and free boundaries*, 347-389. Springer, Dordrecht.

[162] Verhulst, P.F. (1845). La loi d'accroissement de la population. *Nouveaux Memories de l'Académie Royale des Sciences et Belles-Lettres de Bruxelles*, 18, 14-54.

[163] Visser, M. E., & Holleman, L. J. (2001). Warmer springs disrupt the synchrony of oak and winter moth phenology. *Proceedings of the Royal Society of London. Series B: Biological Sciences, 268*(1464), 289-294.

[164] Voigt, W., Perner, J., Davis, A.J., Eggers, T., Schumacher, J., Bährmann, R., Fabian, B., Heinrich, W., Köhler, G., Lichter, D. & Marstaller, R. (2003). Trophic levels are differentially sensitive to climate. *Ecology, 84*(9), 2444-2453.

[165] Volterra, V. (1926). Fluctuations in the abundance of a species considered mathematically. *Nature, 118*(2972), 558-560.

[166] Walkley, M. A., Gaskell, P. H., Jimack, P. K., Kelmanson, M. A., & Summers, J. L. (2005). Finite element simulation of three-dimensional free-surface flow problems. *Journal of Scientific Computing, 24*(2), 147-162.

[167] Walkley, M. A., Gaskell, P. H., Jimack, P. K., Kelmanson, M. A., & Summers, J. L. (2005). Finite element simulation of three-dimensional free-surface flow problems with dynamic contact lines. *International Journal for Numerical Methods in Fluids, 47*(10-11), 1353-1359.

[168] Wang, J., Guan, Y., Wu, L., Guan, X., Cai, W., Huang, J., Dong, W. and Zhang, B. (2021). Changing lengths of the four seasons by global warming. *Geophysical Research Letters, 48*(6).

[169] Wang, X., & Wei, J. (2015). Dynamics in a diffusive predator–prey system with strong Allee effect and Ivlev-type functional response. *Journal of Mathematical Analysis and Applications, 422*(2), 1447-1462.

[170] Wang, M., & Zhao, J. (2014). Free boundary problems for a Lotka–Volterra competition system. *Journal of Dynamics and Differential Equations, 26*(3), 655-672.

[171] Wang, M., & Zhao, J. (2017). A free boundary problem for the predator–prey model with double free boundaries. *Journal of Dynamics and Differential Equations, 29*(3), 957-979.

[172] Wang, M., & Zhang, Y. (2017). Note on a two-species competition-diffusion model with two free boundaries. *Nonlinear Analysis, 159*, 458-467.

[173] Wang, W., Cai, Y., Wu, M., Wang, K., & Li, Z. (2012). Complex dynamics of a reaction–diffusion epidemic model. *Nonlinear Analysis: Real World Applications, 13*(5), 2240-2258.

[174] Wang, S., Zhang, J., Xu, F., & Song, X. (2017). Dynamics of virus infection models with density-dependent diffusion. *Computers Mathematics with Applications, 74*(10), 2403-2422.

[175] Warsi, Z. U. A., & Mastin, C. W. (1982). *Numerical grid generation* (Vol. 1982). J. F. Thompson (Ed.). Amsterdam: North-Holland.

[176] Wathen, A. J., & Baines, M. J. (1985). On the structure of the moving finite-element equations. *IMA journal of numerical analysis, 5*(2), 161-182.

[177] Watkins, A. R., & Baines, M. J. (2017). A Two-Phase Moving Mesh Finite Element Model of Segregated Competition-Diffusion. *Preprint MPCS-2018-07.*

[178] Watkins, A. (2017). *A moving mesh finite element method and its application to population dynamics* (Doctoral dissertation, University of Reading).

[179] Watkinson, A. R., & Gill, J. A. (2002). Dispersal Ecology.

[180] Wedajo, A. J., Bole, B. K., & Koya, P. R. (2018). Analysis of SIR mathematical model for malaria disease with the inclusion of infected immigrants. *IOSR Journal of Mathematics, 14*, 10-21.

[181] Wesseling, P. (2009). *Principles of computational fluid dynamics* (Vol. 29). Springer Science Business Media.

[182] Wesseling, P. (1996). von Neumann stability conditions for the convection-diffusion equation.*IMA journal of Numerical Analysis, 16*(4), 583-598.

[183] Whitaker, S. (1986). Flow in porous media I: A theoretical derivation of Darcy's law. *Transport in porous media, 1*(1), 3-25.

[184] Winslow, A. M. (1966). Numerical solution of the quasilinear Poisson equation in a nonuniform triangle mesh. *Journal of computational physics, 1*(2), 149-172.

[185] Wu, C. H. (2015). The minimal habitat size for spreading in a weak competition system with two free boundaries. *Journal of Differential Equations, 259*(3), 873-897.

[186] Yang, W., Zheng, Q., Shen, J. & Hu, Q., (2022). Pattern Dynamics in a Predator-Prey Model with Diffusion Network. *Complexity.*

[187] Zel'Dovich, Y.B. and Raizer, Y.P. (1966). Physics of Shock Waves and High-Temperature Hydrodynamic Phenomena II, Academic Press, New York.

[188] Zhang, G., & Wang, X. (2014). Effect of diffusion and cross-diffusion in a predator-prey model with a transmissible disease in the predator species. *In Abstract and Applied Analysis*, Hindawi.